Multi-Element Abundances as Probes of Galaxy Growth Across Cosmic Time

Thesis by
Zhuyun Zhuang

In Partial Fulfillment of the Requirements for the
Degree of
Doctor of Philosophy

CALIFORNIA INSTITUTE OF TECHNOLOGY
Pasadena, California

2026
Defended May 22, 2025

Zhuyun Zhuang
ORCID: 0000-0002-1945-2299

To the brave little girl, who endured, who fought, who never gave up—this is the future you made possible.

ACKNOWLEDGMENTS

It has been nineteen years since I read my first book about astronomy, and more than a decade since I made up my mind to (at least try to) become an astronomer and earn a degree in astronomy from here. Even now, it feels almost surreal that this childhood dream is finally coming true. Along this long and winding journey, I have been extraordinarily fortunate to meet many wonderful people who have inspired, encouraged, and supported me through both hardship and triumph. This thesis is dedicated to all those incredible individuals, to whom I owe more thanks than words can express.

First and foremost, to the best advisors I could have ever hoped for, Chuck Steidel and Evan Kirby.

Evan has been a guiding light in my life since I joined his group in my first year. I am deeply grateful for his open-mindedness in allowing me to pursue the research directions I was genuinely passionate about, and for forgiving me for never being excited about r-process or s-process elements. He has always been patient, supportive, and generous with praise, even in moments when I struggled to believe in myself. Thank you, Evan, for listening to and tolerating my endless frustrations about research and life, and still encouraging me with unwavering belief. Being your student has been one of the greatest privileges of my graduate journey.

My heartfelt thanks also go to Chuck, who generously took me in after Evan moved, and under whose mentorship I spent most of my PhD. I have been consistently inspired by Chuck's brilliance, curiosity, and keen scientific insight. I'm especially grateful for him always being available for me, whether for research guidance or for last-minute feedback on paper drafts and proposals. Even though I sometimes complain that many of our two-hour conversations didn't lead to definitive conclusions, I later find them incredibly enlightening and insightful, especially when I encounter new problems in my research or listen to other science talks at conferences. Those long conversations have truly shaped who I am as a researcher today.

I am also grateful to both Evan and Chuck for their steadfast support in proposal writing and Keck observing runs, which have been among the most incredible and unforgettable experiences of my PhD. I extend my thanks as well to Rosalie McGurk and the Keck Observatory staff for their help during these observations.

To the mentors and colleagues I've had the privilege of working with. Thank you to

Nicha Leethochawalit for patiently and repeatedly teaching me how to perform stellar population synthesis and full-spectrum fitting. I am grateful to Karl Glazebrook for introducing me to the world of lensed galaxies. Many thanks to Mia de los Reyes and Yuguang Chen for their invaluable guidance during my early years in graduate school, and to Allison Strom for inspiring conversations about chemical abundances and for always checking in on me whenever I stopped by CIERA. Special thanks to Nik Prusinski for his tremendous help with KCWI data reduction, and for the many soul-searching conversations that pulled me through difficult stretches of research. I am also deeply thankful to my undergraduate advisor, Yong Shi, the first astronomer I worked with and the one who introduced me to the world of observational extragalactic astronomy.

To my thesis committee members — Chris Martin, Phil Hopkins, Mansi Kasliwal, and Vikram Ravi — and to the Caltech Astronomy faculty and staff, thank you for your thoughtful feedback on my thesis plan and for broadening my horizons in astronomy. I especially want to acknowledge Shri Kulkarni and Lin Yan for their early mentorship during my undergraduate research.

To my friends at Caltech. Thank you, Yuhan, for your unwavering support and deep conversations over the years, and for always standing by me even after leaving Pasadena. Thank you, Samantha, Xiaoshan, and Mandy, for all the delicious food and boba, and for cheering me up in difficult times. Thank you, Yapeng, for listening with such patience to my worries, anxieties, and complaints, for the many late-night conversations, and for all the wonderful meals. To the rest of my cohort — Evan N., Yashvi, Viraj, Sarah, and Max — thank you for sharing the ups and downs of our first year, even amidst the challenges of the COVID lockdown. Thank you to Mia, Nik, Jerry, Jean, Ivey, Sam P., Zhihui, Yuanze, Isaac, and the rest of the incredible astrograd community for making my time at Caltech warmer and more vibrant.

To my friends who have shaped different parts of my life. My deepest gratitude goes to Huanghao, one of my best friends since middle school and my roommate for most of my time at Caltech, who has incredibly shared eleven years of academic life with me. Thank you for inspiring me with your strength, brilliance, resilience, and optimism, for your unconditional support in my lowest moments and for sharing all the joys in this journey. I truly cannot imagine graduate school without you. I'm also deeply thankful to Yining for the countless deep conversations across the Pacific Ocean, and for the laughs and tears we've shared over the last decade. I'm so lucky we met on the very first day of college and have remained close ever since.

Special thanks to Shihui and Yudan for accompanying me through the difficult years of my adolescence. My heartfelt gratitude also goes to Jiayi, my steadfast friend since before we could even walk. Thank you for always being there, and for being the person I can share absolutely everything with.

To my loved ones. I owe everything to my mom Ying D., who has selflessly sacrificed so much for my education and my growth and supported me unconditionally, no matter what path I chose. Mom, you are the strongest, most resilient person in my life. None of this would have been possible without your seen and unseen love. Thank you, Guochao, for being my constant through every rise and fall. Thank you, truly, for everything.

Lastly, to the little girl I once was, the one who dared to dream of the stars, even when the world around her felt dim. Her world was small, but her dreams were vast. Every step she took brought me here. Thank you for your courage, your persistence, and for believing in a future I now have the privilege to live. This PhD isn't just mine; it's yours, too. We made it.

ABSTRACT

This thesis presents a comprehensive study of multi-elemental abundances in galaxies across a wide range of stellar masses, star formation rates, and redshifts, aiming to better characterize mass–metallicity relations (MZRs) and to probe the physical processes that govern chemical enrichment in galaxies over cosmic time.

Chapter 2 demonstrates that low- and high-mass stellar MZRs can be placed on a consistent absolute scale by comparing stellar metallicities from resolved and integrated-light spectroscopy in NGC 147, a Local Group dwarf galaxy. The two methods yield consistent $[\mathrm{Fe/H}]_*$ values, validating integrated-light techniques in measuring stellar metallicity in distant galaxies.

In Chapter 3, I analyze deep Keck spectra of two gravitationally lensed, quiescent galaxies at $z \gtrsim 1$. Both galaxies are metal-poor compared to local analogs but share comparable [Mg/Fe]. These results suggest that both galaxies experienced early, rapid star formation and strong outflows that depleted their gas reservoirs and drove early quenching.

Chapter 4 introduces a new sample of 46 star-forming and 2 quiescent systems with $M_* = 10^8$–$10^{10} M_\odot$ at $z \sim 0$, observed with the Keck Cosmic Web Imager (KCWI). Combining with SDSS data, I construct the first consistently derived Fe- and Mg-MZRs from 10^8 to $10^{11.5} M_\odot$. I find that scatter in the stellar MZRs is driven by varying sSFR, with more active galaxies showing lower stellar abundances at fixed mass. This chapter also presents the first comparison of α elements (O and Mg) in stars and the ionized gas beyond the Local Group, revealing a tight $[\mathrm{Mg/H}]_*$–$[\mathrm{O/H}]_\mathrm{g}$ correlation. The finding that $[\mathrm{O/H}]_\mathrm{g}$ generally exceeds $[\mathrm{Mg/H}]_*$ implies star formation is fueled by enriched, well-mixed interstellar medium rather than pristine gas inflows.

Chapter 5 further explores spatially resolved nebular and stellar properties in the KCWI sample. Star-forming dwarfs exhibit clumpy star formation, diverse local ionization conditions, and smooth stellar mass profiles. Some show established gas-phase metallicity gradients, although diffuse ionized gas may bias gradient measurements.

Together, these studies advance our understanding of how elemental abundances evolve across different galaxy masses and redshifts, offering new insights into the processes that regulate galaxy growth, enrichment, and quenching.

PUBLISHED CONTENT AND CONTRIBUTIONS

Zhuang, Z. et al. (Sept. 2024). "Metals in Star-forming Galaxies with KCWI. I. Methodology and First Results on the Abundances of Iron, Magnesium, and Oxygen". In: *ApJ* 972.2, p. 182. DOI: 10.3847/1538-4357/ad5ff8.
Z.Z. participated in the conception of the project, obtained and analyzed the data, and wrote the bulk of the manuscript.

Zhuang, Z. et al. (May 2023). "A Glimpse of the Stellar Populations and Elemental Abundances of Gravitationally Lensed, Quiescent Galaxies at z $\gtrsim$ 1 with Keck Deep Spectroscopy". In: *ApJ* 948.2, p. 132. DOI: 10.3847/1538-4357/acc79b.
Z.Z. participated in the conception of the project, obtained and analyzed the data, and wrote the bulk of the manuscript.

Zhuang, Z. et al. (Oct. 2021). "NGC 147 Corroborates the Break in the Stellar Mass-Stellar Metallicity Relation for Galaxies". In: *ApJ* 920.1, p. 63. DOI: 10.3847/1538-4357/ac1340.
Z.Z. analyzed the data and wrote the bulk of the manuscript.

TABLE OF CONTENTS

LIST OF ILLUSTRATIONS

LIST OF TABLES

Chapter 1

INTRODUCTION

1.1 The Role of Chemical Abundances in Galaxy Evolution

One of the ultimate goals of science—and indeed of all intellectual pursuits—is to understand the existence of human beings as well as all other forms of life around us. As astronomers, one of the ways to answer this profound question is to decipher the universe's remarkable ability to generate and distribute the elements heavier than hydrogen and helium—such as carbon, oxygen, magnesium, and iron—that are the building blocks of life.

Unlike hydrogen and helium that were created within a few minutes after the Big Bang around 13.7 billion years ago, these heavy elements, often referred to as "metals" by astronomers, can only be created by stars. Stars act as cosmic furnaces where nuclear fusion converts hydrogen and helium into heavier elements up to iron. At the end of their life cycles, stars release metals into the interstellar medium (ISM) through supernova explosions or stellar winds, during which elements heavier than iron are produced. Some of these metals are recycled into the next generation of stars, some are expelled from galaxies by outflows driven by stellar feedback or galactic feedback, and others remain in the gas. Meanwhile, relatively pristine gas inflows consisting of little metals from the surrounding circumgalactic medium (CGM) can dilute the chemical abundances of the ISM while serving as fuel to sustain the continuing star formation. The dynamic processes of forming and redistributing these various heavy elements collectively result in an evolving chemical composition of stars and gas as star formation continues. That said, the chemical enrichment of a galaxy is shaped by the interplay among star formation, gas inflows and outflows, and feedback from supernovae and active galactic nuclei (AGN). By characterizing the elemental abundances in stars and gas of galaxies at different stages (i.e., described by their masses, ages, star formation rates, environments, etc.), we can reconstruct the overall galaxy assembly history, assess the efficiency of metal retainment and probe the timescales over which different enrichment processes operate.

1.1.1 Metals as Tracers of Galactic Evolution

Different elements are synthesized in different types of stars and on varying timescales, making multi-element abundance measurements a powerful tool for constraining a

galaxy's star formation and chemical enrichment history (see Nomoto, Kobayashi, and Tominaga, 2013, for a comprehensive review). Among the heavy elements, iron and oxygen are the most commonly measured. Iron is often used as a proxy for stellar metallicity due to the abundance of iron absorption features in stellar spectra, while oxygen serves as a tracer of gas-phase metallicity because it is the most abundant heavy element in the ISM and exhibits strong emission lines in the optical spectrum. When the signal-to-noise (S/N) in the stellar continuum is sufficiently high, magnesium abundances can also be measured, typically using the Mg b triplet near 5170 Å.

Iron-peak elements are primarily produced by Type Ia supernovae, whose progenitors are usually low-mass stars or interacting binaries, with a characteristic delay timescale of $\gtrsim$ 100 Myr, extending up to several Gyr (Maoz, Mannucci, and Brandt, 2012). On the other hand, massive stars with initial mass above $10M_{\odot}$ end their short lives ($\sim$ 10 Myr) as core-collapse supernovae, enriching the ISM with α elements such as oxygen and magnesium. As a result, iron abundances tend to trace enrichment on longer timescales, while oxygen and magnesium reflect more recent chemical enrichment. Galaxies with extended star formation histories (SFH) typically exhibit lower [α/Fe] or [Mg/Fe] ratios, because they have had sufficient time for iron enrichment from delayed Type Ia supernovae.

1.2 Observational Approaches to Measuring Abundances

1.2.1 Stellar Abundances of Iron and Magnesium

Stellar abundance measurements play an important role in understanding the chemical enrichment history of galaxies. There are two primary spectroscopic approaches for determining stellar chemical abundances: resolved stellar spectroscopy and integrated-light spectroscopy. Each approach has its own strengths and limitations, the choice between which largely depends on the distance of the target galaxy. In practice, it is typically not possible to apply both methods to the same system except in special cases, such as presented in Chapter 2.

Resolved Stellar Spectroscopy

In nearby galaxies, individual stars can be resolved and observed with medium- to high-resolution spectroscopy, enabling direct measurements of elemental abundances (such as iron and α elements) in individual stars from absorption features in their stellar atmospheres. Large spectroscopic surveys like APOGEE (Majewski

et al., 2017), which use high-resolution infrared spectroscopy, have mapped multi-element abundances across the Milky Way (Nidever et al., 2014; Hayden et al., 2015). Medium-resolution spectroscopy on large ground-based telescopes, such as the Keck telescopes, has also been used to determine the detailed abundances of red giant stars in dwarf satellite galaxies beyond the Milky Way (e.g., Kirby, Guhathakurta, and Sneden, 2008). Galactic metallicity is then determined as the luminosity-weighted value of metallicity distribution of individual stars. These resolved stellar abundance measurements reveal the metals locked into the stars formed at different epochs, providing the most detailed information on the chemical enrichment history of a galaxy. However, this method is limited to galaxies within the Local Group where most of the galaxies are dwarf satellites, as it is generally infeasible to resolve individual stars in more distant galaxies without gravitational lensing.

Integrated-Light Spectroscopy

For more massive and distant galaxies that cannot be resolved into individual stars, stellar metallicities must be inferred from integrated-light spectroscopy—that is, from the combined starlight of the entire stellar population. This method requires constructing spectral templates of galaxies (i.e., stellar population synthesis (SPS) models) to compare against observed spectra (Figure 1.1) and relies on many assumptions about the underlying stellar properties (see Conroy, 2013, for a comprehensive review).

The simplest such model is the simple stellar population (SSP), which assumes that all stars formed at the same time with the same metallicity and abundance pattern. To construct SSPs across a range of ages and metallicities, one must adopt an initial mass function (IMF), choose stellar isochrones, and use either empirical or synthetic stellar spectral libraries. SSPs have been widely used to measure the ages and metallicities of quiescent galaxies (e.g., Choi et al., 2014; Kriek et al., 2016; Leethochawalit et al., 2018a), as their SFHs are relatively simple. Previous studies have shown that while SSP-based models tend to yield younger ages than those derived from more complex models (Choi et al., 2014), the inferred SSP metallicities are generally robust and consistent with the results measured with more realistic assumptions on the SFHs(Mentz et al., 2016; Leethochawalit et al., 2018a).

For more complex systems like star-forming galaxies, which experience ongoing star

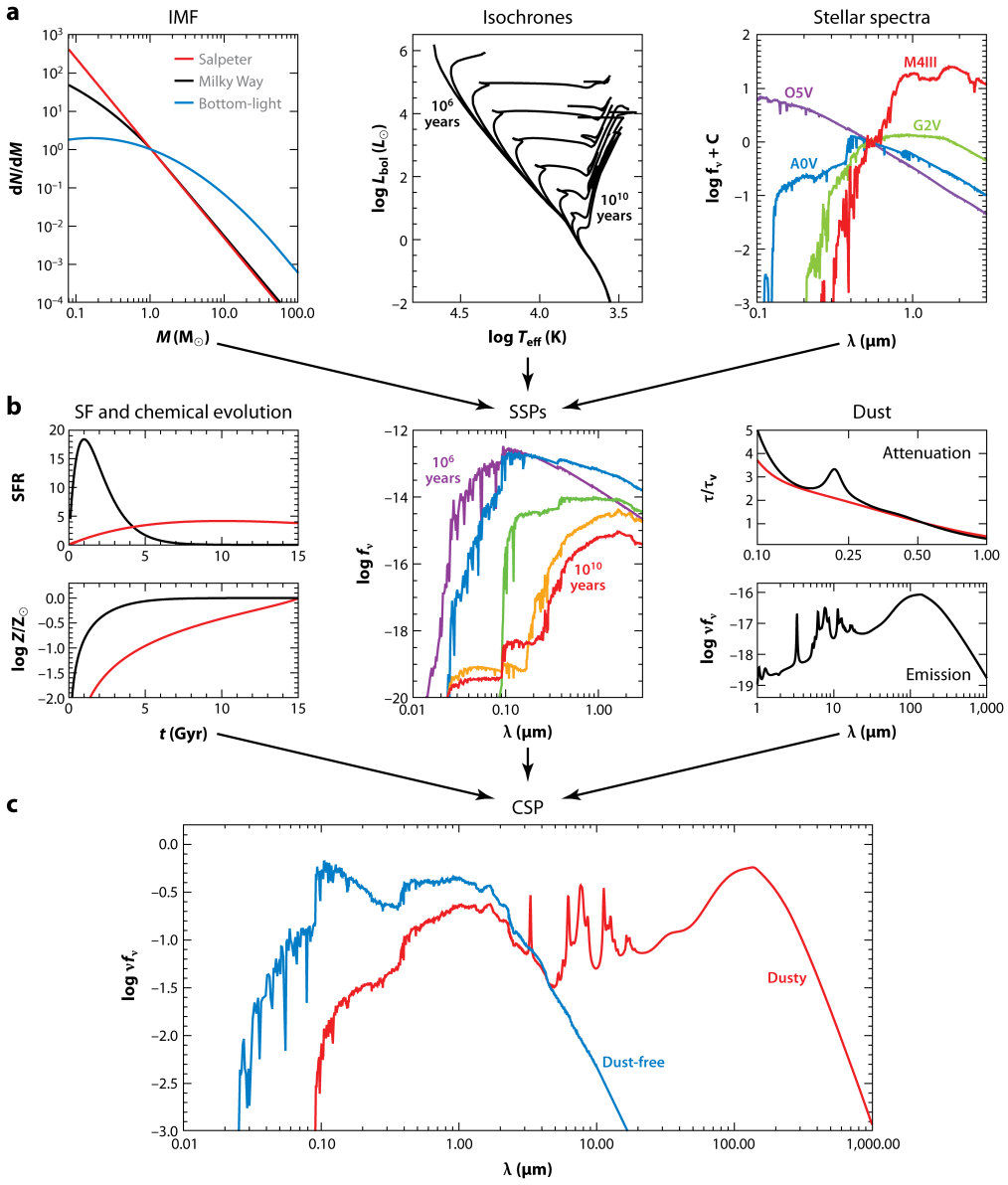

Figure 1.1: Overview of stellar population synthesis. (a) Ingredients used for constructing SSP models: an IMF, isochrones for a range of ages and metallicities, stellar spectra for of different spectral types. (b) Components needed for constructing CSP models: SFH and chemical evolution models, SSPs, and a model for dust attenuation and emission. Figure reproduced from Conroy (2013).

formation, composite stellar population (CSP) models are more appropriate. CSP is a linear combination of SSPs of different ages and metallicities, weighted according to an assumed SFH and chemical evolution history. Dust attenuation and emission can also be incorporated into these models to represent a more realistic galaxy. Because of the additional degrees of freedom, the derived ages and metallicities are more sensitive to the assumed SFH and chemical enrichment history. A common approach is to use either a parametric or non-parametric SFH while assuming a single metallicity for the population (e.g., Carnall et al., 2018; Leja et al., 2019), or to fit the observed spectra with a linear combination of SSPs spanning multiple ages and metallicities (e.g., Cid Fernandes et al., 2005; Cappellari, 2017).

Both SSP and CSP models described above typically assume solar abundance patterns. To measure individual element abundances such as magnesium, models with variable abundance patterns must be constructed. This is commonly done using response functions, which quantify how the theoretical SSP spectrum changes with the enhancement or depletion of a given element relative to solar-scaled models (Conroy et al., 2018). Response functions for elements like Mg are computed at various ages and metallicities (Figure 1.2), and then applied to SSPs based on empirical stellar libraries. This hybrid approach enables more accurate modeling of observed spectra with non-solar abundance patterns, allowing for measurements of element ratios such as [Mg/Fe].

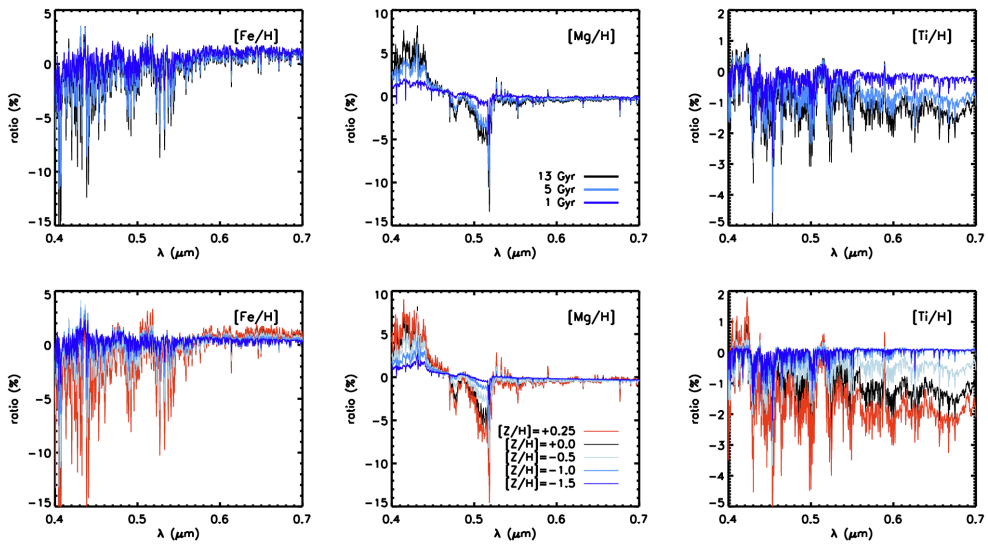

Figure 1.2: Response functions as a function of age and metallicity for Fe, Mg, and Ti. Each response function is defined as the ratio between two theoretical SSPs: one with a non-solar abundance of a single element, and the other with solar-scaled abundance ratios. Figure reproduced from Conroy et al. (2018).

1.2.2 Gas-Phase Oxygen Abundance

Gas-phase oxygen abundance (i.e., gas-phase metallicity) is generally easier to measure than stellar abundances, as it can be inferred from nebular emission lines. Because oxygen is a primary coolant in photoionized gas, its abundance is closely tied to the electron temperature (T_e): a more metal-rich ISM results in more efficient cooling and thus a lower electron temperature. The most and reliable method for measuring gas-phase metallicity is to use metal recombination lines (e.g., Esteban et al., 2014), but these lines too faint ($\sim 10^{-4}$ of Hβ) to be detected in a large statistical sample. The collision-excited auroral lines such as [O III]λ4363 and [O II]$\lambda\lambda$7320,7330 are much brighter than oxygen recombination lines, so they have been more widely used to measure the electron temperature of the high- and low-ionization zones in H II regions in order to infer the oxygen abundance (i.e., the direct T_e method). However, these auroral lines are still much fainter than Hβ ($\sim 10^{-1} - 10^{-2}$ of Hβ) and become even weaker in high-metallicity environments where the gas is cooler, making them increasingly difficult to detect. As a result, obtaining T_e-based metallicities for large samples of galaxies is observationally expensive, requiring long integration times on large telescopes.

A more practical and widely used alternative is the strong-line method, which relies on brighter emission lines such as [O II]$\lambda\lambda$3726,3729, [O III]λ5007, [N II]λ6585, and [S II]$\lambda\lambda$6716,6731. The ratios between these metal lines and the Balmer lines are calibrated either empirically, using galaxies with direct T_e-based measurements (e.g., McGaugh, 1991; Pettini and Pagel, 2004; Pilyugin and Thuan, 2005; Pilyugin and Grebel, 2016), or theoretically, through photoionization models (e.g., Tremonti et al., 2004). More recently, Bayesian frameworks have been developed to infer metallicities by comparing observed emission line fluxes directly to theoretical predictions of photoionization model grids (e.g., Blanc et al., 2015; Strom et al., 2022). Despite these advancements, different strong-line calibrations can yield oxygen abundances that differ by up to ~0.7 dex (Kewley and Ellison, 2008), introducing significant systematic uncertainties in gas-phase metallicity estimates.

1.3 Open Questions in Chemical Evolution of Galaxies

1.3.1 Detailed Abundances Beyond the Local Group

Over the past decade, significant progress has been made in measuring the detailed abundances of stars in dwarf satellite galaxies (e.g., Kirby et al., 2011b; de los Reyes et al., 2020) and in the ionized gas of individual H II regions (e.g., Pilyugin and Thuan, 2005; Berg et al., 2020) within the Local Group, providing deeper

insights into the chemical evolution of nearby galaxies.

However, compared to the detail with which we know the Local Group, we have only a surface understanding of the more distant field galaxies. The dearth of detailed abundance measurements results from the difficulty in determining the abundances of other elements precisely with integrated light spectra of distant galaxies.

More recently, spectroscopic studies have turned to detailed abundances of galaxies beyond the Local Group using modern techniques such as full-spectrum fitting of the stellar continuum (e.g., Conroy et al., 2018), providing us with a deeper understanding of galactic chemical evolution. For instance, Leethochawalit et al. (2019) used the relation between stellar masses and [Mg/H] for quiescent galaxies to constrain the mass-loading factor of galactic outflows. Several works have also used [Mg/Fe] to probe the star formation timescale of quiescent galaxies at higher redshifts (e.g., Choi et al., 2014; Kriek et al., 2016). Some other studies on high-z star-forming galaxies also use [O/Fe] as a stand-in for [α/Fe] (e.g., Steidel et al., 2016), to constrain the star formation timescale because oxygen is also an α element, when [Fe/H] of massive, young stars that just formed out of the ISM can be determined from the deep rest-frame UV spectroscopy[1].

Apart from the detailed abundances of stellar populations at a given epoch, the connections between metals in the gas and stars can also reveal the chemical enrichment histories in star-forming galaxies. Gallazzi et al. (2005) measured the stellar metallicities and compared them with the gas metallicities for the same SDSS galaxies measured by Tremonti et al. (2004). They found that the stellar metallicities exhibit large scatter (at least 0.3 dex) at a fixed gas metallicities for SDSS galaxies. Because the residuals in stellar metallicities with respect to a simple linear fit of the median relation between stellar and gas metallicities show dependence on various galaxy properties (stellar mass, surface density, D4000, specific star formation rate, gas fraction and etc.), they attributed the large scatter observed should result from gas inflows and/or outflows rather than bias caused by the techniques used for stellar and gas metallicity estimates.

Although we can indeed extract useful information from the comparison of stellar and gas metallicities, we should always proceed with caution. While the oxygen abundance represents the instantaneous metal enrichment of the ISM, the iron

[1] [O/Fe] should not be used as a proxy of [α/Fe] when [Fe/H] is determined from rest-optical spectrum. [Fe/H] measured in optical is sensitive to the metallicity of older, lower-mass stars, so [Fe/H] and [O/H] eventually trace chemical enrichment at different epochs.

abundance indicates the amount of metals locked inside the stars integrated over the past SFH. Because the two elements trace the metal content in different phases and formation timescales, it is dangerous to treat both Fe_* to O_{gas} as an indicator of the same "metallicity" between galaxies of different SFHs. Fraser-McKelvie et al. (2022) introduced a new method to compare the metals in the two phases — converting the gas oxygen abundance into the iron-based metallicity using the scaling relations of Nicholls et al. (2017) based on the stellar abundance patterns in H II regions of the Milky Way, Large Magellanic Cloud (LMC), and Small Magellanic Cloud — which they believe to be a better indicator as it removes the intrinsic discrepancies in the elemental abundances (Fe and O in their cases). However, they also admit that this method cannot fully remove the effects of SFH. Moreover, the scaling relations of Nicholls et al. (2017) between [O/H] and [Fe/H] are based on the abundance patterns of only three galaxies, so they still somewhat rely on the specific SFHs.

A better way to connect metals in the stars and the ISM is to compare the stellar-phase magnesium and the gas-phase oxygen. As they are both α elements, their abundance ratio should be less affected by the SFHs than [O/Fe]. As Mg_* and O_{gas} still represent the metals in different phases, they can inform us how the pristine inflows and/or enriched outflows can affect the metals in galaxies. In addition, comparing the $[Mg/Fe]_*$ and [O/Fe] for the same galaxies would allow us to know whether the commonly-used α-enhancement indicator [O/Fe] in the studies of star-forming galaxies at all redshifts needs any systematic corrections.

However, prior to this thesis, no studies had directly compared Mg_* and O_{gas} in distant galaxies beyond the Local Group, because it is extremely challenging to measure Mg_* in highly star-forming galaxies. Such measurements require new SPS models that account for non-solar abundance patterns at young ages, as well as the detection of Mg-sensitive absorption features, which are significantly fainter in young, star-forming stellar populations. In Chapter 4, I develop a novel method to characterize Mg_* in actively star-forming galaxies, by applying the latest SPS models to a new high-quality dataset of low-mass star-forming dwarf galaxies, enabling the first-ever comparison of α elements in the ionized gas and stars beyond the Local Group.

1.3.2 The Stellar Mass–Metallicity Relation (MZR) and Its Challenges

The most direct way to link measured metallicity (either stellar or gas-phase) to a galaxy's evolutionary history is by positioning the sample on the stellar mass–metallicity relation (MZR). In the past few decades, numerous studies have revealed the tight correlation between the stellar masses (luminosities) and the metallicities of galaxies, i.e., the MZR (e.g., Lequeux et al., 1979b; Tremonti et al., 2004; Gallazzi et al., 2005; Kirby et al., 2013; Leethochawalit et al., 2019).

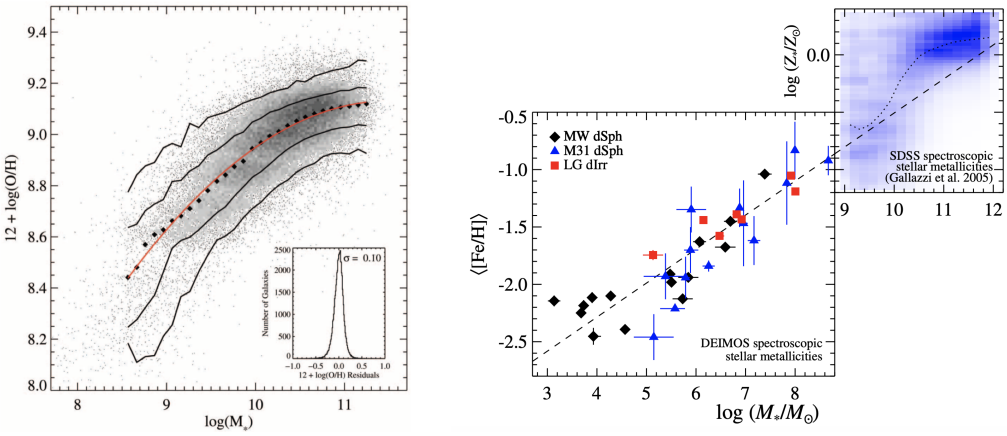

Figure 1.3: Example MZR from the literature. *Left:* Gas-phase MZR measured as the oxygen abundance in the ISM for the SDSS galaxies. *Right:* Stellar MZR measured as the iron abundance in the stellar population for the Local Group satellites and the SDSS galaxies. Figures reproduced from Tremonti et al. (2004) and Kirby et al. (2013).

The observed MZR (Figure 1.3) indicates that more massive galaxies are more metal-rich than less massive ones. The trend can be interpreted as a result of differences in metal retention, wherein high-mass galaxies with deep gravitational potential wells can resist galactic winds and retain more metals (Dekel and Silk, 1986). Recent works have argued that the interplay between accretion, outflow, and star formation may also shape the MZR (e.g., Finlator and Davé, 2008; Calura et al., 2009; Magrini et al., 2012). Figure 1.4 summarizes key physical processes shaping the MZR. The shape of the MZR, especially the slope, is particularly interesting because changes in the MZR slope indicate how the physical processes governing metal retention and the interaction with the surrounding environment vary as galaxies grow in mass.

However, determining the exact shape of the MZR across the full range of galaxy mass is still challenging due to the diverse approaches used to measure stellar and gas-phase metallicity in different mass regimes (see Section 1.2 for more details).

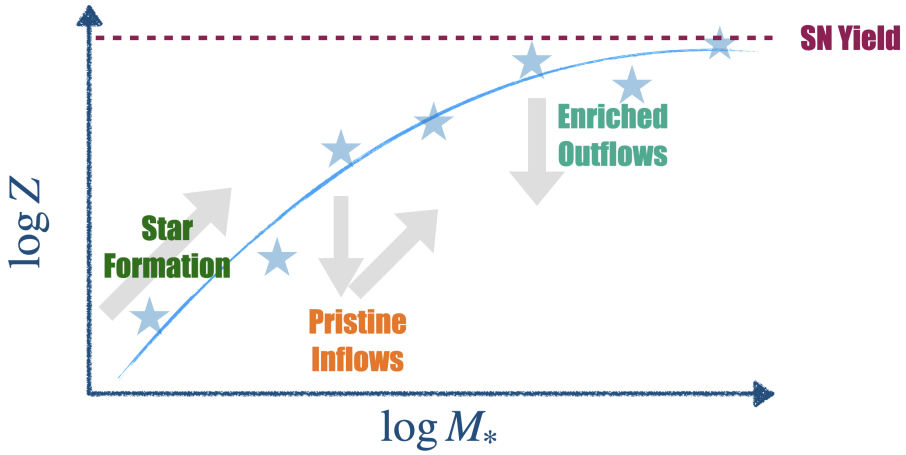

Figure 1.4: A schematic diagram illustrating the key physical processes that shape the MZR. Star formation synthesizes heavy elements, increasing both stellar mass and metallicity. Metal-poor inflows initially dilute gas metallicity but also sustain star formation, ultimately contributing to chemical enrichment. Metal-enriched outflows can remove metals from the galaxy. Over time, the metallicity reaches equilibrium with supernova yields, preventing further enrichment despite continued star formation.

Even if the gas-phase MZR is easier to measure from emission lines, the discrepancies between different metallicity calibrations used in different mass regimes (as discussed in Section 1.2.2) can significantly impact both the slope and normalization of the measured MZR. Most studies have found that the gas-phase MZR has a steep slope in the low-mass regime and flattens at the high-mass end in the local universe, regardless of the calibration used to measure metallicity (e.g., Tremonti et al., 2004; Andrews and Martini, 2013; Blanc et al., 2019). However, the transition in the slope of the gas MZR at $\sim 10^9 M_\odot$ is controversial due to the large systematic errors in different techniques used to measure gas metallicity. While most previous work has revealed a smooth transition in the slope of gas MZR (e.g., Tremonti et al., 2004; Andrews and Martini, 2013), Blanc et al. (2019) found that the slope steepens significantly around $M_* \simeq 10^{9.5-10.1} M_\odot$ and flattens again at a higher stellar mass, suggesting a sharp transition in how galaxies retain their metals with increasing mass.

Similarly, the stellar MZR at $z \sim 0$ derived from resolved stellar spectroscopy for satellites ($M_* \lesssim 10^8\ M_\odot$; Kirby et al., 2013) does not reconcile with that of the massive ellipticals derived from integrated-light spectroscopy ($M_* \gtrsim 10^{9.5}\ M_\odot$; Leethochawalit et al., 2019), with the latter exhibiting a much flatter slope and higher

normalization. This discrepancy may reflect a real physical transition in the stellar MZR between low- and high-mass galaxies, possibly driven by changes in feedback processes that shape the relation (Finlator and Davé, 2008), or it may result from systematic differences between the two measurement techniques, similar to the well-known calibration offsets in gas-phase metallicity indicators. Therefore, a direct comparison of stellar metallicities derived using both resolved and integrated-light approaches is needed to resolve this issue.

Moreover, prior to this thesis, there were few precise measurements of the stellar MZR for individual intermediate-mass galaxies ($10^8 < M_*/M_\odot < 10^9$) in the local universe, making it difficult to determine the exact shape of the stellar MZR between low- and high-mass regimes. This gap largely originates from the challenge of measuring stellar metallicities in the highly star-forming galaxies that dominate this mass range (Tomczak et al., 2014). First, young, massive stars that contribute significantly to the integrated light of a galaxy lack prominent metal absorption lines useful for stellar abundance determination. Second, bright nebular emission lines originating from the ionized gas make it harder to measure the Balmer absorption lines precisely to determine the age of the stellar population. Therefore, deep spectroscopy of highly star-forming dwarfs and advanced SPS models are necessary to disentangle this problem.

Another key question is whether the stellar MZR evolves with redshift, and if so, how. While the redshift evolution of the gas-phase MZR has been well established out to $z \sim 2$–3 (Sanders et al., 2021; Strom et al., 2022), the stellar MZR has only been studied in a large statiscal sample up to $z \sim 0.7$ (Leethochawalit et al., 2018a; Leethochawalit et al., 2019; Beverage et al., 2023). This dearth of data is largely due to the observational challenge of measuring stellar abundances in high-z quiescent galaxies, whose stellar absorption features are extremely faint. Obtaining spectra with sufficient S/N for abundance measurements typically requires 10-20 hours of integration time on large 8-10 m ground-based telescopes to analyze a single galaxy. Therefore, astronomers must either leverage the unprecedented capabilities of the James Webb Space Telescope (JWST), or combine innovative strategies like gravitational lensing with easier access to large ground-based facilities.

Chapter 2 and Chapter 4 demonstrate the new progress made to better characterize the shape of the stellar MZR measured from different elements at $z \sim 0$ across the full range of galaxy masses. Chapter 3 presents new measurements of stellar abundances and abundance ratios of gravitationally lensed, quiescent galaxies at

$z \gtrsim 1$.

1.3.3 Spatial Distribution of Ionized Gas and Stellar Population in Dwarf Galaxies

To fully understand how galaxies grow and evolve into the states we observe today, it is necessary not only to capture the global trends of galaxies across different evolutionary stages using large samples, but also to resolve the internal processes that shape their structures. The development of integral field unit (IFU) spectroscopy has provided a powerful tool for studying the physical mechanisms that drive galaxy evolution on local scales, offering spatially resolved views that connect global galaxy properties to their internal structures and kinematics. Over the past decade, large IFU surveys such as MaNGA (Bundy et al., 2015), SAMI (Croom et al., 2012), and CALIFA (Sánchez et al., 2012) have revolutionized our understanding of galaxy evolution by delivering resolved maps of stellar and nebular properties across thousands of galaxies in the low-redshift universe.

These surveys have uncovered a number of general trends in galaxies with stellar masses above $10^9 M_\odot$. Many of the scaling relations first established on global scales through slit and fiber spectroscopy, such as the star-forming main sequence and the gas-phase MZR, have been shown to hold even at kpc scales (Sánchez et al., 2013). Radial gradients in stellar population age, stellar and gas-phase metallicity, and SFR have been reported in massive galaxies by multiple IFU surveys (e.g., González Delgado et al., 2016; Goddard et al., 2017; Belfiore et al., 2017; Lian et al., 2018a; Zibetti et al., 2020). Spatially resolved maps of nebular emission-line ratios also reveal that ionization conditions can vary significantly across different regions within a galaxy. Actively star-forming regions hosting massive OB stars exhibit distinct line ratios compared to regions dominated by diffuse ionized gas (DIG), where hot evolved stars are thought to be the primary ionizing sources (Belfiore et al., 2015; Zhang et al., 2017). As a result, contributions from the DIG can bias gas-phase metallicity measurements if not properly accounted for (Sanders et al., 2017; Vale Asari et al., 2019).

Despite these advances, many published analyses group galaxies into bins—by stellar mass, SFR, morphology, or specific line ratios—and average all spaxels within a bin to improve S/N and extract robust population-wide trends. While this strategy successfully reveals general behaviors, it tends to obscure the rich internal diversity that can exist even among galaxies with similar global properties. In

particular, rare or unusual spatial trends, present only in a small fraction of galaxies, are often lost in the averaging process.

This limitation becomes especially pronounced when studying dwarf galaxies. Their shallow gravitational potentials make them more susceptible to both internal feedback and external environmental effects. Hydrodynamical simulations predict that star formation in dwarf galaxies proceeds in a bursty, stochastic manner (Hopkins et al., 2023), disrupting the coherent radial gradients commonly observed in more massive galaxies. Therefore, the diversity among dwarf galaxies offers a valuable testbed for studying how feedback, chemical evolution, and environmental interactions affect galaxies on an individual basis.

To answer this question, I have led an observational program to obtain IFU data for a sample of low-mass, star-forming galaxies at $z \sim 0$, using the Keck Cosmic Web Imager (KCWI)—an integral field spectrograph mounted on one of the world's largest ground-based optical telescopes. In Chapter 5, I present the first results on the spatially resolved properties of ionized gas and stellar populations in these dwarf galaxies.

1.3.4 Stellar Populations and Chemical Abundances at $z \gtrsim 1$

Not only can we learn the chemical evolution of nearby galaxies from the detailed abundances, but chemical constraints of high-z galaxies from deep spectroscopy also provide a unique opportunity to understand how and when galaxies form stars and quench in the early universe. The majority of stellar mass in the universe at $z = 0$ resides in the "red sequence" (i.e., passive galaxies), but most of those galaxies were star-forming at $z > 1$. Nonetheless, some of these galaxies were quenched at a lookback time over half of the age of the universe. A full understanding of the end phase of galaxy evolution requires that we examine the galaxies that ceased star formation relatively early.

At high redshifts, most chemical studies have focused on the gas abundances of star-forming galaxies measured from nebular emission lines, which trace the chemical compositions of the ISM at the time of observation and is affected by both star formation and gas inflows/outflows (e.g., Finlator and Davé, 2008; Strom et al., 2022). On the other hand, characterizing the stellar absorption lines and the overall continuum shape of high-z quiescent galaxies, which encode valuable information on the age, stellar abundances and SFH, is much more challenging and invariably requires much deeper spectroscopy due to the faintness of the stellar continuum.

Prior to the launch of JWST and the work presented in this thesis, only *five* quiescent galaxies at $z \gtrsim 1$ had detailed abundance and age measurements (Kriek et al., 2016; Kriek et al., 2019; Jafariyazani et al., 2020), and all of them had especially large stellar masses: $M_* > 10^{10.6}\ M_\odot$.

Gravitational lensing provides a powerful tool to obtain high-quality spectra of faint, high-z quiescent galaxies. By boosting both their apparent brightness and angular size, lensing enables detailed studies with imaging and spectroscopy that would otherwise be infeasible. With the advent of machine learning techniques, an increasing number of strongly lensed systems at high redshift have been identified in deep imaging surveys (e.g., Jacobs et al., 2019b). The time is now ripe to spectroscopically follow up these rare, lensed quiescent galaxies at $z \gtrsim 1$ to deepen our understanding of galaxy formation and chemical enrichment in the early universe.

In Chapter 3, I present a detailed spectral analysis of lensed, quiescent galaxies in the high-z universe to probe galaxy evolution in the early universe.

1.4 Thesis Outline

This thesis is organized into four main science chapters, each addressing a key aspect of measuring and interpreting chemical abundances in galaxies using integrated-light spectroscopy.

Chapter 2 investigates whether integrated-light spectroscopy can recover reliable stellar metallicities by comparing integrated and resolved measurements of NGC 147, a dwarf elliptical satellite of M31, offering insight into the stellar MZR at $z \sim 0$ across the full range of galaxy masses.

Chapter 3 presents a detailed spectral analysis of two gravitationally lensed quiescent galaxies at $z \gtrsim 1$ observed with the Keck telescopes. Using the integrated-light spectroscopy and full-spectrum fitting validated in Chapter 2, the analysis yields robust measurements of [Fe/H], [Mg/Fe], and stellar population ages, enabling a study of the redshift evolution of the stellar MZR and offering insights into the processes responsible for quenching galaxies in the early universe.

Chapter 4 presents a new sample of star-forming dwarf galaxies observed with Keck/KCWI, to further investigate the shape of the stellar MZR in the intermediate-mass regime between the Local Group satellites and massive field ellipticals at $z \sim 0$. Using a novel technique I developed to measure stellar iron and magnesium abundances in star-forming galaxies, this chapter also provides the first direct

comparison of α elements (gas-phase O and stellar Mg) in both stars and the ISM beyond the Local Group.

Chapter 5 extends the analysis of the KCWI sample presented in Chapter 4 to investigate the spatially resolved properties of ionized gas and stellar populations in star-forming dwarf galaxies at $z \sim 0$. Preliminary results show that these galaxies host short-lived, irregular, and clumpy star formation, accompanied by significant spatial variation in local ionization conditions. In contrast, the time-integrated stellar mass profiles appear much smoother, reflecting a more organized underlying structure.

Finally, in Chapter 6, I summarize the main results of this thesis and discuss potential avenues for future research into the chemical evolution of galaxies and the interplay between ionized gas and stellar populations.

Chapter 2

RESOLVING THE DISCREPANCY IN THE STELLAR MASS–METALLICITY RELATION

Zhuang, Z. et al. (Oct. 2021). "NGC 147 Corroborates the Break in the Stellar Mass-Stellar Metallicity Relation for Galaxies". In: *ApJ* 920.1, p. 63. DOI: 10.3847/1538-4357/ac1340.

Abstract

The stellar mass-stellar metallicity relation (MZR) is an essential approach to probing the chemical evolution of galaxies. It reflects the balance between galactic feedback and gravitational potential as a function of stellar mass. However, the current MZR of local dwarf satellite galaxies ($M_* \lesssim 10^8 M_\odot$, measured from resolved stellar spectroscopy) may not be reconcilable with that of more massive galaxies ($M_* \gtrsim 10^{9.5} M_\odot$, measured from integrated-light spectroscopy). Such a discrepancy may result from a systematic difference between the two methods, or it may indicate a break in the MZR around $10^9 M_\odot$. To address this question, we measured the stellar metallicity of NGC 147 from integrated light using the Palomar Cosmic Web Imager. We compared the stellar metallicity estimates from integrated light with the measurements from resolved stellar spectroscopy and found them to be consistent within 0.1 dex. On the other hand, the high-mass MZR overpredicts the metallicity by 0.6 dex at the mass of NGC 147. Therefore, our results tentatively suggest that the discrepancy between the low-mass MZR and high-mass MZR should not be attributed to a systematic difference in techniques. Instead, real physical processes cause the transition in the MZR. In addition, we discovered a positive age gradient in the innermost region and a negative metallicity gradient from the resolved stars at larger radii, suggesting a possible outside-in formation of NGC 147.

2.1 Introduction

In the past few decades, numerous works have revealed the tight correlation between the stellar masses (luminosities) and the metallicities of galaxies, i.e., the stellar mass-metallicity relation (MZR) (e.g., McClure and van den Bergh, 1968; Lequeux et al., 1979a; Tremonti et al., 2004; Lee et al., 2006; Kirby et al., 2013; Leethochawalit et al., 2018b). The observed MZR indicates that more massive

galaxies are more metal-rich than less massive ones. The trend can be interpreted as a result of metal retention, wherein high-mass galaxies with deep gravitational potential wells can resist galactic winds and retain more metals (Dekel and Silk, 1986). Recent works have argued the metallicity may also be regulated by star formation efficiency (e.g., Calura et al., 2009; Magrini et al., 2012) as well as by the interplay between inflow, outflow, and enrichment (Finlator and Davé, 2008). Generally, galactic metallicities are measured in two forms: gas-phase and stellar-phase. While gas-phase metallicity reflects the metals in the interstellar medium (ISM) at the time of observation, stellar metallicity indicates the amount of metals incorporated into the stars at the time they formed, which is less susceptible to instantaneous fluctuations and represents the metal abundance averaged over the star formation history (SFH). Therefore, the stellar MZR is a more stable indicator of the chemical evolution of galaxies than the gas-phase MZR.

The MZR[1] at $z \sim 0$ can be measured from two independent techniques. Local dwarf galaxies can be resolved into stars, so their stellar metallicities are derived from spectroscopy of individual stars (e.g., Kirby et al., 2013). On the other hand, more massive galaxies are too far for us to resolve the stars. Therefore, metallicities are obtained from the integrated-light spectra of whole galaxies (e.g., Gallazzi et al., 2005; Zahid et al., 2013; Leethochawalit et al., 2018b; Leethochawalit et al., 2019). Although the low-mass and high-mass MZRs both indicate more massive galaxies are more metal-rich, they follow different forms of expression. Kirby et al. (2013, hereafter K13) used Geha et al.'s (2010) Keck/DEIMOS spectra to derive the low-mass MZR from resolved stellar spectroscopy in Local Group dwarf galaxies ($M_* \lesssim 10^8 M_\odot$)[2] as [Fe/H] $\propto M_*^{0.30\pm0.02}$, while Leethochawalit et al. (2019, hereafter L19) measured the high-mass MZR from integrated-light spectra of local massive quiescent galaxies ($M_* \gtrsim 10^{9.5} M_\odot$) as [Fe/H] $\propto M_*^{0.11\pm0.02}$. Choi et al. (2014) similarly observed a flat slope in the high-mass MZR, where the metallicities for massive quiescent galaxies ($M_* \geq 10^{10.6} M_\odot$) in the local universe were measured from the stacked spectra in bins of stellar mass. Sybilska et al. (2017) estimated the stellar metallicities for 258 nearby massive quiescent galaxies ($M_* \gtrsim 10^{9.8} M_\odot$) in the ATLAS^{3D} survey (Cappellari et al., 2011) using spectrophotometric indices. They also recovered a high-mass MZR similar to that of L19. All these studies indicate a shallower slope and higher normalization in the high-mass MZR than in

[1] In this paper, MZR refers to the stellar-phase MZR, if not otherwise specified.

[2] K13 measured the stellar metallicities of both quiescent and star-forming dwarf galaxies, but they found no difference in the MZR between these two groups.

the low-mass MZR, such that an extrapolation of the high-mass MZR to low mass would predict much higher metallicities than are observed in low-mass galaxies.

One possible explanation for the discrepancy is that there is a physical break in the MZR around $10^8 - 10^{10} M_\odot$. This behavior would mimic the gas-phase MZR, which follows a single power law at low to intermediate masses ($10^6 M_\odot \lesssim M_* \lesssim 10^{9.5} M_\odot$), and flattens at the high-mass end (e.g., Blanc et al., 2019). The possible transition may result from different feedback mechanisms of the two mass ranges. Theoretically, it has been suggested that energy-driven winds dominate in low-mass galaxies (Murray, Quataert, and Thompson, 2005), while momentum-driven winds dominate in high-mass galaxies (Hopkins, Quataert, and Murray, 2012). Finlator and Davé (2008) also suggested that the observed gas-phase MZR at $z \sim 2$ for massive galaxies indicates the momentum-driven winds are dominant in the outflows of high-mass galaxies. Such a transition in the slope of the stellar MZR was seen by Sybilska et al. (2017), who found that the slope around $10^{9.5} M_\odot$ steepens significantly as compared to that at the lowest and highest masses. However, the stellar MZR derived by Sybilska et al. (2017) does not go below $10^9 M_\odot$, so it cannot fill the mass gap in the stellar MZR and capture the behavior of the MZR across the full range of galaxy masses. The existing measurements in the mass gap are too scarce to constrain the intermediate-mass stellar MZR.

However, the discrepancy in the MZRs may also result from a systematic difference between the two techniques used to measure stellar metallicities. Previous works that tested the consistency between the stellar population parameters—including the metallicities—among various measurement methods have mainly focused on simple systems like globular clusters e.g., González Delgado and Cid Fernandes, 2010; Conroy, Graves, and van Dokkum, 2014; Conroy et al., 2018. So far, only Ruiz-Lara et al. (2018) have compared the metallicity of each SFH age bin obtained from the integrated-light spectrum of Leo A, a star-forming dwarf irregular (dIrr) galaxy with $M_* \sim 3 \times 10^6 M_\odot$, with that measured by Kirby et al. (2017) from individual stars. They found that the integrated-light [Fe/H] at all age bins is higher than the resolved-star [Fe/H]. The differences in [Fe/H] range from $\sim$ 0.25–1.5 dex. However, the differences here can be explained by other reasons, such as the inaccurate modeling of Balmer nebular emission lines, the incompleteness of metal-poor stars in the current stellar libraries, or a negative metallicity gradient, as suggested by Kirby et al. (2017).

In this work, we focus on NGC 147, a dwarf elliptical (dE) satellite of M31 with

$M_* \simeq 10^8 M_\odot$ (K13). This galaxy is a good target to investigate possible systematic differences between different techniques of measuring stellar metallicities. First, the galaxy is near enough (712 kpc; Conn et al. 2012) to obtain individual stellar metallicities but also far enough to be observed in integrated light with an integral field unit (IFU). Second, no H I gas has been detected in NGC 147, so the spectrum is free from nebular emission line contamination. Third, NGC 147 is more metal-rich than Leo A, so it will suffer less from the incompleteness of metal-poor stars in the current stellar libraries.

The main goals of this paper are (1) to determine whether there is a systematic offset between integrated-light and resolved-star spectroscopic measurements of NGC 147's stellar metallicity, (2) to use these measurements to bolster or diminish the evidence of a break in the stellar MZR, and (3) to leverage IFU data cubes to study the spatial distribution of the stellar population in the innermost region. We use both new IFU data cubes and archival resolved-star spectra (Section 2.2). We use a variety of full spectral fitting algorithms (Section 2.3) to estimate the global stellar metallicity and age from integrated light (Section 2.4). Section 2.4.2 specifically addresses goal (1) in determining the consistency between the two different metallicity techniques. We also present some interesting spatial trends of the stellar population that suggest that NGC 147 formed outside in (Section 2.5). We compare our work with the previous literature on the stellar metallicity determinations and discuss the subsequent implications for the MZR (goal 2) in Section 2.6. Finally, we summarize our findings in Section 2.7.

2.2 Observations

2.2.1 Palomar Cosmic Web Imager Sample

Observations and data reduction

Observations for NGC 147 were performed with the Palomar Cosmic Web Imager (PCWI) on 2019 September 23 and 24. PCWI is a medium-resolution integral field spectrograph (IFS) mounted on the Cassegrain focus of the Palomar 200-inch Hale Telescope with a field of view of $60'' \times 40''$. It consists of 24 spatial slices with a width of $\sim 2.5''$ and an in-slice pixel scale of $\sim 0.5''$. The seeing was around $2''$ for two nights, so both the spatial axis along each slice and spectral z-axis are seeing-limited while the spatial axis across the slices was slit-limited. NGC 147 has an effective radius ($R_{\rm eff}$) of $\sim 6.7'$, which means that a single PCWI pointing covers only a small portion of the galaxy. We observed the central regions of the galaxy

within 2′ with three pointings (Figure 2.1), as described in Table 2.1.

Table 2.1: PCWI Observations of NGC 147

Pointing	R.A. (J2000)	Decl. (J2000)	Surface Brightness[a] (g-band mag arcsec^{-2})	Central Wavelength (Å)	Date	Exposure Time (s)
Central	00 33 12.223	+48 30 27.341	21.32	4300	2019 Sep 23	6×900
				5140	2019 Sep 23	6×900
South	00 33 08.561	+48 29 14.526	21.59	4300	2019 Sep 23	4×900
				5140	2019 Sep 24	5×900
North	00 33 15.570	+48 31 48.328	21.58	5140	2019 Sep 24	6×900

Some observations lacked quality sufficient for this study. This table does not include those observations.
[a] Derived from the best-fit surface brightness profile for diffuse light in Crnojević et al. (2014).

The MEDREZ grating was used to provide the largest spectral range (∼ 900Å) that PCWI offers and a resolution of $R \simeq 1500$. With two configurations centered at 4300 Å and 5140 Å, respectively, the spectra span from 3750 Å to 5550 Å, which is sufficient to measure age, metallicity, and Mg enhancement via full-spectrum fitting (Leethochawalit et al., 2018b; Leethochawalit et al., 2019).

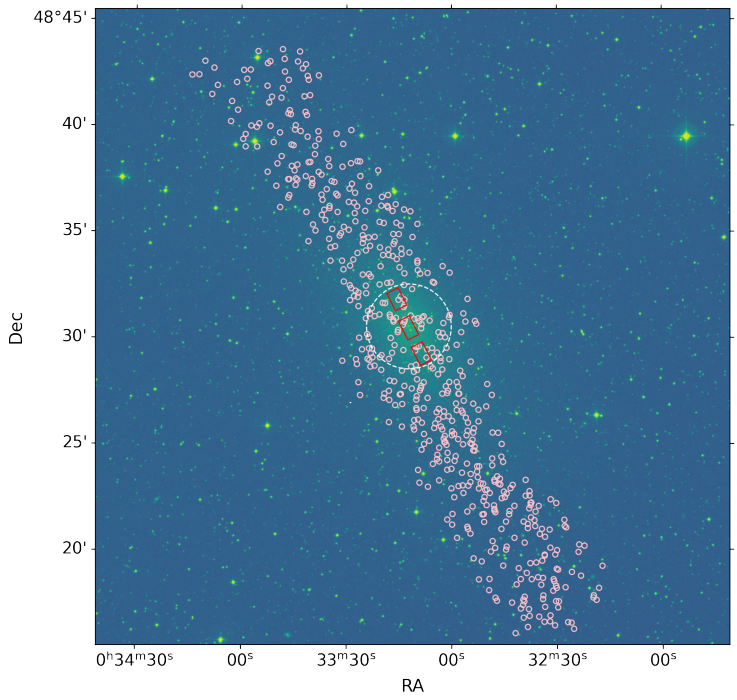

Figure 2.1: Digitized Sky Survey (DSS) image of NGC 147. The red rectangles show the three PCWI fields observed. The dashed circle indicates the circular effective radius. The pink circles show locations of the RGB star samples used in this study.

Because the galaxy is larger than the field of view of PCWI, additional off-field blank-sky observations were taken adjacent to each science observation with the same exposure time for sky subtraction. The weather was cloudy with the Moon

up in the late half of the second night, leading to significant variance in the sky spectra. Therefore, we had to abandon all science frames of the blue side of the north pointing due to inaccurate sky subtraction. Table 2.1 lists all the observations used in this study.

The raw data were reduced using the standard PCWI Data Reduction Pipeline (DRP)[3]. This pipeline converts raw, 2D science frames into flux-calibrated, 3D cubes with spatial positions and wavelengths. PCWI is subject to gravitational flexure because it is mounted at the Cassegrain focus. Flexure induces minor changes in the spectrum, such as alteration of the wavelength solution. Flexure correction in the PCWI DRP relies on cross-correlation of a time series of data cubes. However, the spectral offsets were not completely eliminated after the flexure correction. We recalibrated the wavelength solution by cross-correlating the spatially collapsed spectra of each image with the sky spectrum taken nearest to the night calibration set. In this way, the wavelength solution was standardized to a common reference. We applied only a constant offset and ignored higher-order terms.

The world coordinates of each cube were corrected with `CWITools` (O'Sullivan and Chen, 2020) via comparing the location of known foreground point sources with accurate R.A. and Decl. The sky frames were subtracted from the adjacent science frames directly to obtain the sky-subtracted cubes. The sky-subtracted cubes were coadded using `CWITools`, which calculates the footprint of each input pixel on the coadd frame and distributes flux onto the coadd grid.

The instrumental resolution was measured by fitting the widths of arc lines as a function of wavelength. PCWI uses a ThAr lamp, which gives a dense spectrum of emission lines. As a result, some arc lines were blended. We restricted the arc line list to isolated arc lines in order to eliminate the bias introduced by blended lines. We identified isolated arc lines by setting thresholds on the first and second derivatives of the arc flux. First, we required that the first derivative must be close to zero and that the second derivative must be negative, in order to find the locations of the line peaks. Second, we required that the peak must be sharp rather than having a flat or broadened feature. This means that the first derivative must abruptly change from positive to negative, i.e., that the second derivative must be smaller than some threshold. We experimented with different combinations of the thresholds and visually inspected the result. We found that setting the first derivative of the spectrum to be smaller than 0.2 and the second derivative to be smaller than -0.01

[3]PCWI DRP: `https://github.com/scizen9/pderp`

Table 2.2: Basic Properties of NGC 147

R.A. (J2000)	Decl. (J2000)	M_V (mag)	$m_{i,TRGB}$ (mag)	d_{MW} (kpc)	R_{eff} (arcmin (kpc))	σ_v (km s^{-1})	$\log(M_*/M_\odot)$ (dex)	[Fe/H] (dex)
00 33 12.1	+48 30 31	-15.33	$20.82^{+0.08}_{-0.08}$	712^{+21}_{-19}	6.70 (1.41)	16 ± 1	8.00 ± 0.05	−0.83 ± 0.25

The columns show (1–2) the equatorial coordinates from NED for the galaxy center; (3-6) the absolute total V magnitude, the apparent TRGB i-band magnitude, the de-projected distance from the Milky Way (MW), and the effective radius taken from Crnojević et al. (2014); (7) the velocity dispersion measured from the resolved stars (Geha et al., 2010); and (8-9) the stellar mass and stellar metallicity obtained from the resolved RGB stars taken from K13.

provides relatively clean isolated lines. The FWHMs of the isolated lines were then fitted into a quadratic polynomial to obtain the resolution ($\simeq$ 3.27 Å or 90 km s^{-1}).

However, there was still a slight offset between the blue and red spectra, as we only applied first-order correction. Instead of fitting for the higher-order terms, we transformed the observed wavelengths into the rest frame separately for both wavelength settings. The spatially collapsed spectra of each cube were extracted from the sky-subtracted cubes. We then cross-correlated them with a template galaxy spectrum that was smoothed to the PCWI resolution and re-sampled to the wavelength grid of our data using `SpectRes` (Carnall, 2017). A template with a simple stellar population (SSP) was generated from the Flexible Stellar Population Synthesis (FSPS) (Conroy, Gunn, and White, 2009; Conroy, White, and Gunn, 2010), based on the physical properties of NGC 147 listed in Table 2.2. Because NGC 147 has an extended SFH that ended $\sim$ 4 Gyr ago, we adopted a stellar population age of 8 Gyr, which approximately corresponds to the average age of the stellar population (Weisz et al., 2014). We conducted further analyses only on the rest-frame spectra.

Foreground Star Masking

As shown in Figure 2.1, some bright foreground stars are located in the field of PCWI. We masked them before the spectrum extraction to avoid contamination of the galaxy spectrum. The masking regions were determined from the white-light image. For NGC 147, the tip of the red giant branch has an i-band magnitude of $\sim$ 20.82 (Crnojević et al., 2014), so even the brightest star members would be too faint to be detected individually by PCWI. Therefore, any resolved stars in the field were considered foreground stars. We used the DSS image to identify the foreground stars. For each pointlike source on the DSS image within the PCWI field, we modeled its point spread function (PSF) on the white-light image assuming a 2D elliptical Gaussian profile. The point-source mask was determined as a circle centered at the fitted peak, with a radius of three times the fitted semi-major axis. Nevertheless,

some bright residuals, which may be related to scattered light, were still present in the field. We masked all the regions above 1.35 times the median. We also experimented with several thresholds, and it turned out that 1.35 times the median removed most of the bright extended features, which might have contaminated the spectra, while leaving most of the galaxy contribution.

Spectrum Extraction

IFS data are known to underestimate the variance due to the covariance between adjacent spaxels. This effect originates from the redistribution of the flux from the same pixel onto a new spatial grid when coadding or smoothing the data cubes. When we coadded the single-exposure cubes, the flux within the same slice with a width of ~ 2.5 arcsec was redistributed again into the final coadded image with a pixel scale of 0.58 arcsec. Therefore, the signal-to-noise ratio (S/N) derived from the PCWI DRP was significantly overestimated.

To estimate the true noise, we followed the procedures in O'Sullivan et al. (2020) for PCWI data. First, the variance for each cube was first rescaled by 1.5 to account for the covariance introduced by coadding. For the covariance added by spatially binning the neighboring spaxels, O'Sullivan et al. (2020) measured the true noise ($\sigma_{\rm adjusted}$) in the binned data as

$$\sigma_{\rm adjusted} = [1 + 0.79 \log{(N_b)}]\sigma_{\rm nocov}, \tag{2.1}$$

where $\sigma_{\rm nocov}$ is the noise derived from error propagation and N_b is the number of spaxels in the binned spectrum. For large $N_b \gg 120$, the signals in different spaxels are uncorrelated, so the scaling becomes $\sigma_{\rm adjusted} \simeq 2.6\ \sigma_{\rm nocov}$.

We stacked the extracted spectra from all the coadded cubes into a single spectrum, which resembles the long-slit integrated-light spectra of more massive galaxies. To remove sensitivity to possibly imperfect flux calibration, we normalized the spectra by the median of the flux between 4400 Å and 4800 Å. We then scaled them according to the surface brightness profile measured by Crnojević et al. (2014) (Table 2.1) and summed them to obtain the global spectrum. In this case, the number of spaxels used for spectrum extraction is much larger than 120. Therefore, we scaled the weighted variance by $2.6^2 = 6.76$.

In addition, we extracted the spatially resolved spectra using the Voronoi binning algorithm of Cappellari and Copin (2003), which is one of the most commonly used binning methods in IFS data. It can adaptively combine the spectra in adjacent

pixels to reach a given minimum S/N, and it allows us to adjust the S/N using using Equation 2.1 when optimizing the binning strategy. We only included the central and south pointings for the spatially resolved studies because the north pointing lacks reliable spectral coverage below 4700 Å, which is important to determine the stellar population age. For the central and south pointings, the S/N was calculated from the wavelength range between 4400-4600 Å. We required each bin to have S/N > 20 pix^{-1} (26 Å^{-1}) for the central pointing and S/N > 15 pix^{-1} (20 Å^{-1}) for the south pointing. We made this choice because the south pointing has many fewer bins in the field due to its lower surface brightness. In the end, we have 17 and 4 bins for the central and south pointings, respectively (Figure 2.5).

We further corrected the variance of the stacked spectrum and the spatially resolved spectra by comparing with the best-fit model in order to obtain accurate uncertainties of the stellar population parameters (see Section 2.3).

2.2.2 Keck/DEIMOS Sample

We used archival Keck/DEIMOS (Faber et al., 2003) observations of four slitmasks along the major axis of NGC 147. These observations were originally obtained by Geha et al. (2010). We downloaded the raw data from the Keck Observatory Archive and reduced them with the `spec2d` software (Cooper et al., 2012; Newman et al., 2013).

K13 already measured stellar metallicities from coadded spectra of red giants in NGC 147. However, one of the purposes of this paper is to determine whether individual stellar metallicities are consistent with integrated light. Spectral coaddition is a form of integrated light, which means that the existing measurements in K13 are not appropriate for our purpose. Therefore, we remeasured the stellar metallicities for individual stars.

We measured metallicities by χ^2 fitting to a grid of synthetic spectra, as described by Kirby, Guhathakurta, and Sneden (2008), Kirby et al. (2009), and Kirby et al. (2010). This method uses photometric estimates of effective temperature and surface gravity to guide the fitting. We used photometry from the Pan-Andromeda Archaeological Survey (PAndAS, Martin et al., 2013), which took place at the Canada–France–Hawaii 3.6 m Telescope (CFHT). This photometry is different from that used by K13, which possibly had errors in its zero-points. Only the stars with uncertainties of [Fe/H] smaller than 0.5 dex were included in the further analysis. This cut gives us 317 stars in the sample. The updated measurements are listed in Table 2.3.

Table 2.3: Metallicity Catalog for RGB Stars Observed with Keck/DEIMOS

ID	R.A. (J2000)	Decl. (J2000)	Filter 1	Magnitude 1[a] (mag)	Filter 2	Magnitude 2[a] (mag)	$T_{\rm eff}$ (K)	$\log g$ ($\rm cm\,s^{-2}$)	ξ ($\rm km\,s^{-1}$)	[Fe/H] (dex)
4456	00 32 23.9	+48 19 53.8	g	23.065 ± 0.027	i	20.921 ± 0.012	3744 ± 44	0.26 ± 0.1	2.08	-1.12 ± 0.12
4608	00 32 25.8	+48 18 57.2	g	23.106 ± 0.028	i	21.007 ± 0.013	3770 ± 42	0.32 ± 0.1	2.07	-0.49 ± 0.11
4778	00 32 27.6	+48 18 13.8	g	22.715 ± 0.020	i	21.117 ± 0.014	4126 ± 45	0.62 ± 0.1	2.00	-1.10 ± 0.12
4885	00 32 29.5	+48 17 34.2	g	23.297 ± 0.032	i	20.808 ± 0.011	3592 ± 56	0.04 ± 0.1	2.13	-3.03 ± 0.17
4894	00 32 29.7	+48 19 03.8	g	23.239 ± 0.031	i	21.424 ± 0.018	3929 ± 41	0.64 ± 0.1	1.99	-0.81 ± 0.12
4961	00 32 30.5	+48 19 46.6	g	24.125 ± 0.066	i	21.426 ± 0.018	3528 ± 51	0.23 ± 0.1	2.09	-3.21 ± 0.23
5026	00 32 31.1	+48 18 04.2	g	22.977 ± 0.025	i	21.163 ± 0.014	3936 ± 39	0.53 ± 0.1	2.02	-0.85 ± 0.11
5129	00 32 32.0	+48 16 37.4	g	23.416 ± 0.035	i	21.145 ± 0.014	3748 ± 52	0.31 ± 0.1	2.07	-2.23 ± 0.16
5324	00 32 33.6	+48 16 36.3	g	23.099 ± 0.027	i	21.238 ± 0.015	3923 ± 49	0.54 ± 0.1	2.02	-1.08 ± 0.13
5368	00 32 33.9	+48 17 50.8	g	22.779 ± 0.021	i	21.256 ± 0.016	4232 ± 42	0.72 ± 0.1	1.97	-1.36 ± 0.12
... Additional rows available in the online published version ...										

[a] PAndAS photometry corrected for extinction.

2.3 Methods

We used full-spectrum fitting via stellar population synthesis (SPS) to measure the stellar population of NGC 147. Compared to spectrophotometric indices, full-spectrum fitting derives the stellar population properties using the information from the whole spectrum instead of portions with strong absorption lines, so high-precision measurements can be achieved.

We adopted the fitting method of L19, from which the high-mass MZR was derived, and we refer the reader to that paper for a full description. We chose the same fitting algorithms to minimize the systematic difference caused by different full-spectrum fitting codes and different templates. In summary, L19 used the SSP models from FSPS (Conroy, Gunn, and White, 2009; Conroy, White, and Gunn, 2010) version 3.0 with the Kroupa (2001) initial mass function (IMF), Padova isochrones (Marigo and Girardi, 2007), and the MILES spectral library (Sánchez-Blázquez et al., 2006). The metallicities and ages of the templates range within $-1.98 \leq \log Z \leq 0.20$ and 0.3 Myr–14 Gyr, respectively. We interpreted [Z/H] in the base models as [Fe/H]. In addition to the stellar metallicity [Fe/H], the enhancements of Mg and N were also included using the theoretical response functions from Conroy et al. (2018), which depend on age and metallicity. The templates were smoothed to match with the resolution of the observed data. We fit for the velocity dispersion, stellar population age, [Fe/H] and [Mg/Fe] by interpolating the SSP models. Therefore, the obtained ages and metallicities are SSP-equivalent. Leethochawalit et al. (2018b) tested the SSP assumption by fitting the mock composite stellar population (CSP) model spectra, which have exponentially declining SFHs, with the SSP models, and successfully recovered the true metallicity within 0.1 dex. This result indicates that SSP-equivalent metallicity agrees well with the light- or mass-weighted metallicity. We emphasize that the goal of this paper is to investigate whether the high-mass MZR measured in SSP-equivalent [Fe/H] has systematic offsets relative to the low-mass MZR. As demonstrated in Appendix 2.8, although the choice of SSP or CSP model will affect the stellar age estimates, the measured metallicity is much less affected. Therefore, adopting SSP models will not affect the major conclusion of this paper. We focus on the recovery of SSP-equivalent parameters in the following analyses.

To avoid a possible mismatch in flux calibration between the blue and red spectra, we normalized the spectral continuum on both sides using a spline fit. L19 developed an algorithm to minimize any alteration to the template spectra. The algorithm applies

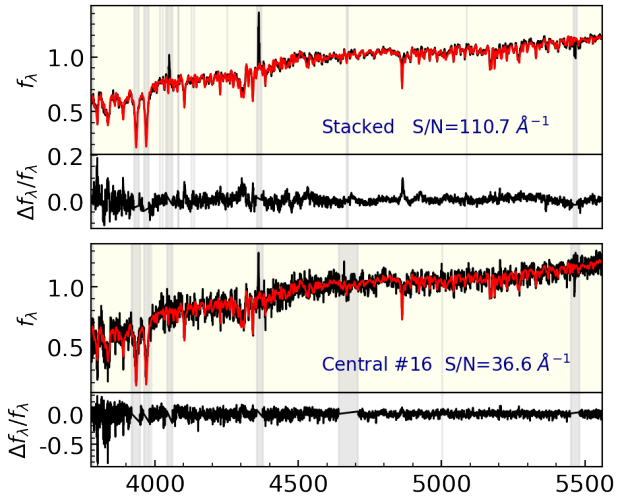

Figure 2.2: Two examples of the observed spectra (black), the corresponding best-fit models (red), and the model residuals (bottom panel of each spectrum). The gray regions are not included in the spectrum fitting. The top panel shows the stacked spectrum from the entire field, which has the highest S/N, while the bottom panel is an example of a spectrum at the lower end of S/N in one Voronoi cell. The S/N is estimated from the residual of the fits.

a synthesized continuum to the observed continuum-normalized spectrum. In the first iteration, we fit the continuum-normalized observed spectrum with continuum-normalized model spectra, and generated a synthesized continuum by fitting a B-spline to the quotient of the continuum-normalized spectrum and the best-fit SSP model spectrum. Subsequent fits were performed on the corrected observed spectrum with unaltered model spectra. The method is described in full detail in L19.

For each spectrum, we performed two separate fits. For the first fit, we only masked out the wavelength regions contaminated by the strong sky line residuals. The Ca II H and K lines were also excluded because of the strong nonlocal thermodynamic equilibrium (NLTE) effects, which the current models poorly reproduce. After the first fit, we masked out the regions that were $\geqslant 3\sigma$ from the best-fit model. We visually inspected these newly masked regions to make sure they deviated from the model due to weak sky features rather than deficiencies in the fitting algorithm. Then, we rescaled the variance derived from Section 2.2.1 by the reduced χ^2 of the first fit to estimate the true noise. We then fit the spectrum with new masking regions and corrected variance again to measure the stellar population properties.

To validate our measurements, we also compared our results with those derived from

Table 2.4: Best-fit stellar population parameters for the stacked spectrum of NGC 147

Row	Quantity	Units	Best-fit value
(1)	$\sigma_{\rm SSP}$	km/s	40.45 ± 1.85
(2)	$\rm Age_{SSP}$	Gyr	$8.11^{+0.74}_{-0.54}$
(3)	$\rm [Fe/H]_{SSP}$	dex	$-1.069^{+0.029}_{-0.031}$
(4)	$\rm [Mg/Fe]_{SSP}$	dex	$0.024^{+0.20}_{-0.20}$
(5)	$\sigma_{\rm alf}$	km/s	$23.59^{+3.35}_{-3.68}$
(6)	$\rm Age_{alf}$	Gyr	$12.50^{+0.32}_{-0.31}$
(7)	$\rm [Fe/H]_{alf}$	dex	$-1.105^{+0.011}_{-0.010}$
(8)	$\rm [Mg/Fe]_{alf}$	dex	$0.090^{+0.017}_{-0.017}$

(1)-(4) are derived from L19's method; (5)-(8) are obtained from the `alf` simple mode.

`alf` (Conroy et al., 2018), which is another full-spectrum fitting algorithm capable of measuring detailed abundances using the Markov Chain Monte Carlo (MCMC) method of parameter estimation. We used the "simple" mode of `alf`, which also assumes SSPs. The [Fe/H] and [Mg/Fe] results from our own code are consistent with those obtained from `alf` within 2σ.

Examples of the observed spectra and best-fit models at the highest and lowest ends of the S/N are shown in Figure 2.2. We summarize our results for the global spectrum in Table 2.4 and for the spatially resolved spectra in Table 2.5.

2.4 Global Properties

In this section, we report the stellar population properties of NGC 147 from the global integrated-light spectrum and compare the best-fit SSP-equivalent results with the updated measurements of the resolved stars.

2.4.1 SSP Age

The best-fit SSP age derived from our method is $8.11^{+0.74}_{-0.54}$ Gyr, while `alf` obtains an age of $12.50^{+0.32}_{-0.31}$ Gyr. We suspect the difference (~ 0.14 dex) may be attributed to systematic discrepancies of the SSP models used in the fitting codes. First, `alf` uses the newer MIST isochrones (Dotter, 2016; Choi et al., 2016) with metallicity coverage larger than that of the Padova isochrones used in our method. Second, the intrinsic spectral resolution of the stellar libraries in `alf` is lower than the instrumental resolution of PCWI, so the observed spectra needed to be smoothed by

Table 2.5: Best-fit stellar population parameters for spatially resolved integrated spectra

Pointing	R.A. (J2000)	Decl. (J2000)	$R_{\rm ellip}$ (arcmin (kpc))	$\rm Age_{SSP}$[a] (Gyr)	$\rm [Fe/H]_{SSP}$[a] (dex)	$\rm [Mg/Fe]_{SSP}$[a] (dex)	$\rm Age_{alf}$ (Gyr)	$\rm [Fe/H]_{alf}$ (dex)	$\rm [Mg/Fe]_{alf}$ (dex)	S/N[b] ($\rm \AA^{-1}$)
Central	00 33 11.72	+48 30 33.8	0.14 (0.03)	$7.08^{+0.69}_{-0.44}$	$-1.11^{+0.03}_{-0.04}$	$0.13^{+0.24}_{-0.28}$	$7.86^{+0.34}_{-0.43}$	$-0.99^{+0.04}_{-0.03}$	$0.14^{+0.05}_{-0.05}$	40.6
	00 33 12.37	+48 30 40.2	0.17 (0.04)	$7.55^{+0.89}_{-0.55}$	$-1.11^{+0.04}_{-0.04}$	$0.44^{+0.20}_{-0.25}$	$11.67^{+0.63}_{-0.52}$	$-1.20^{+0.03}_{-0.03}$	$0.35^{+0.05}_{-0.05}$	39.9
	00 33 13.20	+48 30 35.8	0.25 (0.05)	$7.43^{+0.89}_{-0.54}$	$-1.09^{+0.04}_{-0.04}$	$-0.04^{+0.28}_{-0.29}$	$9.35^{+0.57}_{-0.70}$	$-1.12^{+0.04}_{-0.04}$	$0.09^{+0.06}_{-0.06}$	38.4
	00 33 12.97	+48 30 27.0	0.29 (0.06)	$7.63^{+1.19}_{-0.68}$	$-1.05^{+0.04}_{-0.04}$	$-0.37^{+0.32}_{-0.31}$	$9.40^{+0.55}_{-0.39}$	$-0.96^{+0.03}_{-0.03}$	$-0.11^{+0.05}_{-0.05}$	42.1
	00 33 13.28	+48 30 48.2	0.34 (0.07)	$7.85^{+1.55}_{-0.88}$	$-1.08^{+0.04}_{-0.05}$	$-0.18^{+0.32}_{-0.33}$	$12.14^{+0.81}_{-0.81}$	$-1.21^{+0.03}_{-0.03}$	$-0.03^{+0.06}_{-0.06}$	36.0
	00 33 10.62	+48 30 20.6	0.35 (0.07)	$7.83^{+1.17}_{-0.71}$	$-1.15^{+0.04}_{-0.04}$	$-0.36^{+0.28}_{-0.28}$	$11.05^{+0.54}_{-0.41}$	$-1.28^{+0.03}_{-0.03}$	$-0.10^{+0.05}_{-0.05}$	44.1
	00 33 11.43	+48 30 42.2	0.37 (0.08)	$7.62^{+0.85}_{-0.54}$	$-1.11^{+0.04}_{-0.04}$	$0.09^{+0.25}_{-0.28}$	$12.01^{+0.65}_{-0.64}$	$-1.19^{+0.03}_{-0.03}$	$0.10^{+0.06}_{-0.06}$	39.6
	00 33 12.49	+48 30 15.4	0.42 (0.09)	$8.87^{+1.63}_{-1.12}$	$-1.14^{+0.05}_{-0.05}$	$-0.33^{+0.32}_{-0.31}$	$13.90^{+0.08}_{-0.35}$	$-1.31^{+0.03}_{-0.04}$	$0.01^{+0.06}_{-0.06}$	36.3
	00 33 10.98	+48 30 08.6	0.43 (0.09)	$7.03^{+0.69}_{-0.42}$	$-1.03^{+0.03}_{-0.04}$	$-0.42^{+0.32}_{-0.31}$	$7.17^{+0.34}_{-0.28}$	$-1.03^{+0.03}_{-0.03}$	$-0.02^{+0.04}_{-0.05}$	39.7
	00 33 11.91	+48 30 10.6	0.44 (0.09)	$7.87^{+1.39}_{-0.88}$	$-1.10^{+0.04}_{-0.05}$	$-0.09^{+0.30}_{-0.31}$	$9.96^{+0.57}_{-0.56}$	$-1.07^{+0.03}_{-0.03}$	$-0.05^{+0.06}_{-0.06}$	36.1
	00 33 12.18	+48 30 53.6	0.48 (0.10)	$7.79^{+1.42}_{-0.86}$	$-1.07^{+0.04}_{-0.04}$	$-0.05^{+0.30}_{-0.32}$	$10.87^{+0.70}_{-0.60}$	$-1.12^{+0.04}_{-0.04}$	$0.17^{+0.06}_{-0.06}$	35.1
	00 33 13.95	+48 30 30.2	0.51 (0.11)	$7.98^{+1.38}_{-0.92}$	$-1.11^{+0.04}_{-0.04}$	$0.14^{+0.26}_{-0.29}$	$12.43^{+0.65}_{-0.70}$	$-1.12^{+0.03}_{-0.03}$	$0.05^{+0.06}_{-0.06}$	39.1
	00 33 09.99	+48 30 11.7	0.51 (0.11)	$8.00^{+1.50}_{-0.92}$	$-1.11^{+0.05}_{-0.05}$	$-0.19^{+0.33}_{-0.32}$	$12.60^{+0.76}_{-0.89}$	$-1.18^{+0.03}_{-0.03}$	$-0.06^{+0.06}_{-0.06}$	34.4
	00 33 14.36	+48 30 42.1	0.52 (0.11)	$7.22^{+0.94}_{-0.58}$	$-1.06^{+0.04}_{-0.04}$	$-0.01^{+0.28}_{-0.30}$	$9.25^{+0.55}_{-0.47}$	$-1.06^{+0.04}_{-0.03}$	$0.07^{+0.06}_{-0.06}$	36.9
	00 33 13.59	+48 30 21.7	0.54 (0.11)	$7.72^{+1.26}_{-0.80}$	$-1.10^{+0.04}_{-0.04}$	$-0.09^{+0.30}_{-0.30}$	$12.90^{+0.61}_{-0.69}$	$-1.18^{+0.03}_{-0.03}$	$0.02^{+0.06}_{-0.06}$	37.2
	00 33 12.22	+48 30 01.1	0.69 (0.14)	$7.94^{+1.19}_{-0.73}$	$-1.07^{+0.04}_{-0.04}$	$-0.04^{+0.29}_{-0.30}$	$13.29^{+0.52}_{-0.78}$	$-1.20^{+0.03}_{-0.03}$	$0.13^{+0.05}_{-0.05}$	42.6
South	00 33 08.32	+48 29 22.1	1.33 (0.28)	$8.92^{+1.57}_{-1.07}$	$-1.05^{+0.03}_{-0.04}$	$-0.00^{+0.25}_{-0.29}$	$13.93^{+0.05}_{-0.23}$	$-1.05^{+0.02}_{-0.02}$	$0.03^{+0.05}_{-0.05}$	38.7
	00 33 09.93	+48 29 19.5	1.38 (0.29)	$8.36^{+1.41}_{-0.92}$	$-1.07^{+0.04}_{-0.04}$	$-0.04^{+0.29}_{-0.31}$	$13.56^{+0.35}_{-0.68}$	$-1.08^{+0.03}_{-0.03}$	$0.05^{+0.05}_{-0.04}$	39.9
	00 33 07.47	+48 29 04.0	1.67 (0.35)	$8.73^{+1.72}_{-1.25}$	$-1.10^{+0.04}_{-0.04}$	$-0.09^{+0.29}_{-0.32}$	$13.46^{+0.42}_{-0.98}$	$-1.08^{+0.03}_{-0.03}$	$0.05^{+0.05}_{-0.05}$	38.2
	00 33 09.16	+48 28 59.7	1.76 (0.37)	$8.56^{+1.52}_{-0.95}$	$-1.08^{+0.04}_{-0.04}$	$0.05^{+0.26}_{-0.31}$	$13.81^{+0.16}_{-0.56}$	$-1.10^{+0.03}_{-0.03}$	$0.06^{+0.04}_{-0.04}$	40.0

[a] Best-fit parameters for single stellar population (SSP) models.
[b] Signal-to-noise ratio of the spectra used for fitting.

another σ =100 km s^{-1} before being input to `alf`. Third, even in the simple mode, `alf` includes six more elements than our code does. Degeneracy between the extra free parameters may also affect the posterior distributions and the final results.

Ideally, we would compare the age of the stellar population measured from integrated light to the average ages of individual stars. Unfortunately, it is extremely challenging to measure the ages of individual RGB stars. Generally, the stellar age can only be indirectly estimated by comparing the observed data with stellar models (e.g., Soderblom, 2010). The most commonly used method is to place the observations on a color-magnitude diagram (CMD), and match them with isochrones in a Hertzsprung–Russell diagram. This method works best for main-sequence and subgiant stars and is less effective for old, metal-poor RGB stars. For example, the difference in color between a 9 Gyr and 12 Gyr red giant is on the order of the difference in color between isochrone sets modeling the same star.

We therefore infer the accuracy of the SSP age by comparing it with the age measured from CMD fitting via Hubble Space Telescope (HST) photometry by Weisz et al. (2014). They obtained a mass-weighted age of 7.53 Gyr, more consistent with the SSP age derived from our algorithm than with that derived from `alf`. The agreement suggests that even though NGC 147 has an extended SFH with several stellar populations formed at distinct epochs, the SSP assumption may be valid to recover the mass-weighted age in some cases, though the recovered stellar age is highly model-dependent. Therefore, obtaining a more reliable and consistent measurement of stellar age for galaxies sometimes requires a model of the SFH more complex than an SSP. As suggested in Appendix 2.8, CSP models may be more appropriate to recover the stellar age of complicated systems, although this method would also require higher data quality.

2.4.2 Iron abundance

Before comparing the metallicity determined from integrated light ([Fe/H]$_{\rm SSP}$) to that of the resolved stars ([Fe/H]$_{\rm stars}$), it is important to understand whether the method of averaging [Fe/H]$_{\rm stars}$ would affect the final results. The median, mean, and the inverse variance-weighted mean of [Fe/H]$_{\rm stars}$ are -1.047 ± 0.044, -1.106 ± 0.031 and -0.983 ± 0.024, respectively. As shown in Fig. 2.3, [Fe/H]$_{\rm SSP}$ = $-1.069^{+0.029}_{-0.031}$ from integrated light is consistent with the median and the mean of the [Fe/H]$_{\rm stars}$ within 1σ. On the other hand, [Fe/H]$_{\rm SSP}$ is slightly lower than the weighted mean, although the difference is smaller than 0.1 dex.

We calculated the uncertainties of $[Fe/H]_{SSP}$ according to the methods of L19, which assume perfect model spectra. This assumption is not true in reality. First, NGC 147 has multiple stellar populations, contrary to the model's SSP assumption. Second, even for a simple system with an SSP, the synthetic spectra are generated from the empirical stellar libraries and the theoretical isochrones, none of which is perfect. Therefore, we attribute the small difference ($\lesssim$ 0.1 dex) between the two techniques to systematic error that is not included in the uncertainties of the best-fit parameters. Still, it is appropriate to conclude that the metallicity measured from the resolved stellar spectroscopy is consistent with that derived from the integrated-light spectroscopy for NGC 147. In addition, the consistency between the two methods indicates that the SSP assumption is sufficient to recover the true metallicity of a galaxy with a complicated SFH.

The agreement between the integrated-light and resolved stellar metallicities also implies that the metallicity measured from the center of NGC 147 (covered by PCWI) is representative of the much larger region covered by DEIMOS. Although NGC 147 has a slightly negative metallicity gradient (see Section 2.5), the two methods agree despite their drastically different spatial coverage. If this holds true for more distant galaxies, the limited spatial coverage of galaxy surveys with fiber spectrographs would have less impact on the measurement of the stellar metallicity for galaxies with metallicity gradients as shallow as those of NGC 147. A large-sample study is essential to further investigating the limited-aperture effect on the stellar metallicity recovery but it is beyond the scope of this work.

2.4.3 Magnesium enhancement

Ideally, we would compare Mg abundances measured from integrated light to those measured from resolved stars. It is possible to measure [Mg/Fe] from DEIMOS spectra of individual stars (e.g., Kirby et al., 2010). However, the spectral range of the DEIMOS configuration employed by the archival spectra used in this paper does not reach the Mg b triplet or other strong Mg lines. Instead, the available lines have relatively high excitation potential, and they are consequently weak. This makes it difficult to measure Mg in low-S/N spectra, including those of stars in galaxies as distant as NGC 147. The result of attempting to measure [Mg/Fe] in such galaxies is a bias toward high values of [Mg/Fe][4] because low values of [Mg/Fe] result in the Mg lines becoming lost in the noise.

[4]See Figure 10 of Kirby et al. (2020) for a demonstration of this effect.

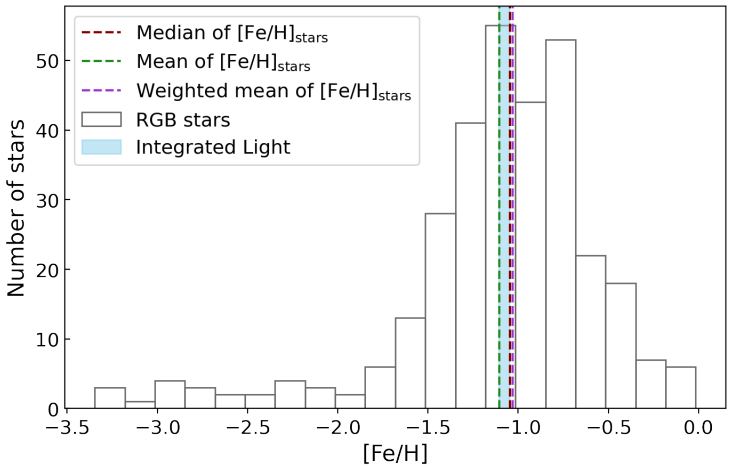

Figure 2.3: The metallicity distribution for the resolved stars analyzed in this sample. The value of $[Fe/H]_{SSP}$ (light blue region) is consistent with the mean (green dashed line), the median (red dashed line) and the inverse-variance weighted mean (blue dashed line) of $[Fe/H]_{stars}$.

An alternative way to validate the $[Mg/Fe]_{SSP}$ is to use the MZR for [Mg/H]. The low-mass MZR for [Mg/H] can be deduced from resolved stellar spectroscopy of MW satellite galaxies (Kirby et al., 2010), which are near enough to allow S/N that overcome the bias against low values of Mg abundances. The high-mass MZR can be measured from integrated-light spectroscopy of more distant galaxies (L19). The low-mass and high-mass MZRs for [Mg/H] predict different values at the mass of NGC 147, as is the case for [Fe/H] (see Section 2.6.2). If $[Mg/H]_{SSP}$ (the sum of the best-fit $[Mg/Fe]_{SSP}$ and $[Fe/H]_{SSP}$) falls on the low-mass MZR ([Mg/H]) for dwarf galaxies, then we have circumstantial evidence that the two methods give similar values of Mg abundance.

We constructed the MZR for [Mg/H] from the measurements of eight MW dwarf spheroidal (dSph) satellites (Kirby et al., 2010). We excluded more distant galaxies due to the aforementioned weak Mg lines, and we excluded most ultrafaint dwarf galaxies due to small sample sizes. We constructed the MZR from an orthogonal, least-squares linear regression taking into account measurement uncertainties in both axes (Akritas and Bershady, 1996). The resulting MZR is $\langle[Mg/H]\rangle = -3.31 + 0.32\log(M_*/M_\odot)$.

As seen in Fig. 2.4, the $[Mg/H]_{SSP}$ of NGC 147 is much more likely to fall on the low-mass MZR (Mg) of dwarf galaxies than on the high-mass one. Considering the low-mass MZR (Mg) was determined only from a few dwarf galaxies at $M_* < 10^8 M_\odot$, the small difference (< 0.2 dex) between the $[Mg/H]_{SSP}$ and the predicted value

might be attributed to an extrapolation error at the mass of NGC 147 or to intrinsic dispersion in the MZR. We therefore conclude that we have tentative evidence that $[\mathrm{Mg/Fe}]_{\mathrm{SSP}}$ is representative of the whole stellar population in the galaxy.

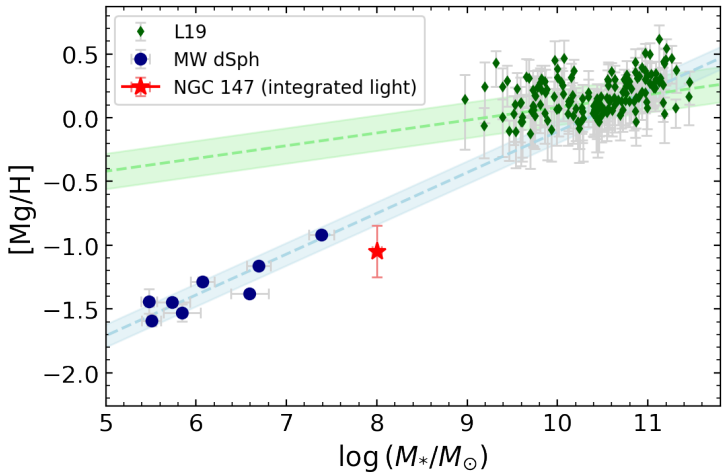

Figure 2.4: The MZR measured from [Mg/H] at $z \sim 0$. The green dashed line shows the high-mass MZR for Mg determined from the integrated spectra of massive quiescent galaxies (green diamonds) by L19. The low-mass MZR for Mg is determined only from the MW dSph satellites (blue circles). The rms for the two best-fit lines are shown in the green and blue bands. The [Mg/H] of NGC 147 measured in this work (red star) is more likely to fall on the low-mass MZR rather than on the high-mass MZR.

2.5 Spatial Distributions of Stellar Population

2.5.1 Population Gradients

Taking the advantage of IFS data, we were able to study the spatial distribution of the stellar population in the innermost region for the first time. We measured the stellar population in each Voronoi cell (Section 2.2.1). Because the north pointing lacks reliable blue spectra below 4700 Å, which are essential to determining the stellar population age, we excluded the north pointing for spatial distribution studies.

Figure 2.5 shows the 2D maps and the radial trends for the SSP-equivalent stellar population age, [Fe/H] and [Mg/Fe]. As demonstrated by Koleva et al. (2011), the SSP-equivalent parameters are sufficient to recover the true population gradients. We calculated the galactocentric elliptical radius using the position angle and ellipticity in Crnojević et al. (2014). We fit a linear model to the gradients for age, [Fe/H], and [Mg/Fe], with the `emcee` MCMC sampler[5] (Foreman-Mackey et al., 2013). The

[5]For each gradient, the initial parameters were obtained from χ^2 minimization. Broad, uniform

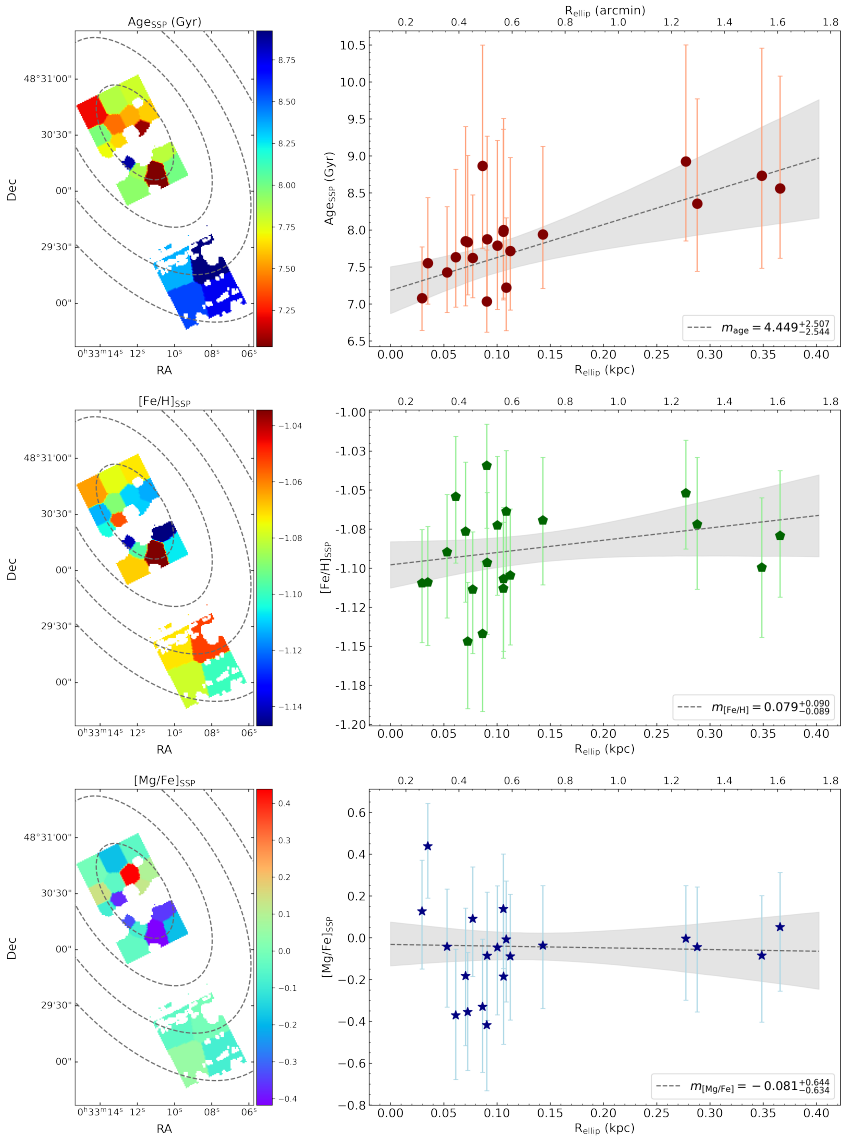

Figure 2.5: The spatially resolved measurements of SSP parameters for the central and south pointings. *Left:* The 2D maps of the best-fit stellar population age, [Fe/H], and [Mg/Fe]. The contours indicate the (projected) galactocentric elliptical radii with 0.1 kpc intervals. *Right:* The radial gradients of the stellar population. The dashed lines represent the best-fit lines from MCMC. The gray shaded region indicates the ranges between the 16th and 84th percentiles.

uncertainties of each parameter were taken to be the asymmetric 68% confidence level of the posteriors.

In the PCWI field, we marginally detected a positive age gradient within 0.4 kpc as $m_{\rm age} = \Delta\left(\frac{\rm age}{R}\right) = 4.5 \pm 2.5$ Gyr kpc^{-1}. The south field is ~ 1.5 Gyr older than the innermost bin. The positive age gradient may suggest that star formation persisted longer in the central region compared to that in more extended regions. However, no age gradient is present in the `alf` measurements. As shown in Table 2.5, around half of the best-fit results are very close to the upper limit of the stellar population age (i.e., the age of the universe), suggesting the age derived from `alf` is not well constrained. We suspect the factors discussed in Section 2.4.1 may also account for the difference. Meanwhile, the detected positive age gradient is consistent with previous literature. Han et al. (1997) also found that the younger stars in NGC 147 are more centrally concentrated than the majority of the old stars. Weisz et al. (2014) measured the SFH from *HST*/WFPC2 photometry in the central regions of NGC 147, which demonstrates that $\sim 20\%$ of the stars were formed within the past 2.5 Gyr. On the other hand, the SFH determined from an *HST*/ACS field targeted at much larger radii suggests NGC 147 had formed 80% of its stars (6^{+2}_{-1}) Gyr ago and its star formation ceased at least 3 Gyr ago (Geha et al., 2015). The different SFHs derived from HST data at different radii are qualitatively consistent with the positive age gradients we measured from integrated-light spectroscopy.

The metallicity is relatively uniform in the PCWI fields, with a slope of $m_{\rm [Fe/H]} = \Delta\left(\frac{\rm [Fe/H]}{R}\right) = 0.08 \pm 0.09$ dex kpc^{-1}. On the other hand, we find a large scatter for [Mg/Fe], with a slope of $m_{\rm [Mg/Fe]} = \Delta\left(\frac{\rm [Mg/Fe]}{R}\right) = -0.08^{+0.64}_{-0.63}$ dex kpc^{-1}. The large uncertainty on the [Mg/Fe] gradient precludes us from drawing conclusions about the relevance of this gradient to the galaxy's SFH. Furthermore, the gradient was estimated from the very central region of the galaxy so it may not represent the whole stellar population.

To investigate the population gradient at larger scales, we made use of the stellar metallicities of resolved RGB stars. As shown in Figure 2.6, the resolved metallicities for the innermost region (~400 pc) show large scatter. There are only 17 stars within the outermost radius of the PCWI fields, so the resolved metallicities may not indicate the characteristic metallicity of the stellar population in this region. The integrated metallicities derived from PCWI data are between the lowest and highest

priors were used. We ran 5000 steps with 32 walkers. Burn-in usually happened after around 40 steps, so the posteriors were well-constrained.

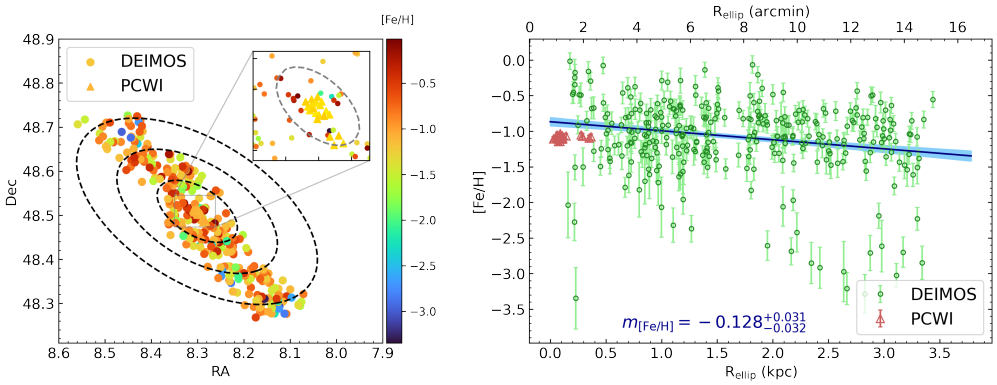

Figure 2.6: Metallicity gradient of NGC 147. *Left:* The metallicity map for the resolved stars (circles) and integrated light (triangles). The black contours demonstrate the galactocentric radii at 4, 8, 12 and 16 kpc, respectively. The inset shows the zoom-in map of the galaxy central part. The gray dashed ellipse is the maximum elliptical radius of the PCWI spatial coverage. The metallicities obtained from the integrated light are very close to those of the individual RGB stars. There is no prominent spatial variance of the stars' metallicities. *Right:* The radial gradient of the metallicity. The best-fit linear gradient of the resolved stars' metallicities is shown by the purple line. A negative slope of ~ -0.13 dex kpc^{-1} is marginally detected.

values of the resolved metallicities. The resolved study reveals a negative gradient of $\Delta\frac{<[Fe/H>}{R} \sim -0.13 \pm 0.03$ dex kpc^{-1}, different from the flat metallicity profile revealed in the PCWI fields. Because the resolved study extends to a much larger radius, we believe that the negative metallicity gradient is more representative of the galaxy population.

The negative metallicity gradient is inconsistent with the flat to positive gradient found by Crnojević et al. (2014) and Vargas, Geha, and Tollerud (2014). Crnojević et al. (2014) estimated the photometric metallicity gradient from the metallicity distribution functions (MDFs) in three radial bins from 2.5 to 6.4 kpc. Their sample consists of stars at much larger radii compared to ours and lacks measurements within 2.5 kpc. In addition, the authors suggested that their gradient may be biased because stars from tidal tails can contribute to the mean stellar metallicity in the outermost region. On the other hand, Vargas, Geha, and Tollerud (2014) measured spectroscopic metallicities from Keck/DEIMOS spectra. Similar to that in K13, the photometry used to estimate the effective temperature and surface gravity possibly had errors in its zero-points, leading to unreliable metallicity estimates. In fact, Vargas, Geha, and Tollerud (2014) reported a mean [Fe/H] for NGC 147 as ~ -0.5 dex, which is around twice the values derived in other literature, including photometric

and spectroscopic estimates (Han et al., 1997; Davidge, 2005; Gonçalves et al., 2007; Geha et al., 2010; Crnojević et al., 2014). We recovered similarly high values of [Fe/H] when we used the questionable photometry. We conclude that we should not compare our gradient to that measured by Vargas, Geha, and Tollerud (2014).

2.5.2 Outside-in Formation of NGC 147?

Stellar population gradients can provide us insight into the evolution of a galaxy. Observational studies have suggested that dSph[6] galaxies in the Local Group generally have positive age gradients and negative metallicity gradients (e.g., Koleva et al., 2011; Kirby et al., 2011a). The observed gradients are usually explained as a result of outside-in formation(e.g., Benítez-Llambay et al., 2016; Revaz and Jablonka, 2018; Genina et al., 2019), where the metals accumulate at the center of the galaxy, and the star formation becomes more concentrated with time. In particular, Genina et al. (2019) identified that ram pressure—imposed by the massive host galaxy when the satellite galaxy falls in—can compress the gas at the center of the satellite galaxy while stripping the gas from the outskirts. Consequently, the star formation at the center can be reignited while the outer regions are quenched, giving rise to the gradients observed in the Local Group dSphs. The age and metallicity gradients of NGC 147 found in this work are in alignment with the outside-in scenario, if the age gradient detected in the PCWI field is real.

As NGC 147 has no H I detection (Young and Lo, 1997), tidal stripping and ram pressure stripping are very likely to have played an important role in quenching the star formation and shaping the observed radial gradients in this galaxy. Crnojević et al. (2014) uncovered the presence of extended tidal tails in NGC 147. The tails indicate a strong tidal interaction with its host galaxy, M31. Geha et al. (2006) found kinematic evidence for tidal disruption in another M31 dE satellite, NGC 205. Mayer et al. (2006) showed that the combined effects of tides and ram pressure are significantly more successful at removing the gas from the dwarfs than tidal stripping alone. In addition, Kormendy (1985) and Kormendy and Bender (2012) also suggested that ram-pressure stripping would be one of the major quenching mechanisms for dSph galaxies in the Local Group.

[6]Some studies call the fainter dwarf ellipticals spheroidal galaxies (Kormendy et al., 2009).

2.6 Discussion

2.6.1 Comparison with previous work

So far, most works investigating the validity of recovering the stellar population, especially the metallicity, from integrated-light spectroscopy have studied relatively simple systems like globular clusters (e.g., González Delgado and Cid Fernandes, 2010; Barber et al., 2014; Conroy et al., 2018), which tend to have formed stars at the same epoch. Very few attempts have been made to directly compare the stellar populations measured from integrated and resolved spectroscopic analyses for complex systems with multiple stellar populations.

Ruiz-Lara et al. (2018) obtained an integrated spectrum of the central part of Leo A, one of the the Local Group's star-forming dIrr galaxies with $M_* \sim 3 \times 10^6 M_\odot$. They derived the SFH and the metallicity of each age bin from the integrated spectrum. They found that while the SFH is consistent with that derived from CMD fitting, the derived metallicity at all age bins is higher than the average value of individual stars obtained by Kirby et al. (2017). The differences in metallicity range from ~ 0.25 dex in the intermediate-age bins to > 1.0 dex in younger-age bins, in contrast to our results for NGC 147.

However, such a discrepancy can be explained by factors other than the intrinsic systematic effects between the two techniques. First, Leo A is still star-forming and therefore has nebular emission. If the modeling of the Balmer emission lines from the ISM was not perfect, it could have affected the depths of the Balmer absorption lines, which heavily affect the measurement of the stellar population age. In turn, this could have affected the measured metallicity according to the age–metallicity degeneracy. As an old, quiescent galaxy, NGC 147 would not suffer the same source of uncertainty. Second, Leo A is metal poor ([Fe/H] ~ -1.5). Most stellar libraries used in the modeling of integrated-light spectra do not contain enough stars with [Fe/H] < -1. If the incompleteness of the metal-poor stars in the stellar libraries causes the discrepancy found by Ruiz-Lara et al. (2018), it will not affect the existing metallcities of more massive and more metal-rich galaxies like NGC 147 derived from integrated light. In addition, Leo A exhibits a stronger metallicity gradient ($\sim$ -0.33 dex/kpc; Kirby et al., 2017) than NGC 147, which may explain the discrepancy between Kirby et al. (2017) and Ruiz-Lara et al. (2018). Kirby et al. (2017) measured stars at larger radii ($\sim 7'$), whereas Ruiz-Lara et al. (2018) observed a total area of $19.2'' \times 7''$ in the central region, corresponding to a region within a 0.15 half-light radius.

On the other hand, Boecker et al. (2020) recovered an age-metallicity distribution of M54 measured from integrated-light spectra that was consistent with the resolved stellar spectra obtained on MUSE. Unlike most other star clusters, M54 has known multiple stellar populations formed at different epochs (Siegel et al., 2007; Alfaro-Cuello et al., 2019). Boecker et al. fit for a linear combination of SSP models to account for the SFH rather than assuming an SSP, and they found excellent agreement between the mass-weighted age and metallicity. The mass-weighted metallicity of the integrated-light spectra is 0.2 dex lower than the mean for the resolved stars, whereas the difference in the light-weighted metallicity is as small as 0.1 dex. The results are similar to ours, suggesting that taking the SFH into account or not does not significantly affect the recovery of metallicity from the integrated spectra. However, their data set is slightly different from ours. First, a number of stars are resolved in the MUSE field of M54, so that the resolved stars would contribute greatly to the integrated-light spectra. Since the resolved stars are the brightest ones among the whole stellar population, one is more likely to obtain consistent light-weighted values from the integrated and resolved analyses even though systematic offsets are present. Second, both the integrated and resolved spectra are obtained on the same instrument; therefore, the instrumental effects would be minimized. Our work moves one step toward validating the comparability of integrated-light spectra of distant galaxies to resolved spectra of local galaxies because we directly compare the measurements from completely unresolved and completely resolved populations.

2.6.2 Implications for the MZR

Measuring the MZR across the full range of galaxy mass is extremely important to unveil how the physical processes regulating metal retention and interaction with the surrounding environment vary as the galaxies grow in mass. However, possible systematic effects between different methods of determining the metallicity obfuscate the exact form of the MZR.

Constructing the MZR from gas-phase metallicities has taught us an important lesson on understanding the role of systematic effects when measuring metallicities in different galaxy types and ages. Previous studies have found that different methods used to measure gas metallicity suffer from systematic offsets (e.g., Nagao, Maiolino, and Marconi, 2006; Kewley and Ellison, 2008; Andrews and Martini, 2013; Yates et al., 2020), and the discrepancy can be as large as 0.7 dex (Kewley and Ellison, 2008). These systematic effects can lead to quantitatively and qualitatively different shapes for the gas-phase MZR. For instance, most studies favor a continuous gas-phase

MZR that exhibits a single power law at low and intermediate mass, and gradually flattens at the high-mass end (e.g., Tremonti et al., 2004; Kewley and Ellison, 2008; Zahid et al., 2013), while Blanc et al. (2019) discovered a sharp transition in the gas-phase MZR, which has a much steeper slope at $10^{9.5} - 10^{10.5} M_{\odot}$. Therefore, it is extremely important to understand the systematic offsets between different methods before placing the MZRs on the same absolute scale.

The literature discussion of systematic effects on galactic stellar metallicities is small relative to the extensive studies on the discrepancies of gas metallicity diagnostics. The different treatment exists partly because it is difficult to apply resolved stellar spectroscopy and integrated-light spectroscopy to the same galaxies. It is impossible to resolve RGB stars in massive galaxies beyond Andromeda, while most local dwarf galaxies are too large to fit in a long-slit spectrograph for integrated-light spectroscopy. So far, only Ruiz-Lara et al. (2018) have compared the stellar metallicity of Leo A determined from integrated light to that obtained from resolved stars. As discussed in Section 2.6.1, the large discrepancy may result from factors other than systematic offsets. The agreement we obtained between resolved stars and integrated light in NGC 147 is encouraging because we adopted the same fitting algorithm used to derive the high-mass MZR L19, which indicates relatively small systematic offsets in the stellar metallicity determination.

As seen in Figure 2.7, the high-mass MZR predicts an [Fe/H] at the mass of NGC 147 that is higher by 0.6 dex relative to the low-mass MZR. Our consistent resolved and integrated metallicity estimates tentatively suggest that the discrepancy between the low-mass MZR and high-mass MZR cannot be attributed to systematic effects intrinsic to the two techniques. We also exclude the possibility that the consistency in the two approaches is biased due to the SSP assumption in Appendix 2.8.Instead, our results support a real break related to physical processes governing the metal content. If the systematic offsets of the resolved and integrated-light methods are indeed as low as what we obtained for NGC 147, it is possible that the stellar MZR may also have a sharp transition, like the gas-phase MZR derived by Blanc et al. (2019). This break in the stellar MZR was also observed by Gallazzi et al. (2005), who measured the stellar MZR from a single method (spectrophotometric indices) rather than comparing the MZRs measured from different methods in different mass ranges. However, the uncertainties of [Fe/H] below $10^{10} M_{\odot}$ are too large to distinguish between the low-mass and high-mass MZRs.

A break in the stellar MZR was also reported by Panter et al. (2008), who measured

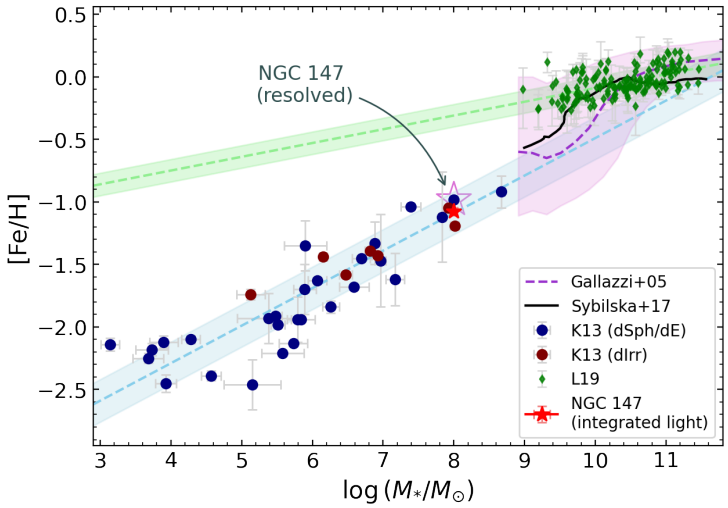

Figure 2.7: The MZR measured from [Fe/H] at $z \sim 0$. This figure is the same as Fig. 2.4, except that the low-mass MZR is obtained from dIrrs in addition to dSphs/dEs. The purple region shows the MZR of local Sloan Digital Sky Survey (SDSS) galaxies using the spectrophotometric indices (Gallazzi et al., 2005). The weighted mean of the [Fe/H] of NGC 147 for resolved stars, which is highlighted by the purple star, is remeasured in this work using updated photometry (Section 2.2.2). The [Fe/H] of NGC 147 measured from integrated light (red star) falls on the low-mass MZR, indicating the systematic difference between the two techniques cannot explain the discrepancy in the MZRs between the two mass ranges.

the stellar MZR for a large sample of local SDSS galaxies above $10^8 M_\odot$ via full-spectrum fitting and discovered a steeper slope for galaxies between $10^8 - 10^{10} M_\odot$ than observed at higher mass. They suggested that the steeper slope was an artificial bias introduced by the limited aperture of the SDSS fibers, which cannot observe the outer region of low-mass galaxies. However, Sybilska et al. (2017) measured the stellar metallicities for dwarf and giant quiescent galaxies from IFS data cubes obtained with the SAURON IFU, which suffers much less from aperture bias. A break was still present in their MZR in the same mass range, further suggesting that the break is very likely to be real.

The two MZRs may indicate a change in the feedback mechanisms as the galaxies grow in mass. Hayward and Hopkins (2017) proposed an analytic model to explain how stellar feedback simultaneously regulates star formation and drives outflows in a turbulent ISM. They argued that the mass-loading factor could decrease dramatically for galaxies above $\sim 10^{10} M_\odot$, so that high-mass galaxies become much less efficient in expelling the metal-enriched ISM. Because the stellar metallicity represents the metals locked inside the stars from the surrounding ISM averaged

over the SFH, the feedback changes can also affect the shape of the stellar MZR indirectly. Unfortunately, the current stellar MZR (Fig. 2.7) has few individual precise measurements for intermediate-mass galaxies ($10^8 < M_*/M_\odot < 10^{10}$), so we cannot determine how the shape of the stellar MZR would change across the full range of galaxy mass. Further studies focusing on the MZR of individual galaxies at intermediate mass are necessary to unveil the nature of the processes regulating the metal cycle and shaping the MZR. Nevertheless, the stellar MZRs of individual dwarf and massive galaxies can be a useful tool to help us understand the physical processes related to galactic chemical evolution. Our work presents the first evidence that it is reasonable to put the two MZRs on the same absolute scale to jointly constrain the shape of the stellar MZR.

Our investigation of systematic effects focused on just one galaxy: NGC 147. It is possible that our result is fortuitous and that a larger ensemble of galaxies would reveal some systematic differences between resolved spectroscopy and integrated light. Nonetheless, our results for NGC 147 suggest that these systematic effects do not play an important role in causing the discrepancy observed between different mass ranges of the stellar MZR. We anticipate observing more galaxies in the future to retire once and for all the possibility that the difference in technique—rather than in astrophysics—is responsible for the discrepancy.

2.7 Conclusions

We measured the stellar population age, [Fe/H], and [Mg/Fe] of the central region ($\lesssim$400 pc, i.e., 2′) in NGC 147 from integrated-light spectra obtained with PCWI. We also provided updated metallicity estimates for 317 RGB stars in the sample of K13. We compared the mean metallicity of the resolved stars with the measurement from integrated light to investigate systematic effects between the two techniques. A summary of our findings is as follows:

1. We recovered the global SSP-equivalent stellar population from integrated spectra and measured the stellar population age= $8.11^{+0.74}_{-0.54}$ Gyr, [Fe/H]= $-1.069^{+0.029}_{-0.031}$ and [Mg/Fe]= $0.024^{+0.20}_{-0.20}$. The iron and magnesium abundances are consistent with the best-fit parameters obtained from `alf`'s simple mode.

2. The best-fit SSP age is only 0.03 dex higher than the mass-weighted age determined from the CMD fitting of Weisz et al. (2014). The difference between $[\mathrm{Fe/H}]_{\mathrm{SSP}}$ and the weighted mean of $[\mathrm{Fe/H}]_{\mathrm{stars}}$ is less than 0.1 dex, implying that the SSP assumption is valid to recover the mean stellar metallicity for a

complex system with multiple stellar populations. It also suggests that the SSP assumption may recover the stellar age in some cases, although it strongly depends on the choice of SSP templates.

3. Making use of the IFS cubes, we detected a marginally positive age gradient in the central regions. Combining this age gradient with the negative metallicity gradient in the resolved stars, it is possible that NGC 147 formed outside in.

4. The resolved and integrated metallicities of NGC 147 are consistent within 0.1 dex, suggesting that systematic effects cannot explain the $\sim$ 0.6 dex discrepancy between the low-mass (K13) and high-mass (L19) stellar MZRs. Therefore, we tentatively conclude that the break in the MZRs at different mass ranges implies some physical mechanism transitions at $10^8 M_\odot < M_* < 10^{10} M_\odot$.

There is only one target in this work, so it is possible that such a small systematic offset ($<$ 0.1 dex) is underestimated. Nevertheless, our analysis of NGC 147 is strong evidence that the systematic effects of different techniques of determining metallicity will not be the major cause of the discrepancy in the stellar MZRs. Future observations are necessary to expand this study to a larger sample in order to verify that the underlying astrophysical processes are ultimately responsible for the changing behavior of stellar MZR.

Acknowledgments

The authors acknowledge the constructive feedback from the anonymous referee, which helped us improve the manuscript. We thank Yuguang Chen, Donal O'Sullivan and James (Don) Neill for useful discussions on PCWI data reduction and covariance correction. We gratefully thank the staff at the Palomar Observatory, including support astronomers Carolyn Heffner and Kevin Rykoski, and telescope operator Kajsa Peffer, for assisting in the observations.

This material is based on work supported by the National Science Foundation under Grant No. AST-1847909. E.N.K. gratefully acknowledges support from a Cottrell Scholar Award administered by the Research Corporation for Science Advancement. M.A.dl.R. acknowledges the financial support of the NSF Graduate Research Fellowship Program.

We are grateful to the many people who have worked to make the Keck Telescope and its instruments a reality and to operate and maintain the Keck Observatory.

The authors wish to extend special thanks to those of Hawaiian ancestry, on whose sacred mountain we are privileged to be guests. Without their generous hospitality, none of the observations presented herein would have been possible. This research has made use of the Keck Observatory Archive, which is operated by the W. M. Keck Observatory and the NASA Exoplanet Science Institute, under a contract with the National Aeronautics and Space Administration.

2.8 Appendix: Comparison with CSP Models

In this section, we investigate whether fitting the data with more complicated CSP models would affect our primary results. Because CSP models have more free parameters and thus require higher-quality data to achieve the same precision, we limit our analysis to the stacked spectrum, which has very high S/N (~ 111 Å^{-1}). Here we present the measured ages and [Fe/H] from three different full spectral fitting codes that fit for multicomponent stellar populations: L19's method (Appendix 2.8.1), `alf` (Appendix 2.8.2), and pPXF (Cappellari, 2017, Appendix 2.8.3). As shown in Figure 2.8, the stellar metallicity estimates are not greatly affected by the choice of models, while the measured stellar ages are more strongly dependent on the assumed SFH. We find that taking the SFH into account leads to greater consistency between different methods and templates than assuming an SSP. Therefore, CSP models may be a more appropriate way to estimate the stellar age of complex systems when the data quality is good enough.

2.8.1 Comparison to the CSP models in L19's fitting code

To investigate whether adopting CSP models would affect the recovered metallicities, we fit for a multicomponent stellar population with ages and weights determined from the SFH measured from CMD fitting to *HST* photometry (Weisz et al., 2014). Instead of fitting for linear combinations of SSP models with different metallicities, we choose to unrealistically assume that all components have the same metallicity. This can reduce the degeneracy of free parameters and approximately estimate the mass-weighted metallicities to the greatest accuracy.

The best-fit metallicities are $[\mathrm{Fe/H}]_{\mathrm{CSP}} = -1.000^{+0.018}_{-0.014}$ and $[\mathrm{Mg/Fe}]_{\mathrm{CSP}} = 0.096^{+0.15}_{-0.37}$. Compared to $[\mathrm{Fe/H}]_{\mathrm{SSP}} = -1.069^{+0.029}_{-0.031}$ and $[\mathrm{Mg/Fe}]_{\mathrm{SSP}} = 0.024^{+0.20}_{-0.20}$, the best-fit metallicities derived from CSP models are higher and closer to the resolved metallicities, further diminishing the systematic offsets between the two techniques. The differences in the recovered [Fe/H] and [Mg/Fe] from SSP models and CSP models are within 0.1 dex; therefore, we conclude that the metallicity measurements

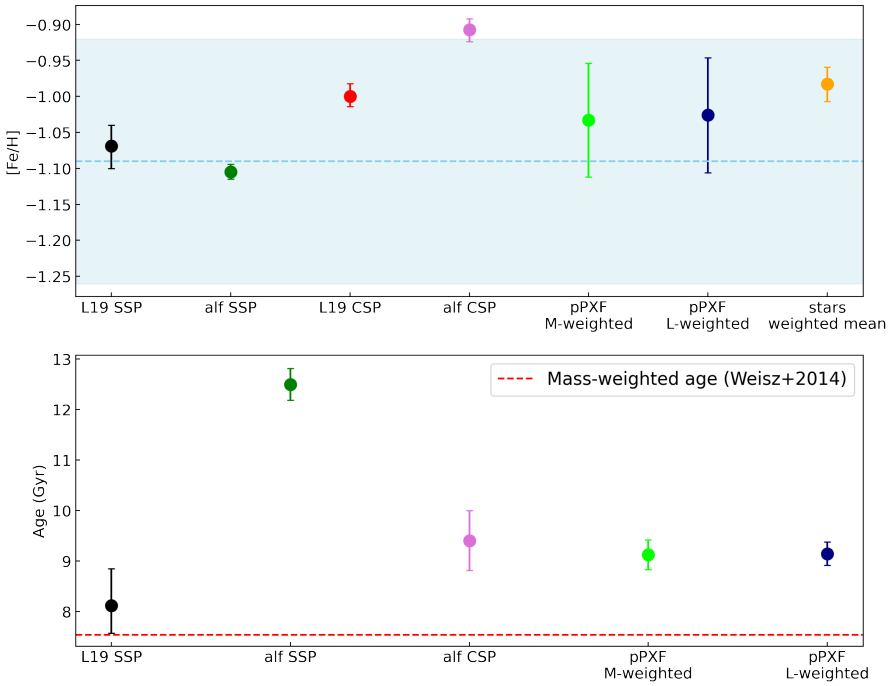

Figure 2.8: The comparison between the measured [Fe/H] (top panel) and stellar ages (bottom panel) in different stellar population models. *Top:* The blue dashed line and the shaded region indicate the [Fe/H] predicted by the low-mass MZR K13 at the mass of NGC 147 and the corresponding 1σ confidence interval. The data points show the measured [Fe/H] (weighted mean for CSP models) via various methods discussed in this work, which are all consistent with the low-mass MZR. *Bottom:* the measured ages (weighted mean for CSP models) via different methods discussed in this work. Among them, only the SSP age derived from L19's method is consistent with the mass-weighted age obtained from the CMD fitting in Weisz et al. (2014) (red dashed line).

are not affected significantly by the choices of SSP and CSP models, consistent with the results of Mentz et al. (2016) and Leethochawalit et al. (2018b).

2.8.2 Comparison to the results from `alf` full mode

In addition to the SSP models in simple mode, `alf` also provides a full mode that fits for two-component stellar populations with an older (>3 Gyr) and a younger population (<3 Gyr), which allows us to approximate the SFH of the galaxy. We fit the stacked spectrum in `alf` full mode.

The mass-weighted age derived in full mode (CSP-equivalent) is ~ 9.4 Gyr. Compared to the SSP-equivalent age (12.5 Gyr) derived in simple mode, the difference between the CSP age and the mass-weighted age from CMD fitting by Weisz et al. (2014) is smaller. The consistency suggests that more complicated stellar population

models are necessary to obtain more accurate stellar age measurements in galaxies. On the other hand, the best-fit results from `alf` full mode indicate that less than 0.5% of the stellar population was formed in the past 3 Gyr, while the SFH revealed by the CMD fitting in Weisz et al. (2014) suggests that ∼20% of stars were formed in the past 2.5 Gyr. We also notice that the CSP age is surprisingly younger than the SSP age, whereas Choi et al. (2014) found that SSP-equivalent ages are younger than both light- and mass-weighted ages derived in models with extended SFHs. The discrepancy may arise from the fact that `alf` assumes two independent starbursts at different epochs rather than extended SFHs. The disagreements above may also suggest that the recovered stellar age is sensitive to the adopted CSP models and their underlying assumptions on SFH, and thus future investigations are important to explore which CSP models are more suitable to measuring the stellar ages of galaxies.

Unlike the large difference seen in ages, the metallicities derived in the two modes are very similar. $[\mathrm{Mg/Fe}]_{\mathrm{CSP}} = 0.064^{+0.018}_{-0.016}$) is consistent with $[\mathrm{Mg/Fe}]_{\mathrm{SSP}}$ within 1σ, while $[\mathrm{Fe/H}]_{\mathrm{CSP}} = -0.907^{+0.015}_{-0.017}$ is slightly higher than $[\mathrm{Fe/H}]_{\mathrm{SSP}}$. The difference between $[\mathrm{Fe/H}]_{\mathrm{CSP}}$ and $[\mathrm{Fe/H}]_{\mathrm{stars}}$ is still within 0.1 dex, which once again demonstrates that the metallicity measurements are less affected by the assumed stellar population models.

2.8.3 Comparisons to pPXF full spectral fitting code

Apart from the two fitting methods discussed in the main text, we test our CSP measurements by running another independent code, pPXF (Cappellari, 2017), which fits for linear combinations of different SSPs to account for complex SFHs in galaxies. For simplicity, α-enhancement is not included. We use the SSP models from the E-MILES library (Vazdekis et al., 2016), generated from the BaSTI isochrones (Pietrinferni et al., 2004) and Kroupa (Kroupa, 2001) IMF. The metallicities and ages of the templates range from −2.27 to 0.4 dex and 0.03 to 14 Gyr, respectively. Because the SSP models assume solar-scaled abundances, the metallicity [M/H] can be interpreted as [Fe/H]. Regularization is used to address some of the deficiencies in pPXF: that it does not necessarily return unique solutions, and that it is very sensitive to the noise in data due to the vast parameter space explored in fitting. The mass- and light-weighted stellar population parameters can be computed from the weights of each SSP component returned by pPXF.

The mass- and light-weighted [Fe/H] are -1.033 ± 0.079 and -1.026 ± 0.08, re-

spectively, consistent with the metallicities measured from other methods. The uncertainties are calculated as the weighted variance of the ages and metallicities of each SSP component. On the other hand, the mass- and light-weighted ages are both 9.96 ± 0.01 Gyr, higher than the SFH-based age measured by Weisz et al. (2014) but similar to the mass-weighted age derived in `alf` full mode, which also uses CSP models. The results suggest that stellar age estimates from integrated-light spectroscopy depend more heavily than metallicity estimates on the assumed SFH.

Chapter 3

STELLAR ABUNDANCES AND AGES OF GRAVITATIONALLY LENSED, QUIESCENT GALAXIES AT $z \sim 1$

Zhuang, Z. et al. (May 2023). "A Glimpse of the Stellar Populations and Elemental Abundances of Gravitationally Lensed, Quiescent Galaxies at z $\gtrsim$ 1 with Keck Deep Spectroscopy". In: *ApJ* 948.2, p. 132. DOI: 10.3847/1538-4357/acc79b.

Abstract

Gravitational lenses can magnify distant galaxies, allowing us to discover and characterize the stellar populations of intrinsically faint, quiescent galaxies that are otherwise extremely difficult to directly observe at high redshift from ground-based telescopes. Here, we present the spectral analysis of two lensed, quiescent galaxies at $z \gtrsim 1$ discovered by the ASTRO 3D Galaxy Evolution with Lenses survey: AGEL1323 ($M_* \sim 10^{11.1} M_\odot$, $z = 1.016$, $\mu \sim 14.6$) and AGEL0014 ($M_* \sim 10^{11.5} M_\odot$, $z = 1.374$, $\mu \sim 4.3$). We measured the age, [Fe/H], and [Mg/Fe] of the two lensed galaxies using deep, rest-frame-optical spectra (S/N $\gtrsim$ 40 Å^{-1}) obtained on the Keck I telescope. The ages of AGEL1323 and AGEL0014 are $5.6^{+0.8}_{-0.8}$ Gyr and $3.1^{+0.8}_{-0.3}$ Gyr, respectively, indicating that most of the stars in the galaxies were formed less than 2 Gyr after the Big Bang. Compared to nearby quiescent galaxies of similar masses, the lensed galaxies have lower [Fe/H] and [Mg/H]. Surprisingly, the two galaxies have comparable [Mg/Fe] to similar-mass galaxies at lower redshifts, despite their old ages. Using a simple analytic chemical evolution model connecting the instantaneously recycled element Mg with the mass-loading factors of outflows averaged over the entire star formation history, we found that the lensed galaxies may have experienced enhanced outflows during their star formation compared to lower-redshift galaxies, which may explain why they quenched early.

3.1 Introduction

How galaxies form and evolve to the state we see today has been a long-standing question in modern astronomy. One way to unveil the evolutionary history of a galaxy is to constrain its chemical composition because the overall metal abundance of a galaxy reflects the interplay among the gravitational potential (e.g., Dekel and Silk, 1986), star formation efficiency (e.g., Calura et al., 2009; Magrini et al., 2012)

and galactic inflows/outflows (e.g., Finlator and Davé, 2008). The well-known mass–metallicity relation (MZR), a tight correlation between galaxy stellar mass and metallicity, has been widely used to investigate the metal retention of galaxies at different masses and redshifts (e.g., Tremonti et al., 2004; Gallazzi et al., 2005; Erb et al., 2006; Finlator and Davé, 2008; Kirby et al., 2013; Lu, Blanc, and Benson, 2015; Ma et al., 2016; Kacprzak et al., 2016; Leethochawalit et al., 2019; Zhuang et al., 2021).

While the majority of previous studies have used metallicity (i.e., gas-phase oxygen abundance or stellar-phase iron abundance) to characterize the chemical abundances of galaxies that cannot be resolved into stars, spectroscopic studies have turned to detailed abundances of galaxies using modern techniques, such as full-spectrum fitting of the stellar continuum to determine stellar abundances (e.g., Conroy et al., 2018). Measuring the abundances of individual α elements (including O, Mg, Si and Ca) in stellar populations is a more effective probe of galactic chemical evolution than measuring iron alone. While iron is primarily produced in Type Ia supernovae of low-mass stars with a delayed explosion timescale, α-elements are synthesized by core-collapse supernovae of massive stars. Because of the difference in their recycling time, bulk α enhancement—[α/Fe]—has been used to measure the duration of star formation historically (e.g., Thomas et al., 2005; Walcher et al., 2015; Kriek et al., 2016), if assuming a closed box where outflows and/or inflows are absent. In addition, α elements can be approximated to be instantaneously recycled given the short lifetime of massive stars, so they can be used in some simple chemical evolution models. For instance, Leethochawalit et al. (2019) used the relation between stellar masses and [Mg/H] for quiescent galaxies derived from chemical evolution models to constrain the mass-loading factors of galactic outflows, when galaxies are assumed to be leaky boxes in this case.

Whereas the stellar abundances of quiescent galaxies have been extensively studied out to $z \sim 0.7$ (Choi et al., 2014; Gallazzi et al., 2014; Leethochawalit et al., 2018a; Leethochawalit et al., 2019; Beverage et al., 2021), we still have limited knowledge about the chemical composition of stellar populations at $z > 1$, especially α-enhancements. A more nuanced understanding of the chemical abundances of high-z galaxies is crucial to develop a full picture of the chemical evolution and enrichment of galaxies through cosmic time. Unlike measuring the gas-phase abundances for high-z star-forming galaxies, which relies on strong emission lines, constraining the stellar abundances for high-z quiescent galaxies requires deep spec-

troscopy to capture the faint stellar absorption lines. Consequently, the few available measurements at $z > 1$ are either based on a stacked spectrum of quiescent galaxies at similar redshifts and masses (e.g., Onodera et al., 2015; Carnall et al., 2022) or ultra-deep spectroscopy, which typically requires tens of hours on large ground-based 8-10 m telescopes for a single galaxy (e.g., Toft et al., 2012; Lonoce et al., 2015; Kriek et al., 2016; Kriek et al., 2019). Several studies have also attempted to determine the stellar metallicity of high-z quiescent galaxies using low-resolution grism spectra obtained with the *Hubble Space Telescope* (HST) (e.g., Morishita et al., 2018; Estrada-Carpenter et al., 2019), but these studies primarily used the continuum shape. Consequently, they cannot characterize the detailed shapes of stellar absorption lines, leading to high degeneracy between stellar metallicity and other galaxy properties, such as age.

Gravitational lensing is a promising way to revolutionize our understanding of faint, high-z quiescent galaxies because it magnifies both the flux and angular resolution of distant galaxies. The magnified flux of lensed galaxies enabled us to obtain comparable or even higher signal-to-noise (S/N) spectra with shorter integration times, allowing us to investigate the stellar population from the faint stellar continua more accurately (e.g., Newman et al., 2018; Jafariyazani et al., 2020; Man et al., 2021). The magnified, lensed galaxies are more extended, providing us an opportunity to resolve the galaxies that are much more compact in the source plane in exquisite detail. With the help of gravitational lensing, early studies were able to reveal unprecedented details of high-z galaxies, such as the metallicity gradient (e.g., Leethochawalit et al., 2016; Jafariyazani et al., 2020) and morphology (e.g., Newman et al., 2018; Man et al., 2021).

In this work, we present the spectral analysis of two gravitationally lensed, quiescent galaxies at $z \gtrsim 1$ discovered by the `ASTRO 3D Galaxy Evolution with Lenses` (`AGEL`) survey (Tran et al., 2022) in order to characterize their stellar populations, especially the stellar elemental abundances. In Section 3.2, we describe our sample and data used for analysis. We explain how we determine the stellar mass and stellar population properties in Section 3.3. We present our results (the measured stellar population age, [Fe/H] and [Mg/Fe]) in Section 3.4 and discuss their physical implications in Section 3.5. Finally, we summarize our findings in Section 3.6. Throughout this work we assume a flat ΛCDM cosmology with $\Omega_m = 0.3$, $\Omega_\Lambda = 0.7$ and $H_0 = 70$ km s^{-1} Mpc^{-1}.

3.2 Galaxy Sample and Data

3.2.1 The Lensed Galaxies

The two gravitationally lensed galaxies, AGEL132304+034319 (hereafter AGEL1323) at $z = 1.016$ and AGEL001424+004145 (AGEL0014) at $z = 1.374$, were identified as part of the AGEL survey (Tran et al., 2022). The AGEL survey performed spectroscopic observations on strong gravitational lenses selected from the Dark Energy Survey (DES; Abbott et al., 2018) and the Dark Energy Camera Legacy Survey (DECaLS; Dey et al., 2019) to measure their redshifts. These lensed galaxy candidates were discovered using convolutional neural networks (Jacobs et al., 2019b; Jacobs et al., 2019a) and were notable for their red arcs. AGEL1323 was also independently discovered by the COOL-LAMPS Surveys as COOL J1323+0343 (Sukay et al., 2022) in a visual search of the northern galactic cap portion of the southern DECaLS dataset.

Neither galaxy displayed emission lines in the identification spectra from AGEL survey, indicating their quiescent nature. As shown in Figure 3.1, AGEL1323 is a five-image[1] system lensed by a group of galaxies with three visible clumps, while AGEL0014 is an arc spanning at least 3″ lensed by a foreground lens galaxy. The magnified flux of the lensed images make the two galaxies ideal for studying the detailed abundances and spatially resolved kinematics with deep spectroscopy. While this paper focuses on the chemical abundances of the lensed galaxies, Sweet et al. (in prep.) will present a high-resolution kinematic analysis of AGEL1323 in an upcoming paper.

In 2021, we acquired deeper follow-up observations with Keck/LRIS and Keck/MOSFIRE for the galaxies to capture the portion of the rest-frame optical between 3600 Å and 5500 Å, which is sufficient to recover the ages and Fe and Mg abundances of the stellar population (Leethochawalit et al., 2018a; Leethochawalit et al., 2019; Zhuang et al., 2021). In this section, we describe the spectroscopic and photometric data used for the stellar population analyses (Table 3.1).

3.2.2 Spectroscopy

Keck/LRIS

We observed AGEL1323 with LRIS on the Keck I telescope with the D560 dichroic, 400/8500 grating and 1″ slit width for the red side for a total of 6 hours. The seeing varied between $\sim 0.8''$ and $\sim 1.1''$ throughout the night. We determined a FWHM

[1] Two of the lensed images are only visible in high resolution HST imaging (Figure 3.2).

Table 3.1: Spectroscopic and Photometric Observations of the Lensed Galaxies

Object	R.A. (J2000)	Decl. (J2000)	z_{spec}	Instrument	Date	Integration Time	S/N[a] (Å^{-1})
AGEL1323	$13^h23^m04^s.1$	$+03^d43^m19^s.4$	1.016	Keck/LRIS	2021-04-05	6.0 h	60
				Keck/MOSFIRE-Y	2021-04-17	5.0 h	50
				*Keck/MOSFIRE-Y	2021-04-17	786 s	-
				*Keck/MOSFIRE-K_s	2021-04-17	105 s	-
				*HST/WFC3-F200LP	2022-06-18	600 s	-
				*HST/WFC3-F140W	2022-06-18	598 s	-
AGEL0014	$00^h14^m24^s.3$	$+00^d41^m45^s.5$	1.374	Keck/MOSFIRE-Y	2021-08-17	1.5 h	50
				Keck/MOSFIRE-J	2021-08-17	1.5 h	40
				*Keck/MOSFIRE-J	2021-10-30	1830 s	-
				*Keck/MOSFIRE-K_s	2021-10-30	1668 s	-

[a] S/N of the stacked spectra, including all lensed images. The S/N was calculated as median ratio of the noise array to the flux array in the wavelength range of 4000–5500Å. For this purpose, the noise array was not augmented by χ^2. That augmentation applies only to the reported uncertainties on stellar population parameters (see Section 3.3.3).
* Photometric observations.

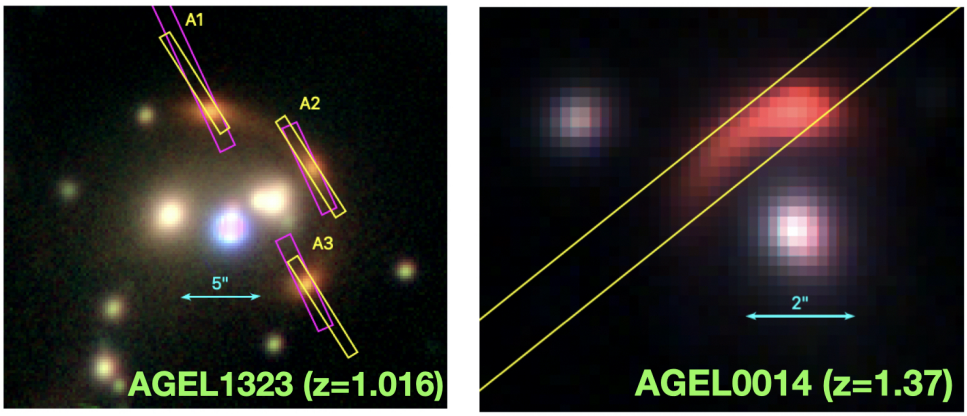

Figure 3.1: Color images of AGEL1323 (top) and AGEL0014 (bottom). The images were constructed using HSC *ri*-band and MOSFIRE-K_s imaging. The MOSFIRE (yellow) and LRIS (magenta) slits are overplotted.

of 6.47 Å from the spectrum of the arc lamp, corresponding to 3.21 Å in the rest frame. The spectral energy distribution of AGEL1323 is such that the blue side of the LRIS spectrum had insufficient flux for a meaningful analysis.

The data were reduced with PypeIt (Prochaska et al., 2020a; Prochaska et al., 2020b), a semi-automatic software that performs flat field correction, cosmic ray removal, wavelength calibration, flexure correction via sky lines, heliocentric corrections, sky subtraction and spectral extraction. Because we used HgNeArCdZn lamps, different from the archived arcs in PypeIt, we calibrated the wavelength solution by visually identifying the arc lines instead of using the automatic line detecting algorithms. The extracted 1D spectra of each image of AGEL1323 (A1, A2, and A3) were flux-calibrated and coadded separately after the main run of PypeIt. The telluric corrections were performed directly on the coadded science spectra, which

fits a fifth-order polynomial model representing the continuum of the galaxy and spectral regions sensitive to telluric absorption to a grid of telluric spectral templates. Readers are referred to PypeIt's website[2] for details. The coadded spectra for the three lensed images were stacked with inverse variation weighting to maximize the S/N in order to better characterize the stellar population properties.

Keck/MOSFIRE

We observed AGEL1323 with MOSFIRE Y-band on Keck I telescope MOSFIRE-Y using a slit width of 0.7″ for the slit mask for 5 hours. The seeing was around 1″, yielding a FWHM of $\sim$ 2.5 Å. On the second night, we observed AGEL0014 using a slit width of 1.0″ for a total of 3 hours in Y and J band. The seeing was around 0.4″ on the second night, providing a FHWM of $\sim$ 3.5 Å in the Y-band and $\sim$ 4.4 Å in the J-band.

The raw data were reduced using the MOSFIRE DRP[3] to generate a coadded 2D spectrum for the entire night. Generally, the MOSFIRE DRP expects that the data were taken with a standard dithering pattern of ABAB within the slits, which results in one positive and one negative trace in the differential image. However, we adopted a non-standard dither pattern for AGEL1323 because the small separations ($\sim$ 7″) between the three lensed images do not allow enough room to nod within the slits. We therefore required the telescope to nod across the slits. The mask was designed to have two pairs of slits separated by 23.94″, corresponding to the length of three slits. Three traces of the three lensed images were present on the different slits at the two different telescope pointings. This strategy made the differential image consist of either a positive or a negative trace in one slit. We modified the DRP slightly to handle the sky subtraction to account for this nodding solution. In each slit of the differential image, the light profile was generated from the median of 2D spectrum. We then fit a Gaussian profile to the light profile and masked out the regions within 2σ where most of the light is from the galaxy. We then estimated the sky background from the unmasked regions. We also experimented with a few choices of thresholds and found that 2σ masking could give the cleanest background while keeping enough signal from the galaxy.

One-dimensional (1D) spectra were extracted from the 2D spectrum produced by the DRP using MOSPEC (Strom et al., 2017). We used optimal extraction (Horne,

[2]PypeIt: https://pypeit.readthedocs.io/en/release/index.html
[3]MOSFIRE DRP: https://keck-datareductionpipelines.github.io/MosfireDRP/

1986). The flux calibration was performed by comparing the observed spectrum of the standard star with the Vega spectrum scaled to its J-band magnitude. A B-spline was fitted to the ratio of the scaled spectrum to the observed spectrum to derive the response curve. We then applied the curve to other extracted science spectra to obtain the flux-calibrated, telluric-corrected spectrum of each science target.

3.2.3 Photometry

Ground-based Imaging

To construct the lens model, we obtained MOSFIRE images for AGEL1323 and AGEL0014 on 2021 Apr 5 and 2021 Oct 30, respectively. The sky was clear on both nights, with an average seeing of 0.82″ on Apr 5 and 0.65″ on Oct 30. We reduced the images by using the standard IRAF commands to perform dark subtraction, flat correction, and sky subtraction. The final images have a 5σ limiting magnitude of 24.88 mag in the J-band and 24.38 mag in the K_s-band for AGEL0014, and 23.93 mag in the Y-band and 23.14 mag in the K_s-band for AGEL1323 on a pixel-to-pixel basis. We performed the flux calibration by comparing the instrumental magnitudes of 2MASS stars in the field obtained from SExtractor (Bertin and Arnouts, 1996) with the values in 2MASS Point Source Catalog (Skrutskie et al., 2006).

In addition, the public images of AGEL1323 and AGEL0014 in the Hyper Suprime-Cam (HSC) Subaru Strategic Program DR3 (Aihara et al., 2022) were used for lens modeling (Section 3.3.2).

HST/WFC3

We used F140W and F200LP images from HST/WFC3 from program 16773 (PI Glazebrook). The target was observed in the IR/F140W filter for 3 exposures of 200 seconds, and in the UVIS/F200LP filter for 2 exposures of 300 seconds (Shajib et al., 2022a; Shajib et al., 2022b). The images were reduced using the STScI DrizzlePac software package to align the separate exposures, as well as correct for background distortion and remove flagged cosmic rays. Within the AstroDrizzle function, we customized the WCS for the final stacked output to rotate the filters in the same orientation. We set the final pixel size of “0.08 to match the F200LP filter with the scaling of filter F140W. To create the mock-RGB combined image in Figure 3.2, we used the Lupton et al. (2004) algorithm implemented in astropy's make_lupton_rgb.

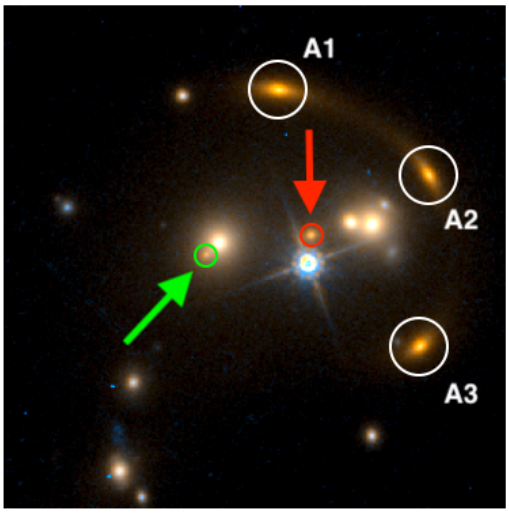

Figure 3.2: The HST/WFC3 color image of AGEL1323 constructed with F200LP and F140W imaging. The counter-image and the central image are marked by the green and red circle, respectively.

3.3 Methods

3.3.1 Lens Modeling

To obtain a reliable mass estimate, a lens model is needed to calculate the magnification factor and yield the delensed stellar mass. We used the lens modeling software PyAutoLens[4] (Nightingale and Dye, 2015; Nightingale, Dye, and Massey, 2018; Nightingale, Hayes, and Griffiths, 2021; Nightingale et al., 2021) to fit the observed images.

Although Sukay et al. (2022) already constructed the lens model for AGEL1323 by fitting the Magellan/FourStar H-band image with LENSTOOL (Jullo et al., 2007) and derived a magnification factor of $\mu = 74^{+49}_{-28}$, our HST data reveals a fifth image of the source that was not identified by Sukay et al. (2022). The counter-image is very close to one of the lens galaxies and marked by the green arrow in Figure 3.2. Our results differ from those of Sukay et al. because the counter-image is visible only with the high spatial resolution of our HST images. As a result, our lens model results in a significantly lower magnification.

AGEL1323 is a group scale lens containing multiple lens galaxies. We fit the HST F200LP imaging data. We first subtract the light of the two brightest galaxies marked with black crosses in Figure 3.3, by fitting elliptical Sérsic light profiles. To this foreground subtracted data we apply a custom mask (drawn via a graphical

[4] https://github.com/Jammy2211/PyAutoLens

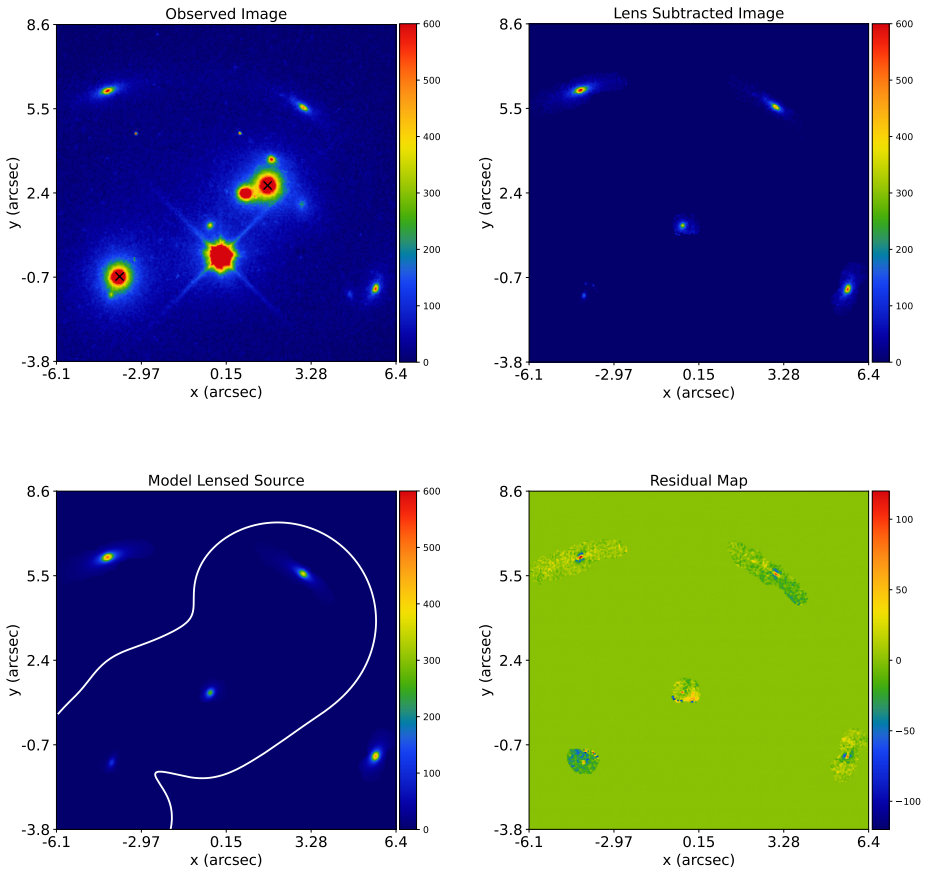

Figure 3.3: The observed HST F200 image (upper left), observed image with a model for the foreground lensing galaxies subtracted (upper right), best-fit model lensed source (bottom left) and residual map (bottom right) of lens modeling performed with `PyAutoLens`. Cut-outs were extracted from the full HST F200 image shown in Figure 3.2. The white line plotted over the bottom left panel is the lens model's tangential critical curve. In the lens-subtracted image, five distinct multiple images are seen, which are all reproduced by the lens model. The units of the colorbar are counts.

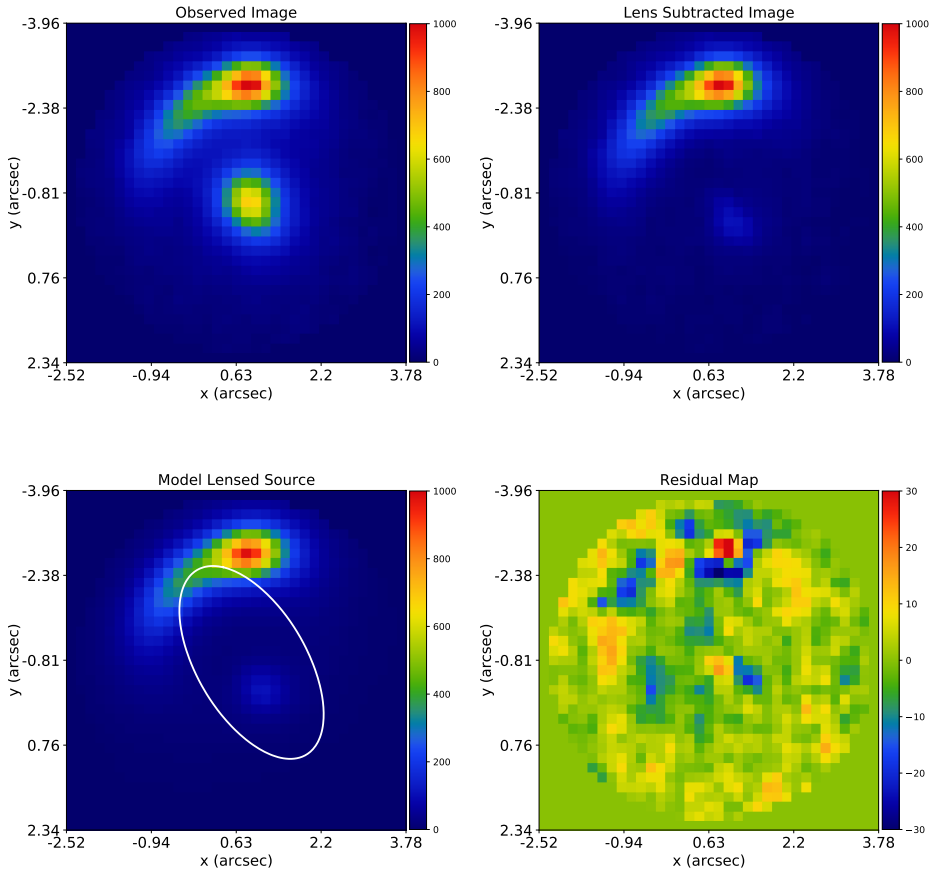

Figure 3.4: The observed MOSFIRE-K_s image (upper left), observed image with a model for the foreground lensing galaxy subtracted (upper right), best-fit model lensed source (bottom left) and residual map (bottom right) of lens modeling performed with `PyAutoLens`. The units of the colorbar are counts. Cut-outs were extracted from the full MOSFIRE-K_s image shown in Figure 3.1. The white line plotted over the bottom left panel is the lens model's tangential critical curve. In the lens-subtracted image, a faint counter-image is seen around ($x = 0.7''$, $y = -0.7''$), which is successfully recovered in the model lensed source.

user interface) which retains only the lensed source's multiple images. We then fit a mass model where the mass of the two galaxies marked with black crosses in Figure 3.3 are singular isothermal ellipsoids, and the group's host dark matter halo is modeled with a spherical NFW profile (Navarro, Frenk, and White, 1997). The NFW profile's concentration is set to the mean of the mass-concentration relation of Ludlow et al. (2016). The source is again modeled by an elliptical Sérsic profile. We fit the mass and source profiles simultaneously. As shown in Figure 3.3, the best-fit model successfully reproduces all five images, including the central image. We define the magnification μ as the ratio of the total image-plane flux of the source divided by the total source-plane flux, and infer a value of $\mu = 14.55^{+0.55}_{-1.07}$.

For AGEL0014, we performed the fitting on the MOSFIRE-K_s image. For the lens galaxy, we fit an elliptical Sérsic light profile for its light and singular isothermal ellipsoid for its mass. For the source, we fit an elliptical Sérsic light profile. We fit all three components simultaneously, using the nested sampling algorithm `dynesty` (Speagle, 2020). As shown in Figure 3.4, the best-fit model successfully detects a faint source counter image, which is offset ~ 0.5" from the lens galaxy center and is not visible until after the lens light subtraction. For the magnification we infer a value of $\mu = 4.33^{+0.16}_{-0.11}$.

3.3.2 Stellar Mass Estimates

The lensed stellar masses were measured by fitting the broadband spectral energy distribution (SED). For AGEL1323 we used photometry from DECaLS grz, HSC-ri, MOSFIRE-YK_s and HST/WFC3-F140W. We adopted HSC-$grizy$ and MOSFIRE-YK_s for the photometry of AGEL0014. For each galaxy, we smoothed the high resolution images to match the point spread function (PSF) with the one that has lowest resolution and extracted the photometry from the reduced images with `SExtractor` (Bertin and Arnouts, 1996). We padded the photometric uncertainties to 0.1 mag if the formal errors are smaller than that to account for possible systematics originated from complicated morphologies of the lensing system. The photometry is corrected for Galactic reddening using the $E(B-V)$ values measured by Schlafly and Finkbeiner (2011).

We modeled the SED assuming an delayed exponentially declining (delayed-τ) SFH with BAGPIPES (Carnall et al., 2018; Carnall et al., 2019). We used the Calzetti et al. (2000) dust extinction law and required the attenuation in the V band (A_V) to be varied between $0 < A_V < 2$. The redshift for each galaxy has a Gaussian

prior centered at z_{spec} in the AGEL catalog, with a standard deviation of 0.005. The other free parameters and their priors are stellar mass ($9 < \log(M_*/M_\odot) < 15$), stellar metallicity ($-2 < \log(Z/Z_\odot) < 0.4$), time since the onset of star formation (30 Myr $< T_0 < t_{obs}$[5]), and the e-folding SFR timescale (30 Myr $< \tau <$ 10 Gyr). As shown in Figure 3.5, the SED models yield a lensed stellar mass of $\log(M_*/M_\odot) = 12.3 \pm 0.1$ and $\log(M_*/M_\odot) = 12.1 \pm 0.1$ for AGEL1323 and AGEL0014, respectively, which translates a delensed stellar mass of $\log(M_*/M_\odot) = 11.13 \pm 0.10$ and $\log(M_*/M_\odot) = 11.48 \pm 0.09$ when the magnification is corrected.

To quantify the systematic uncertainties of stellar masses due to different assumptions on SFH, we also performed SED fitting with four other SFH models, including single burst, single exponentially declining, log-normal, and double-power-law SFHs. The root-mean-square (RMS) errors among the best-fit stellar masses[6] of different models are used as estimates of the systematic uncertainties (0.02 dex for AGEL1323 and 0.08 dex for AGEL0014). In the end, we obtained a delensed stellar mass of $\log(M_*/M_\odot) = 11.13 \pm 0.10$ for AGEL1323 and $\log(M_*/M_\odot) = 11.48 \pm 0.12$ for AGEL0014. We also performed some robustness tests: experimenting with different detection and analysis thresholds for SExtractor, including spectroscopic data for SED fitting, and only fitting for the photometry reported by Sukay et al. (2022). All the results are consistent with our reported values within 1σ.

For both galaxies, the delensed stellar masses of the two galaxies derived from the SED fitting and the velocity dispersion determined from the full-spectrum fitting (Section 3.3.3) are consistent with the stellar mass–velocity dispersion relation of quiescent galaxies at $z \sim 1$ (Belli, Newman, and Ellis, 2014; Mendel et al., 2020).

3.3.3 Stellar Population Fitting

We analyzed the combined spectra using the full-spectrum fitting algorithm absorption line fitter (alf, Conroy and van Dokkum, 2012; Conroy et al., 2018) because of its capability of measuring detailed elemental abundances in addition to overall stellar metallicity, [Fe/H]. alf uses MIST isochrones (Choi et al., 2016) and empirical stellar spectra (Sánchez-Blázquez et al., 2006; Villaume et al., 2017), along with a theoretical response function covering a wide range of elemental abundances. This code operates on the continuum-normalized spectrum by fitting a high-order polynomial to the ratio of the model and data to avoid potential issues with imperfect flux calibration and dust attenuation. This functionality also allows alf to

[5] t_{obs} stands for the age of the universe at the observed redshift.

[6] The best-fit stellar masses here mean the median value of the 1D posterior distribution.

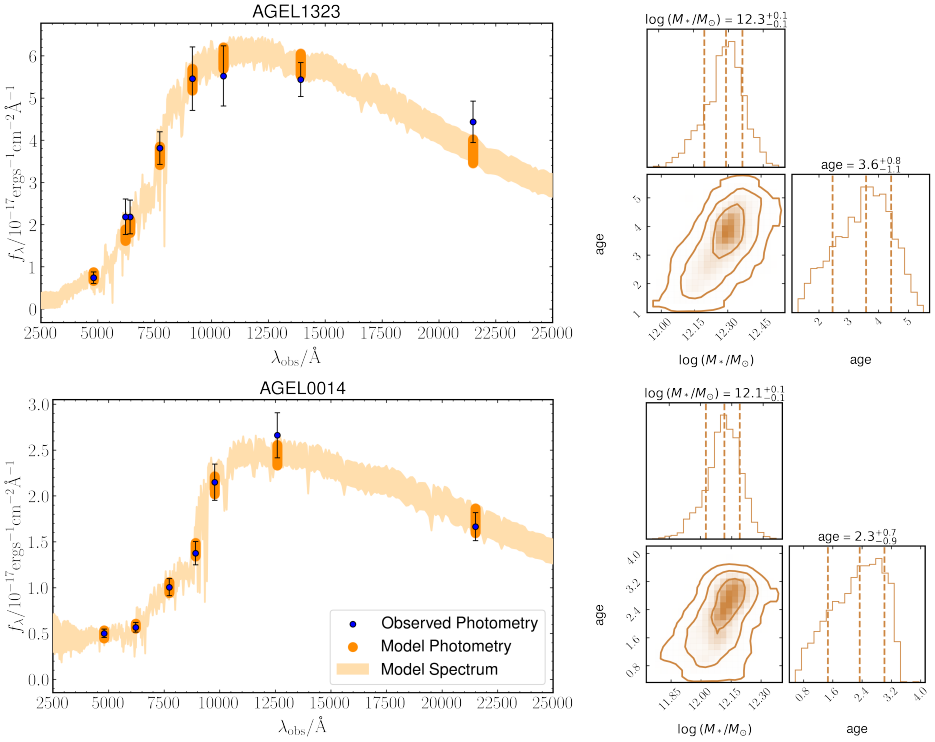

Figure 3.5: Broadband SED fitting of AGEL1323 and AGEL0014. *Left*: The observed photometry and the SED model of AGEL1323 (top) and AGEL0014 (bottom) assuming delayed-τ SFH derived by BAGPIPES (Carnall et al., 2018; Carnall et al., 2019). The observed and model photometry are shown by the navy and orange dots, respectively. For AGEL1323, the photometric data is from the DECaLS *grz*-band, HSC *ri*-band, MOSFIRE-YK$_s$ and HST/WFC3-F140W. For AGEL0014, the photometry is from HSC *grizy*-band and MOSFIRE-JK$_s$. The orange regions show the 1σ confidence interval of model spectra (light orange) and model photometry (dark orange). *Right*: The posterior distributions and covariances of the lensed stellar mass and the mass-weighted stellar age averaged over the SFH determined from BAGPIPES for AGEL1323 (top) and AGEL0014 (bottom). The contours represent the 1σ, 2σ and 3σ level.

fit multiple spectra of the same source taken on various instruments with different flux calibrations and instrumental resolutions. The fitting is accomplished with the ensemble Markov Chain Monte Carlo (MCMC) sampler `emcee` (Foreman-Mackey et al., 2013) to efficiently explore a large parameter space.

We used `alf`'s simple mode, which assumes a simple stellar population (SSP) and a fixed Kroupa (2001) initial mass function (IMF). It simultaneously fits for the recession velocity, velocity dispersion, stellar age, stellar metallicity [Fe/H], and the abundances of C, N, O, Na, Mg, Si, Ca, and Ti. The resulting stellar population parameters are SSP-equivalent, which are similar to light-weighted age and abundances. Following Beverage et al. (2021), the default priors were used, except that of maximum age was set to be 1 Gyr older than the age of universe at the observed redshift to fully explore the parameter space and to avoid a truncated posterior distribution. The recovered parameters are consistent with the results when the maximum allowed age is the age of universe at the observed redshift. Although `alf` also has a full mode describing a double-component stellar population, Conroy et al. (2018) indicated that the simple mode is more reliable when only the blue optical spectrum is available. Zhuang et al. (2021) also found out that the abundances derived from the `alf` simple mode are more consistent with those obtained from resolved stellar spectroscopy. Therefore, the following analysis focuses on the results obtained from the simple mode.

Given the quality and wavelength coverage of our data, we focused on the age, [Fe/H], and [Mg/Fe] derived from `alf`. We chose to measure Mg for two reasons. First, Mg is one of the α-elements that is mainly produced by core-collapse supernovae. Due to the short lifetime of massive stars, its recycling time can be approximated as instantaneous, for which magnesium is a good tracer of the overall galaxy evolution. For instance, Leethochawalit et al. (2019) used [Mg/H] of quiescent galaxies as a proxy to constrain the mass-loading factor of outflows averaged over the entire SFH. Second, the Mg *b* triplet at 5170 Å, which minimally overlaps with absorption features of other elements, is available in our spectra, allowing us to determine the Mg abundance reliably.

We excluded any regions below 4000 Å for the `alf` fitting because the difficulty of matching the continuum around the 4000 Å break may introduce some errors in the recovered abundances [7]. This also excluded the Ca II H and K lines from the fitting, which is known to have strong non-local thermodynamic equilibrium (NLTE) effects

[7] Private communication with Meng Gu.

Table 3.2: Stellar Population Properties of the Lensed Galaxies

Row	Quantity	Unit	AGEL1323	AGEL0014
(1)	$\log M_*$	$M_\odot$	11.13 ± 0.10	11.48 ± 0.12
(2)	σ_v	km s^{-1}	183^{+7}_{-8}	263^{+18}_{-16}
(3)	$t_{\rm SSP}$	Gyr	$5.6^{+0.8}_{-0.8}$	$3.1^{+0.8}_{-0.3}$
(4)	$[{\rm Fe/H}]_{\rm SSP}$	dex	$-0.30^{+0.08}_{-0.07}$	$-0.26^{+0.10}_{-0.11}$
(5)	$[{\rm Mg/Fe}]_{\rm SSP}$	dex	$0.19^{+0.08}_{-0.09}$	$0.28^{+0.13}_{-0.13}$
(6)	$[{\rm Mg/H}]_{\rm SSP}$	dex	$-0.11^{+0.10}_{-0.11}$	$0.02^{+0.13}_{-0.14}$
(7)	$\chi^2_{\rm SSP}$/d.o.f	-	3.88	3.80

Rows show (1) the delensed stellar mass estimates; (2-7) the velocity dispersion, stellar ages, [Fe/H], [Mg/Fe], [Mg/H] and the reduced χ^2 determined from `alf`'s simple mode assuming an SSP. The errors here have been corrected for the systematic uncertainties originated from the imperfect models and underestimated noise from the pipelines (See Section 3.3.3).

that the current models poorly reproduce (Conroy et al., 2018). For each spectrum, we ran two iterations to remove the sky line residuals. In the first iteration, we only masked out the regions where the telluric features cannot be corrected. After the first fit, the pixels with 4σ deviations from the best-fit model were masked to reduce the contamination of bright sky lines to the fitting. We then re-fit the spectrum with the new pixel mask to determine the best-fit model and the corresponding stellar population parameters. The reduced χ^2 of each spectrum is greater than 1, which may result from either models imperfections or underestimated flux uncertainties from the data reduction pipeline. Therefore, the uncertainties reported in Table 3.2 are rescaled by the square root of the reduced χ^2 to incorporate the systematic errors that were not captured by the posterior distribution and the random errors. We experimented with different degrees of polynomials for continuum normalization and found out that all the measurements are consistent with each other.

The observed spectra and best-fit models determined by `alf`'s simple mode, as well as the posterior distributions of the corresponding model parameters without the error correction, are shown in Figure 3.6 for AGEL1323 and Figure 3.7 for AGEL0014. We list all measured parameters in Table 3.2.

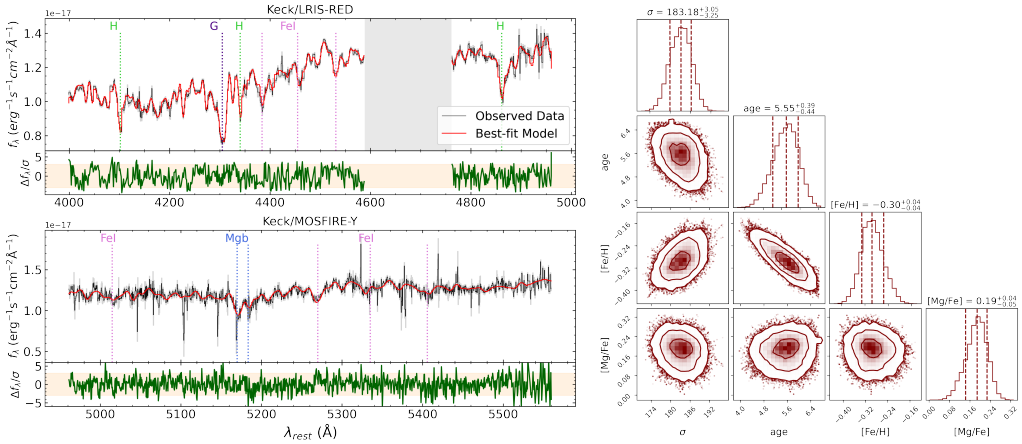

Figure 3.6: *Left*: The observed spectrum (black) and best-fit SSP model (red) used in this work for AGEL1323. The gray areas represent the 1σ uncertainties of the observed spectrum. We masked out a small portion in the LRIS-red spectrum for AGEL1323 because of the telluric features that cannot be corrected. The green lines show the ratio of the model residuals over the uncertainties, with the 3σ regions indicated by the shaded beige regions. *Right*: Corner plot showing the posterior distributions and covariances among velocity dispersion (σ), age, [Fe/H], and [Mg/Fe] of the best-fit model. The uncertainties shown here are the random errors obtained from the posterior distribution, without being corrected for the systematic errors (See Section 3.3.3). The contours demonstrate the 1σ, 2σ and 3σ levels.

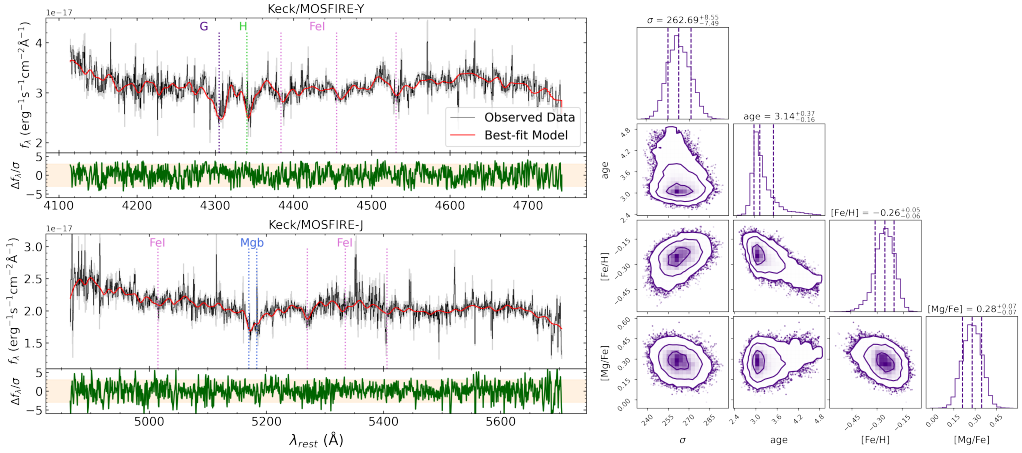

Figure 3.7: Same as Figure 3.6, but showing the results of AGEL0014.

3.4 Results

3.4.1 Old Ages and Possible Rapid Star Formation

The measured SSP ages of AGEL1323 and AGEL0014 are 5.6±0.3 Gyr and $3.1^{+0.8}_{-0.3}$ Gyr, respectively, both corresponding to a formation redshift of $z_{\rm form} \gtrsim 4$. Although the SSP assumption may be too simple compared to the true SFHs, the SSP age is still a good indicator of the time when most of stars were formed in a galaxy considering its bias towards the youngest population. In other words, our `alf` results suggest that the majority of the stellar populations in the two galaxies were formed less than 2 Gyr after the Big Bang, indicating that they must have experienced rapid star formation to reach the stellar masses we see today.

3.4.2 Chemical Abundances of the Lensed Galaxies

In Figure 3.8, we show the measured [Fe/H], [Mg/Fe], [Mg/H] of the AGEL galaxies compared with other quiescent galaxies at different redshifts as a function of stellar mass. To minimize the systematic effects between various full-spectrum fitting algorithms based on different model assumptions, we limit our comparison to those derived using the `alf` simple mode. We compare our results with the LEGA-C sample at $z \sim 0.7$ (Beverage et al., 2021) and other quiescent galaxies at $z \gtrsim 1$ (Kriek et al., 2016; Kriek et al., 2019; Carnall et al., 2022). We also plot a sample of local SDSS galaxies ($z \sim 0.05$) as reference. The SDSS sample is taken from Leethochawalit et al. (2019), who randomly selected 152 quiescent galaxies from the Gallazzi et al. (2005) sample in the mass range $10^9 - 10^{11.5} M_\odot$. We re-measured their abundances with `alf` using the same wavelength range as the spectra of the lensed galaxies for consistency. We excluded the galaxies for which posterior distributions hit the upper or lower limits of the priors, leaving a sample of 123 galaxies. The best-fit $z \sim 0$ MZRs of [Fe/H] [Fe/H], [Mg/Fe], and [Mg/H] for the updated `alf` measurements of nearby SDSS galaxies are:

$$\begin{aligned} [\mathrm{Fe/H}] &= (-0.14 \pm 0.01) + (0.14 \pm 0.02) M_{10} \\ [\mathrm{Mg/H}] &= (0.06 \pm 0.01) + (0.20 \pm 0.02) M_{10} \\ [\mathrm{Mg/Fe}] &= (0.20 \pm 0.01) + (0.06 \pm 0.01) M_{10}, \end{aligned} \tag{3.1}$$

where $M_{10} = \log [M_*/10^{10} M_\odot]$. These relations are shown in Figure 3.8 to show the evolution in the mass–metallicity relation for the samples at different redshifts.

The lensed galaxies and most of the high-z galaxies are more metal-poor than their local counterparts with similar stellar masses, consistent with the redshift evolution of the MZR found by Choi et al. (2014) and Leethochawalit et al. (2019). However,

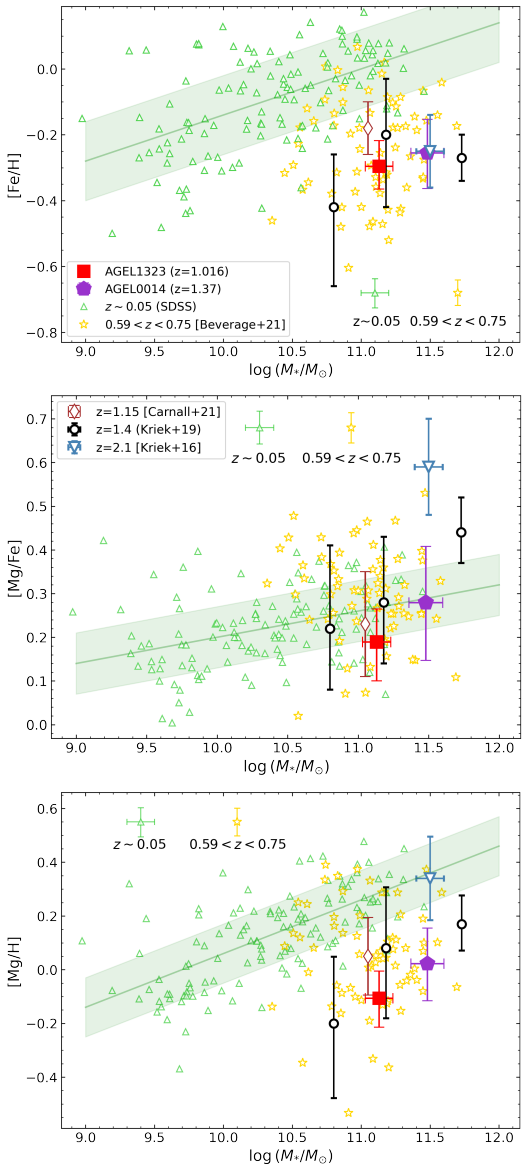

Figure 3.8: The [Fe/H] (top), [Mg/Fe] (middle) and [Mg/H] (bottom) as a function of stellar mass for quiescent galaxies. AGEL1323 at $z = 1.016$ and AGEL0014 at $z = 1.37$ are plotted as a filled square and a pentagon, respectively. The SDSS galaxies at $z \sim 0.05$ (open green triangles) are taken from Leethochawalit et al. (2019) but re-measured with `alf` for consistency. The open yellow stars show the measurements for the LEGA-C sample at $0.59 < z < 0.75$ by Beverage et al. (2021). The abundances of individual high-z quiescent galaxies measured by Kriek et al. (2016) (blue open down triangle) and Kriek et al. (2019) (black open circles) as well as that of a stacked spectrum at $z = 1.15$ determined by Carnall et al. (2022) are plotted for comparison. The green solid lines and shaded regions represent the best-fit linear relations and intrinsic scatter of the $z \sim 0.05$ SDSS galaxies.

the [Fe/H] of the AGEL galaxies, along with other high-z galaxies, appear to be comparable to those of the LEGA-C $z \sim 0.7$ galaxies. This finding does not necessarily contradict the redshift evolution. Leethochawalit et al. (2019) estimated that the normalization of the MZR decreases 0.04 dex per observed Gyr, which translates to a decrease of 0.2 dex in [Fe/H] from $z \sim 0$ to $z \sim 0.7$, and roughly 0.1 dex from $z \sim 0.7$ to $z \sim 1.4$. If we assume the intrinsic scatter of the MZR ~ 0.06 dex at $z \lesssim 0.54$, Leethochawalit et al., 2019 has negligible redshift evolution, the combined effects of the observed uncertainties and intrinsic scatter in [Fe/H] at a given stellar mass can account for why the AGEL galaxies have similar [Fe/H] as LEGA-C galaxies at lower redshifts. A larger sample would be necessary to further investigate the redshift evolution of the MZR at high-z.

Jafariyazani et al. (2020) found one quiescent galaxy at $z \sim 2$ to be more metal-rich ($[\mathrm{Fe/H}] = 0.26$) than most quiescent galaxies at any redshift. Because this measurement is a significant outlier in metallicity compared to most of the previous studies, which discovered more metal-poor quiescent galaxies at higher redshifts, we do not include the result by Jafariyazani et al. (2020) in our comparison. It is beyond the scope of this work to understand why that galaxy at $z \sim 2$ is significantly more metal-rich than other high-z quiescent galaxies.

The measurements of [Mg/Fe] of the AGEL galaxies are comparable to those in the nearby universe at similar masses, although the scatter in the mass–[Mg/Fe] relations of LEGA-C galaxies makes it hard to know if there is any redshift evolution between $z \sim 0$ and $z \sim 0.7$. Typically, [Mg/Fe] can be used to probe the SFH. Because iron has a more delayed production timescale than magnesium, Kriek et al. (2016) and Kriek et al. (2019) used the measured [Mg/Fe] as a proxy for star formation duration when assuming a closed box model, suggesting that high-z quiescent galaxies with enhanced [Mg/Fe] should have shorter star formation timescales. Therefore, the redshift evolution in the mass–[Mg/Fe] relation may reveal whether high-z galaxies have SFHs distinct from those at lower redshifts.

However, the existing studies of redshift evolution in the mass–[Mg/Fe] relation are quite controversial. Leethochawalit et al. (2019) found that [Mg/Fe] is smaller at higher redshifts at fixed stellar mass for cluster quiescent galaxies below $z \lesssim 0.54$, while Kriek et al. (2019) and Beverage et al. (2021) did not detect any significant redshift evolution for LEGA-C galaxies at $z \sim 0.7$ and three quiescent galaxies at $z \sim 1.4$. Given the current sample size, the mass–[Mg/Fe] relation appears to be similar at local and $z \gtrsim 1$ and thus in favor of what Beverage et al. (2021) and

Kriek et al. (2019) found, but again a larger sample would be needed for stronger constraints.

The absence of significant α-enhancement of the lensed galaxies is unexpected because we expect old, quiescent galaxies to have enhanced [α/Fe] ratios. The unexpected result inspired us to consider carefully whether the measured [Mg/Fe] from `alf` might be underestimated due to imperfect flux calibrations. As a full-spectrum fitting algorithm, `alf` adopts the information from the whole spectrum, including the continuum and metal absorption lines, to constrain the Mg abundance. Conroy et al. (2018) indicated that the continuum between 4000 Å and 5300 Å is also sensitive to Mg abundance, for which any small mismatch between the continuum level of the model spectrum and that of the observed data due to imperfect flux calibrations over a wider wavelength range may bias the measurement of [Mg/Fe]. For each galaxy, we generated `alf` model spectra with different [Mg/Fe] but fixed all other parameters to the best-fit values returned by `alf`.

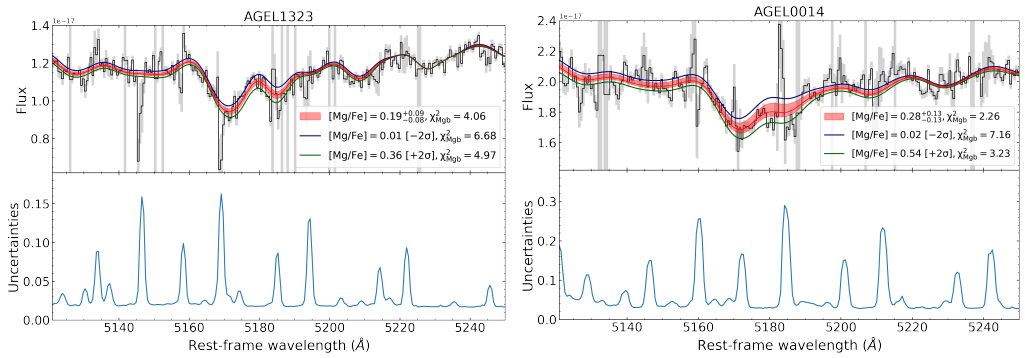

Figure 3.9: The model spectra with different [Mg/Fe] vs. the observed spectra for AGEL1323 (top) and AGEL0014 (bottom) near the Mg b triplet at ~5170 Å. In each plot, the upper panel shows the models corresponding to 68% confidence interval of the best-fit [Mg/Fe] by the red region. The model spectra at 2σ deviation from the median of [Mg/Fe] are overplotted by the blue and green lines for comparison. The masked pixels are marked by the grey vertical regions. The 1σ random errors of the observed spectra are indicated by the grey-shaded regions. The lower panel of each plot is the error spectrum, representing the sky background. The models with higher or lower [Mg/Fe] give poorer fits to the Mg b triplet, which validates our measured [Mg/Fe] from `alf`.

Figure 3.9 shows model spectra with [Mg/Fe] varying within 2σ of the best-fit value compared to the observed data near the Mg b triplet region for each galaxy. We chose the Mg b triplet because it is the most prominent Mg feature in the observed wavelength range. These narrow atomic features are less affected by the flux calibrations than wider Mg-bearing molecular bands nearby. We evaluate the

reduced χ^2 near the Mg b for model spectra with 2σ higher or lower [Mg/Fe] than the best-fit value and compare them with that of the best-fit model. As shown in Figure 3.9, for both lensed galaxies, neither a more α-rich nor a more α-poor model can better describe Mg b triplet than the best-fit model does, which validates our measured [Mg/Fe] obtained from the full-spectrum fitting.

We now scrutinize the expectation that [Mg/Fe] should be enhanced in old, quiescent galaxies. In fact, the shape of SFH, merger history, the delayed explosion time of Type Ia supernovae and the presence of outflows/inflows can all affect the final [Mg/Fe] at the time when the galaxies quenched. For this reason, a galaxy that rapidly built its mass (e.g., over $\sim$ 1 Gyr) does not necessarily have to be very α-enhanced. We have seen such evidence in the Local Group. de los Reyes et al. (2022, among others) found that Sculptor, a dwarf spheroidal galaxy in the Local Group, finished forming stars within ~0.9 Gyr, but has only a moderate α-enhancement of $[\mathrm{Mg/Fe}] \approx 0.2$, comparable to [Mg/Fe] of our lensed galaxies.

In addition, [Mg/Fe] of the lensed galaxies appears to be positively correlated with stellar mass, consistent with the findings of Kriek et al. (2019). We believe future *James Webb Space Telescope* (JWST) observations would be able to yield more reliable measurements of [Mg/Fe] in order to constrain the mass–[Mg/Fe] relation in the high-z universe (Nanayakkara et al., 2022).

With the new measurements of our lensed galaxies, a mass dependence of [Mg/H] emerges for quiescent galaxies at $z \gtrsim 1$, suggesting that [Mg/H] is likely to be correlated with stellar mass in the high-z universe. The `AGEL` galaxies and other high-z galaxies appear to have lower [Mg/H] compared to local quiescent galaxies. This redshift evolution in the mass–[Mg/H] relation is contradictory to the results of Leethochawalit et al. (2019), who argued for universal relations for quiescent galaxies at $z \lesssim 0.54$. While the discrepancy may result from different full-spectrum fitting algorithms used to determine [Mg/H], it is more likely that galaxies observed at $z > 1$, especially those that formed at $z > 3$, may have experienced qualitatively different physical processes shaping the final [Mg/H]. We discuss one of the possible origins in Section 3.5.2.

3.5 Discussion

3.5.1 Dependence of Abundances on Galaxy Formation Time

As many literature studies have reported the evolution of the MZR with observed redshift for quiescent galaxies (e.g., Gallazzi et al., 2014; Choi et al., 2014;

Leethochawalit et al., 2019), it is natural to ask whether such evolution is driven by galaxies' observed redshifts (age of the universe when galaxies were observed) or formation redshifts (age of the universe when galaxies formed). In other words, should we expect galaxies located at similar redshifts or those forming stars at similar time to have similar metal abundances? Leethochawalit et al. (2019) studied the evolution of the MZR below $z \lesssim 0.54$ and argued that evolution of metallicity is more fundamental with *formation* redshift when mass dependence is removed. Following Leethochawalit et al. (2019), we investigate the dependence of abundances on galaxy formation time here.

We first examine the measured [Fe/H], [Mg/Fe] and [Mg/H] as a function of SSP age obtained from `alf`'s simple mode for quiescent galaxies at various redshifts. As shown in Figure 3.10, [Fe/H] of high-z quiescent galaxies are distinct from those of local SDSS quiescent galaxies at a given SSP age, while such significant difference is not seen in [Mg/H]. At a certain SSP age, high-z quiescent galaxies are relatively more metal-poor and more α-enhanced compared to local counterparts. This scenario is expected as high-z galaxies have less time for Type Ia supernova explosion for iron production. The lack of prominent [Mg/H] separation between local and high-z populations can be explained by the short recycling timescale of magnesium. The distributions of [Mg/Fe] for high-z and local populations are slightly different, as the production of iron and magnesium both affect this trend.

If high-z galaxies evolve passively and remain quenched to $z \sim 0$, their stellar abundances would not change significantly due to the absence of new star formation. Because high-z quiescent galaxies are believed to be the progenitors of local quiescent galaxies, we expect the high-z populations to overlap with the local counterparts in age–abundance plots once the age differences are corrected. Here, we approach this problem in a reverse way. If we ignore the small metallicity change as galaxies evolve passively, we can correct the age differences between the high-z and local galaxies by tracing back the age of the universe at galaxy formation, which is the difference between the age of the universe at the observed redshift and the measured SSP age for each galaxy. As can be seen in the second column of Figure 3.10, the differences of [Fe/H] and [Mg/Fe] between high-z galaxies and local galaxies are attenuated when we compare them as a function of galaxy formation time rather than SSP age.

We further remove the first-order mass dependence of abundances by subtracting the best-fit MZRs at $z \sim 0$ (Equation 3.1) from the observed abundances. The deviations

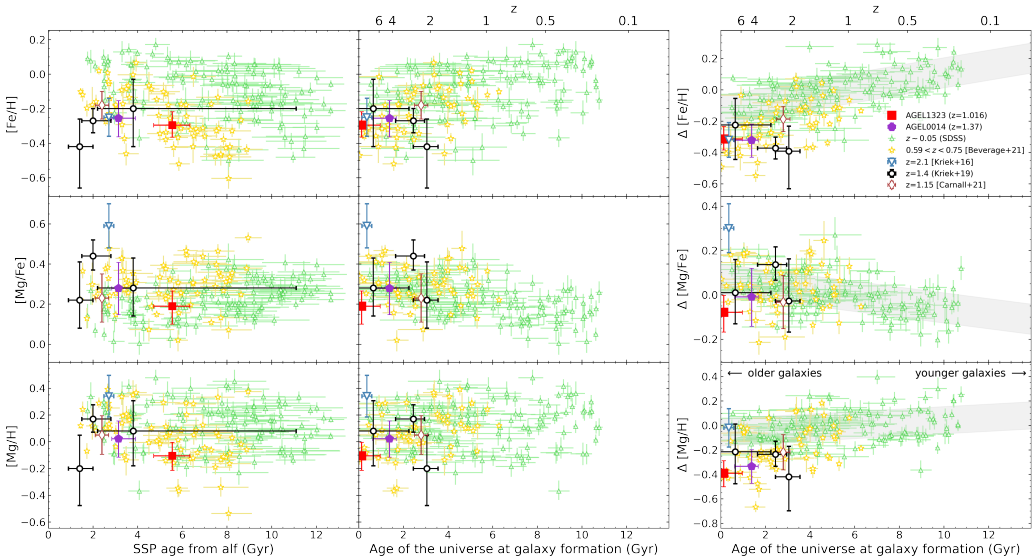

Figure 3.10: Dependence of [Fe/H], [Mg/Fe], and [Mg/H] on galaxy formation time. *Left:* Dependence of [Fe/H], [Mg/Fe], and [Mg/H] on the SSP age (first column) and galaxy formation time (second column). *Right*: Dependence of abundances on the galaxy formation time with the stellar mass dependence removed (see Section 3.5.1). The grey shaded regions show the 68% confidence interval for $z \sim 0$ SDSS galaxies. The symbols for galaxies at different redshifts are the same as in Figure 3.8.

in the right panels of Figure 3.10 demonstrate how galaxy formation time affects the final abundances. At $z \sim 0$, the evolution in [Fe/H] and [Mg/Fe] with formation time is 0.024 ± 0.003 dex per Gyr and -0.013 ± 0.002 dex per Gyr, respectively. On the contrary, we do not detect a significant dependence of [Mg/H] on galaxy formation time for local galaxies, with the best-fit slope of 0.010 ± 0.004 dex per formation Gyr. The weak evolution of [Mg/H] with formation age is in agreement with the short recycling timescale of magnesium. As can be seen in Figure 3.10, the LEGA-C and high-z galaxies exhibit similar evolution of abundances when the dependence on mass and observed redshift is removed. The tighter relations in [Fe/H] and [Mg/Fe] imply that at a fixed stellar mass, the galaxy formation time since the Big Bang plays more fundamentally determines stellar metallicity and α-enhancement than the observed redshift.

Still, [Fe/H] and [Mg/H] of the LEGA-C galaxies and high-z galaxies are systematically lower than local galaxies when the dependence on mass and age is removed, although the differences are relatively small. The discrepancy for high-z galaxies implies that additional mechanisms are needed to explain the small offset.

One possibility is that not all high-z quiescent galaxies evolve passively. There is a

chance that some of them may rejuvenate and form younger stars in a later epoch. Recent studies have suggested that accretion of satellite galaxies is important to explain the size growth of massive elliptical galaxies across cosmic time (e.g., Oser et al., 2010; Greene et al., 2013; Oyarzún et al., 2019, and references therein). Such mergers may trigger star formation in originally quenched galaxies. If some of these high-z quiescent galaxies were at the temporary quenching phase between two starbursts, they would have a higher [Fe/H] and a younger formation time when reaching $z \sim 0$. We believe this scenario may be necessary to explain the redshift evolution of the MZR in Figure 3.8. As high-z quiescent galaxies evolve to $z \sim 0$ passively, they would become less massive and slightly more metal-poor. It appears that the most massive galaxies cannot move to the local sequence unless they can get metal-enriched in the later epoch, which would require either new star formation or mergers with much more metal-rich systems. The latter is less likely to happen because massive galaxies tend to accrete more metal-poor satellite galaxies (Oser et al., 2010).

With the few available measurements at $z \gtrsim 1$, we conclude that galaxy formation time would still be the key factor determining the metal abundances in quiescent galaxies below $z \lesssim 2$. At the same time, it is possible that some of the high-z galaxies may re-start forming stars at a later epoch. A larger sample of quiescent galaxies at $z \gtrsim 1$ would be necessary to confirm this possible rejuvenation in star formation.

3.5.2 Enhanced outflows during the star formation

To understand why AGEL1323 and AGEL0014 quenched so early in the universe, we use the measured [Mg/H] to constrain the outflows of the lensed galaxies during their star formation. Leethochawalit et al. (2019) presented a simple analytic chemical evolution model for quiescent galaxies that connects instantaneously recycled metals to the time-averaged mass-loading factor, based on the work of Lu, Blanc, and Benson (2015). Readers are encouraged to read Leethochawalit et al. (2019) for the details of the model. To summarize, the mass-loading factor here is defined as the ratio of the mass outflow rate to the SFR, averaged over the entire SFH. They also assume that:

1. The interstellar medium (ISM) where star formation occurs is perfectly mixed.

2. Metals are instantaneously recycled.

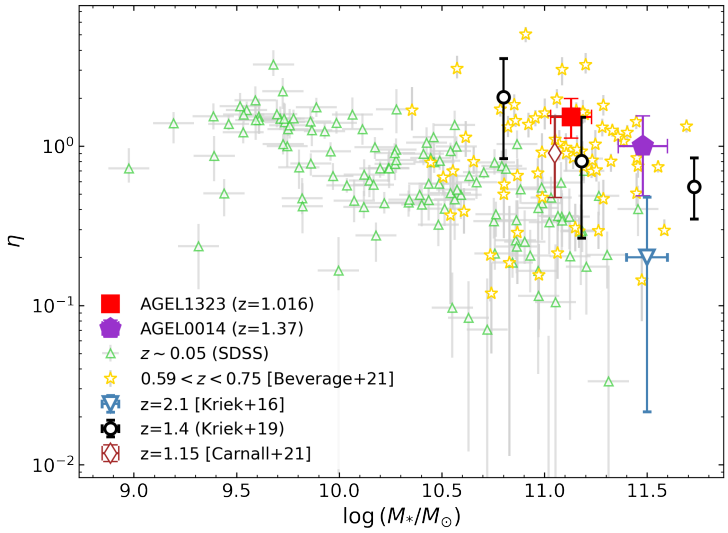

Figure 3.11: The mass-loading factor (η) inferred from the measured [Mg/H] as a function of stellar mass for quiescent galaxies. The sample and the symbols are the same as Figure 3.8. The two AGEL galaxies appear to have higher mass-loading factors than nearby galaxies at similar masses.

3. Outflows and inflows are permitted, but only the outflows can significantly affect the total metal budget in the ISM.

Because magnesium is the product of core-collapse supernovae of short-lived stars, it can be approximated as an instantaneously recycled element and thus fit into the model above. If assuming that no or minimal amount of gas is left in the quiescent galaxies, the abundance of an instantaneously recycled element would be

$$Z_{*,\mathrm{quiescent}} \approx \frac{y}{1+\frac{\langle\eta\rangle}{1-R}}, \tag{3.2}$$

where y is the supernova yield and R is the return mass fraction defined to be the fraction of the mass of a stellar generation that returns to the interstellar medium from short-lived massive stars and stellar winds. $Z_{*,\mathrm{quiescent}}$ can be substituted as the absolute Mg abundance of quiescent galaxies. Following Leethochawalit et al. (2019), we adopted the solar abundance of Mg from Asplund et al. (2009) and the yield as three times the solar Mg abundance (Nomoto et al., 2006) to calculate the absolute Mg abundance. The return fraction is set to $R = 0.46$ (Lu, Blanc, and Benson, 2015) for all galaxies.

In Figure 3.11, we show the mass-loading factors inferred from the measured [Mg/H] for quiescent galaxies at various redshifts. The AGEL galaxies—as well as other

high-z galaxies—appear to have higher mass-loading factors than nearby quiescent galaxies, implying that galaxies may have enhanced outflows when they were forming stars in the early universe. The strong outflows would naturally cause the two galaxies to lose gas quickly and thus can no longer sustain further star formation.

The observational constraints on the mass-loading factors for high-z galaxies are qualitatively consistent with the FIRE simulations (Hayward and Hopkins, 2017), which predict that η increases significantly as redshift increases at $M_* \gtrsim 10^{10} M_\odot$. Therefore, it will be essential to perform similar studies when a larger sample of high-z quiescent galaxies at $z > 1$ is available in order to further investigate whether there is a redshift evolution in the mass-loading factor as suggested by the FIRE simulations.

3.5.3 Comparison with Sukay et al. (2022)

Sukay et al. (2022) derived the stellar population properties of AGEL1323 via a joint fit of photometry and spectroscopy with `Prospector` (Johnson et al., 2021). They adopted a non-parametric SFH model with seven age bins to characterize the stellar population. In this work, we instead measure the stellar population via full-spectrum fitting algorithms `alf` assuming an SSP or two SSPs (i.e., one or two age bins). Sukay et al. (2022) used the spectrum obtained on Alhambra Faint Object Spectrograph and Camera (ALFOSC) at the 2.56 m Nordic Optical Telescope (NOT) with a total integration time of 80 minutes. The low-resolution spectrum ($R = 590$) covers the rest-frame wavelength between 2820 Å and 5030 Å and thus is unable to resolve most of the faint metal absorption lines which is important to robustly constrain the stellar metallicity.

Our new Keck spectra therefore are much deeper and have a much higher resolution. The Keck spectra cover the rest-frame optical between 3600-5500 Å, which includes many more metal absorption lines essential to the determination of [Fe/H] and [Mg/Fe]. We prefer an SSP model over more complicated SFHs because its simplicity reduces the degeneracy among free parameters. Although we adopted a different SFH model, the SSP age in this work is still in qualitatively good agreement with the SFH derived by Sukay et al. (2022). We obtained an SSP age of 5.6 ± 0.8 Gyr, while the SFH derived by Sukay et al. (2022) indicates an absence of prominent star formation activity until ∼3 Gyr ago. Both results indicate that AGEL1323 is an old system that quenched very early in the universe.

We measured elemental abundances of [Fe/H] $= -0.30^{+0.08}_{-0.07}$ and [Mg/Fe] =

$0.19^{+0.08}_{-0.09}$. If we convert our measurements to total metallicity as [Z/H] = [Fe/H] + 0.94[Mg/Fe] (Thomas, Maraston, and Bender, 2003), the total metallicity is [Z/H] = -0.12 ± 0.11, which is consistent with Sukay et al.'s best-fit stellar metallicity, $\log(Z/Z_\odot) = -0.19$.

3.5.4 Comparison between the ages and metallicities derived from different approaches

While we primarily focus on the ages and the metallicities derived from `alf` with full-spectrum fitting, we also measured the stellar populations with SED fitting to estimate the stellar masses (Section 3.3.2). Here we briefly discuss the differences in the measurements from the two approaches.

Since we adopt the delayed-τ model in the broadband SED fitting, we compare the mass-weighted stellar ages averaged over the SFHs with the SSP ages derived from `alf`. As shown in Figure 3.5, we obtained a mean stellar age of $3.6^{+0.8}_{-1.1}$ Gyr for `AGEL`1323 and $2.3^{+0.7}_{-0.9}$ Gyr for `AGEL`0014. Although the ages derived from broadband SED fitting are still consistent with the SSP ages within 2σ, they are systematically lower than the values measured with `alf`. The mean stellar ages vary slightly across different SFH models, but all of them predict ages younger than the SSP ages while remaining consistent with `alf`'s measurements within 2σ. Even if such age differences can be attenuated by conducting a joint fitting of photometry and spectroscopy with BAGPIPES, the measured ages of both galaxies are still lower than those measured from `alf`.

As for the stellar metallicities, we determine the $[\mathrm{Z/H}]_{\mathrm{BAGPIPES}} = -0.20^{+0.07}_{-0.08}$ for `AGEL`1323 and $[\mathrm{Z/H}]_{\mathrm{BAGPIPES}} = -0.17^{+0.03}_{-0.04}$ for `AGEL`0014 when the red spectrum covering the Mg b triplet and Fe I lines is included for each galaxy. The delayed-τ SFH with a single metallicity is assumed. The stellar metallicities measured from the joint fitting of photometry and spectroscopy are therefore consistent with the [Fe/H] determined by `alf` within 1σ, although BAGPIPES still yields higher metallicity measurements. The BAGPIPES measurement of [Z/H] of `AGEL`1323 is also within 1σ of the total metallicity when we convert the `alf`'s measurements of [Fe/H] and [Mg/Fe] into [Z/H] as [Z/H] = [Fe/H] + 0.94[Mg/Fe] (Thomas, Maraston, and Bender, 2003), for consistency with other recent work (e.g., Kriek et al., 2019; Carnall et al., 2019). However, the total metallicities of `AGEL`0014 are consistent between the two approaches within 2σ.

Even though the stellar ages and metallicities measured from SED fitting with BAG-

PIPES and full-spectrum fitting with `alf` appear to be consistent with each other, SED fitting systematically recovers younger and more metal-rich populations than full-spectrum fitting does. Several factors may account for the potential systematic effects, such as different SSP templates and the choices of SFH models. The fitted wavelength region may also affect the results. BAGPIPES only allows one spectrum to be included in the fit while `alf` can analyze two spectra obtained on different instruments/gratings. SED fitting also spans a much wider spectral range than full-spectrum fitting. There is no doubt that different spectral regions are sensitive to stellar populations at different ages. With the current sample of only two galaxies, it is beyond the scope of this work to quantify the possible systematic differences in the stellar population parameters measured with different approaches.

3.6 Conclusions

We presented the deep rest-frame optical spectra obtained on the Keck I telescope for two gravitationally lensed, massive quiescent galaxies at $z \gtrsim 1$: AGEL1323 ($\log(M_*/M_\odot) \sim 11.1$) and AGEL0014 ($\log(M_*/M_\odot) \sim 11.5$). The high S/N of the spectra enabled us to robustly characterize the stellar population and elemental abundances of the lensed galaxies via full-spectrum fitting under the SSP assumption. A summary of our findings is as follows:

1. We determined the stellar metallicities as $[\mathrm{Fe/H}] = -0.30^{+0.08}_{-0.07}$ for AGEL1323 ($z = 1.016$) and $[\mathrm{Fe/H}] = -0.26^{+0.10}_{-0.11}$ for AGEL0014 ($z = 1.374$). Compared with low-z galaxies at similar masses, the lensed galaxies in our sample are more metal-poor, consistent with other stellar metallicity measurements of quiescent galaxies at similar redshift Kriek et al. (2019) and Carnall et al. (2019). This tentatively indicates that the redshift evolution of the stellar MZR should be in place at $z \lesssim 1.4$. When we remove the mass dependence of metallicity for quiescent galaxies at different redshifts, we find that galaxies of the same masses that formed at the same time have similar metallicities, regardless of their observed redshift. This result implies that the evolution of the stellar MZR is more fundamental with formation redshift than with observed redshift.

2. We also measured the α-enhancements for two lensed galaxies as $[\mathrm{Mg/Fe}] = 0.19^{+0.08}_{-0.09}$ for AGEL1323 and $[\mathrm{Mg/Fe}] = 0.28 \pm 0.13$ for AGEL0014. The lensed galaxies have comparable [Mg/Fe] as their low-z counterparts, despite of their old ages.

3. We obtained SSP-equivalent ages of 5.6 ± 0.8 Gyr for AGEL1323 and $3.1^{+0.8}_{-0.3}$ Gyr for AGEL0014. Considering the observed redshifts and stellar masses of the lensed galaxies, the old ages show that the majority of the stellar population formed very rapidly in the galaxies (less than 2 Gyr after the Big Bang). Using a simple chemical evolution (Leethochawalit et al., 2019), we inferred mass-loading factors of the galaxies from the measured [Mg/H]. The high mass-loading factors imply that the two galaxies both experienced enhanced outflows during their star formation, which may have led to their early quenching.

This work has demonstrated how gravitational lensing can further our understanding of the chemical evolution of quiescent galaxies in the high-redshift universe. At the moment, there are still just a handful of robust stellar abundance measurements for quiescent galaxies at $z \gtrsim 1$. Therefore, larger samples would be necessary to systematically investigate the relation between stellar mass, stellar abundances, and the inferred mass-loading factors of high-z quiescent galaxies. The early data from JWST have revealed numerous new lens candidates that may be quiescent galaxies from even higher redshifts than those presented in this work. The upcoming bounty of spectroscopic and imaging data will revolutionize our knowledge of chemical enrichment histories of quiescent galaxies in the early universe.

Acknowledgments

The authors acknowledge the insightful and constructive feedback from the anonymous referee, which helped us improve the manuscript. We would also like to thank Meng Gu for helpful advice on full-spectrum fitting with `alf` and Allison Strom for useful discussions on MOSFIRE data reduction and analysis with MOSPEC. We gratefully thank the staff at the W. M. Keck Observatory, including support astronomers Luca Rizzi, Carlos Alvarez and Jim Lyke, and telescope operators Arina Rostopchina, Julie Renauld-Kim, and Heather Hershey, for assisting in the observations.

We are grateful to the many people who have worked to make the Keck Telescope and its instruments a reality and to operate and maintain the Keck Observatory. The authors wish to extend special thanks to those of Hawaiian ancestry, on whose sacred mountain we are privileged to be guests. Without their generous hospitality, none of the observations presented herein would have been possible.

This material is based on work supported by the National Science Foundation under

Grant No. AST-2233781 (E.N.K.) and AST-2009278 (C.C.S.). Z.Z., E.N.K. and C.C.S. acknowledge financial support from National Aeronautics and Space Administration (NASA) through the FINESST program (No. 80NSSC22K1755). K.G., T.N. and C.J. acknowledge support from Australian Research Council (FL180100060). S.M.S. acknowledges funding from the Australian Research Council (DE220100003). T.J. and K.V.G.C. gratefully acknowledge financial support from NASA through grant HST-GO-16773, the Gordon and Betty Moore Foundation through Grant GBMF8549, and the National Science Foundation through grant AST-2108515. Parts of this research were conducted by the Australian Research Council Centre of Excellence for All Sky Astrophysics in 3 Dimensions (ASTRO 3D), through project number CE170100013.

This work makes use of observations with the NASA/ESA Hubble Space Telescope obtained from the Mikulski Archive for Space Telescopes at the Space Telescope Science Institute (STScI), which is operated by the Association of Universities for Research in Astronomy, Incorporated, under NASA contract NAS5-26555. Support for Program number GO-16773 was provided through a grant from the STScI under NASA contract NAS5-26555.

Chapter 4

METALS IN STAR-FORMING GALAXIES WITH KCWI: GLOBAL ABUNDANCES

Zhuang, Z. et al. (Sept. 2024). "Metals in Star-forming Galaxies with KCWI. I. Methodology and First Results on the Abundances of Iron, Magnesium, and Oxygen". In: *ApJ* 972.2, p. 182. DOI: 10.3847/1538-4357/ad5ff8.

Abstract

Understanding the chemical enrichment of different elements is crucial to gaining a complete picture of galaxy chemical evolution. In this study, we present a new sample of 46 low-redshift, low-mass star-forming galaxies at $M_* \sim 10^{8-10} M_\odot$ along with two quiescent galaxies at $M_* \sim 10^{8.8} M_\odot$ observed with the Keck Cosmic Web Imager (KCWI), aiming to investigate the chemical evolution of galaxies in the transition zone between Local Group satellites and massive field galaxies. We develop a novel method to simultaneously determine stellar abundances of iron and magnesium in star-forming galaxies. With the gas-phase oxygen abundance $(O/H)_g$ measured using the strong line method, we are able to make the first-ever apples-to-apples comparison of α elements in the stars and the ISM. We find that the $[Mg/H]_*$–$[O/H]_g$ relation is much tighter than the $[Fe/H]_*$–$[O/H]_g$ relation, which can be explained by the similar production processes of α elements. Most galaxies in our sample exhibit higher $[O/H]_g$ than $[Fe/H]_*$ and $[Mg/H]_*$. In addition, we construct mass–metallicity relations (MZRs) measured as three different elements (Fe_*, Mg_*, O_g). Compared to the gas O-MZR, the stellar Fe- and Mg-MZRs show larger scatter driven by variations in specific star formation rates (sSFR), with star-forming galaxies exhibiting higher sSFR and lower stellar abundances at fixed mass. The excess of $[O/H]_g$ compared to stellar abundances as well as the anti-correlation between sSFR and stellar abundance suggests that galaxy quenching of intermediate-mass galaxies at $M_* \sim 10^{8-10} M_\odot$ is primarily driven by starvation.

4.1 Introduction

Heavy elements are invaluable tracers of the evolutionary history of galaxies. The amount of metals (i.e., metallicity) residing in the interstellar medium (ISM) and stellar population of a galaxy is governed by the interplay between the gravitational

potential well (e.g., Dekel and Silk, 1986), nucleosynthesis during star formation (e.g., Kobayashi, Karakas, and Lugaro, 2020), efficiency of gas mixing in the ISM (e.g., Veilleux, Cecil, and Bland-Hawthorn, 2005), galactic outflows driven by stellar and AGN feedback (e.g., Murray, Quataert, and Thompson, 2005; Faucher-Giguère, Quataert, and Hopkins, 2013; Hopkins et al., 2014), and pristine inflows from the circumgalactic and intergalactic medium (CGM and IGM) over cosmic time (e.g., Kereš et al., 2005).

Over the past five decades, significant progress has been made in measuring metallicities in galaxies from the Local Group to the high-redshift universe. Using emission line diagnostics that trace gas metallicity of galaxies, Lequeux et al. (1979a) first discovered a correlation between stellar masses and gas metallicities of the ISM in star-forming galaxies, which is known as the mass–metallicity relation (MZR). Later, Tremonti et al. (2004) measured the gas metallicities of $\sim 53,000$ star-forming galaxies in the Sloan Digital Sky Survey (SDSS) from emission lines and confirmed that the gas metallicity is strongly correlated with stellar mass in all SDSS star-forming galaxies. Gallazzi et al. (2005) also discovered a similar correlation between stellar mass and stellar metallicity measured from stellar absorption features for a sample of 44,254 galaxies drawn from the SDSS survey. The trend was later confirmed by other works using various methods to measure metallicities in the SDSS galaxies (e.g., Andrews and Martini, 2013; Zahid et al., 2017). Previous studies have also found that both the stellar MZR and the gas MZRs exist in the Local Group satellite galaxies (e.g., Lee et al., 2006; Berg et al., 2012; Kirby et al., 2013). More recently, astronomers have shown that the MZR exists at all different redshifts, establishing the stellar MZR of quiescent galaxies up to $z \sim 2$ (Choi et al., 2014; Kriek et al., 2019; Leethochawalit et al., 2019; Zhuang et al., 2023; Beverage et al., 2024) and the gas MZR of star-forming galaxies up to $z \sim 10$ (e.g., Erb et al., 2006; Steidel et al., 2014; Maiolino and Mannucci, 2019; Sanders et al., 2020; Strom et al., 2022; Curti et al., 2023). All these studies suggest that at fixed stellar mass, high-z galaxies tend to have lower metallicities than their local counterparts. These trends are also captured by large cosmological simulations (e.g., Ma et al., 2016; De Rossi et al., 2017; Torrey et al., 2019).

Generally, measurements of the MZR are based on the abundance of a single element: iron abundance $[\mathrm{Fe/H}]_*$ for stars and oxygen abundance $[\mathrm{O/H}]_\mathrm{g}$ for ionized gas in the ISM. The gas-phase MZR indicates the chemical enrichment in the current ISM as galaxies grow in mass, while the stellar MZR represents the metals locked in stars

averaged over the entire star formation history (SFH). While most work to date has focused on measuring either the stellar or the gas-phase MZR, usually for passively evolving (e.g., Leethochawalit et al., 2019) or star-forming galaxies (e.g., Curti et al., 2020) respectively, recent work has attempted to relate the gas metallicity measured from nebular emission lines to the stellar metallicity determined from the stellar continuum for nearby (e.g., Lian et al., 2018b; Fraser-McKelvie et al., 2022, from the rest-optical continuum) and high-z star-forming galaxies (e.g., Steidel et al., 2016; Topping et al., 2020; Strom et al., 2022, from the rest-FUV continuum to which young OB stars primarily contribute the observed features). Such work has found that the two abundance measurements do not yield the same "metallicity" for galaxies with significant ongoing star formation, where gas metallicity measured as oxygen abundance is significantly higher than stellar metallicity that uses iron abundance as a proxy. Moreover, these comparison studies have shown that gas-phase and stellar metallicities scale with stellar masses differently, resulting in different shapes (slopes and normalizations) of the gas-phase and stellar MZRs in the nearby and high-z universe (e.g., Fraser-McKelvie et al., 2022; Strom et al., 2022).

The mismatch between the stellar and gas-phase metallicity is likely to result from the different recycling times of iron and oxygen. Oxygen is an α element produced primarily by core collapse supernovae (CCSNe) on characteristic timescales of < 10 Myr, while the production of Fe is dominated by Type Ia supernovae (SNe) with characteristic delay times $\gtrsim 400$ Myr (Burbidge et al., 1957; Tinsley, 1980; Chen, Hu, and Wang, 2021). If a galaxy has formed a substantial fraction of its stars in the relatively recent past, the abundance of α elements relative to iron, [α/Fe], will be much higher than the solar ratio. In addition, if [Fe/H]$_*$ is measured from the rest-frame optical instead of UV spectrum, the result reflects the chemical enrichment of relatively old, low-mass stars because the stellar photospheric features of young OB stars reside primarily in the rest-frame UV. The oxygen abundance measured from emission lines instead indicates the amount of metals that reside in the current ISM, which better represents the level of chemical enrichment of the youngest stars. The combined effects of the distinct recycling times of iron and oxygen and the stars at different ages to which stellar and gas-phase metallicity are sensitive make it less straightforward to interpret the relation between metallicities in different phases.

A better way to approach this problem would be to relate two elements for which the abundance ratio is less sensitive to the short-timescale details of the SFH. Magne-

sium in the stars is useful here. Because oxygen and magnesium are both α elements, their abundance ratio should be much less affected by the varying delayed timescale of Type Ia SNe than [O/Fe] derived from the optical spectrum. Comparing $[Mg/H]_*$ of the stellar population with $[O/H]_g$ can therefore inform us about the degree to which metal-poor gas accretion or metal-rich outflows have affected the overall galactic metallicity. Relating the abundances of gas-phase oxygen, stellar iron, and stellar magnesium allows us to correlate chemical enrichment at different timescales. In addition, $[Mg/Fe]_*$ provides unique insights on the chemical enrichment history of a galaxy.

In this work, we present a novel technique to determine $[Fe/H]_*$ and $[Mg/Fe]_*$ of star-forming galaxies via full-spectrum fitting of the optical stellar continuum. We apply this technique to a new sample of low-redshift, low-mass star-forming galaxies between $10^8 M_\odot$ and $10^{10} M_\odot$ observed with the Keck Cosmic Web Imager (KCWI; Morrissey et al., 2018), yielding the first-ever apples-to-apples comparison of α elements in different phases.

The KCWI sample consists of star-forming galaxies in the transition zone between the Local Group dwarf satellite galaxies and massive field galaxies that have been well-studied by large spectroscopic surveys. The sample's purpose is to fully understand the shape of the stellar MZRs across the full range of galaxy masses. A simple extrapolation of the stellar MZR of satellite galaxies in the Local Group ($M_* \lesssim 10^8 M_\odot$, Kirby et al., 2013) appears to disagree with measurements of more massive, quiescent galaxies in the field ($M_* \gtrsim 10^{9.5} M_\odot$, Leethochawalit et al., 2019). At $M_* \sim 10^9 M_\odot$, the high-mass and low-mass MZRs are discrepant in $[Fe/H]_*$ by ~ 0.6 dex, much larger than the scatter of either MZR (see Figure 7 in Zhuang et al. 2021). In our previous work (Zhuang et al., 2021), we ruled out the possibility that the large discrepancy originates from systematic differences in the techniques used to estimate $[Fe/H]_*$ of galaxies at different masses, and we suggested that there is a transition mass in the stellar MZR in the local universe. Constraining the shape of the MZR, especially the stellar one, in the transition mass is essential to unveil how the physical processes regulating metal retention and interaction with the surrounding environment vary as galaxies grow in mass.

The main goals of this paper are (1) to compare stellar and gas-phase abundances of a new sample of low-mass star-forming galaxies observed with KCWI; (2) to construct the MZR of our sample measured from three different elements (O_g, Fe_* and Mg_*); and (3) to quantify the shape of the stellar MZR for galaxies beyond the

Local Group in order to put constraints on the chemical evolution of galaxies. The structure of this paper is as follows. We describe the basic properties of the sample, the observations, and data reductions in Section 4.2. In Section 4.3, we present the methods used for emission line measurements and gas-phase metallicity determination. In Section 4.4, we explain the new technique used in this work to measure $[Fe/H]_*$ and $[Mg/Fe]_*$ of star-forming galaxies. We present our measurements from the KCWI data in Section 4.5 and discuss their implications when combining the abundance measurements of more massive SDSS galaxies in Section 4.6. Finally, we summarize our findings in Section 4.7. Throughout this work we assume a flat ΛCDM cosmology with $\Omega_m = 0.3$, $\Omega_\Lambda = 0.7$ and $H_0 = 70$ km s^{-1} Mpc^{-1}.

4.2 Data

We use KCWI mounted at Nasmyth focus on the Keck II telescope to obtain the spectroscopic data for our analysis. We describe the sample selection in Section 4.2.1, global properties of galaxies estimated from broadband photometry in Section 4.2.2, and summarize the KCWI observations and data reduction in Section 4.2.3.

4.2.1 Target Selection

Our sample consists of 46 star-forming galaxies at $z < 0.06$ in a stellar mass range of $10^8 - 10^{10} M_\odot$ (Table 4.1). We chose this mass range because it represents the transition from the Local Group dwarf galaxies to the well-studied massive galaxies in the Hubble flow. The weak stellar absorption features of heavily star-forming galaxies dominant in this mass range has prevented observers from obtaining reliable measurements of not only stellar metallicity but also $[Mg/Fe]_*$ of individual star-forming dwarfs from large spectroscopic optical surveys. Aiming to measure stellar and gas-phase abundances simultaneously of the same star-forming galaxies, we acquired very high-quality integral field spectroscopic data for this small sample to reveal their faint stellar features.

19 galaxies were selected from the clumpy galaxy catalog compiled by Mehta et al. (2021) that made use of the classification provided by the citizen science-powered *Galaxy Zoo* based on the SDSS Stripe82 images, while the other 27 galaxies were selected from the SDSS MPA-JHU catalog (Brinchmann et al., 2004; Tremonti et al., 2004). All these targets were randomly selected from the parent catalogs based on their stellar masses. We restricted our sample to galaxies with sSFR between $10^{-9} - 10^{-11}$ yr^{-1} based on the SDSS MPA-JHU catalog (*galSpecLine*, SDSS DR17; Brinchmann et al., 2004; Tremonti et al., 2004), a range that is representative of

typical SDSS star-forming galaxies.

Additionally, two quiescent galaxies, 0241-0810 and 0125-0024 at $\log(M_*/M_\odot) \sim 8.8$, were added to the sample as filler targets to investigate whether low-mass quiescent galaxies exhibit stellar abundances distinct from star-forming galaxies at similar masses. 0241-0810 is in the vicinity of the massive elliptical galaxy NGC 1052 with a similar radial velocity. The dwarf galaxy likely belongs to a virialized group structure in the environment of NGC 1052 (Román, Castilla, and Pascual-Granado, 2021). However, 0125-0024 is identified as an isolated dwarf galaxy at least 1 Mpc away from the nearest massive galaxy ($\log(M_*/M_\odot) > 10$) by Kado-Fong et al. (2020) from the SDSS.

4.2.2 Photometry, Broadband SED Fitting and Size Measurements

Although the SDSS catalog provides stellar masses and SFRs measured from SDSS $ugriz$ photometry, we performed our own spectral energy distribution (SED) fitting with BAGPIPES (Carnall et al., 2018; Carnall et al., 2019) using photometry from far-UV to mid-IR wavelengths to obtain more reliable estimates of galaxies' global properties.

We retrieved the publicly-available coadded science images from the *Galaxy Evolution Explorer* (*GALEX*; Martin et al., 2005), the Sloan Digital Sky Survey (SDSS; York et al., 2000), the Panoramic Survey Telescope and Rapid Response System (PS1; Flewelling et al., 2020), and the Wide-field Infrared Survey Explorer (WISE; Wright et al., 2010) through the unblurred coadds of the WISE imaging (unWISE) archive (Lang, 2014). For each galaxy, we first calculated the flux densities (f_k) in each band k with the same elliptical aperture defined as the Kron (1980) radius of the PS1-i image. To account for the resolution mismatch in different filters, each PS1-i detection image was downgraded to the resolutions in other photometric bands, from which we estimated the flux densities in the same aperture as $f'_{\mathrm{ps1-i,k}}$. The final photometry $f_{k,\mathrm{final}}$ in the band k was calculated as:

$$f_{k,\mathrm{final}} = \frac{f'_{\mathrm{ps1-i,k}}}{f_{\mathrm{ps1-i}}} f_k \tag{4.1}$$

All the photometry was then corrected for Galactic reddening using the $E(B-V)$ values measured by Schlafly and Finkbeiner (2011).

The SFRs and stellar masses were derived from BAGPIPES, a Bayesian-SED fitting code. We assumed a delayed exponentially declining (delayed-τ) SFH for each galaxy. We fixed the redshifts at the values in the SDSS catalog and adopted the

Calzetti et al. (2000) dust attenuation relation with a uniform prior of $0 < A_V < 2$. Nebular emission models based on the CLOUDY photoionization code (Ferland et al., 2017) with a varying ionization parameter $-4 < \log U < -2$ were included to account for the contribution from emission lines and nebular continuum. The other free parameters and their priors were stellar mass formed ($7 < \log(M_*/M_\odot) < 12$), stellar metallicity ($-2 < \log(Z/Z_\odot) < 0.4$), time since the onset of star formation (1 Myr $< T_0 <$ 14 Gyr), and the e-folding SFR timescale (1 Myr $< \tau <$ 100 Gyr). We assumed uniform priors on the logarithmic scale for all the free parameters. The best-fit SFRs and stellar masses were taken as the 50$^{\text{th}}$ percentile of the marginalized 1D posterior distribution. We experimented with four other SFHs: single exponentially declining, log-normal, double-power-law, and constant SFHs. The root-mean-square (RMS) errors of the best-fit values (i.e., the median of the posteriors) between different SFH models are quoted as the reported uncertainties.

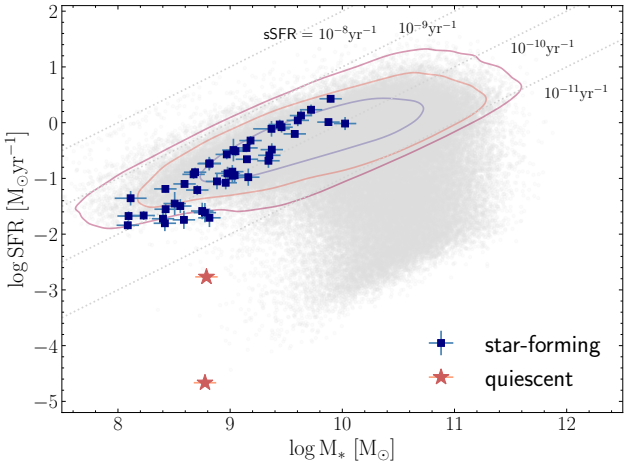

Figure 4.1: SFR as a function of stellar mass of the star-forming (blue squares) and quiescent (red stars) galaxies in our sample. The contours show the SDSS SFMS at a similar redshift range ($z < 0.06$) taken from the GSWLC catalog (Salim et al., 2016) at 1-3 σ. The grey dots indicate all the GSWLC galaxies at the same redshift range as our sample.

All star-forming galaxies in our sample have typical SFRs and stellar masses like those in the SDSS "star-forming main sequence" (SFMS), as shown in Figure 4.1, except for the two quiescent galaxies. For 38 out of 48 galaxies in our sample, SFR and mass measurements are available from the GALEX-SDSS-WISE Legacy Catalog (GSWLC) (Salim et al., 2016; Salim, Boquien, and Lee, 2018). For 26 of these galaxies, the stellar masses and the SFRs we measured are consistent with the GSWLC estimates within 2σ uncertainties. However, we emphasize that the major conclusions in this work remain unchanged when using the mass and SFR

estimates from the GSWLC catalog. The derived masses and SFRs are listed in Table 4.1. The SED-based SFR estimates of two spectroscopically confirmed quiescent galaxies show large uncertainties due to their faint UV fluxes, so their best-fit SFRs are only a proxy of their quiescent nature and should be taken with caution.

Table 4.1: General Properties of the KCWI Galaxy Sample

Galaxy	RA (J2000)	Dec (J2000)	z^a	$\log M_*{}^b$ [$M_\odot$]	$\log SFR^b$ [$M_\odot$ yr^{-1}]	R_e (kpc)
2225−0046	22 25 07.92	−00 46 06.03	0.016	8.09±0.10	−1.84 ± 0.08	0.76±0.01
0231−0043	02 31 32.17	−00 43 36.63	0.009	8.09±0.10	−1.67 ± 0.08	1.05±0.02
0133−0109	01 33 41.39	−01 09 29.76	0.016	8.11±0.14	−1.36 ± 0.13	1.07±0.02
2329+1552	23 29 46.17	+15 52 38.96	0.009	8.23±0.10	−1.67 ± 0.08	0.53±0.01
2152−0110	21 52 22.46	−01 10 15.95	0.016	8.40±0.10	−1.72 ± 0.13	0.97±0.01
0845+5145	08 45 54.52	+51 45 11.12	0.014	8.42±0.10	−1.80 ± 0.14	0.69±0.01
2334+0029	23 34 14.80	+00 29 07.28	0.024	8.42±0.10	−1.19 ± 0.07	1.31±0.03
0121−0853	01 21 51.93	−08 53 10.63	0.018	8.43±0.10	−1.55 ± 0.10	0.85±0.01
0013−0956	00 13 45.42	−09 56 03.67	0.013	8.51±0.10	−1.45 ± 0.21	0.83±0.01
0155−0037	01 55 01.92	−00 37 35.27	0.023	8.56±0.10	−1.50 ± 0.12	1.32±0.03
0140−0012	01 40 52.90	−00 12 49.52	0.018	8.59±0.10	−1.74 ± 0.16	1.19±0.03
0023−0939	00 23 48.32	−09 39 09.85	0.020	8.59±0.10	−1.10 ± 0.06	1.03±0.01
0233+0038	02 33 03.92	+00 38 41.59	0.024	8.67±0.10	−0.93 ± 0.08	1.20±0.01
0256−0010	02 56 32.90	−00 10 51.13	0.029	8.69±0.10	−0.89 ± 0.08	2.04±0.01
2259−0019	22 59 03.19	−00 19 45.82	0.016	8.71±0.10	−1.21 ± 0.09	1.32±0.01
2300−0832	23 00 51.88	−08 32 13.36	0.025	8.75±0.10	−1.58 ± 0.15	1.26±0.06
0233−0819	02 33 05.84	−08 19 08.79	0.019	8.77±0.10	−1.61 ± 0.17	1.08±0.01
0125−0024	01 25 06.09	−00 24 31.22	0.016	8.78±0.10	-4.67^c	1.24±0.03
0241−0810	02 41 35.06	−08 10 24.52	0.005	8.79±0.10	-2.77^c	0.79±0.01
2301+1451	23 01 06.26	+14 51 16.74	0.024	8.81±0.11	−0.74 ± 0.12	1.73±0.12
0332−0600	03 32 00.36	−06 00 42.77	0.018	8.82±0.10	−1.71 ± 0.17	1.17±0.03
2131−0613	21 31 03.64	−06 13 58.27	0.025	8.82±0.10	−0.73 ± 0.10	1.84±0.01
0850+6145	08 50 39.67	+61 45 44.42	0.024	8.88±0.10	−1.05 ± 0.14	1.23±0.01
0256−0707	02 56 34.76	−07 07 11.12	0.017	8.96±0.10	−1.08 ± 0.12	1.84±0.04
0033+0012	00 33 14.83	+00 12 03.66	0.014	8.97±0.10	−0.57 ± 0.09	2.04±0.02
2137+1243	21 37 52.51	+12 43 42.63	0.031	8.98±0.11	−0.91 ± 0.12	1.75±0.01
0137−0942	01 37 43.57	−09 42 36.36	0.019	9.02±0.10	−0.88 ± 0.12	2.49±0.01
0040−0017	00 40 35.09	−00 17 37.19	0.019	9.02±0.10	−0.95 ± 0.12	2.39±0.05
0136+1356	01 36 15.18	+13 56 43.26	0.024	9.03±0.10	−0.49 ± 0.20	1.88±0.05
2304−0933	23 04 30.86	−09 33 03.58	0.032	9.04±0.10	−0.94 ± 0.12	1.85±0.01
0309−0041	03 09 58.06	−00 41 39.58	0.037	9.05±0.10	−0.51 ± 0.09	3.57±0.10

continued

Table 4.1: General Properties of the KCWI Galaxy Sample

Galaxy	RA (J2000)	Dec (J2000)	z^a	$\log M_*{}^b$ [$M_\odot$]	$\log SFR^b$ [$M_\odot$ yr^{-1}]	R_e (kpc)
0019−0004	00 19 17.04	−00 04 11.50	0.040	9.15±0.10	−0.45 ± 0.08	2.95±0.09
0208+0048	02 08 48.30	+00 48 01.41	0.020	9.15±0.10	−0.66 ± 0.05	3.84±0.05
0306−0033	03 06 24.96	−00 33 04.38	0.025	9.16±0.10	−0.98 ± 0.15	1.58±0.04
0346+0023	03 46 06.86	+00 23 24.93	0.031	9.18±0.10	−0.32 ± 0.08	2.56±0.05
0243+0032	02 43 33.19	+00 32 45.29	0.028	9.34±0.10	−0.68 ± 0.13	3.13±0.05
2318+0105	23 18 01.34	+01 05 13.31	0.030	9.35±0.10	−0.59 ± 0.11	3.97±0.05
2206−0041	22 06 46.12	−00 41 17.40	0.029	9.37±0.16	−0.11 ± 0.14	1.64±0.01
2243+0040	22 43 58.53	+00 40 25.70	0.039	9.37±0.10	−0.48 ± 0.11	4.07±0.06
0334+0106	03 34 06.02	+01 06 15.19	0.049	9.44±0.10	−0.03 ± 0.09	3.87±0.01
0317−0004	03 17 20.20	−00 04 37.04	0.022	9.46±0.10	−0.08 ± 0.10	3.86±0.03
2211+0006	22 11 47.47	+00 06 49.79	0.057	9.58±0.10	−0.20 ± 0.06	4.00±0.19
0245−0045	02 45 57.45	−00 45 12.27	0.054	9.60±0.10	0.04 ± 0.10	5.05±0.10
0030−0042	00 30 13.43	−00 42 28.45	0.041	9.63±0.10	0.13 ± 0.10	2.74±0.01
2139+0019	21 39 56.73	+00 19 23.69	0.050	9.72±0.10	0.23 ± 0.09	4.60±0.06
0407−0634	04 07 04.64	−06 34 02.15	0.038	9.88±0.10	0.01 ± 0.06	4.75±0.06
0254+0103	02 54 50.52	+01 03 26.97	0.043	9.90±0.10	0.43 ± 0.06	6.48±0.02
0140−0013	01 40 47.46	−00 13 05.74	0.058	10.02±0.10	−0.02 ± 0.12	6.28±0.12

[a] Redshifts are taken from SDSS DR17 (Abdurro'uf et al., 2022).

[b] The stellar masses and SFRs are derived from broadband SED fitting with BAGPIPES.

[c] Galaxies 0125-0024 and 0241-0810 are quiescent. The SED-based SFRs may not reflect the true level of star formation activity and thus only serve as a proxy of their quiescent nature.

We decided to re-measure the sizes of the galaxies in our sample in spite of the existing size measurements in the SDSS catalog, because some of them with multiple star-forming clumps are mis-labeled as several individual galaxies instead of one galaxy in the SDSS catalog. Because of their complex light profiles, we chose to fit the Petrosian (1976) half-light radius (R_e) independent of the assumption on galaxy light profiles. We estimated the Petrosian half-light radii of our sample from the PS1-*i* image using the `PetroFit` package (Geda et al., 2022). The size measurements and the associated errors are listed in Table 4.1.

4.2.3 KCWI Observations

The KCWI data were taken over the course of five nights in October 2021 and September to November 2023. The seeing varied between $\sim$ 1.0″ and $\sim$ 2.0″ throughout the five nights. Table 4.2 describes the observations of each galaxy. The total exposure time for each galaxy ranged from 5 minutes to 100 minutes. We used

the BL grating with the Medium Slicer centered at 4500 Å, which gives a field of view (FoV) of 16.5″×20.4″ and wavelength coverage of 3500–5600 Å[1]. From the arc spectra, we determined a spectral resolution FWHM of 2.5 Å ($\sigma \sim 70$ km s^{-1}) for both nights. We observed most of the galaxies at multiple position angles (the orientation of the KCWI slices on the sky) to maximize the spatial resolution and minimize covariance during stacking. To perform sky subtraction for the galaxies with their angular sizes comparable or even larger than the IFU FoV, we either placed multiple pointings on the target to obtain the in-field sky or took off-field sky frames adjacent to the science frames with half of the science exposure time.

Table 4.2: KCWI observations of the Galaxy Sample

Galaxy	z	Exposure (s)	Position Angles (deg)	Date	Airmass	Off-field Sky	Equivalent Extraction Radius[a] (R_e)
2225−0046	0.016	2320	0, 90	2023-09-23	1.12		1.1
0231−0043	0.009	5160	70, 160	2021-10-02	1.07	✓	1.6
0133−0109	0.016	4200	50, 140	2021-10-02	1.16		1.7
2329+1552	0.009	950	90	2023-09-23	1.04	✓	1.4
2152−0110	0.016	2710	0,90	2023-09-23	1.14		1.6
0845+5145	0.014	1985	0, 90	2023-11-05	1.22		2.1
2334+0029	0.024	2350	0, 90	2023-10-13	1.06	✓	1.6
0121−0853	0.018	2000	0, 90	2023-10-13	1.15		1.8
0013−0956	0.013	1265	0, 90	2023-09-23	1.21	✓	1.2
0155−0037	0.023	1900	0, 90	2023-11-05	1.27		1.2
0140−0012	0.018	2000	0, 90	2023-10-13	1.18		1.5
0023−0939	0.02	1000	0	2023-10-13	1.15	✓	1.2
0233+0038	0.024	2000	0, 90	2023-11-05	1.24		1.4
0256−0010	0.029	2965	0, 120, 240	2023-11-05	1.07		1.3
2259−0019	0.016	3670	30, 90, 150	2023-09-23	1.10		1.0
2300−0832	0.025	2057	0	2023-09-23	1.14		1.5
0233−0819	0.019	2000	0, 90	2023-11-05	1.22		1.5
0125−0024	0.016	2336	0, 90	2023-10-13	1.07	✓	0.9
0241−0810	0.005	1000	0	2023-11-05	1.15	✓	1.2
2301+1451	0.024	2340	0, 90	2023-10-13	1.12		1.5
0332−0600	0.018	2000	0, 90	2023-11-05	1.24		1.5
2131−0613	0.025	2000	0, 90	2023-10-13	1.15		1.3
0850+6145	0.024	1000	90	2023-11-05	1.35		1.4
0256−0707	0.017	2000	0, 90	2023-11-05	1.13	✓	1.4
0033+0012	0.014	1200	45	2021-10-02	1.14	✓	1.8
2137+1243	0.031	2250	0,90	2023-09-23	1.15		1.7
0137−0942	0.019	2000	80, 170	2023-09-23	1.16	✓	1.1
0040−0017	0.019	2400	110	2021-10-10	1.11	✓	1.9
0136+1356	0.024	1547	0, 90	2023-10-13	1.04		1.9
2304−0933	0.032	2000	0, 90	2023-10-13	1.16		1.7
0309−0041	0.037	3900	170	2021-10-10	1.24	✓	1.2
0019−0004	0.04	4800	0	2021-10-02	1.43		1.8
0208+0048	0.02	2700	90	2021-10-10	1.06	✓	1.5
0306−0033	0.025	2000	0, 90	2023-11-05	1.14		1.6
0346+0023	0.031	1800	70, 160	2021-10-02	1.06	✓	1.6

continued

[1]For the galaxies observed in 2023, we also have KCWI red channel data covering a spectral range of 6300–9500 Å. For consistency between data taken in different nights, we consider only the KCWI blue spectra. We are preparing a separate article (Z. Zhuang et al. in prep.) that will discuss the red optical data.

Table 4.2: KCWI observations of the Galaxy Sample

Galaxy	z	Exposure (s)	Position Angles (deg)	Date	Airmass	Off-field Sky	Equivalent Extraction Radius[a] (R_e)
0243+0032	0.028	2400	90	2021-10-10	1.07	✓	1.7
2318+0105	0.03	3600	60, 150	2021-10-10	1.11	✓	1.5
2206−0041	0.029	1200	0, 90	2021-10-02	1.13		2.2
2243+0040	0.039	3600	50	2021-10-10	1.18		1.8
0334+0106	0.049	1985	0, 90	2023-11-05	1.28		0.6
0317−0004	0.022	600	140	2021-10-10	1.14	✓	1.4
2211+0006	0.057	2400	0, 90	2021-10-10	1.24		1.5
0245−0045	0.054	1800	90	2021-10-10	1.14	✓	1.5
0030−0042	0.041	1200	45	2021-10-02	1.19		1.5
2139+0019	0.05	1200	0, 90	2021-10-02	1.13	✓	1.3
0407−0634	0.038	2000	0, 90	2023-11-05	1.39	✓	0.9
0254+0103	0.043	2400	20, 110	2021-10-02	1.20	✓	1.6
0140−0013	0.058	2700	80, 170	2021-10-02	1.07		1.4

[a] Because we used an irregular aperture to extract the spectrum for each galaxy, we estimate the equivalent binning radius as the fraction of the effective radius using the square root of the ratio of the area used for KCWI spectrum extraction and the area within $1R_e$.

Data Reduction

We reduced the KCWI data using a modified version of the publicly available KCWI data reduction pipeline with the updates detailed in Prusinski et al. (in prep.)[2]. This pipeline converts raw, 2D science frames into flux-calibrated, 3D data cubes with a spatial sampling of $0.29''\times 0.68''$ and a spectral dispersion of 1 Å per pixel. It also allows us to scale the off-field sky frames for sky subtraction. The reduced data cubes were aligned, stacked, and resampled to a new spatial grid with a spatial sampling of $0.3''\times 0.3''$ and a dispersion of 1 Å per spectral channel using the KCWIKit package[3] (Chen et al., 2021; Prusinski and Chen, 2024).

Binning and Covariance Correction

In this work, we focus only on the spatially integrated properties of the entire galaxies; results from a spatially-resolved analysis will be presented in future work (Zhuang et al., in prep). The integrated spectra for each galaxy were obtained by summing the spectra of spaxels with S/N > 1 per spectral pixel in the stellar continuum between 4200 Å and 4400 Å. As listed in Table 4.2, the extraction regions are equivalent to the area within 0.6–2.2 R_e for the galaxies in our sample. We selected regions based the S/N threshold instead of adopting a uniform aperture for spectrum extraction in order to maximize the S/N from the galaxies. As we further demonstrate in Appendix 4.8.1, any aperture bias that results from the irregular extraction region affects our main results negligibly.

[2] https://github.com/prusinski/KCWI_DRP

[3] https://github.com/yuguangchen1/KcwiKit

The IFU data underestimate the variance of the spatially-binned data due to covariance between adjacent spaxels, so we need to correct the variance of the binned spectra. This issue originates from the redistribution of the flux in the same pixel onto the new spatial grid when stacking the data. If we adopted standard error propagation to calculate the variances of the stacked data cubes assuming the adjacent pixels are independent of each other, the variances would be underestimated.

As suggested by O'Sullivan and Chen (2020) the error of a KCWI data cube can be corrected as

$$\sigma_{\rm measured} = C[1 + \alpha \log{(N_b)}]\sigma_{\rm nocov}, \tag{4.2}$$

for $N_b \lesssim N_{\rm thresh}$, and as

$$\sigma_{\rm measured} = C[1 + \alpha \log{(N_{\rm thresh})}]\sigma_{\rm nocov}, \tag{4.3}$$

for $N_b > N_{\rm thresh}$, where $N_{\rm thresh}$ represents the kernels beyond which the pixels become uncorrelated.

To measure the correction parameters C, α, and $N_{\rm thresh}$, we followed the method developed by de los Reyes et al. (2023). In brief, we first simulated mock sky cubes as Gaussian noise centered at zero with variances determined from the variance cubes of the science frames. The variance values of mock sky cubes are the same as those of science cubes. The data and variance cubes of the mock sky were passed through the same stacking procedures as the science cubes. The $\sigma_{\rm measured}$ were calculated as the standard deviation of the mock sky data, while the $\sigma_{\rm nocov}$ were estimated as the median of the variance for the stacked sky cube. We then fit the $\sigma_{\rm measured}$ and $\sigma_{\rm nocov}$ to Equation (4.2) and (4.3) to derive α and $N_{\rm thresh}$.

Finally, the covariance correction factor from Equation (4.2) and (4.3) was multiplied into the flux uncertainties of the stacked spectra, which we previously calculated from error propagation without accounting for covariance.

4.3 Emission-Line Measurements

The following section details the spectral analysis for gas-phase abundance measurements. Prior to the spectral analysis, the spectra were first corrected for Galactic extinction using the Galactic reddening maps of Schlafly and Finkbeiner (2011). We adopted the Galactic extinction law by O'Donnell (1994) to calculate the dereddening correction. The spectra are converted to the rest frame using the spectroscopic redshifts in the SDSS DR17 catalog (Abdurro'uf et al., 2022).

4.3.1 Disentangling stellar continuum and emission lines

The first step in the spectral analysis is to separate the stellar continuum and emission lines in order to measure properties of the stellar population and the nebular gas. To do this, we performed a simultaneous fit of the stellar continuum and emission lines of the integrated spectrum using the Penalized Pixel-Fitting method (`pPXF`; Cappellari and Emsellem, 2004; Cappellari, 2017; Cappellari, 2023), which is a χ^2-minimization code that fits for a linear combination of simple stellar population (SSP) models at different ages and metallicities to account for complex SFHs of star-forming galaxies.

For the stellar population synthesis (SPS) templates, we generated SSP models from the Flexible Stellar Population Synthesis code (FSPS; Conroy, Gunn, and White, 2009; Conroy and Gunn, 2010) version 3.2, assuming a Kroupa (2001) IMF, the MIST isochrones (Choi et al., 2016), and the MILES stellar spectral libraries (Sánchez-Blázquez et al., 2006). The SSP models accessed through the PYTHON-FSPS bindings (Foreman-Mackey, Sick, and Johnson, 2014) have metallicities spanning the range [Fe/H] = −2.0 to +0.5 with an interval of 0.25 dex, corresponding to the grid of the MIST isochrones. The ages range from log(Age)[yr] = 5.0 to 10.2 with an interval of 0.2 dex.

Given that the instrumental resolution of KCWI ($\sim$ 2.5 Å in the observed frame) is slightly higher than that of the FSPS SSP templates (2.54 Å in the rest frame), the observed spectra were convolved with a Gaussian kernel to match the spectral resolution of the SSP templates. We also restricted the spectral analysis to rest-frame wavelengths between 3650 Å and 5500 Å.

Inspired by the MaNGA data-analysis pipeline (Westfall et al., 2019), we ran two iterations of `pPXF` for each spectrum to better constrain the stellar kinematics and stellar continuum. In the first iteration, the spectral regions around potential emission lines (Table 4.3) in the velocity range of ±400 km s^{-1} were masked to determine the stellar kinematics. We included an eighth-order additive Legendre polynomial and an eighth-order multiplicative Legendre polynomial in the fit of the stellar continuum, motivated by the experience of the MaNGA team (Westfall et al., 2019; Belfiore et al., 2019) to improve the quality of kinematics results. The two polynomials allow the overall shape of the model spectra to better match that of the data, which may suffer from imperfect flux calibration and small inaccuracies in the dust extinction correction. Each fit ran `pPXF` twice. After the first run with the default emission-line mask, we used a moving boxcar with a wavelength width of 100 Å ($\sim$

7000 km s^{-1}) to determine the local mean and standard deviation of the fit residual. We then re-ran the fit with the updated mask excluding the $> 3\sigma$ outliers.

In the second iteration, we fixed the stellar kinematics to the values determined from the first iteration and performed a simultaneous fit of emission lines and stellar continuum. The emission lines and their constraints used in the fits are listed in Table 4.3. As suggested by Sarzi et al. (2006) and Oh et al. (2011), this approach is preferable to fitting the emission lines separately on a continuum-subtracted spectrum, which tends to overestimate the emission line fluxes and widths when a small mismatch exists between the stellar continuum and SPS models. Figure 4.2 shows an example of a best-fit model obtained with the joint fitting from the second iteration along with the observed spectrum.

This method provides measurements of integrated emission line fluxes that properly account for the stellar continuum. Additionally, we obtain a emission-free stellar continuum spectrum by subtracting the best-fit emission line model from the observed spectrum; we will use this stellar continuum spectrum in Section 4.4 to estimate stellar abundances.

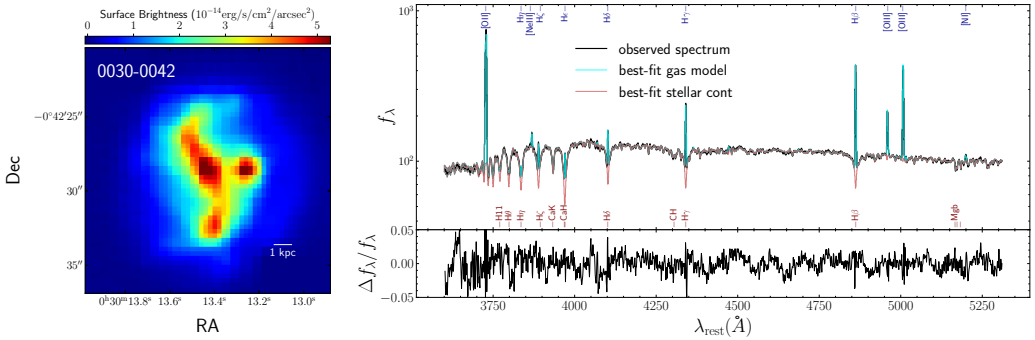

Figure 4.2: *Left:* Example KCWI white-light image computed by integrating the spectrum in the wavelength direction for each spatial pixel. *Right:* Example integrated KCWI spectrum of the same galaxy (top) and the model residual (bottom). In the top panel, the observed integrated spectrum is shown in black, while the best-fit model of the stellar continuum and the emission lines are shown in cyan and red, respectively. The y-axis is on a logarithmic scale. Prominent emission lines (blue) and stellar absorption features (red) are marked in the top and middle panels. The full set of the emission lines included in the fit is listed in Table 4.3.

4.3.2 Gas-phase oxygen abundance

The intrinsic dust attenuation of each galaxy was calculated from the Balmer decrement Hγ/Hβ, because the spectral range of the KCWI-blue data did not include Hα. Assuming Case B recombination, $T_e = 10,000$ K and $n_e = 100$ cm^{-3}, the theoretical

Table 4.3: Emission-Line Parameters

ID	Line Name	$\lambda^a_{\rm rest}$ (Å)	Fixed Ratio
1	H16	3704.913	...
2	H15	3713.034	...
3	H14	3723.003	...
4	[O II]λ3726	3727.092	...
5	[O II]λ3729	3729.875	0.28–1.47 [O II]λ3726[b]
6	H13	3735.436	...
7	H12	3751.217	...
8	H11	3771.701	...
9	Hθ	3798.976	...
10	He Iλ3820	3820.691	...
11	Hη	3836.472	...
12	[S III]λ3856	3857.111	...
13	[Ne III]λ3869	3869.860	...
14	He Iλ3889	3889.749	...
15	Hζ	3890.151	...
16	[Ne III]λ3967	3968.590	0.31 [Ne III]λ3869
17	Hϵ	3971.195	...
18	He Iλ4026	4027.328	...
19	[S II]λ4069	4069.749	...
20	[S II]λ4076	4077.500	0.40 [S II]λ4069
21	Hδ	4102.892	...
22	Hγ	4341.684	...
23	[O III]λ4363	4364.436	...
24	He Iλ4471	4472.734	...
25	[Fe III]λ4658	4659.414	...
26	He IIλ4686	4687.015	...
27	He Iλ4713	4714.466	...
28	Hβ	4862.683	...
29	He Iλ4922	4923.305	...
30	[O III]λ4959	4960.295	0.34 [O III]λ5007
31	[Fe III]λ4985	4985.900	...
32	[Fe III]λ4986	4987.200	...
33	[O III]λ5007	5008.240	...
34	He Iλ5016	5017.077	...
35	[N I]λ5198	5199.349	...
36	[N I]λ5200	5201.705	0.37 [N I]λ5198

[a] Ritz wavelengths in vacuum from the National Institute of Standards and Technology (NIST) Atomic Spectra database (`https://physics.nist.gov/PhysRefData/ASD/lines_form.html`).

[b] The line ratio of [O II]λ3726/[O II]λ3729 is only allowed to vary in the range of 0.28–1.47, as required by atomic physics (Osterbrock and Ferland, 2006).

ratio of Hγ/Hβ is 0.47 (Osterbrock and Ferland, 2006). The intrinsic $E(B-V)$, derived from the theoretical ratio of Hγ/Hβ along with the Cardelli, Clayton, and Mathis (1989) dust extinction law, was applied to the emission-line measurements to yield the dereddened line fluxes for nebular oxygen abundance determination.

Ideally, nebular oxygen abundances would be measured from the reliable direct T_e method, which directly determines the electron temperature of ionized gas. However, the direct T_e method relies on the detection of auroral lines, such as [O III]λ4363, which are exceedingly faint, especially for relatively metal-rich systems. We detected [O III]λ4363 in fewer than 1/3 of the sample. We therefore used an empirical strong-line calibration derived from T_e-based measurements to estimate the gas-phase oxygen abundance for constructing an unbiased MZR. We will discuss the gas-phase oxygen abundances derived from different approaches in more detail in future work focusing on the KCWI-red data (Zhuang et al., in prep.).

For the present, we use the "R calibration" (Pilyugin and Grebel, 2016), defined as:

$$\begin{aligned}(\mathrm{O/H})_{R,U} = {} & 8.589 + 0.022\ \log(R_3/R_2) + 0.399\ \log N_2 \\ & + (0.164\ \log(R_3/R_2) + 0.589 \log N_2 - 0.137) \\ & \times \log R_2,\end{aligned} \tag{4.4}$$

when $\log N_2 \geq -0.6$; and

$$\begin{aligned}(\mathrm{O/H})_{R,L} = {} & 7.932 + 0.944\ \log(R_3/R_2) + 0.695\ \log N_2 \\ & + (0.970 - 0.291\ \log(R_3/R_2) - 0.019 \log N_2) \\ & \times \log R_2,\end{aligned} \tag{4.5}$$

when $\log N_2 < -0.6$, where $R_2 = I_{[\mathrm{O\,II}]\lambda3727+\lambda3729}/I_{\mathrm{H}\beta}$, $R_3 = I_{[\mathrm{O\,III}]\lambda4959+\lambda5007}/I_{\mathrm{H}\beta}$, and $N_2 = I_{[\mathrm{N\,II}]\lambda6548+\lambda6584}/I_{\mathrm{H}\beta}$[4].

Because our full sample of the KCWI data does not cover the spectral region of [N II]$\lambda\lambda$6548,6584, we use the emission line fluxes of Hα and [N II] from the SDSS MPA-JHU catalog (*galSpecLine*, SDSS DR17; Brinchmann et al., 2004; Tremonti et al., 2004). Assuming Case B recombination at $T_e = 10,000$ K and $n_e = 100\,\mathrm{cm}^{-3}$, the N_2 ratio is calculated assuming that

[4]The N_2 ratio defined by Pilyugin and Grebel (2016) is different from the commonly used "N2" index used by other strong line calibrations (e.g., Pettini and Pagel, 2004), where $N_2 = \log([\mathrm{N\,II}]\lambda6584/\mathrm{H}\alpha)$ instead.

$$\begin{aligned} N_2 &= I_{[\mathrm{N\,II}]\lambda6548+\lambda6584}/I_{\mathrm{H}\beta} \\ &= I_{[\mathrm{N\,II}]\lambda6548+\lambda6584}/I_{\mathrm{H}\alpha} \times 2.86. \end{aligned} \tag{4.6}$$

Combining R_2 and R_3 based on the KCWI measurements with the SDSS results for N_2, we derive the gas-phase oxygen abundance of each galaxy using Equations (4.4) and (4.5), with results listed in Table 4.4. The reported uncertainties are the square root of the quadrature sum of the systematic uncertainty of the R calibration (0.1 dex, Pilyugin and Grebel, 2016; Pilyugin et al., 2018) and the random errors from the flux measurement uncertainties. Our measurements from KCWI+SDSS data are consistent within 1σ of the values derived from using only the SDSS emission line fluxes.

4.4 Stellar Abundance Determination

Stellar abundances of iron and magnesium can be measured from spectral indices of stellar absorption lines sensitive to the stellar population parameters (e.g., Thomas et al., 2005; Thomas et al., 2010), or full-spectrum fitting that utilizes the information from the entire spectrum (e.g., Choi et al., 2014; Conroy et al., 2018). In this work, we use the full-spectrum fitting method that relies on galaxy templates with variable [Mg/Fe] to constrain [Mg/Fe] in our star-forming galaxies. Existing models for measuring the detailed abundances of individual α elements (`alf`, Conroy et al., 2018), can only be applied to quiescent galaxies because the models exist only for older populations, usually > 1 Gyr in age.

In order to fit galaxies with a wide range of ages, we made use of the latest FSPS SSP models with variable [α/Fe] (Park et al., in prep.), as detailed in Section 4.4.1, in order to estimate [Mg/Fe] in the star-forming galaxies. The updated model was designed to capture variation in [α/Fe] over the full range of possible stellar ages, from 0.1 Myr to 20 Gyr. This was achieved by constructing a new set of stellar spectral libraries and isochrones (see Park et al., in prep., for details).

Similar to existing SSP models with variable [α/Fe] (Vazdekis et al., 2015; Knowles et al., 2023), our models assume that all α elements (O, Ne, Mg, Si, S, Ca, and Ti) vary in lock-step (i.e., [Mg/Fe] = [α/Fe]). One must be cautious when interpreting an inferred [α/Fe] as identical to [Mg/Fe]; as addressed in Choi et al. (2014) and Beverage et al. (2023), individual α elements may not track each other in quiescent galaxies when each α element is fitted separately using `alf`. To mitigate this issue,

we developed our own fitting algorithm (Section 4.4.2) and show in Section 4.4.3 that our measured [α/Fe] represents [Mg/Fe] consistent with the `alf` results in the sample galaxies.

4.4.1 SSP models with variable [α/Fe]

To construct SSP models with variable [α/Fe], we followed the methodology described by Conroy and van Dokkum (2012) and Conroy et al. (2018). At a given age and metallicity, the SSP spectrum (f) of arbitrary [α/Fe] can be calculated as:

$$f([\alpha/\mathrm{Fe}]) = f_{\mathrm{base}}([\alpha/\mathrm{Fe}]_{\mathrm{lib}}) \frac{f_{\mathrm{theo}}([\alpha/\mathrm{Fe}])}{f_{\mathrm{theo}}([\alpha/\mathrm{Fe}]_{\mathrm{lib}})}, \tag{4.7}$$

where f_{base} is the base empirical SSP model and f_{theo} is the synthetic SSP template with arbitrary abundance pattern from theoretical models. The ratio $f_{\mathrm{theo}}([\alpha/\mathrm{Fe}])/f_{\mathrm{theo}}([\alpha/\mathrm{Fe}]_{\mathrm{lib}})$ is the "response function" which indicates the relative change in the spectrum due to a change in [α/Fe] from the base model.

For the base empirical model, we adopted the FSPS SSP models generated using the MILES stellar libraries (hereafter FSPS-MILES SSPs) described in Section 4.3.1. Because all the available empirical SSP models including FSPS-MILES SSPs do not have α variation, we have to resort to theoretical models. The theoretical SSP models (hereafter FSPS-C3K SSPs) were generated with FSPS using the Kroupa IMF (Kroupa, 2001), α-enhanced MIST isochrones (Dotter, et al., in prep), and the theoretical C3K stellar model grids (Park et al., in prep). The FSPS-C3K SSPs have the same grid in age and metallicity as the FSPS-MILES SSP models and span a wide range of [α/Fe] ([-0.2, 0.0, 0.2, 0.4, 0.6]).

Because our goal is to determine [Mg/Fe], we used the relation for [Mg/Fe] as a function of [Fe/H] for MILES stars reported by Milone, Sansom, and Sánchez-Blázquez (2011) as a proxy for $[\alpha/\mathrm{Fe}]_{\mathrm{lib}}$ at a given [Fe/H]. The theoretical SSP model at a given $[\alpha/\mathrm{Fe}]_{\mathrm{lib}}$ is derived from linear interpolation of two adjacent grids. We therefore obtain our new SSP models with variable age, [Fe/H], and [α/Fe] using Equation 4.7. The final models have 27 grid steps in age ($\log(\mathrm{Age})[\mathrm{yr}] = 5.0$ to 10.2 at an interval of 0.2 dex), 11 grid steps in [Fe/H] ($[\mathrm{Fe/H}] = -2.0$ to 0.5 at an interval of 0.25 dex), and 5 grid setps in [α/Fe] ($[\alpha/\mathrm{Fe}] = -0.2$ to 0.6 at an interval of 0.2 dex).

4.4.2 Model fitting

We developed a two-step fitting approach to measure both [Fe/H] and [Mg/Fe] of the star-forming galaxies in our sample.

In the first step, we use `pPXF` to fit the full emission-free stellar continuum spectrum of each galaxy from 3650 to 5500 Å in the rest frame to infer the SFHs for each galaxy (the top panel of Figure 4.3). It fits for a linear combination of discrete SSPs at different ages, [Fe/H] and [α/Fe], along with the stellar velocity dispersion and offset from the initial spectroscopic redshift in the SDSS catalog to the observed spectrum. The young galaxies in our sample could have SFHs that are more complex than can be described by simple parameterizations (i.e., an SSP). Therefore, the non-parametric approach of `pPXF` is appropriate for our case. In this paper, we use the SFHs only to derive average ages (described below). The full SFHs will be analyzed in the future. Appendix 4.8.2 gives a complete justification of our use of non-parametric SFH fits. Each SSP model is normalized over the spectral range 4800–5500 Å for "light-weighted" property estimates. Similar to the fits described in Section 4.3.1, we ran two iterations for each spectrum. The 3σ outliers from the first iteration are masked in the second iteration to remove pixels affected by imperfect subtraction of emission lines. The error spectra are also scaled by the square root of the reduced χ^2 of the first iteration to yield more reasonable estimates of the stellar population uncertainties. Following Cappellari (2023), "regularization" was also employed in the fitting with `regul` = 30 to recover a relatively smooth SFH. We also included a ninth-order multiplicative Legendre polynomial as a "nuanced" parameter to account for internal dust extinction and/or imperfect flux calibration.

Following Cappellari (2023), the light-weighted properties are derived according to

$$\langle \log \mathrm{Age} \rangle = \frac{\sum_i w_i \times \log \mathrm{Age}_i}{\sum_i w_i}, \tag{4.8a}$$

$$\langle [\mathrm{Fe/H}] \rangle = \frac{\sum_i w_i \times [\mathrm{Fe/H}]_i}{\sum_i w_i}, \tag{4.8b}$$

$$\langle [\alpha/\mathrm{Fe}] \rangle = \frac{\sum_i w_i \times [\alpha/\mathrm{Fe}]_i}{\sum_i w_i}, \tag{4.8c}$$

where w_i is the weight of the i^{th} SSP template returned by `pPXF`.

In the second step, we re-fit the stellar continuum limited to the rest-frame spectral region 4800–5500 Å (the bottom panel of Figure 4.3). As we will demonstrate in Section 4.4.3, a second fit is necessary to recover a value closer to the [Mg/Fe] consistent with the `alf` measurements. In the real galaxy spectra, individual α elements may not track each other (Thomas, Maraston, and Bender, 2003; Conroy, Graves, and van Dokkum, 2014; Choi et al., 2014; Beverage et al., 2023); the derived [α/Fe] from the first iteration is sensitive not only to Mg but also to other α

elements, such as Ca. The spectral region 4800–5500 Å contains most of the Fe- and Mg- sensitive features (i.e., the Mg b triplet, Fe5270, Fe5335) as well as the age indicator Hβ. For example, Vazdekis et al. (2015) found that they could reproduce values of [Mg/Fe] consistent with the literature for two massive ellipticals only if the fits were limited to the stellar continuum in the range 4800–5500 Å; the fits failed when they were performed using a larger spectral range.

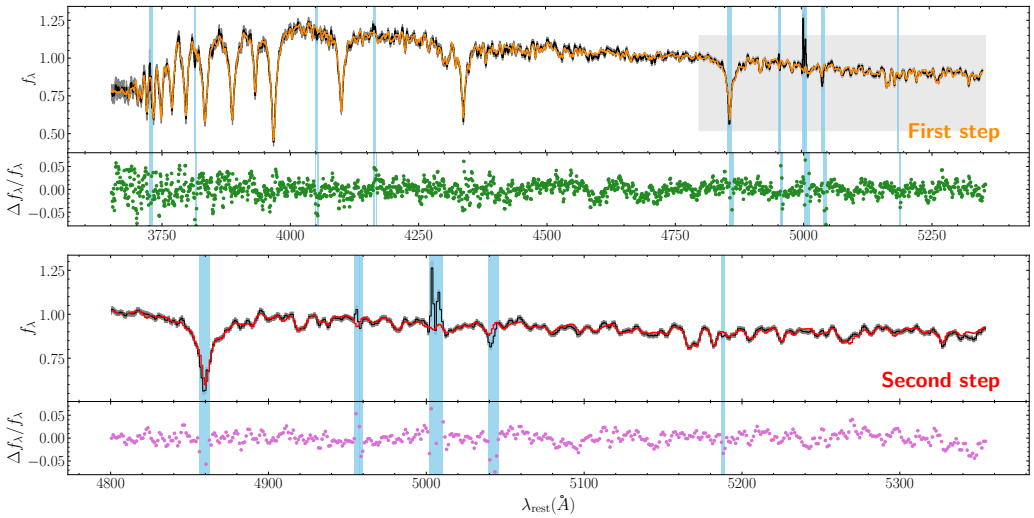

Figure 4.3: Illustration of the two-step approach for the same star-forming galaxy in Figure 4.2. The flux densities are normalized to have median in the spectral region 4800-5500 Å. Note that the two panels cover different wavelength ranges of the same spectrum. *Top*: The emission-line-subtracted stellar spectrum (black), best-fit `pPXF` model spectrum (orange), and the model residual (green) in the first fitting step, which operates on the entire KCWI spectrum. The blue shaded regions indicate the masked pixels that are 3σ outliers in the first iteration. The gray shaded region marks the spectral regions used in the second step. *Bottom*: the stellar continuum (black), best-fit model (red), and the model residual (pink) in the second fitting step of the same spectrum, which operates on the spectral region $\sim$ 4800 – 5500 Å. The blue shaded regions are the same masked pixels inherited from the first step. In this iteration, [Fe/H] and [Mg/Fe] are allowed to vary, but the SFH and the stellar kinematics are fixed to the values determined in the first step.

To fit the spectral region 4800–5500 Å, we fixed the non-parametric SFHs and stellar kinematics to the values recovered in the first step. We retained the weights of each age bin returned by the first step, but allowed [Fe/H] and [α/Fe] to vary within each bin in the second iteration.

We followed the continuum correction approach of `alf` (Conroy et al., 2018) by including in the fitting process a fourth-order multiplicative polynomial in the form of $p(\lambda) = \sum_{i=0}^{4} c_i(\lambda - \mu)^i$, where μ is the mean wavelength of the region being fit.

The polynomial degree was determined by $n = (\lambda_{\rm max} - \lambda_{\rm min})/200$ Å so that the correction is flexible enough to account for any mismatch in the continuum shape due to imperfect flux calibration or dust attenuation, but not so flexible that it over-fits regions containing real broad absorption features. In each iteration, we calculated the ratio of the data and model, masked the spectral regions with strong stellar absorption features and gas emission lines, and performed a least-squares polynomial fit to the unmasked pixels. The data were then compared with the altered model multiplied by the best-fit polynomial to calculate the likelihood. We experimented with different polynomial orders, including $n = 0$ and $n = (\lambda_{\rm max} - \lambda_{\rm min})/100$ Å and found that the changes of the recovered abundances are within the reported uncertainties.

The fits were accomplished using `dynesty` (Speagle, 2020), a Python package for dynamic nested sampling capable of estimating the Bayesian posterior distribution. For each age bin, we adopted a uniform prior for [Fe/H] in the range $[-2.0, 0.5]$ and a uniform prior for [α/Fe] in the range $[-0.2, 0.6]$. The SSP models at non-gridpoint values of model parameters were calculated via linear interpolation. Using the posteriors of [Fe/H] and [α/Fe] in each age bin from `dynesty` along with Equations (4.8b) and (4.8c), we obtained the posterior distributions of the light-weighted [Fe/H] and [α/Fe] for each galaxy. All the galaxies have converged, single-peaked posteriors. The best-fit results are quoted as the median of the 1D marginalized posteriors. Because the maximum a posteriori (MAP) estimates for some galaxies fell outside the 1σ (68%) confidence interval, but were always within the 2σ interval, the quoted uncertainties are based on the 2σ confidence interval (i.e., 2.5% and 97.5% percentiles).

4.4.3 Verification of Magnesium Abundance Measurement

As mentioned above, one must be cautious when interpreting the measured [α/Fe] as [Mg/Fe] if the SPS models used for analysis tie all the α elements together (i.e., the case of our analysis). If α elements do not track each other—for instance, [Ca/Fe] ~ 0 when [Mg/Fe] > 0 (Choi et al., 2014; Beverage et al., 2023)—then the derived [α/Fe] may not reflect [Mg/Fe]. In fact, Leethochawalit et al. (2019) showed in their Appendix A that [Mg/Fe] was underestimated by $\sim 0.1 - 0.2$ dex when the SSP models were fit with the response functions of individual α elements fixed to the same value. Therefore, it is essential to validate that our method recovers the correct [Mg/Fe] rather than an amalgam of different elements, i.e., [α/Fe].

As a result, we seek to understand how to interpret the measured [α/Fe], age, and

[Fe/H] via the two-step approach along with the new SPS models before applying the method to our KCWI sample. To validate the two-step method, we made use of the sample of 123 SDSS quiescent galaxies compiled by Leethochawalit et al. (2018b), which has existing measurements of individual [Mg/Fe], [Fe/H] and SSP age from `alf` by Zhuang et al. (2023). We re-measured their light-weighted age, [Fe/H] and [α/Fe] using the two-step method described in Section 4.4.2 in order to compare them with the existing results obtained from `alf`.

To illustrate the need for the two-step method, we also experimented with fits using only a single iteration of `pPXF`. We performed the fits with two different spectral regions: the spectral range of KCWI-blue overlapping with those of the empirical SSP models ($\sim$ 3650 – 5500 Å), which is essentially the first step in the two-step method, and the spectral region 4800-5500 Å, which contains most of the Fe- and Mg- sensitive features present in the full spectrum. The `pPXF` setup was the same as the one described in Section 4.4.2. To estimate the uncertainties in the `pPXF` measurements, we adopted the "wild bootstrap method" (Davidson and Flachaire, 2008) following the example described by Cappellari (2023)[5]. In summary, after running the first `pPXF` regularized fit with `regul` = 30, we bootstrapped the residuals and repeated the `pPXF` fit 100 times with no regularization. For each iteration, we calculated the light-weighted properties using Equation 4.8. The uncertainties were estimated as the standard deviations of the distributions for the light-weighted properties.

Figure 4.4 compares [α/Fe] measured from the two-step and one-step methods with [Mg/Fe] derived by `alf` (Zhuang et al., 2023); Figure 4.5 shows the same comparison for [Fe/H]. For each method, we calculated the reduced χ^2 between the `alf` results and our new measurements as:

$$\chi^2_\nu = \frac{1}{N}\sum_i^N \frac{(m_{i,\mathrm{Alf}} - m_{i,\mathrm{X}})^2}{\sigma^2_{i,\mathrm{Alf}} + \sigma^2_{i,\mathrm{X}}}, \tag{4.9}$$

where $m_{i,\mathrm{Alf}}$ and $\sigma_{i,\mathrm{Alf}}$ indicate the measurements and the uncertainties from `alf`, while $m_{i,\mathrm{X}}$ and $\sigma_{i,\mathrm{X}}$ represent those from the three methods illustrated above.

As can be seen in the middle panels of Figure 4.4, [α/Fe] derived using `pPXF` is significantly lower than [Mg/Fe] from `alf` for highly α-enhanced spectra when we fit the entire spectral range of KCWI ($\sim$ 3650 – 5500 Å), with a χ^2_ν = 11.2. On the

[5] `https://github.com/micappe/ppxf_examples/blob/main/ppxf_example_population_bootstrap.ipynb`

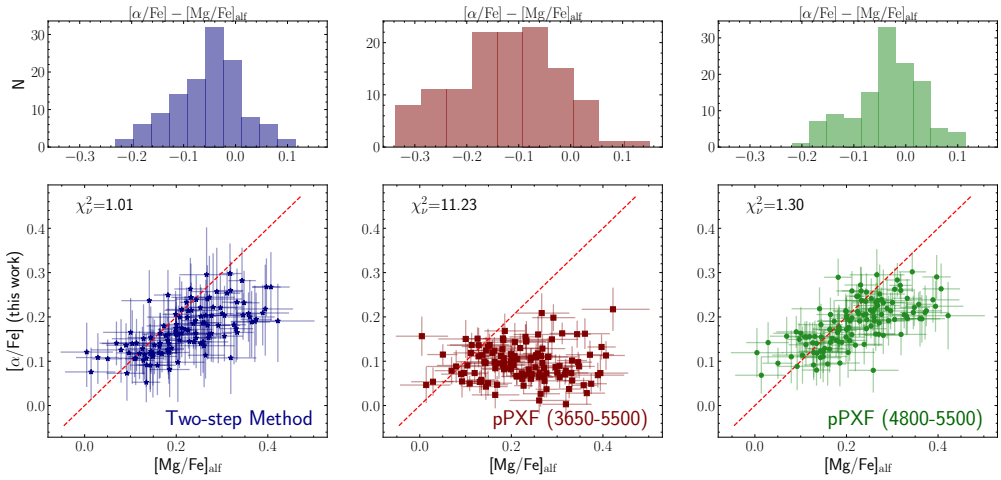

Figure 4.4: Comparison of [Mg/Fe] for the massive SDSS quiescent galaxies compiled by Leethochawalit et al. (2019) measured from `alf` by Zhuang et al. (2023) and from the methods presented in Section 4.4.3. Here we show the measurements of [α/Fe] derived from the two-step method (purple stars) in the left column, those from fitting the entire spectra ($\sim$ 3650 – 5500 Å) via `pPXF` (red squares) in the middle column, and those from fitting the spectral regions of $\sim$ 4800 – 5500 Å (green circles) in the right column. In each column, the top panel shows the difference between the new results and `alf` measurements, while the lower panel demonstrates the direct comparison between the measurements. The red dashed lines indicate equal values for both axes. The weighted RMS (σ) is also shown in each panel.

other hand, the two-step method as well as the `pPXF` fit over a narrower region of 4800 – 5500 Å, give a much closer estimate of [Mg/Fe], with χ^2_ν = 1.01 and 1.30, respectively.

It might seem that the single-step fit over a limited spectral range (4800 – 5500 Å) performs as well as the two-step approach. However, Figure 4.5 shows that fitting a narrower region between 4800 – 5500 Å overestimates [Fe/H] by $\sim$ 0.2 dex on average compared to `alf`. The difference can be up to 0.5 dex for the most metal-poor galaxy in the SDSS sample. On the contrary, the two-step method and the `pPXF` fit of the entire KCWI spectral coverage both give measurements of [Fe/H] consistent with `alf` yielding χ^2_ν = 0.85 and 0.94, respectively.

The discrepancy can be explained by the fact that most of the spectral features sensitive to the stellar population age and SFH reside near the Balmer/4000 Å breaks, so ignoring them inhibits the breaking of the age–metallicity degeneracy. This effect can be seen in Figure 4.6, where we compare the light-weighted age derived from `pPXF` using two different regions with the SSP age determined by `alf`. The `pPXF` fit of the region between 4800 Å and 5500 Å significantly underestimates

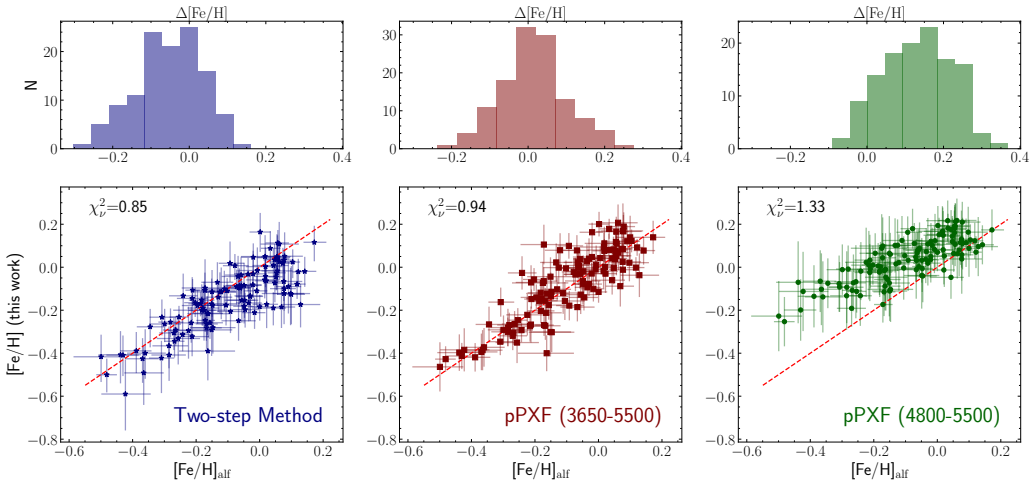

Figure 4.5: As for Figure 4.4, but comparing measurements of [Fe/H].

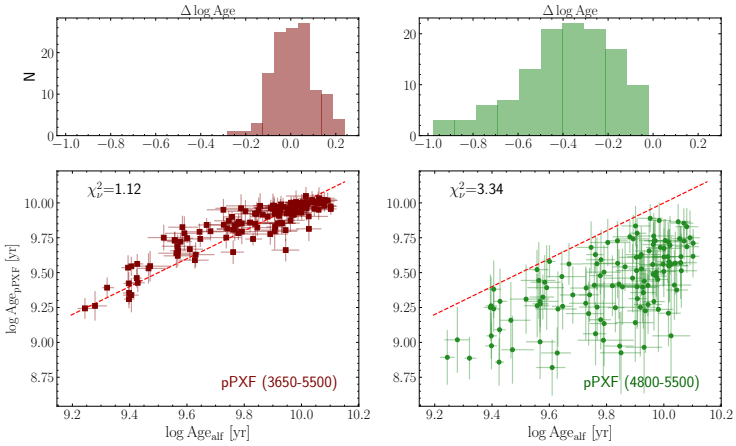

Figure 4.6: As for Figure 4.4, but comparing measurements of stellar population age.

the stellar population age, while the fit of the full KCWI spectrum recovers consistent age estimates even though `pPXF` and `alf` assume different forms for the SFH. The results of the `pPXF` fit over different regions are in agreement with the direction of the age–metallicity degeneracy: because the models predict younger stellar populations due to a lack of age constraints from NUV and bluer optical features, they have to compensate for the deeper absorption features from older stars by increasing [Fe/H].

The tests performed above use quiescent galaxies which still have deep Hβ absorption present to constrain stellar population age to some extent when we fit over a narrower range of 4800 – 5500 Å. This issue would be more severe in low-mass, star-forming galaxies in our KCWI sample because they host younger stellar populations with higher star formation activity. The shallower Hβ absorption and the

contamination of the Hβ from the ionized gas would prohibit the single-step fit over a limited range from yielding a reasonable age estimate. We therefore have to use the information from the full spectrum to minimize the age–metallicity degeneracy.

We note that the χ^2_ν of the two-step method in the cases of [Fe/H] and [Mg/Fe] are both slightly smaller than that of the best `pPXF` fit, which may result from larger uncertainties in the two-step method. We emphasize that we adopted the two-step because it is a compromise to recover reasonable value of [Fe/H] and [Mg/Fe] of the star-forming galaxies in our sample. We do not imply that the two-step method is significantly better in measuring [Fe/H] or [Mg/Fe] alone for quiescent galaxies than running `pPXF` directly.

To conclude, we have demonstrated above that our novel two-step approach can recover [Mg/Fe] and [Fe/H] consistent with the `alf` measurements, even using the SSP models that lock all the α element variation together, while a single-step fit (over either the full KCWI spectral coverage or a portion of the spectrum (4800 – 5500 Å) carrying most of the Fe- and Mg- sensitive features) via `pPXF` would underestimate [Mg/Fe] or overestimate [Fe/H]. Our two-step method preserves the age constraints from the full spectrum while reducing the contamination from other α elements that might not track Mg. Now, we apply the two-step approach to the KCWI star-forming galaxies to constrain their stellar [Fe/H] and [Mg/Fe][6]. Table 4.4 lists the stellar abundance measurements derived from the two-step approach described in Section 4.4.2. Table 4.4 also reports the stellar velocity dispersion and the light-weighted age obtained from the first step of the two-step method, along with the uncertainties determined from 100 bootstraps of the residuals.

Table 4.4: The Derived Properties of the KCWI Star-Forming Galaxies

Galaxy	z	$\log M_*$ $[M_\odot]$	σ_* km s^{-1}	$\langle \log \mathrm{Age} \rangle_*$ [yr]	$[\mathrm{Fe/H}]_*$ dex	$[\mathrm{Mg/Fe}]_*$ dex	$12 + \log (\mathrm{O/H})_\mathrm{g}$ dex
2225−0046	0.016	8.09±0.10	54.8±3.5	8.96±0.05	$-0.88^{+0.09}_{-0.11}$	$0.09^{+0.06}_{-0.06}$	7.90±0.11
0231−0043	0.009	8.09±0.10	56.7±3.1	8.81±0.05	$-1.07^{+0.14}_{-0.15}$	$0.19^{+0.09}_{-0.09}$	7.74±0.10
0133−0109	0.016	8.11±0.14	61.7±3.4	8.56±0.08	$-1.02^{+0.16}_{-0.16}$	$0.16^{+0.08}_{-0.09}$	7.90±0.10
2329+1552	0.009	8.23±0.10	42.3±2.2	9.07±0.04	$-0.72^{+0.07}_{-0.08}$	$0.18^{+0.05}_{-0.05}$	8.24±0.10
2152−0110	0.016	8.40±0.10	49.4±4.6	9.13±0.07	$-1.02^{+0.10}_{-0.11}$	$0.14^{+0.08}_{-0.08}$	8.20±0.10
0845+5145	0.014	8.42±0.10	64.5±2.5	8.89±0.06	$-0.56^{+0.08}_{-0.10}$	$0.15^{+0.06}_{-0.05}$	8.27±0.10
2334+0029	0.024	8.42±0.10	56.9±4.6	8.70±0.06	$-1.10^{+0.20}_{-0.17}$	$0.10^{+0.07}_{-0.09}$	7.97±0.10
0121−0853	0.018	8.43±0.10	51.0±2.8	8.85±0.05	$-0.54^{+0.09}_{-0.08}$	$0.06^{+0.04}_{-0.05}$	8.10±0.10
0013−0956	0.013	8.51±0.10	44.7±3.0	9.00±0.04	$-0.53^{+0.08}_{-0.10}$	$0.22^{+0.06}_{-0.05}$	8.22±0.11
0155−0037	0.023	8.56±0.10	69.0±3.3	8.93±0.05	$-1.16^{+0.11}_{-0.11}$	$0.08^{+0.06}_{-0.07}$	7.92±0.10

continued

[6]In the following analysis, we refer the [α/Fe] measured from the two-step method as [Mg/Fe].

Table 4.4: The Derived Properties of the KCWI Star-Forming Galaxies

Galaxy	z	$\log M_*$ $[M_\odot]$	σ_* km s^{-1}	$\langle \log \mathrm{Age} \rangle_*$ [yr]	$[\mathrm{Fe/H}]_*$ dex	$[\mathrm{Mg/Fe}]_*$ dex	$12 + \log(\mathrm{O/H})_g$ dex
0140−0012	0.018	8.59±0.10	58.0±2.8	8.85±0.05	$-0.50^{+0.06}_{-0.08}$	$0.10^{+0.05}_{-0.05}$	8.12±0.10
0023−0939	0.02	8.59±0.10	55.2±3.9	8.87±0.06	$-0.86^{+0.09}_{-0.10}$	$0.18^{+0.06}_{-0.06}$	8.15±0.10
0233+0038	0.024	8.67±0.10	51.7±3.3	8.92±0.06	$-0.87^{+0.11}_{-0.11}$	$0.14^{+0.07}_{-0.07}$	8.25±0.10
0256−0010	0.029	8.69±0.10	65.0±3.7	8.84±0.06	$-1.06^{+0.10}_{-0.11}$	$0.21^{+0.08}_{-0.08}$	8.13±0.10
2259−0019	0.016	8.71±0.10	49.2±3.0	9.14±0.06	$-0.51^{+0.09}_{-0.11}$	$0.10^{+0.05}_{-0.06}$	8.39±0.10
2300−0832	0.025	8.75±0.10	47.6±3.1	9.05±0.05	$-0.82^{+0.13}_{-0.06}$	$0.08^{+0.05}_{-0.07}$	8.16±0.11
0233−0819	0.019	8.77±0.10	53.7±2.1	8.95±0.04	$-0.50^{+0.06}_{-0.09}$	$0.09^{+0.04}_{-0.04}$	8.12±0.11
0125−0024	0.016	8.78±0.10	50.5±1.9	9.74±0.04	$-0.45^{+0.06}_{-0.08}$	$0.12^{+0.06}_{-0.07}$	-[a]
0241−0810	0.005	8.79±0.10	54.7±1.8	9.79±0.03	$-0.68^{+0.04}_{-0.03}$	$0.13^{+0.05}_{-0.05}$	-[a]
2301+1451	0.024	8.81±0.11	47.9±3.5	8.87±0.06	$-0.77^{+0.13}_{-0.13}$	$0.09^{+0.06}_{-0.07}$	8.19±0.10
0332−0600	0.018	8.82±0.10	52.7±2.4	9.04±0.06	$-0.42^{+0.06}_{-0.07}$	$0.09^{+0.04}_{-0.05}$	8.20±0.12
2131−0613	0.025	8.82±0.10	57.8±3.9	8.78±0.07	$-0.96^{+0.13}_{-0.13}$	$0.20^{+0.07}_{-0.07}$	8.20±0.10
0850+6145	0.024	8.88±0.10	64.6±4.8	9.06±0.08	$-0.69^{+0.09}_{-0.11}$	$0.10^{+0.06}_{-0.06}$	8.35±0.11
0256−0707	0.017	8.96±0.10	60.3±2.5	8.93±0.04	$-0.44^{+0.06}_{-0.07}$	$0.12^{+0.05}_{-0.05}$	8.29±0.10
0033+0012	0.014	8.97±0.10	61.5±2.3	8.72±0.04	$-0.63^{+0.10}_{-0.10}$	$0.17^{+0.06}_{-0.06}$	8.26±0.10
2137+1243	0.031	8.98±0.11	56.5±4.4	8.95±0.07	$-0.83^{+0.09}_{-0.11}$	$0.19^{+0.06}_{-0.07}$	8.26±0.11
0137−0942	0.019	9.02±0.10	60.3±2.2	8.71±0.04	$-0.57^{+0.07}_{-0.10}$	$0.10^{+0.05}_{-0.05}$	8.14±0.10
0040−0017	0.019	9.02±0.10	50.1±2.7	8.72±0.04	$-0.53^{+0.08}_{-0.08}$	$0.08^{+0.05}_{-0.05}$	8.19±0.10
0136+1356	0.024	9.03±0.10	58.0±3.3	8.60±0.05	$-0.62^{+0.09}_{-0.11}$	$0.09^{+0.06}_{-0.06}$	8.26±0.10
2304−0933	0.032	9.04±0.10	60.0±2.4	8.84±0.05	$-0.73^{+0.08}_{-0.09}$	$0.21^{+0.07}_{-0.06}$	8.29±0.10
0309−0041	0.037	9.05±0.10	66.9±3.9	8.72±0.06	$-0.84^{+0.11}_{-0.12}$	$0.12^{+0.06}_{-0.06}$	8.28±0.10
0019−0004	0.04	9.15±0.10	69.9±3.9	8.74±0.05	$-0.78^{+0.13}_{-0.13}$	$0.09^{+0.07}_{-0.07}$	8.37±0.10
0208+0048	0.02	9.15±0.10	46.0±3.1	8.93±0.05	$-0.65^{+0.08}_{-0.08}$	$0.15^{+0.05}_{-0.05}$	8.36±0.10
0306−0033	0.025	9.16±0.10	49.0±2.6	9.04±0.04	$-0.54^{+0.08}_{-0.10}$	$0.17^{+0.05}_{-0.05}$	8.46±0.10
0346+0023	0.031	9.18±0.10	64.2±3.5	8.81±0.06	$-0.89^{+0.11}_{-0.12}$	$0.21^{+0.07}_{-0.08}$	8.31±0.10
0243+0032	0.028	9.34±0.10	49.4±2.9	8.75±0.06	$-0.70^{+0.10}_{-0.10}$	$0.20^{+0.06}_{-0.06}$	8.34±0.10
2318+0105	0.03	9.35±0.10	65.4±3.0	8.82±0.05	$-0.71^{+0.08}_{-0.08}$	$0.22^{+0.06}_{-0.05}$	8.36±0.11
2206−0041	0.029	9.37±0.16	65.9±2.6	8.43±0.06	$-0.72^{+0.13}_{-0.13}$	$0.22^{+0.09}_{-0.09}$	8.34±0.10
2243+0040	0.039	9.37±0.10	57.7±4.8	8.76±0.05	$-0.83^{+0.09}_{-0.10}$	$0.13^{+0.06}_{-0.06}$	8.25±0.10
0334+0106	0.049	9.44±0.10	77.4±4.7	8.13±0.07	$-0.35^{+0.10}_{-0.12}$	$0.12^{+0.06}_{-0.05}$	8.32±0.10
0317−0004	0.022	9.46±0.10	55.4±2.3	8.62±0.05	$-0.58^{+0.09}_{-0.09}$	$0.15^{+0.05}_{-0.05}$	8.32±0.10
2211+0006	0.057	9.58±0.10	50.3±4.6	8.43±0.09	$-0.43^{+0.12}_{-0.11}$	$0.17^{+0.06}_{-0.06}$	8.47±0.10
0245−0045	0.054	9.60±0.10	55.9±3.5	8.49±0.06	$-0.35^{+0.10}_{-0.10}$	$0.13^{+0.06}_{-0.06}$	8.38±0.10
0030−0042	0.041	9.63±0.10	63.8±2.2	8.63±0.04	$-0.53^{+0.09}_{-0.09}$	$0.17^{+0.05}_{-0.05}$	8.56±0.10
2139+0019	0.05	9.72±0.10	66.3±3.6	8.58±0.08	$-0.83^{+0.20}_{-0.21}$	$0.18^{+0.09}_{-0.09}$	8.51±0.10
0407−0634	0.038	9.88±0.10	59.9±3.6	9.13±0.07	$-0.18^{+0.08}_{-0.09}$	$0.09^{+0.05}_{-0.05}$	8.46±0.11
0254+0103	0.043	9.90±0.10	71.2±3.3	8.61±0.06	$-0.82^{+0.13}_{-0.13}$	$0.20^{+0.08}_{-0.07}$	8.45±0.10
0140−0013	0.058	10.02±0.10	76.4±2.5	8.57±0.04	$-0.40^{+0.09}_{-0.10}$	$0.21^{+0.05}_{-0.05}$	8.48±0.10

The columns show (1) the galaxy ID; (2-3) the spectroscopic redshift and the spectroscopic redshift from Table 4.1; (4-5) the stellar velocity dispersion and light-weighted ages measured from the pPXF fit of the entire KCWI spectra (Sections 4.4.2 and 4.4.3); (6-7) the $[\mathrm{Fe/H}]_*$ and $[\mathrm{Mg/Fe}]_*$ estimated from the two-step method (Section 4.4.2); (8) the gas-phase oxygen abundance obtained from the R calibration by Pilyugin and Grebel (2016) described in Section 4.3.2.

[a] The absence of emission lines in the quiescent galaxies prevents us from determining their gas-phase metallicities.

4.5 Results

4.5.1 Comparison between stellar and gas-phase abundances

We now compare the ionized gas-phase oxygen abundances with the stellar abundances of iron and magnesium for our sample. For a more direct comparison, we convert the gas-phase metallicity $12 + \log(\mathrm{O/H})$ into $[\mathrm{O/H}]_\mathrm{g}$ using the solar oxygen abundance of $12 + \log(\mathrm{O/H})_\odot = 8.69$ (Asplund et al., 2009).

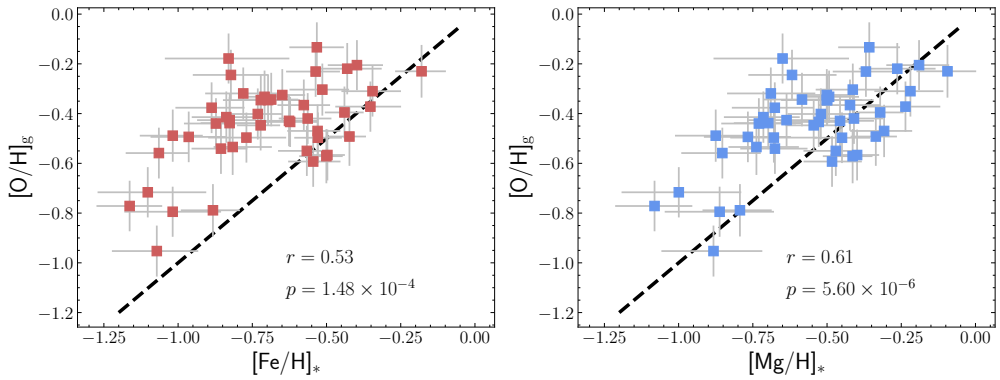

Figure 4.7: Comparison of $[\mathrm{O/H}]_\mathrm{g}$ with $[\mathrm{Fe/H}]_*$ (left) and $[\mathrm{Mg/H}]_*$ (right). The dashed-dotted lines indicate the one-to-one relation (i.e., $[\mathrm{O/H}]_\mathrm{g} = [\mathrm{X/H}]_*$). The weighted Pearson coefficients r and the p-values of the null hypothesis are shown in each panel.

Figure 4.7 shows the comparison between the gas-phase oxygen abundance $[\mathrm{O/H}]_\mathrm{g}$ and the stellar iron abundance $[\mathrm{Fe/H}]_*$ of our sample. We derive a inverse-variance weighted Pearson coefficient $r = 0.53$ and the corresponding p-value $p = 1.48 \times 10^{-4}$, indicating that the $[\mathrm{O/H}]_\mathrm{g}$ and the $[\mathrm{Fe/H}]_*$ are correlated at the $\sim 3.8\sigma$ level. Four galaxies exhibit lower $[\mathrm{O/H}]_\mathrm{g}$ than $[\mathrm{Fe/H}]_*$, but at $< 2\sigma$ significance. The remaining galaxies in our sample exhibit higher $[\mathrm{O/H}]_\mathrm{g}$ than $[\mathrm{Fe/H}]_*$. On average, $[\mathrm{O/H}]_\mathrm{g}$ is higher than $[\mathrm{Fe/H}]_*$ by 0.25 dex, in agreement with the results of Fraser-McKelvie et al. (2022) for a sample of more massive star-forming galaxies at $M* > 10^9 M_\odot$ observed by the SAMI Galaxy Survey. The discrepancy is not surprising, given that the two elemental abundances trace the chemical enrichment of different stellar populations. The $[\mathrm{Fe/H}]_*$ presented here is measured from the rest-frame optical stellar continuum, so the measured $[\mathrm{Fe/H}]_*$ indicates the chemical enrichment for older stellar populations. On the contrary, the $[\mathrm{O/H}]_\mathrm{g}$ is a proxy for the chemical enrichment in regions where the youngest OB stars have just formed out of the ISM. In addition, the different formation timescales of oxygen and iron can also contribute to the abundance offset. Iron is primarily formed by Type Ia SNe that explode $\gtrsim 300 - 400$ Myr after the initial starburst, while oxygen, an α

element, is produced by core-collapse SNe of massive stars a $\sim$ 10 Myr timescale. As a result, the chemical enrichment of iron is expected to lag behind that of oxygen, especially for galaxies that have formed the majority of their stars in the past Gyr before the Type Ia SNe began exploding, although the difference would be attenuated if galaxies have smoother and more sustained SFHs. The combined effects of the distinct stellar populations probed by oxygen and iron and the disparate formation timescales can naturally explain the lower $[\mathrm{Fe/H}]_*$ in Figure 4.7.

As mentioned above, it is complicated to interpret the relation between $[\mathrm{Fe/H}]_*$ and $[\mathrm{O/H}]_\mathrm{g}$ because Fe is delayed relative to O. On the other hand, comparing the abundance of gas-phase oxygen and stellar magnesium is a more direct comparison between the metals in the gas and stars because magnesium is another α element produced by the same mechanism as oxygen. $[\mathrm{Mg/H}]_*$ traces the SFH-averaged stellar abundance and can be interpreted as an approximation of the gas-phase abundance averaged over the SFH of the galaxies.

In the right panel of Figure 4.7, we compare $[\mathrm{O/H}]_\mathrm{g}$ and $[\mathrm{Mg/H}]_*$, which is the sum of the $[\mathrm{Fe/H}]_*$ and $[\mathrm{Mg/Fe}]_*$ derived in Section 4.4.2. $[\mathrm{Mg/H}]_*$ is still lower than $[\mathrm{O/H}]_\mathrm{g}$, but as expected, the differences between $[\mathrm{O/H}]_\mathrm{g}$ and $[\mathrm{Mg/H}]_*$ (0.11 dex) are significantly smaller compared to $[\mathrm{Fe/H}]_*$ (0.25 dex). The Pearson coefficient of the $[\mathrm{O/H}]_\mathrm{g}$–$[\mathrm{Mg/H}]_*$ relation ($r = 0.61$) is higher than that of the $[\mathrm{O/H}]_\mathrm{g}$–$[\mathrm{Fe/H}]_*$ with a p-value lower by two orders of magnitude, suggesting that $[\mathrm{O/H}]_\mathrm{g}$ is more linearly correlated with $[\mathrm{Mg/H}]_*$. Among 46 star-forming galaxies in our sample, 23 of them have consistent $[\mathrm{O/H}]_\mathrm{g}$ and $[\mathrm{Mg/H}]_*$ within 1σ, whereas 19 galaxies have slightly higher $[\mathrm{O/H}]_\mathrm{g}$ than $[\mathrm{Mg/H}]_*$ at the $1-3\sigma$ level. We note that we measure $[\mathrm{O/H}]_\mathrm{g}$ using strong-line calibrations based on the T_e metallicity scale, which is likely to underestimate the actual $(\mathrm{O/H})_\mathrm{gas}$ due to temperature fluctuations in the H II regions (García-Rojas and Esteban, 2007). If we convert the T_e-based measurements to the abundance scale based on recombination lines and photoionization models by adding 0.24 dex to the measured $[\mathrm{O/H}]_\mathrm{g}$ (Esteban et al., 2014; Blanc et al., 2015; Steidel et al., 2016), all star-forming galaxies would have higher $[\mathrm{O/H}]_\mathrm{g}$ than $[\mathrm{Mg/H}]_*$. Most of (or all) galaxies in our sample therefore have higher $[\mathrm{O/H}]_\mathrm{g}$ because the youngest populations are more chemically enriched. Nevertheless, the reduced lag between $[\mathrm{O/H}]_\mathrm{g}$ and $[\mathrm{Mg/H}]_*$ arises from the fact that the two elements are produced by the same process, rendering them less sensitive to the shapes of the SFHs.

Even though we have demonstrated that stellar magnesium indeed tracks gas-phase oxygen more closely than stellar iron does, we emphasize that the $[\mathrm{Mg/H}]_*$ and the

$[O/H]_g$ are not fully consistent for all galaxies in our sample as discussed above. One would always expect that $[O/H]_g$ is higher than $[Mg/H]_*$ unless star formation is occurring in metal-poor gas from external accretion. Therefore, one should be cautious when using $[O_g/Fe_*]$ as a substitute for $[\alpha/Fe]_*$ in star-forming galaxies if $[Fe/H]_*$ is determined from the rest-frame optical spectrum[7]. In this case, using the difference of $[O/H]_g$ and $[Fe/H]_*$ as a proxy for $[\alpha/Fe]_*$ may overestimate $[Mg/Fe]_*$.

4.5.2 The gas-to-stellar abundance ratio as a function of galaxy properties

Aiming to understand the connection between metals in different phases, we explore how the gas-to-stellar abundance ratios (more accurately, their logarithmic difference), $\Delta Z_{O,Fe}$ and $\Delta Z_{O,Mg}$ depend on different galaxy properties in Figures 4.8 and 4.9, respectively. We define two gas-to-stellar abundance ratios as:

$$\Delta Z_{O,Fe} = [O/H]_{gas} - [Fe/H]_* \tag{4.10a}$$

$$\Delta Z_{O,Mg} = [O/H]_{gas} - [Mg/H]_*. \tag{4.10b}$$

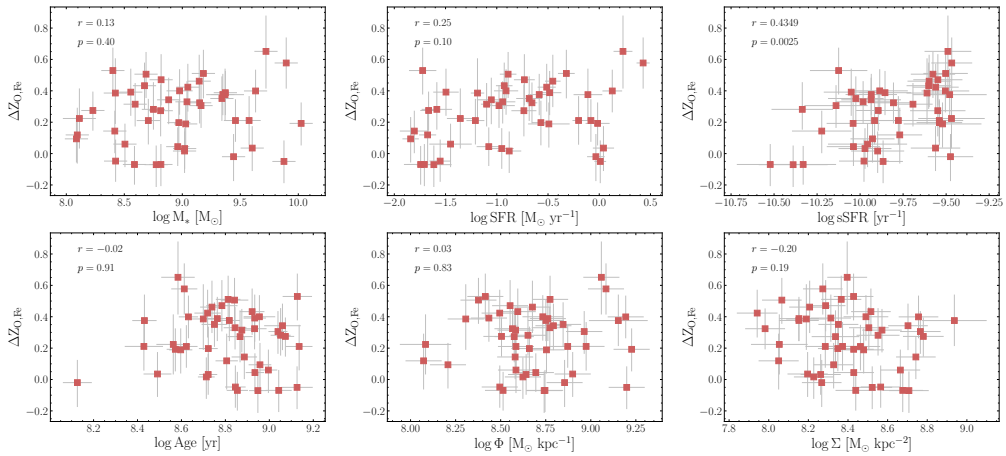

Figure 4.8: The differences between $[O/H]_g$ and $[Fe/H]_*$ ($\Delta Z_{O,Fe}$) as a function of different galaxy properties, including stellar mass (top left), SFR (top middle), sSFR (top right), light-weighted stellar population age (bottom left), $\log \Phi$ (bottom middle) and $\log \Sigma$ (bottom right). The weighted Pearson coefficients (r) and the p-values are shown in each panel.

We explore the dependence of these quantities on six galaxy properties: (1) stellar mass, (2) SFR, (3) sSFR, (4) light-weighted age derived from the full-spectrum fitting, (5) $\log \Phi = \log (M_*/R_e)$, a proxy for the gravitational potential well, and (6)

[7] $[Fe/H]_*$ determined from the FUV stellar continuum is sensitive mostly to young OB stars. [O/Fe] is commonly used in high-z galaxies when their rest-FUV stellar continuum can be easily obtained from ground- or space-based telescopes.

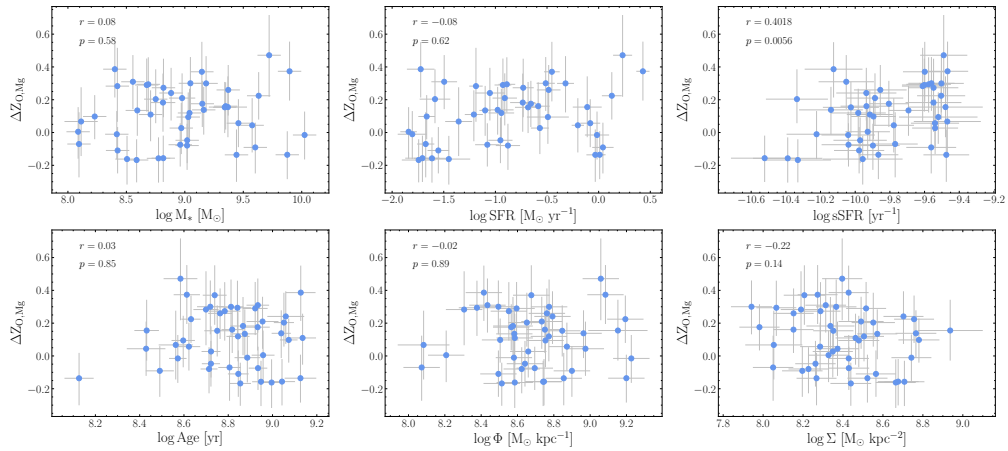

Figure 4.9: Similar to Figure 4.8, but for the differences between $[O/H]_g$ and $[Mg/H]_*$ ($\Delta Z_{O,Mg}$).

$\log \Sigma = \log (M_*/R_e^2)$, a proxy for stellar mass surface density. The properties are chosen because they are known to be correlated/anti-correlated either with stellar/gas abundances (e.g., Tremonti et al., 2004; Gallazzi et al., 2005; Mannucci et al., 2010), or with the gas-to-stellar abundance ratios for more massive star-forming galaxies (e.g., Fraser-McKelvie et al., 2022). To quantify whether these galaxy properties are correlated with $\Delta Z_{O,Fe}$ and $\Delta Z_{O,Mg}$, we calculate inverse variance-weighted Pearson coefficients (r) and corresponding p-values for each relation.

Among all the relations investigated, we find that $\Delta Z_{O,Fe}$ and $\Delta Z_{O,Mg}$ are significantly correlated (i.e., p-value < 0.05) only with sSFR. A similar trend was also found by Fraser-McKelvie et al. (2022), who compared the stellar and gas-phase metallicity of the star-forming galaxies at $\log (M_*/M_\odot) \gtrsim 10^{8.5}$ in the SAMI sample. Because Fraser-McKelvie et al. (2022) did not measure $[Mg/H]_*$, they converted the measured gas-phase metallicity in the oxygen-based scale into the iron-based scale using the empirical abundances in the Milky Way, Large Magellanic Cloud (LMC), and Small Magellanic Cloud (SMC) by Nicholls et al. (2017). This conversion was intended to account for the difference in the recycling time of oxygen and iron. In contrast, our analysis allows for an apples-to-apples comparison of stellar and gas-phase abundances of α elements, without relying on abundance patterns based on specific galaxies.

One might expect that $\Delta Z_{O,Fe}$ and $\Delta Z_{O,Mg}$ would be correlated with sSFR. $\Delta Z_{O,Fe}$ and $\Delta Z_{O,Mg}$ reflect the differences in the level of chemical enrichment between that of the current ISM and that obtained when the bulk of the stars that dominate the current optical spectrum were forming, i.e., in the past, weighted roughly by light.

The measured stellar abundances are therefore a proxy for the ISM abundances around 600 – 700 Myr (the typical light-weighted age in this sample) ago. A galaxy with higher sSFR would have experienced a larger increase in ISM abundance over the same interval of time, leading to a larger value of $\Delta Z_{\rm O,Fe}$ and $\Delta Z_{\rm O,Mg}$. While the correlation between $\Delta Z_{\rm O,Fe}$ and sSFR ($r = 0.43$) is slightly stronger than that between $\Delta Z_{\rm O,Mg}$ and sSFR ($r = 0.40$), the differences are not significant.

Perhaps surprisingly, $\Delta Z_{\rm O,Fe}$ and $\Delta Z_{\rm O,Mg}$ lack a strong dependence on SFR (see Figures 4.8 and 4.9). It is well known that at a given stellar mass, galaxies with higher SFRs tend to have more metal-poor ISM (Mannucci et al., 2010) because their high gas fractions dilute the current gas-phase metallicity. However, $[\rm Fe/H]_*$ and $[\rm Mg/H]_*$, the amount of metals locked in the stars averaged over the entire SFH, are expected to be much less influenced by the current SFR because they have only a weak dependence on the current star formation. If there is a universal "fundamental" MZR of galaxies, where the normalization of the gas MZR decreases as SFR goes up, $\Delta Z_{\rm O,Fe}$ and $\Delta Z_{\rm O,Mg}$ should be correlated with SFR. The absence of dependence on SFR here implies that the stellar MZR is not universal for galaxies at different SFRs, as we will further discuss in Section 4.5.3.

We do not detect significant correlations of $\Delta Z_{\rm O,Fe}$ or $\Delta Z_{\rm O,Mg}$ with stellar mass, $\log \Phi$, or $\log \Sigma$, while Fraser-McKelvie et al. (2022) found that the gas-to-stellar abundance ratio is anti-correlated with mass and $\log \Phi$ and uncorrelated with $\log \Sigma$ after correcting the abundance scale offsets between iron and oxygen. The discrepancy may be attributed to the different mass range in the current sample as compared to that of Fraser-McKelvie et al. (2022) – the two anti-correlations found by Fraser-McKelvie et al. (2022) are driven primarily by galaxies with $\log M_*/M_\odot \gtrsim 10^{9.5}$ and $\log \Phi \gtrsim 9.25$ (their Figure 10), whereas our sample consists of much less massive galaxies. It could be that the trends with mass and $\log \Phi$ have not yet been established in dwarf galaxies.

Finally, we find that both $\Delta Z_{\rm O,Fe}$ and $\Delta Z_{\rm O,Mg}$ are uncorrelated with the light-weighted age. We suspect that this is because the star-forming galaxies in our sample are extremely young with light-weighted ages < 1 Gyr. It could be that the trends with age have not yet been established.

4.5.3 The Mass–Metallicity Relation

The left column of Figure 4.10 shows the gas-phase O-MZ$_{\rm g}$R, stellar Fe-MZ$_*$R, and stellar Mg-MZ$_*$R along with the mass–$[\rm Mg/Fe]_*$ relation color-coded by their

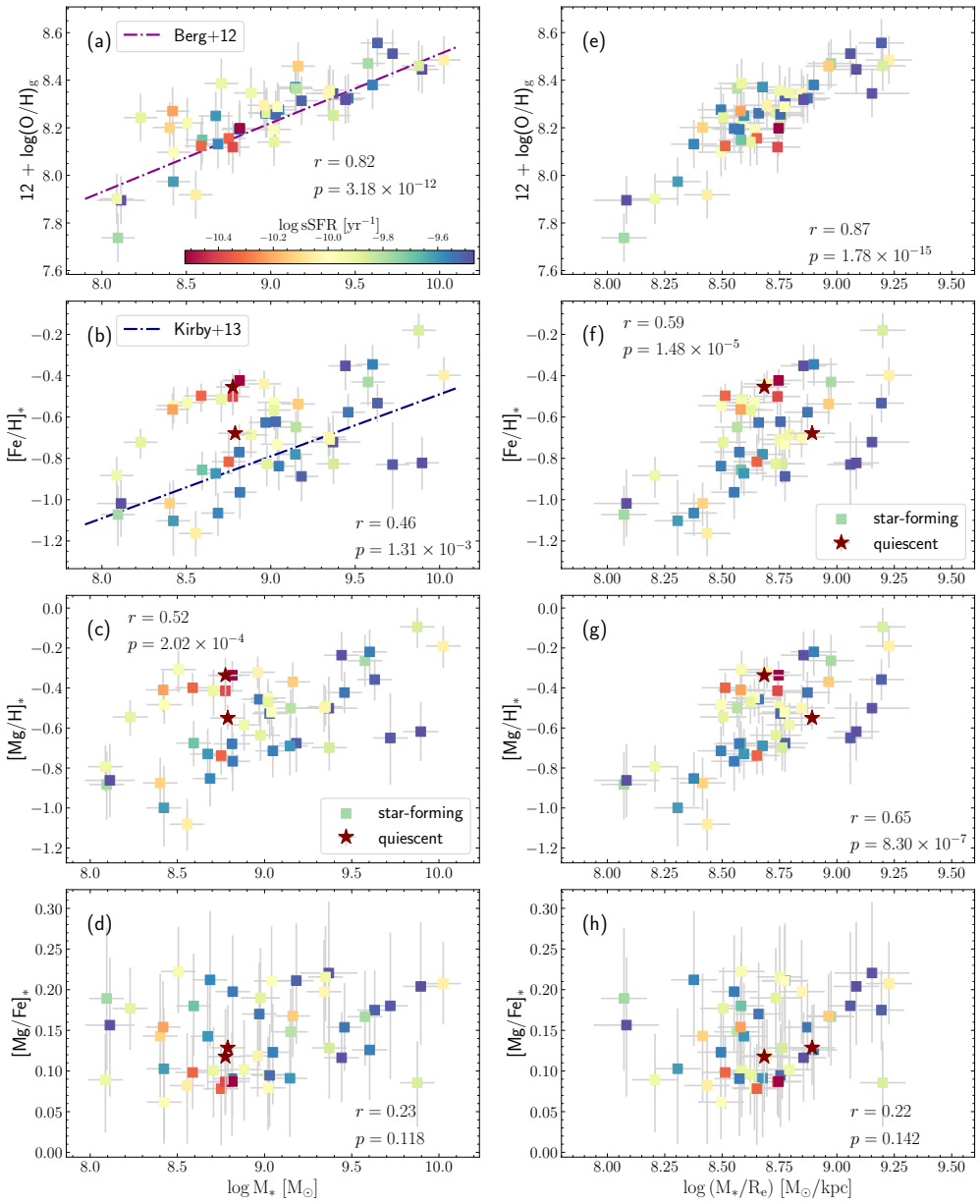

Figure 4.10: MZRs of the KCWI sample. *Left*: The O-MZ$_g$R (a), Fe-MZ$_*$R (b), Mg-MZ$_*$R (c), and the mass-[Mg/Fe]$_*$ relation (d) of the KCWI sample. In panel (a), the magenta dashed-dotted line shows the O-MZ$_g$R of local dwarf galaxies derived from the direct method (Berg et al., 2012). In panel (b), the blue dashed-dotted line shows the Fe-MZ$_*$R of Local Group satellites obtained from resolved stellar spectroscopy (Kirby et al., 2013). *Right*: The gas-phase (O/H)$_g$ (e), stellar [Fe/H]$_*$ (f), stellar [Mg/H]$_*$ (g), and [Mg/Fe]$_*$ (h) as a function of $\log \Phi = \log (M_*/R_e)$ of the KCWI sample. In each panel, the star-forming galaxies (squares) are color-coded by their sSFRs. The two quiescent galaxies are shown by the dark red stars. The weighted Pearson coefficients r and the p-values of the null hypothesis are listed in each panel.

sSFRs in panels (a) - (d), respectively. For each relation, we calculated the weighted Pearson coefficient and the p-value of the null hypothesis to quantify their linearity. Nevertheless, there is no theoretical reason to expect the MZRs should be linear across this mass range (e.g., Ma et al., 2016), as simple linear relation do not capture the flatness of the MZ_*R as we later discuss in Section 4.6.1. We pick the Pearson coefficient only for its simplicity to describe this small data set. Overall, we recover significant correlations between stellar mass and abundances of three elements with $p < 0.05$, but do not detect significant correlation between stellar mass and $[Mg/Fe]_*$. Among the three MZRs, we find that the O-MZ_gR is the most linear relation with $R = 0.82$. The Mg-MZ_*R ($R = 0.52$) is more linear than Fe-MZ_*R ($R = 0.46$). In panel (d), the dwarf quiescent galaxies as well as the star-forming galaxies with the lowest sSFRs in our sample have lower $[Mg/Fe]_*$ than the rest of our sample. The low $[Mg/Fe]_*$ in these galaxies that are already or almost quenched indicate that their past star formation may have lasted for a protracted period of time, as the star formation there would have to occur in gas whose ISM is already enriched in iron by Type Ia SNe. The $[Mg/Fe]_*$ of the star-forming galaxies with higher sSFRs show large variations in our sample. There is no reason to expect their $[Mg/Fe]_*$ to be related to stellar mass because these galaxies are still actively forming stars with evolving $[Mg/Fe]_*$.

We also compare our O-MZ_gR and Fe-MZ_*R with the literature on the local dwarf galaxies in Figure 4.10. The O-MZ_gR of the star-forming galaxies in our KCWI sample in panel (a) exhibits a relatively tight linear relation and is consistent with the O-MZ_gR derived from the direct T_e method by Berg et al. (2012) for local dwarf galaxies at $M_* \sim 10^{6-9.7} M_\odot$. Our Fe-$MZ_*R$ in panel (b), instead, does not completely fall on the extrapolation of the low-mass Fe-MZ_*R of the Local Group satellites at $M_* \lesssim 8.5 M_\odot$ (Kirby et al., 2013). Most of the star-forming galaxies with high sSFRs fall on the extrapolation of the low-mass MZ_*R of Local Group dwarf satellite galaxies measured by Kirby et al. (2013), while most of the star-forming galaxies with higher $[Fe/H]_*$ at fixed mass that lie above the extrapolation of the low-mass MZ_*R have lower sSFRs. The shape of the Mg-MZ_*R in panel (c) is very similar to the Fe-MZ_*R. The disagreement between our Fe-MZ_*R and the relation of Kirby et al. (2013) is not surprising because many physical processes such as outflows are changing rapidly with galaxy mass. Furthermore, theoretical predictions do not necessarily predict linear MZRs (e.g., Ma et al., 2016). For instance, Davé, Finlator, and Oppenheimer (2012) suggested that the slope of the MZR strongly depends on the primary feedback processes regulating galaxy growth

and driving outflows. They found that the slope of the simulated MZR can be changed easily by altering the mass dependence of the mass-loading factor of the outflows alone. Because star-forming galaxies at $10^8 M_\odot \lesssim M* \lesssim 10^{10} M_\odot$ are likely to different feedback processes than that of the Local Group satellites, we do not expect Fe-MZ$_*$Rs in this mass range to be consistent with the relation by Kirby et al. (2013).

It has been controversial whether star-forming and quiescent galaxies should exhibit distinct MZ$_*$Rs. For the dwarf satellite galaxies ($\log(M_*/M_\odot) \lesssim 8.5$) in the Local Group, Kirby et al. (2013) found that star-forming and quiescent dwarf galaxies in the Local Group fall on a universal MZ$_*$R and have similar [Fe/H]$_*$ at a given mass. However, large spectroscopic surveys such as SDSS, MaNGA and SAMI of massive field galaxies ($\log(M_*/M_\odot) \gtrsim 9$) suggest that star-forming galaxies generally have more metal-poor stars than quiescent galaxies at the same masses (e.g., Gallazzi et al., 2021; Neumann et al., 2021; Vaughan et al., 2022). When we look at the two quiescent galaxies in our sample on the Fe-MZ$_*$Rs, we find that only one of them, the more metal-poor 0241-0810 has similar [Mg/H]$_*$ and [Fe/H]$_*$ as those of heavily star-forming galaxies at the same mass. The other quiescent galaxy 0125-0024 that is more metal-rich, instead, has comparable [Fe/H]$_*$ and [Mg/H]$_*$ to the KCWI star-forming galaxies with suppressed sSFRs (the yellow to orange squares in Figure 4.10). To confirm that the two quiescent galaxies indeed possess different metal content, we also measured their [Fe/H]$_*$ and [Mg/H]$_*$ using `alf` by Conroy et al. (2018), and we recovered the same results to within 1σ.

The distinct [Fe/H]$_*$ and [Mg/H]$_*$ of the two quiescent galaxies may be explained by their different environments. 0241-0810 is located in the vicinity of the massive elliptical galaxy NGC 1052, and it has similar radial velocity to that of NGC 1052 (Román, Castilla, and Pascual-Granado, 2021). The projected distance between 0241-0810 and NGC 1052 is around $\sim$ 50-60 kpc, while the projected virial radius of NGC 1052 is 390 kpc (Forbes et al., 2019), suggesting that 0241-0810 is likely to be a satellite of NGC 1052. The overdense environment where 0241-0810 resides might explain why it is consistent with the low-mass MZ$_*$R of the Local Group dwarfs. In particular, galaxies in dense environments can be rapidly quenched by external effects, like ram pressure stripping. Therefore, a galaxy that would have naturally evolved to a higher normalization on the MZ$_*$R may have been prevented from doing so due to a sudden cessation of star formation. On the other hand, 0125-0024 is an isolated dwarf galaxy identified by Kado-Fong et al. (2020) with

no massive galaxies nearby. This galaxy does not fall on the Fe-MZ$_*$R of the Local Group dwarfs, possibly because it evolved naturally without external causes for gas removal.

Surprisingly, compared to the O-MZ$_g$R in panel (a), the Fe- and Mg-MZ$_*$Rs in panels (b) and (c) show much larger scatters in Figure 4.10. The scatter in both MZ$_*$Rs appears to be driven by different sSFRs (indicated with a color bar in Figure 4.10). Because the stellar abundances represent the metals averaged over a much longer timescale than the instantaneous metal content in the current ISM, [Fe/H]$_*$ and [Mg/H]$_*$ are expected to be less “stochastic" and have less reason to depend on SFR/sSFR. Instead, we see the opposite behavior here.

It has been suggested that the scatter of the MZ$_g$R could be underestimated from the strong line estimators (see discussions in Section 7.3 of Andrews and Martini (2013) and Section 7.2 in Section of Steidel et al. (2014)). In brief, the empirical strong line calibrations used to infer Z_g are not perfect correlations between T_e-based measurements and strong line ratios, and thus have their own calibration errors (e.g., 0.1 dex for the R calibration used in this work). For example, if we accounted for the $\sim$ 0.1 dex scatter of the "R" index-based metallicities against direct T_e measurements as a source of systematic uncertainty in our measures of oxygen abundances, the implied *intrinsic* scatter in the MZgR becomes uncomfortably small. Additionally, as shown in Steidel et al. (2014), the relative intensities of the strong emission lines used in these empirical calibrations are sensitive to the changes not only in (O/H)$_g$ but also the excitation parameter and the hardness of the stellar radiation field. These parameters are also strongly correlated with stellar mass and sSFR, and thus yield a tighter relation than the *actual* MZ$_g$R. Besides, the empirical relations are calibrated to the T_e-based abundance measurements of local H II regions that only span a limited parameter space in physical properties such as excitation parameter while distant galaxies have much more diverse physical conditions, so the Z_g obtained with the strong line methods may not capture the change in physical properties related to SFR as well as the direct method.

Although the scatter of the MZ$_g$R of local dwarf galaxies measured from the direct T_e method (0.15 dex, Berg et al., 2012) is comparable to the scatter of our O-MZ$_g$R in Figure 4.10, we believe it is not a fair comparison. There are only 11 galaxies in the sample of Berg et al. (2012) in the similar mass range of our KCWI sample, which span a narrower range of sSFR (based on the measurements of the same sample by Dale et al., 2023) than our sample. We might expect the scatter of the MZ$_g$R

inferred from the direct T_e method to be larger for a larger sample of star-forming galaxies with more diverse sSFRs. Indeed, the MZ_gR of the SDSS stacked spectra[8] measured by Andrews and Martini (2013) using the direct T_e method has much greater scatter. At $M_* \sim 10^{8.5} M_\odot$, $[O/H]_g$ can differ by up to ~ 0.6 dex between the most star-forming and quiescent galaxies. We therefore conclude that the scatter of our O-MZ_gR is likely to be underestimated due to the strong line method used in this work.

The scatter in the MZ_*R driven by sSFR/SFR has seldom been discussed in the literature. As shown in panels (b) and (c) of Figure 4.10, the Mg-MZ_*R appears to be more linear than the Fe-MZ_*R, as the Mg-MZ_*R has a larger Pearson coefficient. This implies that the large scatter of the Fe-MZ_*R can partially attributed to the varying delay time of Type Ia SNe in galaxies. It is unclear whether the O-MZ_gR is indeed tighter than the Mg-MZ_*R, or whether the difference in scatter is driven by the aforementioned systematics due to the strong line method. The stellar measurements of star-forming galaxies could also suffer from systematics due to the limitations of the current SPS models and the age–metallicity degeneracy, as we further discuss in Section 4.6.4. However, we still believe that the large scatter in the Fe- and Mg-MZ_*Rs as well as our stellar abundance measurements of the star-forming galaxies should be robust, because we see that the two quiescent galaxies (marked by stars in Figure 4.10) — which are expected to suffer much less from the age-metallicity degeneracy — have distinct $[Fe/H]_*$ and $[Mg/H]_*$ despite having similar stellar masses.

We therefore conclude that the MZ_*Rs of Fe and Mg in the mass range between the Local Group satellites and more massive field galaxies exhibit large scatter driven by their varying sSFRs and the host environments. They should not be described by a single relation, especially not a single power law, as we further discuss in Section 4.6.1. We also emphasize that our results do not directly imply the stellar MZRs are bimodal with a metallicity gap at $\log(M_*/M_\odot) \sim 8.5$. The gap is more likely to originate from the selection bias in the sample, as we see a similar gap in the $\log M_*$–$\log$ SFR plane in Figure 4.1.

[8]The metallicity obtained from the stacked spectra may suffer from the contamination in diffuse ionized gas ionized by the evolved, hot stars and thus also has its own systematics as we further discuss in Appendix 4.8.3

4.5.4 Abundances and Abundance Ratio as a function of Gravitational Potential

Recently, Vaughan et al. (2022) investigated the relation between stellar metallicity and $\log \Phi = \log (M_*/R_e)$ for low-redshift galaxies from Data Release 3 of the SAMI galaxy survey (Croom et al., 2021), and found that star-forming and quiescent galaxies form a single sequence on the Φ–Z plane, with an offset of $\Delta[\mathrm{Z/H}] \approx 0.1$ dex. They argued that the Φ–Z relation is more fundamental than the MZR, which they explained as a result of galaxies with deeper gravitational potentials (and thus larger Φ) retaining more metals from galactic outflows.

To investigate, we constructed the Φ–Z relation of $(\mathrm{O/H})_\mathrm{g}$, $[\mathrm{Fe/H}]_*$, and $[\mathrm{Mg/H}]_*$, as well as the Φ–$[\mathrm{Mg/Fe}]_*$ relation for our sample in the right column of Figure 4.10. For each relation, we listed their weighted Pearson coefficient and the p-value of the null hypothesis to in each panel of Figure 4.10.

Still, the scatter of the Φ–Z relation for $(\mathrm{O/H})_\mathrm{g}$ (panel (e) in Figure 4.10) is significantly smaller than that of the relations for $[\mathrm{Fe/H}]_*$ (panel (f)) and $[\mathrm{Mg/H}]_*$ (panel (g)). As discussed above, it is possible that the scatter in the Φ–Z_g relation is underestimated due to the strong line method used here.

By moving from the mass–metallicity plane to the Φ–metallicity plane, we see that the relations for $(\mathrm{O/H})_\mathrm{g}$, $[\mathrm{Fe/H}]_*$ and $[\mathrm{Mg/H}]_*$ all become tighter and more linearly-correlated, as the Pearson coefficients (and the p-value) are significantly higher (smaller) in the Φ–Z relations. In particular, the differences in stellar abundances between galaxies with different sSFRs become smaller.

However, the dependence on sSFR is not completely eliminated when we switch to the Φ–Z relations (panels (e)-(g) in Figure 4.10). At a given Φ, most star-forming galaxies with lower sSFRs still have higher $[\mathrm{Fe/H}]_*$ and $[\mathrm{Mg/H}]_*$. The scatters in the stellar Φ–Z_* relation measured from iron and magnesium are ~ 0.5 dex and 0.4 dex, respectively, which are much larger than the ≈ 0.1 dex offset between quiescent and star-forming galaxies suggested by Vaughan et al. (2022) for the SAMI sample. The disagreement between our results and those of Vaughan et al. (2022) may be explained by the different SFHs of galaxies at different masses. Dwarf galaxies are known to have more bursty SFHs than massive galaxies (Emami et al., 2019). The diverse SFHs of the low-mass galaxies, coupled with the delayed timescale of Type Ia SNe, can result in a wide range of stellar abundances at a given mass or Φ compared to more massive galaxies. The larger scatter we observe may originate from the dominance of dwarf galaxies in our sample. The majority of the SAMI sample of

Vaughan et al. (2022) instead contains more massive galaxies at $M_* > 10^{10} M_\odot$. In fact, the scatter in the low-mass bins ($M_* \lesssim 10^{9.5} M_\odot$) of the SAMI sample (Figure 3 of Vaughan et al. 2022) are also $> 0.3 - 0.5$ dex even though the mean offset is nearly zero.

Finally, when we plot $[\mathrm{Mg/Fe}]_*$ as a function of Φ, we find that the scatter remains similar to that of the mass–$[\mathrm{Mg/Fe}]_*$ relation. Star formation and SNe continue in the star-forming galaxies, so their $[\mathrm{Mg/Fe}]_*$ continues to evolve. Therefore, there is no reason to expect them to be correlated with any general properties of galaxies, as we saw in the trends for massive quiescent galaxies (Choi et al., 2014; Leethochawalit et al., 2019; Zhuang et al., 2023).

We conclude that both the stellar and gas-phase elemental abundances of the rapidly evolving low-mass galaxies are jointly shaped by stellar mass, sSFR (or SFH), size, and the host environment, while the gas-to-stellar abundance ratios of low-mass star-forming galaxies are more related to their sSFR (or SFH).

4.6 Discussion

4.6.1 A Further Look at the Stellar MZR

To further investigate the shape of the $\mathrm{MZ_*R}$s across the full range of galaxy masses, we construct the MZRs of more massive galaxies drawn from SDSS. We focus the discussion on the shape of the $\mathrm{MZ_*R}$s only, rather than the $\mathrm{MZ_gR}$ for the KCWI+SDSS sample because the strong line *R* calibration employed in determining the oxygen abundance in the KCWI sample is more suitable for metal-poor, low-mass galaxies but inappropriate for more massive galaxies, as detailed in Appendix 4.8.3. Because different gas metallicity calibrations are known to have significant systematics and thus affect the shape of the $\mathrm{MZ_gR}$, we decided not to construct the $\mathrm{MZ_gR}$ beyond the KCWI sample in this paper.

As pointed out in our previous work (see Figure 7 in Zhuang et al. 2021), the linear extrapolation of the $\mathrm{MZ_*R}$ of the Local Group satellite galaxies ($M_* \lesssim 10^8 M_\odot$, Kirby et al., 2013) appears to disagree with measurements of more massive, quiescent galaxies in the field ($M_* \gtrsim 10^{9.5} M_\odot$, Leethochawalit et al., 2019). At $M_* \sim 10^9 M_\odot$, they predicted different $[\mathrm{Fe/H}]_*$ by up to ~ 0.6 dex. By comparing the stellar metallicity of NGC 147, a dwarf elliptical satellite of Andromeda, derived from resolved stellar spectroscopy and integrated-light spectroscopy, we ruled out the possibility that the apparent discrepancy originates from systematic differences in the methods used for stellar metallicity estimates. Instead, the consistent results

from the two approaches present the first evidence that it is reasonable to put the MZ$_*$Rs measured from different approaches on the same scale.

To give an unbiased comparison of the Fe-MZ$_*$R of the Local Group dwarfs, the KCWI sample, and the SDSS galaxies, we re-measured the stellar abundances of the SDSS quiescent galaxy sample compiled by Leethochawalit et al. (2019) using the two-step method proposed in Section 4.4.2. We also selected a subsample of 124 star-forming galaxies from Gallazzi et al. (2005) using criteria similar to those of Leethochawalit et al. (2019). The selection criteria, the stellar mass estimates, and the abundance measurements are detailed in Appendix 4.8.3.

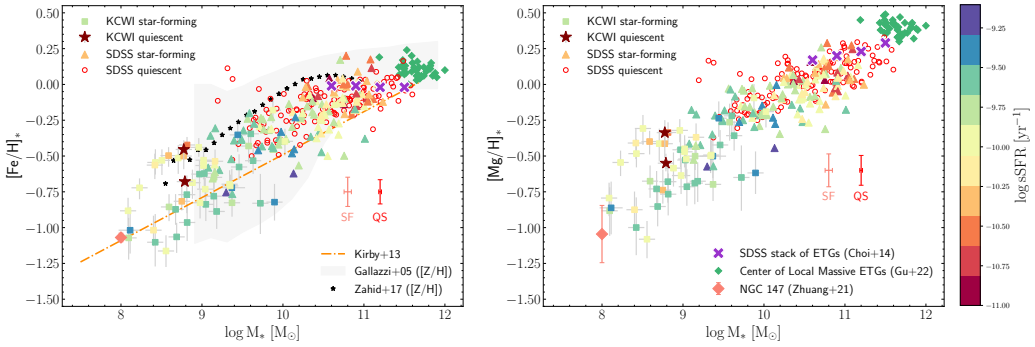

Figure 4.11: The MZ$_*$Rs of iron (left) and magnesium (right) for the KCWI sample (squares for the star-forming galaxies, and dark red stars for the quiescent galaxies) and the SDSS sample (triangles for the star-forming galaxies, red open circles for the quiescent galaxies). The typical measurement errors of the SDSS star-forming (SF) and quiescent (QS) galaxies are shown in each panel. The star-forming galaxies are color-coded by their SFRs. The local MZ$_*$Rs measured in other works (Gallazzi et al., 2005; Kirby et al., 2013; Choi et al., 2014; Zahid et al., 2017) and the stellar abundance measurements of individual galaxies in the local universe (Zhuang et al., 2021; Gu et al., 2022) are shown. A detailed review of all references in the plot is in Section 4.6.1.

The left panel of Figure 4.11 shows the Fe-MZ$_*$Rs of the KCWI and the SDSS samples along with the extrapolation of that of the Local Group dwarfs (Kirby et al., 2013), as well as some measurements from the literature. First, our updated high-mass Fe-MZ$_*$R of the SDSS quiescent galaxies (red circles) is still inconsistent with the extrapolation of low-mass Fe-MZ$_*$R of the Local Group dwarfs (red dashed line). They disagree by $\gtrsim 0.5$ dex in [Fe/H]$_*$ at $\log(M_*/M_\odot) \sim 9$, similar to the results in our previous work (Zhuang et al., 2021), which indicates that the Fe-MZ$_*$R cannot be described a single power law across the full range of mass. Second, the Fe-MZ$_*$R of the SDSS quiescent sample (red circles) agrees with the `alf` measurements of the [Fe/H]$_*$ of the stacked spectra of early-type galaxies (ETGs) by Choi et al. (2014)

(purple crosses) and those of the center of local ETGs in the MASSIVE survey (Gu et al., 2022) (green diamonds).

The left panel of Figure 4.11 also compares our results with other existing high-mass MZ_*Rs measuring the total stellar metallicity $[Z/H]_*$ instead of distinguishing between $[Fe/H]_*$ and $[Mg/H]_*$. We interpret the measured $[Z/H]_*$ in Gallazzi et al. (2005) (gray band) and Zahid et al. (2017) (black stars) as $[Fe/H]_*$ for the following reason. Gallazzi et al. (2005) used the spectrophotometric indices defined in the SPS models of Bruzual and Charlot (2003) to measure $[Z/H]_*$. These indices in Bruzual and Charlot (2003) were chosen to be the ones that are not sensitive to the change in $[\alpha/Fe]_*$ and capable of recovering solar-scaled metallicity (i.e., $[Fe/H]_*=[Z/H]_*$). Zahid et al. (2017) determined $[Z/H]_*$ using full-spectrum fitting technique with the FSPS models derived from the solar-scaled MIST isochrones (Choi et al., 2016) and the MILES stellar spectral libraries (Sánchez-Blázquez et al., 2006), similar to the FSPS-MILES SSPs models presented in Section 4.4.1. The metallicities of MILES stellar library were also measured in terms of $[Fe/H]_*$. Therefore, the measured $[Z/H]_*$ by Zahid et al. (2017) should also best interpreted as $[Fe/H]_*$ instead of $[Mg/H]_*$. The MZ_*R of all SDSS galaxies in the MPA-JHU sample by Gallazzi et al. (2005), regardless of their quiescence or star-forming state, exhibits scatter larger than 1 dex at $\log(M_*/M_\odot) \sim 9$ and therefore is consistent with both the low-mass MZ_*R of Kirby et al. (2013) and our high-mass MZ_*R of the SDSS sample. The MZ_*R measured from stacked spectra of SDSS star-forming galaxies in different mass bins by Zahid et al. (2017) did not quantify the scatter of the MZ_*R of star-forming galaxies. Their relation has overall higher normalization than our high-mass MZ_*R of the SDSS star-forming and quiescent sample, which might result from the different wavelength ranges, SPS models, and algorithms used in the full-spectrum fitting.

The Fe-MZ_*Rs of the KCWI and the SDSS samples are derived using the same approach. They are free from the systematic effects of different fitting methods and thus yield the most straightforward and interpretable relation of $[Fe/H]_*$ of galaxies at different masses. First, the SDSS star-forming galaxies exhibit large scatter in their $[Fe/H]_*$ compared to their quiescent counterparts, with the most heavily star-forming examples lying well below the high-mass MZ_*R of the quiescent galaxies. The trend is similar in the KCWI sample. The dwarf galaxies at the low mass end of the KCWI sample ($\log(M_*/M_\odot) \sim 8$) have comparable $[Fe/H]_*$ as that of NGC 147 derived from `alf` (Zhuang et al., 2021). The combined results of the KCWI

and SDSS samples suggest that the Fe-MZ$_*$R at $M_* > 10^8 M_\odot$ is not linear. Our result reveals that the transition in the MZ$_*$R between the Local Group satellites and massive field galaxies in the SDSS is largely shaped by the change in star-formation activity indicated by sSFR and the environment.

We also compare the Mg-MZ$_*$R of the KCWI and SDSS samples in the right panel of Figure 4.11. Our updated Mg-MZ$_*$R of the SDSS quiescent galaxies is consistent with the results measured from the stacked spectra of the SDSS ETGs by Choi et al. (2014) but lower than the [Mg/H]$_*$ of the center of local ETGs in the MASSIVE survey (Gu et al., 2022). The behavior of the Mg-MZ$_*$R is similar to Fe-MZ$_*$R, although the scatter of the Mg-MZ$_*$R of the star-forming galaxies in the KCWI sample and the SDSS sample is slightly smaller. Still, we find that at $M_* \gtrsim 10^9 M_\odot$, more heavily star-forming galaxies have lower [Mg/H]$_*$ than the quiescent galaxies at similar masses. Although there is yet no measurement of the Mg-MZ$_*$R of the Local Group satellites, we show that the dwarf elliptical galaxy NGC 147 (Zhuang et al., 2021) and the quiescent satellite candidate 0241-0810 have [Mg/H]$_*$ comparable to those of the more heavily star-forming galaxies in the KCWI sample.

To conclude, Fe- and Mg-MZ$_*$Rs beyond the Local Group do not appear to be linear and cannot be described by a relatively tight linear relation. The stellar abundances of the star-forming galaxies beyond $\sim 10^8 M_\odot$ are much more diverse and exhibit larger scatter that probably depends on factors other than stellar mass.

4.6.2 The sSFR Dependence of Stellar Abundance

Upon a closer look at Figure 4.11, we can tentatively see the dependence on sSFR of the Fe- and Mg-MZ$_*$Rs of star-forming galaxies in both the dwarf galaxies ($M_* \lesssim 10^9 M_\odot$) in the KCWI sample and the massive galaxies ($M_* \gtrsim 10^{10} M_\odot$) in the SDSS sample, whereas such dependence on sSFR is less obvious for galaxies at $M_* \sim 10^{9-10} M_\odot$. A similar behavior is seen in the MZ$_g$R, where galaxies with higher SFRs at fixed mass are generally more metal-poor (e.g., Mannucci et al., 2010), likely due to the higher gas fraction diluting the gas metallicity in the ISM.

Recently, Looser et al. (2024) reported a smooth relation between stellar mass, SFR and the light-weighted stellar metallicity in their study of 7,323 MaNGA galaxies at $\log(M_*/M_\odot) > 9$ and referred to the relation as stellar fundamental metallicity relation, suggesting a potential correlation between stellar metallicity and SFR/sSFR. Looser et al. divided the MaNGA sample into six groups based on their offsets from the SFMS (somewhat similar to sSFR) and constructed the stellar

MZR within each group. They found that at $\log(M_*/M_\odot) \gtrsim 9.5$ the MZ_*R of the galaxies below the SFMS (i.e., more quiescent) have a higher normalization than that of the galaxies above the SFMS (i.e., more starbursty). They argued that the sSFR dependence of the MZ_*R suggests that the metal contents of galaxies are primarily governed by long-lasting inflow of metal-poor gas accretion from the IGM/CGM instead of short-lived "episodic" accretion that only affects the gas metallicity, consistent with the theoretical models of IGM/CGM accretion by (Forbes et al., 2014; Torrey et al., 2019).

Although our sample size is much smaller than that of Looser et al. (2024), we pushed the stellar mass limit down to $\log(M_*/M_\odot) \sim 8$, bridging the gap between the Local Group satellites (in which the stellar metallicity dependence on their sSFR is absent) and the massive galaxies (where the dependence on the sSFR has already been established). In addition, the Mg-MZ_*R of the sample presented in this work is a better analog of O-MZ_gR because the trend will be less disrupted by the delay time of Type Ia SNe.

Additionally, Garcia et al. (2024) observed similar strong dependence of the normalization of the MZ_*R on the sSFR from the hydrodynamic simulations Illustris, TNG, and EAGLE. This finding is similar to the observations in this work and that of Looser et al. (2024). Garcia et al. (2024) suggested that the similar sSFR dependence of the MZ_*R and MZ_gR can be attributed to the tight correlation between stellar and gas-phase metallicities in the simulation suites, and thus the MZ_*R inherits the shape of the MZ_gR. Nevertheless, they were also concerned that the sub-grid treatment of the ISM employed in these simulations can only produce smooth stellar feedback. Consequently, the SFR/sSFR dependence discovered in their work may break down if galaxies have very bursty SFHs which may significantly disrupt the processes that allows stellar metallicities to catch up to the gas-phase metallicities.

4.6.3 Implications for Galaxy Growth and Quenching

The interplay between stellar and gas-phase abundances we measure from the KCWI sample, as well as the stellar abundance dependence on mass, SFR, and environment, may provide us a hint as to the chemical enrichment history of galaxies as they grow and quench.

First, Figure 4.11 shows that dwarf quiescent galaxies in different environments can have distinct stellar abundances at similar masses. The dwarf satellite candidate 0241-0810 that is more metal-poor falls on the extrapolation of the low-mass MZ_*R

of the Local Group satellites, implying that galaxies in the group environment would still evolve along the low-mass MZ_*R established in the Local Group. It is possible that galaxy 0241-0810 was quenched through ram pressure stripping (first proposed by Gunn and Gott 1972) that efficiently removed all the cold gas and resulted in fast quenching, and thus may not have had enough time to leave the low-mass MZ_*R before becoming quiescent (e.g., Mayer et al., 2006). The isolated dwarf quiescent galaxy 0125-0041 that is more metal-rich instead was less impacted by environmental effects during its star formation. It might have quenched more slowly than 0241-0810, so that it would have had more time to form more metal-rich stars before the cessation of star formation.

The dwarf star-forming galaxies in our sample that are on their way to quiescence in Figure 4.11 could have experienced gas starvation (Peng, Maiolino, and Cochrane, 2015; Trussler et al., 2020). When the supply of metal-poor gas from the surrounding CGM/IGM lags behind the gas consumption of the star formation, star formation would continue in the progressively more metal-enriched ISM and form more metal-rich stars, which can explain why these dwarf star-forming galaxies with low sSFRs have significantly higher stellar abundances than those that are still actively forming stars at the similar masses. The starvation scenario is also supported by the higher $[O/H]_g$ compared to the $[Mg/H]_*$ in most galaxies in our KCWI sample (Figure 4.7). If the metal-poor gas inflows were dominant in driving star formation in these galaxies, one would expect $[O/H]_g$ lower than the $[Mg/H]_*$. Although gas metallicity calibrations are known to have many systematic effects (Kewley and Ellison, 2008) and the absolute oxygen abundance scale may be off, the R calibration (Pilyugin and Grebel, 2016) adopted in this work is calibrated to the T_e-based measurements, which are usually lower than the gas-phase metallicity measurements based on nebular recombination lines or photoionization models (Esteban et al., 2014; Blanc et al., 2015; Steidel et al., 2016; Strom et al., 2018). In other words, if we have underestimated the true $[O/H]_g$, it only strengthens our conclusion about starvation. In addition, the prominent differences of the stellar abundances between the galaxies with enhanced and suppressed SFRs at similar masses might suggest that most of the chemical enrichment (at least for the elements that substantially affect the light-weighted stellar abundance) occurs when galaxies are approaching quiescence. This finding is consistent with Leung et al. (2024), who found that the post-starburst galaxies in the MaNGA survey significantly increased their stellar metallicity during the recent starbursts.

Once galaxies grow above above $\sim 10^{10} M_{\odot}$, the MZ$_*$Rs of star-forming and quiescent galaxies both become flattened in Figure 4.11. Massive galaxies have deeper gravitational potential well that can retain an increasingly large fraction of their metals. Theoretically, it has been suggested that energy-driven winds that are more efficient in ejecting metals dominate in low-mass galaxies (e.g., Murray, Quataert, and Thompson, 2005), while momentum-driven winds that drive less intense outflows dominate in high-mass galaxies (e.g., Hopkins, Quataert, and Murray, 2012; Davé, Finlator, and Oppenheimer, 2012). Consequently, these massive galaxies retain more metals than low-mass galaxies. At this stage, massive galaxies tend to start being strongly affected by a combination of "starvation" and "cessation" of star formation due to the increasing prevalence of AGN feedback (e.g., Weinberger et al., 2018), and thus generate metals much less efficiently. Additionally, the ISM of the massive galaxies that have been significantly chemically enriched contains high level of metals deposited by stellar winds and SNe and are almost saturated, so they will not increase metallicity significantly even if star formation continues. All of these combined effects lead to the flattened slope we observe in Figure 4.11. The levels of scatter in the Fe- and Mg-MZ$_*$Rs of the SDSS star-forming galaxies are still much larger than those of the quiescent galaxies, given that the SDSS star-forming galaxies still have very diverse sSFRs and would contribute to the distinct stellar abundances at fixed masses as we discuss above.

4.6.4 Limitations and Caveats of This Study

We now discuss potential limitations and caveats of this study that may affect our results.

First, our sample is restricted to the star-forming galaxies with sSFRs in the range of 10^{-9}–10^{-11} yr^{-1}, so our conclusions must be limited to galaxies with sSFRs in that range. We excluded starburst galaxies due to the difficulty in determining their stellar abundances from the weak stellar absorption features in the rest-frame optical. Assuming that the dependence of stellar abundance on sSFR would exist in galaxies at all different sSFRs, it is possible that the dwarf starburst galaxies would lie even below the extrapolation of the low-mass MZ$_*$R of the Local Group satellites, resulting in even larger scatter in the Fe- and Mg-MZ$_*$Rs than the ones in Figure 4.10. As shown in Figure 4.1, the sample is also not evenly distributed in the log M_*–log SFR plane. The current sample lacks many star-forming galaxies with intermediate sSFRs at $M_* \sim 10^{8.5} M_{\odot}$, so the MZ$_*$Rs in Figure 4.10 are slightly bimodal. We hypothesize that denser sampling would reveal a continuous change

in the normalization of MZ_*R with increasing sSFR. The scatter in the MZ_gR may also increase if starburst galaxies are included because previous works have found significant correlation between sSFR and $(O/H)_g$ (e.g., Mannucci et al., 2010; Andrews and Martini, 2013).

Second, our sample contains only two quiescent galaxies residing in distinct environments. A larger sample would be needed to take a census of the metal content of dwarf galaxies in different environments, in order to resolve whether environment is as important in shaping the MZ_*R as we suspect from this work.

Third, because 40% of the KCWI sample lacks the Hα+[N II]$\lambda\lambda$6549, 6585 coverage[9], we determined the gas-phase oxygen abundances of our sample from a combination of line ratios measured from the KCWI spectra and SDSS spectra. Therefore, we had to assume that the [N II]/Hα ratio remains constant within galaxies because the KCWI FoV is much larger than the SDSS fiber aperture. We cannot construct the MZ_gR using direct T_e measurements because we detected [O III]λ4363 in less than $1/3$ of the sample. The only strong line calibration that does not require the red optical line ratios is R_{23} (e.g., Pilyugin and Thuan, 2005) which is known as a double-branched calibration (see Figure 8 of Pilyugin and Grebel 2016 for an example)[10]. In addition, any strong-line calibration onto the direct T_e abundance scale (like the R calibration used here) may underestimate the *actual* gas-phase O/H in galaxies, as discussed in Section 4.6.3.

Finally, we acknowledge that the stellar abundances we measure from the two-step method might still suffer from systematic effects. Due to the lack of SPS models that directly quantify the variation in $[Mg/Fe]_*$, we still have to rely on models that vary all α elements together with respect to Fe. Although we validated the method for quiescent galaxies in Section 4.4.3, it is possible that the two-step method may be subject to different systematic errors in star-forming galaxies due to the combined effects of the age–metallicity degeneracy and the difficulty in recovering the age of young galaxies (Carnall et al., 2019). The most direct way to verify the two-step method is to apply it to a nearby star-forming galaxy where we can measure its $[Mg/Fe]_*$ from its resolved stellar population, similar to the recent work done in dwarf elliptical galaxies or globular clusters with multiple stellar populations

[9]The red channel of the KCWI was not available until the summer of 2023, after some of our data were obtained.

[10]The R_{23} calibration is relatively insensitive to galaxies with oxygen abundances falling near turnover of the curve at $12 + \log(O/H) \sim 8.0$–8.4, which coincides with the gas-phase metallicity of most galaxies in our sample.

(Ruiz-Lara et al., 2018; Boecker et al., 2020; Zhuang et al., 2021).

4.7 Summary

In this work, we presented a sample of 46 star-forming and two quiescent galaxies with $M_* \sim 10^{8-10} M_\odot$ observed with Keck/KCWI, with the aim of understanding the shape of the MZ$_*$R in the relatively unexplored mass range between the Local Group dwarf satellite galaxies and massive field galaxies, as well as the connection between the metals in the stars and the ISM. Our findings are as follows:

1. Applying SPS models with variable [α/Fe] directly to the stellar continuum with `pPXF` significantly underestimates [Mg/Fe]$_*$ or overestimates [Fe/H]$_*$ (Figures 4.4 and 4.5). To solve this problem, we developed a two-step method that is capable of recovering the [Fe/H]$_*$ and [Mg/Fe]$_*$ of the stellar population.

2. We determined the gas-phase oxygen abundances via the R calibration (Pilyugin and Grebel, 2016) and the stellar iron and magnesium abundances via the two-step method within the same galaxies of our KCWI sample. For the first time, we can not only relate the stellar and gas-phase metallicity but also make an apples-to-apples comparison of α elements within the same galaxies. The correlation between [O/H]$_\mathrm{g}$ and [Mg/H]$_*$ is tighter than that of [O/H]$_\mathrm{g}$ and [Fe/H]$_*$. Furthermore, [O/H]$_\mathrm{g}$ is higher than [Fe/H]$_*$ and [Mg/H]$_*$ in most galaxies, suggesting that new stars are forming in gas that has participated in the overall chemical enrichment of the ISM, and not in metal-poor gas that has recently been accreted.

3. The gas-to-stellar abundance ratios, $\Delta Z_\mathrm{O,Fe}$ and $\Delta Z_\mathrm{O,Mg}$, are correlated with sSFR but do not depend on stellar mass, SFR, light-weighted age, $\log \Phi$ (a proxy for the gravitational potential), or $\log \Sigma$ (the stellar mass surface density).

4. We constructed the ionized O-MZ$_\mathrm{g}$R and the Fe-MZ$_*$R and Mg-MZ$_*$R of our KCWI sample, and we found that the scatters in the Fe- and Mg-MZ$_*$Rs are significantly larger than that of the O-MZ$_\mathrm{g}$R. Further work would be necessary to understand the origin of these scatters. The observed scatters in the MZ$_*$Rs are primarily driven by varying sSFRs. At a given mass, star-forming galaxies with higher sSFRs exhibit lower [Fe/H]$_*$ and [Mg/H]$_*$. The relations become tighter in the Φ–Z plane, but the dependence on sSFR is not eliminated. For

the two quiescent galaxies in our sample, the dwarf satellite candidate 0241-0810 is more metal poor, has comparable stellar abundances to the heavily star-forming galaxies at similar masses, while the isolated dwarf quiescent galaxy 0125-0041 is more metal-rich and exhibits abundances similar to the star-forming galaxies with low sSFRs.

5. We compared the Fe- and Mg-MZ$_*$Rs of our KCWI sample with those of more massive SDSS galaxies and found that they could not be described by a single linear relation. At a fixed mass, heavily star-forming galaxies still tend to have lower [Fe/H]$_*$ and [Mg/H]$_*$ than quiescent galaxies. This suggests that the increasing scatter in the stellar abundances at a fixed M_* exhibited by the KCWI dwarfs may be driven, at least in part, by the sSFR tracing the remaining gas supply. This trend also supports a physical scenario in which starvation is primarily responsible for quenching galaxies in the field.

This work is the first paper in a series whose goal is to understand the chemical evolution of low-mass galaxies at low redshift, especially those that remain actively star-forming, over the mass range $M_* \sim 10^{8-10} M_\odot$ based on IFU data cubes. While we are limited by the sample size, the high-quality data obtained with a 10 m telescope allows us to place unprecedented constraints on the chemical enrichment of galaxies in the mass range intermediate between Local Group satellites and massive galaxies that have been well-studied by large spectroscopic surveys. In the future, we will leverage the spatial information from the IFU data and investigate the spatially-resolved elemental abundances in the stellar and gas phases, which will provide unparalleled details to interpret the chemical evolution of star-forming dwarf galaxies.

Acknowledgments

The authors acknowledge the insightful and constructive feedback of the anonymous referee. We thank Yuguang Chen, Allison Strom, Adam Carnall, Claudia Maraston, and Ryan Sanders for useful discussions. We are grateful to the many people who have worked to make the Keck Telescopes and their instruments a reality and to operate and maintain the Keck Observatory, including support astronomers Greg Doppmann and Rosalie McGurk, and telescope operator Tony Connors. The authors wish to recognize and acknowledge the very significant cultural role and reverence that the summit of Maunakea has always had within the Native Hawaiian community.

We are most fortunate to have the opportunity to conduct observations from this mountain.

This material is based on work supported by the National Aeronautics and Space Administration (NASA) under FINESST Grant No. 80NSSC22K1755 (Z.Z. and C.C.S.). E.N.K. acknowledges the support from the National Science Foundation (NSF) under CAREER Grant No. AST-2233781. C.C.S. has been supported in part by NSF grant No. AST-2009278. C.C. acknowledges support from NSF-AST-131547. Most of the data presented herein were obtained at Keck Observatory, which is a private 501(c)3 non-profit organization operated as a scientific partnership among the California Institute of Technology, the University of California, and NASA. The Observatory was made possible by the generous financial support of the W. M. Keck Foundation.

4.8 Appendices

4.8.1 Appendix A: Potential Aperture Effect

The main analysis in this work made use of the spectra obtained from summing the spaxels with S/N > 1 in the stellar continuum. To explore whether this extraction approach would introduce any bias due to the potential metallicity radial gradients in these galaxies, we also extracted the spectra from four different circular apertures, with diameters ranging from 1″ to 4″, and measured their stellar abundances using the method described in Section 4.4.2. We did not measure the gas metallicity because the scatter in gas metallicity is more likely driven by the calibration method instead of an aperture effect, as detailed in Section 4.5.3.

We show the Fe- and Mg-MZ$_*$Rs of the KCWI sample extracted using different aperture sizes in Figure 4.12 and 4.13, respectively. Compared to the MZ$_*$Rs obtained from the entire KCWI data cube (roughly around 6″ to 20″ in diameter; Figure 4.10), the overall shape and the scatter of the MZ$_*$Rs remained largely unchanged when smaller aperture sizes are used, indicating that potential radial gradients and aperture effects are not responsible for driving the large scatter in the MZ$_*$Rs. The dependence of the stellar abundances on sSFR remains present across all aperture sizes.

4.8.2 Appendix B: Comparison of stellar population age derived from different SFH models

Here we discuss the light-weighted stellar population ages of the KCWI sample derived assuming different SFH models and fitting methods. Figure 4.14 com-

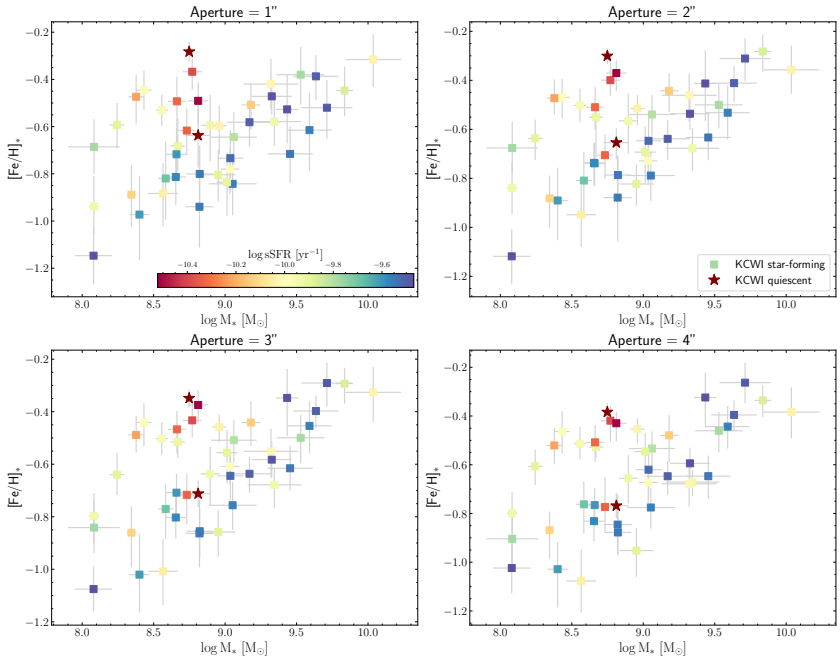

Figure 4.12: The Fe-MZ$_*$R of the KCWI star-forming (squares) and quiescent (stars) sample, measured from the spectra extracted from different circular apertures (1″ – 4″). The star-forming galaxies are color-coded by their sSFRs. The overall shape and the scatter of the Fe-MZ$_*$R remains largely unchanged across different sizes of aperture.

pares the light-weighted ages derived using `pPXF` (i.e., the first step of the two-step method) assuming non-parametric SFHs with those derived from broadband SED fits using BAGPIPES assuming four different parametric SFHs: delayed exponential, log-normal, double-power-law, and constant. The light-weighted ages obtained from spectral analysis are broadly consistent with those obtained from SED fits, particularly for an assumed constant SFH. The consistency indicates that invoking a non-parametric SFH that allows star formation to occur at any time and to accommodate any possible shape of the SFH does not introduce any significant bias to the light-weighted age measurement. Given that broadband photometry is more sensitive to stellar populations formed at different epochs due to its wider spectral coverage than KCWI spectroscopy, Figure 4.14 shows that the light-weighted ages derived from `pPXF` spectral fits in the relatively narrow wavelength range 3650–5500 Å are reasonable.

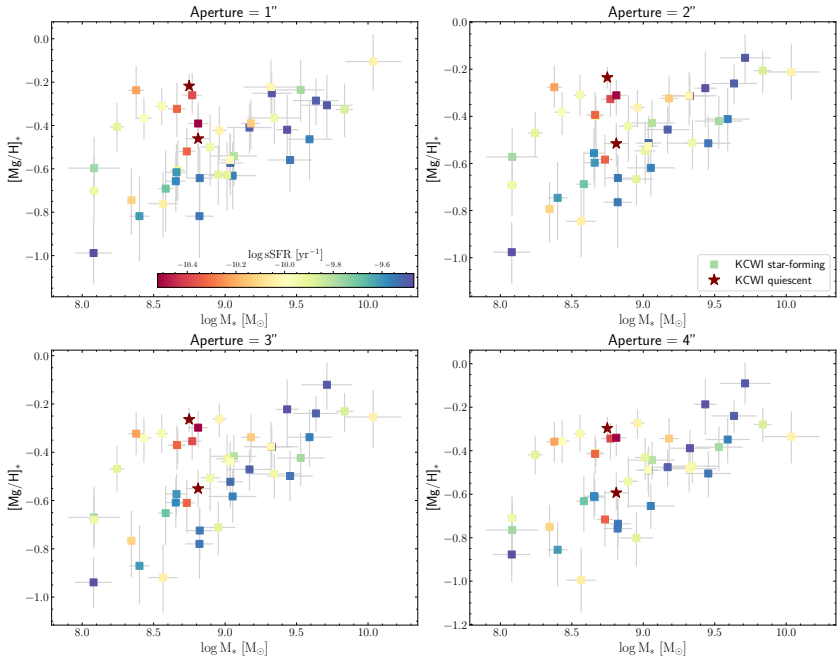

Figure 4.13: Similar to Figure 4.12, but comparing the Mg-MZ$_*$R measured from different apertures.

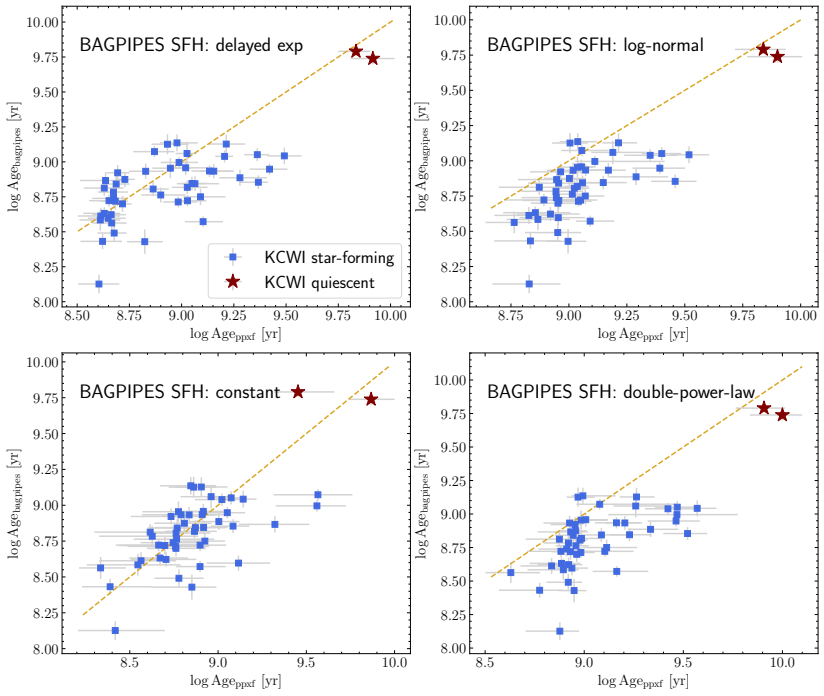

Figure 4.14: Comparison of light-weighted stellar population age derived from SED fitting using BAGPIPES and from full-spectrum fitting using pPXF for the star-forming (blue squares) and quiescent (red stars) galaxies in our KCWI sample. In each panel, the one-to-one line is shown by the yellow dashed line.

4.8.3 Appendix C: The Selection and Abundance Measurements of the SDSS Sample

We adopt the SDSS quiescent sample selected by Leethochawalit et al. (2018b). In summary, Leethochawalit et al. (2018b) selected a sample of 152 quiescent galaxies with Hα EW < 1 Å from 44,254 SDSS spectra from Gallazzi et al. (2005). In each bin of 0.1 dex in stellar mass spanning from 10^9 to $10^{11.5} M_\odot$, they randomly selected at most eight quiescent galaxies, yielding a subsample of 152 quiescent galaxies.

In this work, we selected the SDSS star-forming sample in a similar way to Leethochawalit et al. (2018b). We restricted the galaxies to the SFMS with sSFRs in the range of 10^{-11} and 10^{-9} yr^{-1} using the sSFRs from the SDSS MPA-JHU catalog (*galSpecExtra*, SDSS DR17; Kauffmann et al., 2003a; Brinchmann et al., 2004; Salim et al., 2007). Similarly, we randomly selected at most eight star-forming galaxies in each bin of 0.1 dex in the mass range of $10^{9-11.5} M_\odot$.

We cross-matched the subsamples with the GSWLC catalog to obtain stellar mass estimates for comparison with the KCWI sample. As the stellar masses of the KCWI sample were derived from BAGPIPES assuming the Kroupa (Kroupa, 2001) IMF, the Chabrier-based (Chabrier, 2003) stellar masses in the GSWLC catalog were adjusted to Kroupa-based values by applying an offset of +0.025 dex (Salim et al., 2007). To be consistent with the KCWI spectra, we limited the wavelength range of the SDSS spectra to 3650 – 5500 Å and measured the ages, [Fe/H]$_*$, and [Mg/Fe]$_*$ in the same manner as Section 4.4. We excluded the galaxies with errors in [Fe/H]$_*$ > 0.15 dex to provide a clear trend, yielding 125 quiescent and 124 star-forming galaxies in the SDSS sample. The stellar masses and SFRs of the SDSS sample are shown in Figure 4.15.

We do not discuss the best-fit O-MZ$_g$R of the SDSS star-forming galaxies in Section 4.6 because it becomes flat around $\log(M_*/M_\odot) \sim 10.2$ (Figure 4.16). It is unclear to us whether the flattening of the SDSS O-MZ$_g$R results from the underlying physical mechanisms governing the metal retention or originates from the systematics in the R calibration, as Pilyugin and Grebel (2016) only validated the R calibration to the T_e-based measurements up to $12 + \log(\mathrm{O/H}) \gtrsim 8.7$. Because the KCWI data cannot cover many nebular features sensitive to gas-phase metallicity in the red optical, we refrain from experimenting with other strong-line calibrators in this comparison. It is beyond the scope of this paper to investigate how the systematics of different gas metallicity indicators could affect the high-mass MZ$_g$R of the SDSS galaxies.

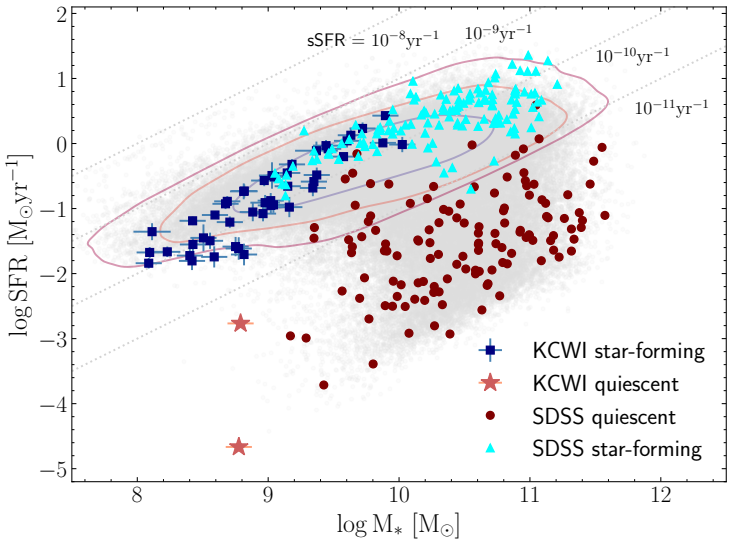

Figure 4.15: SFR as a function of stellar mass of the galaxies in our KCWI and SDSS samples. The blue squares and red stars represent the star-forming and the quiescent galaxies of the KCWI sample, while the cyan triangles and dark red dots indicate the star-forming and the quiescent galaxies described in Appendix 4.8.3. The contours show the SDSS SFMS at a similar redshift range ($z < 0.06$) taken from the GSWLC catalog (Salim et al., 2016) at 1-3 σ. The grey dots indicate all the GSWLC galaxies in the same redshift range as those in our sample.

Nevertheless, we trust that the R calibration is reliable for the low-mass galaxies in our KCWI sample, which all have $12 + \log(\mathrm{O/H}) < 8.6$. The O-MZ$_g$R of the KCWI sample also agrees with that of the local dwarf galaxies measured by Berg et al. (2012) using the T_e method. However, our gas-phase metallicities and those measured by Berg et al. (2012) are lower than the MZ$_g$R measured by Andrews and Martini (2013) for stacked SDSS spectra via the T_e method. Andrews and Martini (2013) included a large sample of galaxies with galaxies at various sSFRs when they generated the stacked spectra. The emission from diffuse ionized gas (DIG) ionized by evolved, hot stars becomes increasingly important when the sSFR is low. As pointed out by Sanders et al. (2017), the contamination from DIG tends to affect the emission line fluxes from the low-ionization species and lower the electron temperature estimate in the low-ionization zone. Consequently, the gas metallicity derived from the stacked spectra with significant contribution from DIG would be overestimated. Although our sample also consists of star-forming galaxies with low sSFRs, we measured the gas metallicity for individual galaxies where DIG contribution should be much less significant. We therefore suspect that the contamination from DIG in the sample of Andrews and Martini (2013) may explain

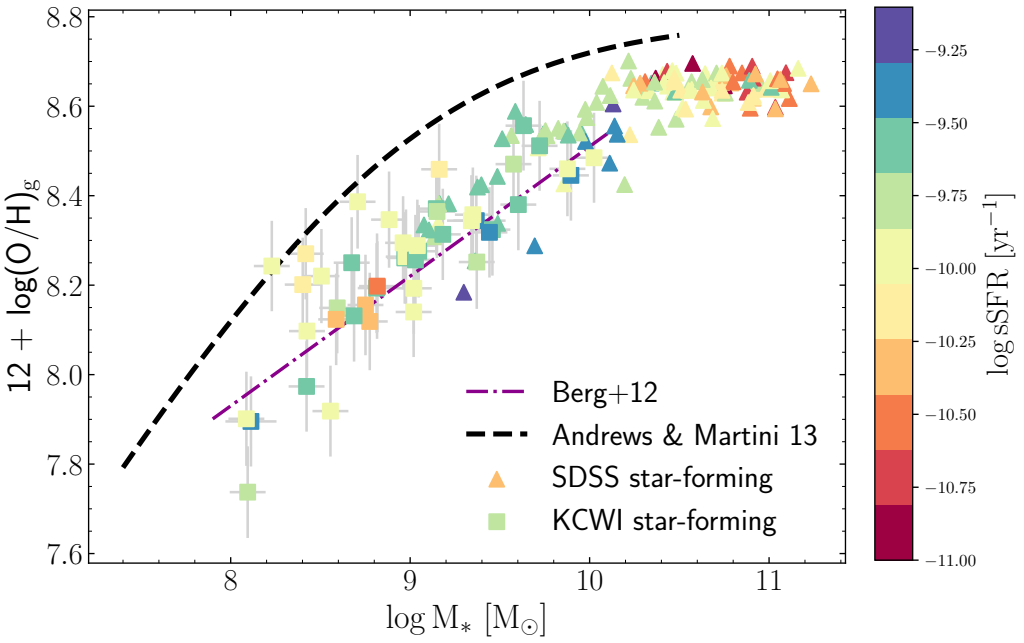

Figure 4.16: The O-MZ$_g$R of the KCWI sample and the SDSS sample, color-coded by the sSFRs. The O-MZR of the local dwarf galaxies (and the associated 1σ confidence interval, Berg et al., 2012) and the stacked spectra of the SDSS galaxies (Andrews and Martini, 2013) derived from the direct T_e method are shown by the purple dashed-dotted line (and shaded region) and the black dashed line, respectively.

the discrepancy.

Chapter 5

METALS IN STAR-FORMING GALAXIES WITH KCWI: SPATIALLY RESOLVED NEBULAR AND STELLAR POPULATION PROPERTIES

In this chapter, we extend our analysis of star-forming dwarf galaxies observed with KCWI, as introduced in Chapter 4 (Zhuang et al., 2024, hereafter Paper I), to explore their spatially resolved stellar and nebular properties in greater depth. While the previous analysis was based solely on KCWI-blue data, here we conduct a joint analysis combining both the blue and red channels of the KCWI. The observations and data reduction are described in Section 5.1. In Section 5.2, we present the methods used to determine the spatially resolved properties of ionized gas and stellar populations. We present the preliminary results on the spatially resolved properties in Section 5.3.

5.1 Data

5.1.1 Sample

In the previous chapter, we presented the first results of 46 star-forming galaxies in a mass range of $10^8 - 10^{10} M_\odot$ observed on the KCWI in 2021B and 2023B. In this chapter, we focus on 27 galaxies of the sample observed in 2023B (Table 5.1) with the blue (KCWI) and red (KCRM) red coverage, 25 of which have stellar masses $M_* \lesssim 10^9 M_\odot$ and two of have stellar masses $10^{9.5} \lesssim M_* \lesssim 10^{10} M_\odot$, allowing us to better characterize spatially resolved nebular properties. All targets were randomly selected from the SDSS MPA-JHU catalog (Brinchmann et al., 2004; Tremonti et al., 2004) to have $10^8 M_\odot \lesssim M_* \lesssim 10^9 M_\odot$ and specific star formation rates (sSFR) between 10^{-9} and 10^{-11} yr^{-1}.

We re-measured the stellar masses and star formation rates (SFR) of our sample by fitting broadband photometry from FUV to mid-IR wavelengths with BAGPIPES (Carnall et al., 2018; Carnall et al., 2019) assuming an exponentially declining (delayed-τ) star formation history (SFH). We made use of the publicly available images from the *Galaxy Evolution Explorer* (*GALEX*; Martin et al., 2005), the Sloan Digital Sky Survey (SDSS; York et al., 2000), the Panoramic Survey Telescope and Rapid Response System (PS1; Flewelling et al., 2020), and the Wide-field Infrared Survey Explorer (WISE; Wright et al., 2010). The photometry and spectral energy

distribution (SED) fitting was described in full detail in Paper I.

Table 5.1: General Properties of the KCWI Galaxy Sample

Galaxy	RA (J2000)	Dec (J2000)	z^a	$\log M_*$ [b] $[M_\odot]$	$\log SFR^b$ $[M_\odot\ yr^{-1}]$
2225−0046	22 25 07.92	−00 46 06.03	0.016	8.09±0.10	−1.84 ± 0.08
2329+1552	23 29 46.17	+15 52 38.96	0.009	8.23±0.10	−1.67 ± 0.08
2152−0110	21 52 22.46	−01 10 15.95	0.016	8.40±0.10	−1.72 ± 0.13
0845+5145	08 45 54.52	+51 45 11.12	0.014	8.42±0.10	−1.80 ± 0.14
2334+0029	23 34 14.80	+00 29 07.28	0.024	8.42±0.10	−1.19 ± 0.07
0121−0853	01 21 51.93	−08 53 10.63	0.018	8.43±0.10	−1.55 ± 0.10
0013−0956	00 13 45.42	−09 56 03.67	0.013	8.51±0.10	−1.45 ± 0.21
0155−0037	01 55 01.92	−00 37 35.27	0.023	8.56±0.10	−1.50 ± 0.12
0140−0012	01 40 52.90	−00 12 49.52	0.018	8.59±0.10	−1.74 ± 0.16
0023−0939	00 23 48.32	−09 39 09.85	0.020	8.59±0.10	−1.10 ± 0.06
0233+0038	02 33 03.92	+00 38 41.59	0.024	8.67±0.10	−0.93 ± 0.08
0256−0010	02 56 32.90	−00 10 51.13	0.029	8.69±0.10	−0.89 ± 0.08
2259−0019	22 59 03.19	−00 19 45.82	0.016	8.71±0.10	−1.21 ± 0.09
2300−0832	23 00 51.88	−08 32 13.36	0.025	8.75±0.10	−1.58 ± 0.15
0233−0819	02 33 05.84	−08 19 08.79	0.019	8.77±0.10	−1.61 ± 0.17
2301+1451	23 01 06.26	+14 51 16.74	0.024	8.81±0.11	−0.74 ± 0.12
0332−0600	03 32 00.36	−06 00 42.77	0.018	8.82±0.10	−1.71 ± 0.17
2131−0613	21 31 03.64	−06 13 58.27	0.025	8.82±0.10	−0.73 ± 0.10
0850+6145	08 50 39.67	+61 45 44.42	0.024	8.88±0.10	−1.05 ± 0.14
0256−0707	02 56 34.76	−07 07 11.12	0.017	8.96±0.10	−1.08 ± 0.12
2137+1243	21 37 52.51	+12 43 42.63	0.031	8.98±0.11	−0.91 ± 0.12
0137−0942	01 37 43.57	−09 42 36.36	0.019	9.02±0.10	−0.88 ± 0.12
0136+1356	01 36 15.18	+13 56 43.26	0.024	9.03±0.10	−0.49 ± 0.20
2304−0933	23 04 30.86	−09 33 03.58	0.032	9.04±0.10	−0.94 ± 0.12
0306−0033	03 06 24.96	−00 33 04.38	0.025	9.16±0.10	−0.98 ± 0.15
0334+0106	03 34 06.02	+01 06 15.19	0.049	9.44±0.10	−0.03 ± 0.09
0407−0634	04 07 04.64	−06 34 02.15	0.038	9.88±0.10	0.01 ± 0.06

[a] Redshifts are taken from SDSS DR17 (Abdurro'uf et al., 2022).

[b] The stellar masses and SFRs are derived from broadband SED fitting with BAGPIPES.

5.1.2 KCWI Observations

The KCWI observations were conducted over three nights in the 2023B semester, with an average seeing of approximately $\sim$1″. All targets were observed using the medium slicer, providing a field of view (FoV) of 16.5″ × 20.4″. For the blue channel, we used the BL grating centered at 4500 Å, yielding a spectral resolution FWHM of 2.5 Å and a wavelength coverage of 3500–5500 Å. For the red channel, we used the RL grating centered at 7800 Å, with a spectral resolution FWHM of 4 Å and a wavelength range of 6300–9500 Å.

For most galaxies, we rotated the position angles (i.e., the orientation of the KCWI slices on the sky) in order to minimize covariance when stacking exposures. Each pointing included at least three five-minute exposures in the red channel to facilitate more effective cosmic ray (CR) removal, along with a single exposure in the blue channel matched in total integration time. The total exposure time per galaxy ranged from 15 to 60 minutes. For galaxies with angular sizes comparable to the KCWI FoV, we also obtained off-field sky frames adjacent to the science frames to enable accurate sky subtraction.

We reduced the KCWI-blue data using a modified version of the publicly available KCWI data reduction pipeline (DRP), incorporating the updates described in Chen et al. (2021) and N. Prusinski et al. (in prep.)[1]. This pipeline produces sky-subtracted, flux-calibrated 3D data cubes with a spatial sampling of 0.29″× 0.68″ and a spectral dispersion of 1 Å per pixel for individual exposures.

We used the same pipeline to reduce the red channel data. To ensure spatial alignment between the two channels, we set the reference wavelength for differential atmospheric refraction (DAR) in the red channel to 4500 Å, matching the value used for the blue channel. However, the red data are affected by long-tailed cosmic rays that are not effectively removed by the default CR removal algorithm in the DRP, which uses the astroscrappy package (McCully et al., 2018). To address this, we created CR masks using the new `kcrm_create_crmsk` function in the KCWIKit package (Chen et al., 2021; Prusinski and Chen, 2024)[2]. The algorithm compares each exposure with the median image of all exposures at a given pointing to identify outliers, and we found that 3σ clipping was sufficient to mask CR-contaminated pixels. We did not perform CR removal for standard star observations, as their short integration times (less than one minute) make CR contamination much less

[1] `https://github.com/yuguangchen1/KCWI_DRP/tree/KCWIKit`
[2] `https://github.com/yuguangchen1/KcwiKit`

of a concern, and only the broad spectral shape is needed to estimate the inverse sensitivity function.

We also skipped sky subtraction and flux calibration of the red-channel science frames and their associated sky frames (if available). The standard KCWI DRP uses a single master b-spline sky model across all slices for sky subtraction, which requires highly accurate flat-fielding, wavelength calibration, and a uniform line spread function (LSF) across all the slices. While this method has been shown to work well for the blue channel (e.g., Chen et al., 2021; de los Reyes et al., 2023; Zhuang et al., 2024), it can leave significant residuals in regions with dense sky lines, especially when science signals overlap with sky features (Figure 5.1).

To overcome these limitations, we developed KSkyWizard[3], a standalone GUI-based Python tool for post-processing DRP-reduced red-channel cubes. KSkyWizard reads in non-sky-subtracted, DAR-corrected cubes (`icubed` files) and performs sky subtraction, flux calibration, and telluric correction[4]. To account for imperfect flat-fielding and spatial variations in the LSF, we adopted the Zurich Atmosphere Purge (ZAP; Soto et al., 2016) package, an algorithm based on principal component analysis (PCA) to model the sky from blank regions of the cube or from the blank sky frame. ZAP uses continuum filtering to disentangle narrow sky lines from broader features in the science target and reconstructs the sky model in each spaxel independently, significantly reducing sky residuals while preserving the flux of the target. KSkyWizard serves as a GUI wrapper for ZAP, providing features such as wavelength cropping, white-light image generation (for science region masking), and sky model configuration. Users can apply ZAP either with in-field sky (using a mask) or with an adjacent sky frame, and choose between global PCA or segmented PCA in the multiple regions following Soto et al. (2016). Its interactive interface allows users to iteratively adjust masks and spectral segments until optimal results are achieved.

KSkyWizard also performs flux calibration and telluric correction. The standard DRP estimates the inverse sensitivity function by fitting a polynomial to user-defined regions, which often fails if dense telluric regions are present, especially in the red end of the spectrum. KSkyWizard refines this by fitting a cubic-spline interpolation to the standard star spectrum using user-defined knots, improving the fit in telluric regions. The corrected spectrum of the standard star is then passed

[3] `https://github.com/zhuyunz/KSkyWizard`

[4] KSkyWizard can also refine the sky subtraction of already sky-subtracted cubes generated by the DRP.

to PypeIt (Prochaska et al., 2020a; Prochaska et al., 2020b) to generate a telluric model at the airmass of the standard star, which is then scaled to match the airmass of the science target and applied for telluric correction. Figure 5.1 compares a sky-subtracted spectrum produced by KSkyWizard with that from the standard DRP. The KSkyWizard result shows significantly reduced sky residuals and improved correction of telluric absorption features.

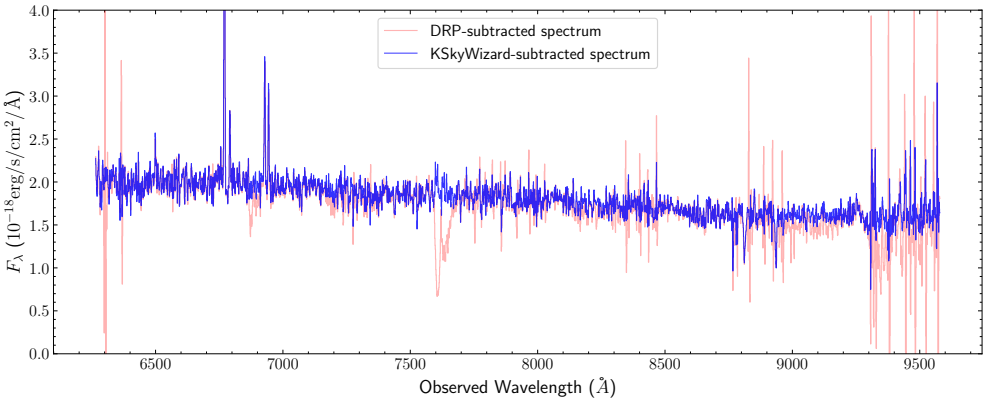

Figure 5.1: Comparison of an example sky-subtracted spectrum produced by the standard KCWI DRP (red) and by KSkyWizard (blue). Both spectra were extracted from the same 2″ diameter aperture centered on the target.

Finally, the sky-subtracted, flux-calibrated data cubes from both channels of all pointings for a given target were aligned, stacked, and resampled to a common spatial grid with $0.3'' \times 0.3''$ spatial sampling and 1 Å spectral dispersion using the KCWIKit package[5] (Chen et al., 2021; Prusinski and Chen, 2024).

5.2 Analysis

5.2.1 Summary of the Fitting Algorithms

We developed our own custom Python pipeline to analyze the stacked KCWI data cubes to obtain high-level data products, including emission line maps and spatially resolved stellar population parameters, by following the general procedures of the MaNGA data-analysis pipeline (DAP) (Westfall et al., 2019). The main purpose of this pipeline is to extract the maps of nebular and stellar population properties separately for further measurements via the penalized pixel-fitting method (`pPXF`) by Cappellari (2017), a χ^2 minimization code that fits for a linear combination of simple stellar population (SSP) models at different ages and metallicities.

[5] `https://github.com/yuguangchen1/KcwiKit`

We generated SSP models using the PYTHON-FSPS package (Foreman-Mackey, Sick, and Johnson, 2014), the Python wrapper of the Flexible Stellar Population Synthesis code (FSPS; Conroy, Gunn, and White, 2009; Conroy and Gunn, 2010) version 3.2, assuming a Kroupa (2001) IMF, the MIST isochrones (Choi et al., 2016), and the MILES stellar spectral libraries (Sánchez-Blázquez et al., 2006). The SSP models have metallicities spanning the range $[\mathrm{Fe/H}] = -2.0$ to $+0.5$ with an interval of 0.25 dex, the same as the grid of the MIST isochrones, and ages ranging from $\log(\mathrm{Age})\,[\mathrm{yr}] = 5.0$ to 10.2 with an interval of 0.2 dex.

Because the MILES stellar spectral library has a spectral coverage of $3525 - 7500$ Å, we excluded the spectral regions beyond 7500 Å in the KCWI data for further analysis in this work. We save the very red end of the spectra for future analysis. The spectral regions below 3650 Å were also excluded from the analysis because strong nebular continuum in the highly star-forming regions blueward of the Balmer break might affect the estimation of stellar population properties obtained from the full-spectrum fitting (Byler et al., 2017; Miranda et al., 2025).

All spaxels with an average signal-to-noise ratio (S/N) per wavelength channel, weighted by the SDSS-g band response function (i.e., $\mathrm{S/N}_g$), greater than 0.5 are included in the spatially resolved analysis. We tested several $\mathrm{S/N}_g$ thresholds and found that adopting a relatively loose criterion of $\mathrm{S/N}_g > 0.5$ allows us to retain spaxels in the outskirts—where only emission lines are typically detected—without introducing significant bias in the integrated stellar continuum within each spatial bin (see Section 5.2.2).

Before continuing the spectral analysis, we corrected the spectra for Galactic extinction using the $E(B-V)$ value from Schlafly and Finkbeiner (2011). We adopt the Galactic extinction law by O'Donnell (1994) to calculate the de-reddening correction.

5.2.2 Stellar Kinematics

We first measured the spatially resolved stellar kinematics using `pPXF`. Following the approach adopted by the MaNGA team (Westfall et al., 2019; Belfiore et al., 2019), we included both an eighth-order additive Legendre polynomial and an eighth-order multiplicative Legendre polynomial in the stellar continuum fit. These polynomials allow the model spectra to better match the overall shape of the observed spectra, which may suffer from imperfect flux calibrations and dust attenuation. To better determine stellar kinematics, we masked spectral regions within a velocity range of

± 400 km s^{-1} around potential emission lines (see Table 5.2).

Table 5.2: Emission-Line Parameters

ID	Line Name	$\lambda^a_{\rm rest}$ (Å)	Fixed Ratio	ID	Line Name	$\lambda^a_{\rm rest}$ (Å)	Fixed Ratio
1	H16	3704.9133	...	27	He Iλ4713	4714.466	...
2	H15	3713.0335	...	28	Hβ	4862.683	...
3	H14	3723.0035	...	29	He Iλ4922	4923.3051	...
4	[O II]λ3726	3727.092	...	30	[O III]λ4959	4960.295	0.34 [O III]λ5007
5	[O II]λ3729	3729.875	...	31	[Fe III]λ4985	4985.9	...
6	H13	3735.4365	...	32	[Fe III]λ4986	4987.2	...
7	H12	3751.2174	...	33	[O III]λ5007	5008.24	...
8	H11	3771.7012	...	34	He Iλ5016	5017.0769	...
9	Hθ	3798.9757	...	35	[N I]λ5198	5199.349	...
10	He Iλ3820	3820.691	...	36	[N I]λ5200	5201.705	0.37 [N I]λ5198
11	Hη	3836.472	...	37	[O I]λ6300	6302.046	...
12	[S III]λ3856	3857.111	...	38	[S III]λ6312	6313.8	...
13	[Ne III]λ3869	3869.86	...	39	[O I]λ6364	6365.536	0.33 [O I]λ6300
14	He Iλ3889	3889.749	...	40	[N II]λ6548	6549.86	0.33 [N II]λ6583
15	Hζ	3890.1506	...	41	Hα	6564.608	...
16	[Ne III]λ3967	3968.59	0.31 [Ne III]λ3869	42	[N II]λ6583	6585.27	...
17	Hϵ	3971.1951	...	43	He Iλ6678	6679.994	...
18	He Iλ4026	4027.328	...	44	[S II]λ6716	6718.295	...
19	[S II]λ4069	4069.749	...	45	[S II]λ6731	6732.674	...
20	[S II]λ4076	4077.5	0.40 [S II]λ4069	46	OI]λ7002	7004.161	...
21	Hδ	4102.8922	...	47	He Iλ7065	7067.228	...
22	Hγ	4341.6837	...	48	[A III]λ7136	7137.75	...
23	[O III]λ4363	4364.436	...	49	He Iλ7281	7283.357	...
24	He Iλ4471	4472.734	...	50	[O II]λ7320	7321.687	...
25	[Fe III]λ4658	4659.414	...	51	[O II]λ7330	7332.22	...
26	He IIλ4686	4687.015	...				

[a] Ritz wavelengths in vacuum from the National Institute of Standards and Technology (NIST) Atomic Spectra database (`https://physics.nist.gov/PhysRefData/ASD/lines_form.html`).

To obtain reliable kinematic measurements, we binned the spectra spatially to reach a minimum S/N threshold. We used the Voronoi binning algorithm of Cappellari and Copin (2003), a widely adopted method for IFU data, which adaptively groups neighboring spaxels to meet the target S/N. However, because resampling during the stacking process introduces covariance between adjacent pixels, the variance of the binned spectra tends to be underestimated. To correct for this effect, we applied the empirical correction formula from O'Sullivan and Chen (2020):

$$\sigma_{\rm measured} = C[1 + \alpha \log(N_b)]\sigma_{\rm nocov}, \tag{5.1}$$

for $N_b \lesssim N_{\rm thresh}$, and as

$$\sigma_{\rm measured} = C[1 + \alpha \log(N_{\rm thresh})]\sigma_{\rm nocov}, \tag{5.2}$$

for $N_b > N_{\rm thresh}$, where N_b is the number of spaxels in a bin, and $N_{\rm thresh}$ is the threshold beyond which covariance becomes negligible. The parameters C, α, and $N_{\rm thresh}$ were determined following the procedure outlined in Paper I and de los Reyes

et al. (2023). We adopted a target covariance-corrected S/N$_g$ of 20 for the Voronoi binning, which can give comparable precision to the S/N threshold used in MaNGA DAP (see Figure 19 in Westfall et al. (2019) for details).

Within each spatial bin, we ran `pPXF` twice. After an initial fit using the default emission-line mask, we additionally masked $> 3\sigma$ outliers and repeated the fitting to refine the stellar kinematic measurements.

5.2.3 Simultaneous Fit of Gas and Stars

Next, we adopted a hybrid binning scheme similar to that used by Belfiore et al. (2019) to optimize the spatially resolved measurement of emission lines. The stellar kinematics determined for each spatial bin were remapped back to the individual spaxels within that bin. We then performed a simultaneous fit of the emission lines and stellar continuum using `pPXF`, with the stellar kinematics fixed to the values obtained in the previous stage. As suggested by Sarzi et al. (2006) and Oh et al. (2011), this approach is preferred over fitting emission lines on a continuum-subtracted spectrum, as the latter way can lead to overestimates of line fluxes and widths in the presence of even small mismatches between the data and the stellar templates.

In the joint fit, we included an eighth-order multiplicative Legendre polynomial to account for imperfect flux calibration and dust attenuation. We excluded additive polynomials, as they can artificially alter absorption line strengths and bias the recovery of stellar population parameters. The emission lines included in the fit are listed in Table 5.2, with doublet ratios fixed to their theoretical values based on atomic physics. All emission lines were tied to share the same velocity and velocity dispersion to improve constraints on weaker lines.

In addition, we performed the same fitting procedure on the integrated spectra to estimate the global properties of each galaxy. For each object, we generated two types of integrated spectra: one by summing all spaxels used in the spatially resolved analysis (i.e., those with S/N$_g$ > 0.5), and another extracted from a $3''$ diameter circular aperture centered on the target, consistent with the SDSS fiber aperture.

5.2.4 Strong-Line Ratios and Gas-phase Abundances

To ensure reliable measurements of the ionization parameter and gas-phase abundances in individual spaxels, we restricted our analysis to those with S/N > 3 in

[O II]$\lambda\lambda$3726,3729, Hβ, [O III]λ5007, Hα, [N II]λ6583, and [S II]$\lambda\lambda$6716,6731.

We then constructed spatially resolved maps of emission-line ratios sensitive to metallicity and/or ionization parameter for each galaxy. Throughout this chapter, we adopt the abbreviations listed in Table 5.3 to refer to the emission-line ratios used in the subsequent analysis. Unless otherwise noted, all line ratios have been corrected for dust attenuation using the Balmer decrement, Hα/Hβ, assuming Case B recombination with $T_e = 10,000$ K and $n_e = 100$ cm^{-3}, which yields a theoretical Hα/Hβ ratio of 2.86 (Osterbrock and Ferland, 2006). The observed Balmer decrement was compared to this theoretical value, and the extinction correction was applied to each emission-line map using the Cardelli, Clayton, and Mathis (1989) extinction law.

Table 5.3: Definitions of Strong-line Ratios

Notation	Line Ratio
R2	$\log$ ([O II]$\lambda\lambda$3726, 3729/Hβ)
R3	$\log$ ([O III]λ5007/Hβ)
N2	$\log$ ([N II]λ6583/Hα)
S2	$\log$ ([S II]$\lambda\lambda$6716, 6731/Hα)
R23	$\log$ [([O II]$\lambda\lambda$3726, 3729 + [O III]$\lambda\lambda$4959, 5007) /Hβ]
O32	$\log$ ([O III]$\lambda\lambda$4959, 5007/[O II]$\lambda\lambda$3726, 3729)
O3N2	$\log$ ([O III]λ5007/Hβ) $-$ $\log$ ([N II]λ6583/Hα)

Note. The $\lambda\lambda$ notation refers to the sum of both lines.

The direct T_e method, which estimates nebular abundances from the electron temperature of ionized gas, is considered the most reliable approach for determining gas-phase metallicity from the optical spectrum. However, it requires the detection of faint auroral lines such as [O III]λ4363 or [O II]$\lambda\lambda$7320,7330, which are typically much weaker than Hβ and become increasingly difficult to detect at higher metallicities. Even though our sample consists of low-metallicity dwarf galaxies, auroral lines were only detected in a few spaxels, predominantly in the cores of the most actively star-forming regions. Consequently, we adopted the empirical strong-line calibration known as the "R calibration" from Pilyugin and Grebel (2016) to derive the maps of nebular abundances as[6]:

[6]The N_2, R_2 ratios defined by Pilyugin and Grebel (2016) are different from the commonly used "N2" and "R3" indices defined in Table 5.3.

$$
\begin{aligned}
12 + \log(\mathrm{O/H})_{R,U} = {} & 8.589 + 0.022\ \log(R_3/R_2) + 0.399\ \log N_2 \\
& + (0.164\ \log(R_3/R_2) + 0.589 \log N_2 - 0.137) \\
& \times \log R_2,
\end{aligned}
\tag{5.3}
$$

when $\log N_2 \geq -0.6$; and

$$
\begin{aligned}
12 + \log(\mathrm{O/H})_{R,L} = {} & 7.932 + 0.944\ \log(R_3/R_2) + 0.695\ \log N_2 \\
& + (0.970 - 0.291\ \log(R_3/R_2) - 0.019 \log N_2) \\
& \times \log R_2,
\end{aligned}
\tag{5.4}
$$

when $\log N_2 < -0.6$, where $\log R_2 = R2$, $\log R_3 = \log I_{[\mathrm{O\,III}]\lambda 4959+\lambda 5007}/I_{\mathrm{H}\beta} = R3 + 0.127$, and $\log N_2 = \log I_{[\mathrm{N\,II}]\lambda 6548+\lambda 6584}/I_{\mathrm{H}\beta} = N2 + 0.58$.

In addition, we employed the strong-line calibration from Eq. 13 of Pilyugin and Grebel (2016), which uses the N2 and R2 ratios to infer the spatially resolved nitrogen abundance as:

$$
\begin{aligned}
\log(\mathrm{N/O}) = {} & -0.657 - 0.201 \log N_2 \\
& + (0.742 - 0.075 \log N_2) \times \log(N_2/R_2),
\end{aligned}
\tag{5.5}
$$

where $\log R_2 = R2$ and $\log N_2 = N2 + 0.58$.

Given that DIG can enhance the strength of low-ionization emission lines and inflate ratios such as N2, O2, and S2 (Zhang et al., 2017), we also derived gas-phase metallicities using the O3N2 calibration from Pettini and Pagel (2004):

$$
12 + \log(\mathrm{O/H})_{\mathrm{O3N2}} = 8.73 - 0.32 \times \mathrm{O3N2}. \tag{5.6}
$$

The O3N2-based metallicity is expected to be less sensitive to DIG contamination because H II regions and DIG tend to overlap in the [O III]/Hβ versus [N II]/Hα diagnostic diagram (Zhang et al., 2017; Sanders et al., 2017).

5.2.5 Stellar Mass Density, Light-weighted Age and Star Formation Density

Alongside the emission-line measurements, we also estimated the stellar mass surface density and light-weighted stellar age (normalized over the spectral range 3650–5500 Å) in each spaxel based on the joint fitting procedure described in Section 5.2.3. We did not attempt to derive spatially resolved stellar metallicities due

to the insufficient S/N in individual spaxels. However, we consider the recovered light-weighted ages to be reliable, as their spatial distribution closely follows that of the D4000 index (Figure 5.2). The D4000 index, defined as the ratio of the average flux density between 4000–4100 Å and 3850–3950 Å (Balogh et al., 1999), serves as a robust age-sensitive tracer of stellar populations, particularly in low S/N data.

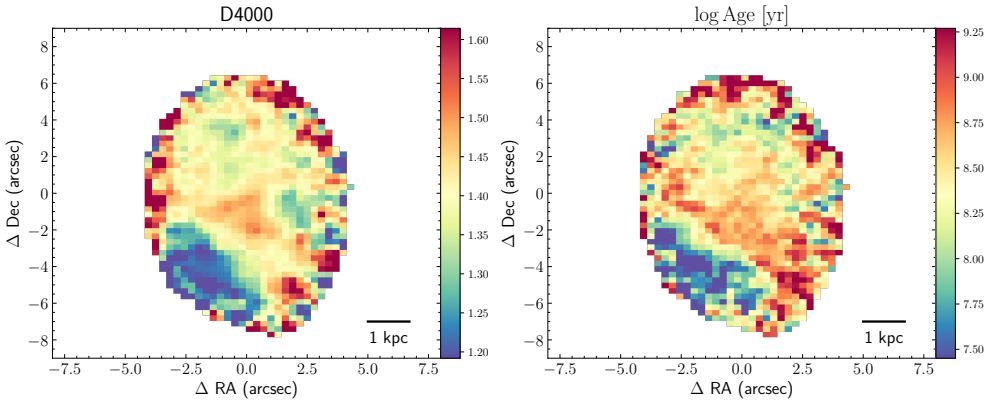

Figure 5.2: Comparison between the D4000 index (left) and light-weighted age (right) for an example galaxy from the KCWI sample. The D4000 index is defined following Balogh et al. (1999) as the ratio of the average flux density in the continuum bands 4000–4100 Å and 3850–3950 Å, after correcting for emission-line contributions.

To estimate the SFR surface density $\Sigma_{\rm SFR}$, we converted the dust-corrected Hα surface density, $\Sigma_{\rm H\alpha}$, to $\Sigma_{\rm SFR}$ using the calibration of Kennicutt (1998):

$$\Sigma_{\rm SFR}(\mathrm{M_\odot\,yr^{-1}\,kpc^{-2}}) = 7.9\times10^{-42}\Sigma_{\rm H\alpha}(\mathrm{erg\,s^{-1}\,kpc^{-2}}). \tag{5.7}$$

The sSFR surface density, $\Sigma_{\rm sSFR}$, was then derived as $\Sigma_{\rm sSFR} = \Sigma_{\rm SFR} - \Sigma_*$.

5.3 Results

In Figure 5.3, we present example composite maps from the KCWI data cube for galaxy 2259-0019, including the continuum image (a) and emission line map (b). Panels (c) through (l) show ten additional maps of derived quantities based on the analysis described in Section 5.2: (c) gas velocity relative to the systemic redshift, (d) stellar surface density (Σ_*), (e) star formation rate surface density ($\Sigma_{\rm SFR}$), (f) specific star formation rate surface density ($\Sigma_{\rm sSFR}$), (g) light-weighted stellar population age, (h) O32 (used as a proxy for ionization parameter), (i) S2, (j) gas-phase metallicity based on the O3N2 calibration from Pettini and Pagel (2004), and (k–l) gas-phase oxygen and nitrogen abundances, respectively, derived using

the strong-line calibration of Pilyugin and Grebel (2016). Maps for the rest of the galaxy sample are provided in Appendix 5.4.

5.3.1 Star Formation Morphology and Clumpiness

We find that 19 out of 27 galaxies host at least one off-center star-forming clump, while the remaining eight show more centrally concentrated or nuclear star formation. This implies the fraction of star-forming galaxies with off-center clumps ($f_{\rm clumpy}$) in our sample is around 70%. This is significantly higher than the $f_{\rm clumpy} \sim$ 3–4% reported for low-mass, star-forming galaxies ($9 < \log(M_*/M_\odot) < 9.8$) at $z \sim 0$ (Shibuya et al., 2016; Adams et al., 2022).

However, Shibuya et al. (2016) and Adams et al. (2022) adopted a much stricter criterion proposed by Guo et al. (2015) to identify clumpy galaxies, relying on luminosity thresholds rather than visual inspection. Specifically, they required that the ratio of clump to galaxy UV or SDSS-u luminosity exceed 8%. In contrast, we identify clumpy galaxies through visual inspection of $\Sigma_{\rm SFR}$. As a next step, we will estimate the ratio of clump to galaxy Hα luminosity (as a proxy for UV luminosity) to replicate the selection method used by Shibuya et al. (2016) and Adams et al. (2022), allowing for a more stringent test of whether our sample indeed exhibits a significantly higher $f_{\rm clumpy}$.

5.3.2 Ionization and Excitation Structure

The spatial distribution of O32, a proxy for the ionization parameter, is even more patchy than the star formation itself. Most off-center star-forming clumps show elevated O32 values, consistent with more ionizing photons from young, massive stars. However, the peaks in O32 do not always align with the highest $\Sigma_{\rm SFR}$ regions. This mismatch could arise from multiple effects. First, O32 increases at low metallicity, so its enhancement in outer star-forming clumps may partly reflect metallicity gradients. Second, the ionization parameter decreases with increasing gas density. Thus, even regions with similar ionizing photons can show higher O32 if the gas density is lower. Unfortunately, we cannot precisely measure the local gas density, as the [O II]λ3729/λ3726 and [S II]λ6716/λ6731 ratios are in the low-density limit across most galaxies.

When examining the S2 maps, we find a strong local-scale anti-correlation between O32 and S2 across all galaxies. Regions with higher excitation, indicated by elevated O32 values, consistently exhibit lower S2. This trend arises because S^+ ions have a relatively low ionization potential, making them more abundant in low-ionization

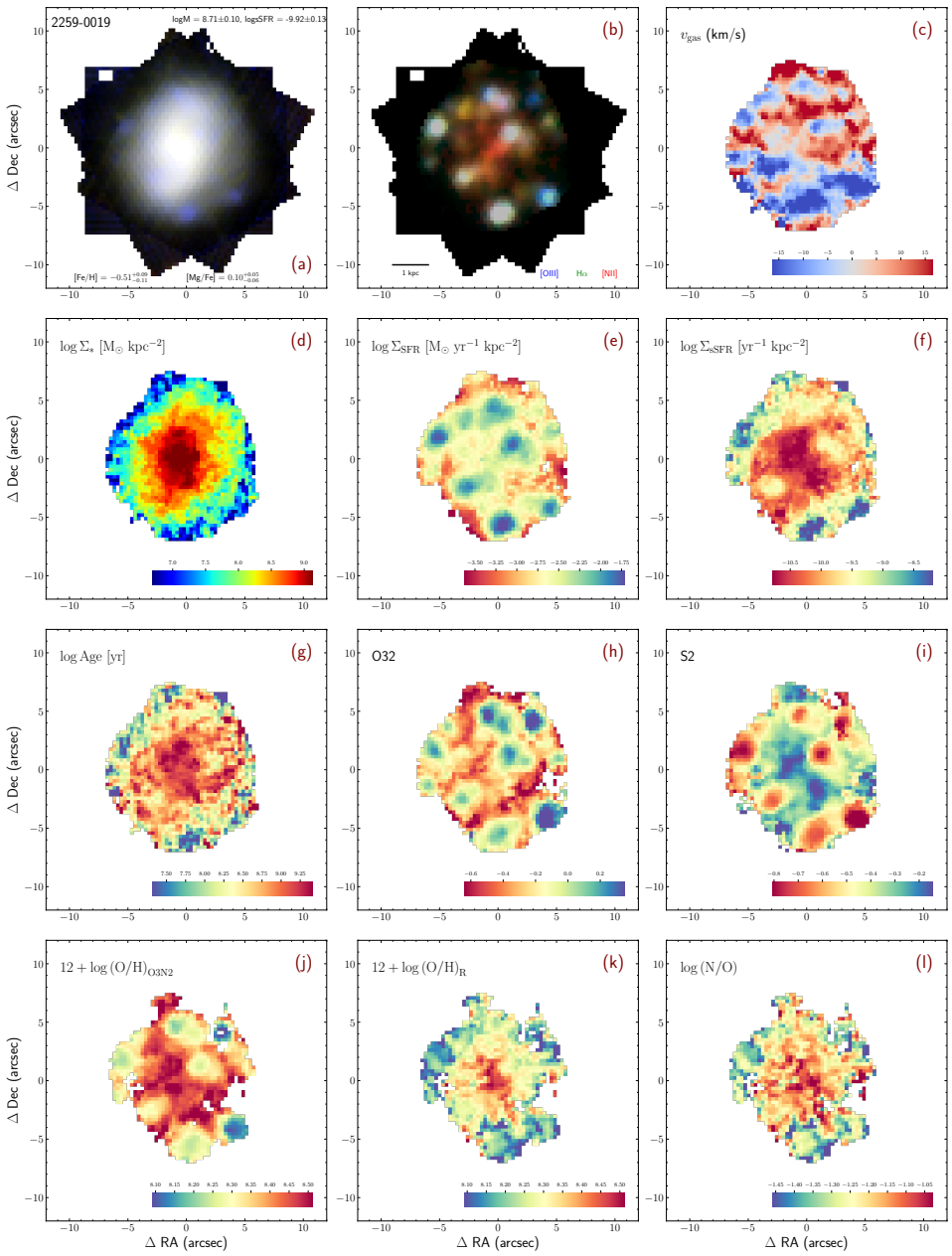

Figure 5.3: KCWI maps of 2259-0019. (a) A broadband image constructed using *g* (blue), *i* (green), and *z* (red) filters, synthesized from the KCWI data cube of galaxy 2259-0019 by convolving each spaxel's spectrum with the corresponding PS1 filter response; (b) a composite emission-line image combining [O III] (blue), Hα (green), and [N II] (red) maps from the same data cube; (c) the gas velocity map; (d) the stellar mass surface density Σ_*; (e) the SFR surface density $\Sigma_{\rm SFR}$ obtained from the dust-corrected $\Sigma_{\rm H\alpha}$; (f) the sSFR rate surface density; (g) the light-weighted stellar age map; (h) the O32 map, used as a proxy for the ionization parameter; (i) the S2 map; (j) the gas-phase metallicity map derived from the O3N2 diagnostic using the calibration of Pettini and Pagel (2004); and (k–l) gas-phase oxygen and nebular abundances derived using the calibrations from Pilyugin and Grebel (2016).

zones. In addition, the DIG that is likely ionized by hot, evolved stars rather than the young massive stars in H II regions tends to show enhanced S2 (Zhang et al., 2017). These observations motivate further investigation into the underlying stellar populations in regions with varying S2 and O32 values, and the extent to which they influence line ratios that are sensitive to local ionization conditions.

5.3.3 Chemical Abundance Patterns

The nebular abundances are relatively uniform and more homogeneous compared to star formation and local ionization. The nitrogen-to-oxygen ratio $\log(\mathrm{N/O})$ is much more uniform across most spaxels and typically stays below -1.0, consistent with primary nitrogen production. In contrast, gas-phase oxygen abundances exhibit more spatial variation. Most galaxies show flat or mildly negative radial gradients, with central regions being slightly more metal-rich.

However, a handful of galaxies display inverted metallicity gradients, where the central regions have lower oxygen abundance than the outskirts. These galaxies also show intense central star formation and younger stellar populations in the core.

The metallicity structure depends on the calibration method used. The O3N2-based maps (Pettini and Pagel, 2004) tend to follow O32 more closely, while the metallicity maps derived from the R-calibration of Pilyugin and Grebel (2016) show smoother distributions with less dependence on local excitation. As discussed further in Section 6.2.1, the presence of DIG may complicate this comparison, and measuring direct-T_e metallicities—even just in the core of the star-forming clumps and in the integrated spectra—would help resolve these ambiguities.

5.3.4 Stellar versus Nebular Morphologies

Despite the clumpy and irregular appearance of Σ_{SFR} and nebular properties, the stellar mass profiles (Σ_*) are generally smooth and regular. Even the most disturbed systems, such as 2131-0613 (hosting two infalling/accreted off-center star-forming complexes) and 2334+0029 (with a quenched tidal tail), maintain undisturbed stellar mass profiles. This is consistent with expectations from simulations, which predict that massive star-forming clumps are short-lived ($\lesssim$ 500 Myr; Bournaud et al. 2014; Mandelker et al. 2014). While ionized gas and star formation can appear chaotic, the time-integrated stellar mass reflects the longer-term structural stability of the galaxy.

In contrast, light-weighted age profiles are more strongly influenced by recent star-

bursts and appear less smooth than the stellar mass profiles. This is because the starlight is dominated by the brightest stellar populations, which are typically those formed most recently.

5.3.5 Gas Kinematics

Of the 27 galaxies, five show no evidence for coherent rotation in their gas velocity maps. While the remaining 22 exhibit some rotation, only eight have clearly defined rotation axes. The other 14 systems display disturbed or asymmetric velocity fields, possibly due to ongoing mergers, accretion events, or turbulence driven by stellar feedback. A detailed dynamical modeling effort will be needed to disentangle these possibilities and assess whether the kinematic irregularities stem from internal or external processes.

5.3.6 Large Spread in Spatially Resolved Line Ratios

The KCWI maps in Figures 5.3 and 5.5–5.30 reveal substantial spatial variations in emission-line ratios within individual dwarf galaxies. In Figure 5.4, we further discuss this phenomenon using one example galaxy, 2259−0019. Although we present only this case in detail, we emphasize that similar behavior is seen across our entire sample.

In the [N II]-BPT diagram (panel c of Figure 5.4), the dashed curve denotes the empirical demarcation line by Kauffmann et al. (2003b), which separates pure star-forming regions from composite systems, while the solid line represents the theoretical upper limit of pure star formation from photoionization models by Kewley et al. (2001), beyond which additional ionizing sources such as AGN are required to explain the line ratios. The spaxel measurements of 2259−0019 exhibit a clear gradient in this diagram. Compared to the off-center star-forming knots, the galaxy center shows higher [N II]/Hα (N2) and slightly lower [O III]/Hβ (R3), leading to a $\sim$ 0.3 dex difference in N2 between the central SDSS-equivalent spectrum and the global spectrum. The full spread in N2 across the galaxy spans nearly $\sim$ 1 dex, significantly larger than the observational uncertainties of the global spectrum. Spaxels with enhanced N2 (yellow to red colors) show line ratios consistent with the locus of SDSS star-forming galaxies, while the bluer star-forming spaxels exhibit line ratios that more closely resemble individual H II regions.

In the [S II]-BPT diagram (panel d), the solid line again shows the SF demarcation by Kewley et al. (2001), and the dashed line represents the empirical division between Seyfert and low-ionization narrow emission-line regions (LINERs) as defined by

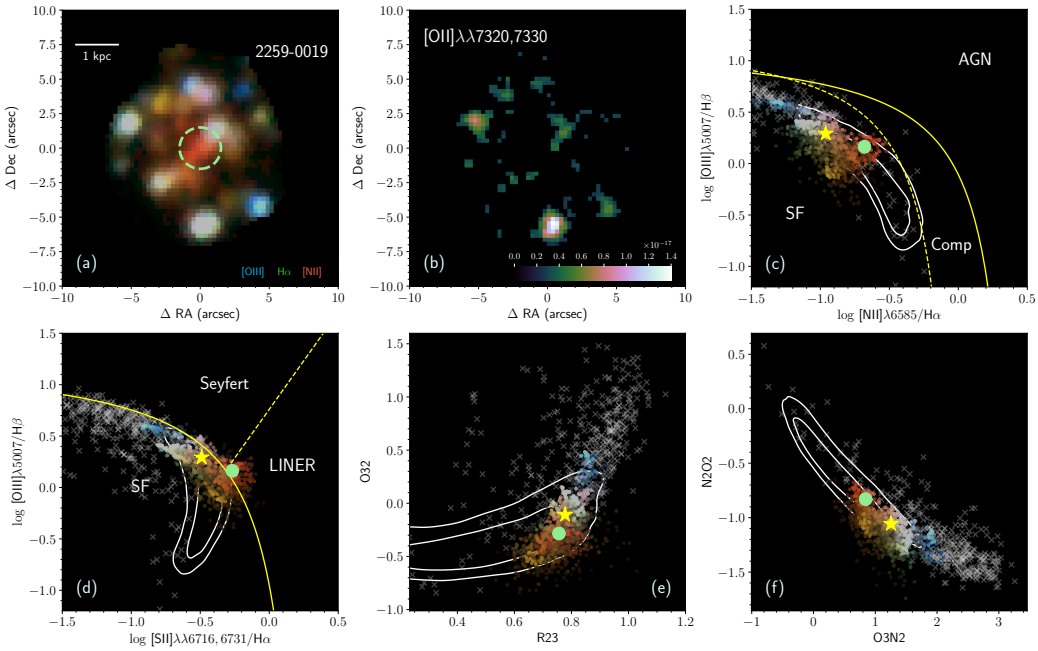

Figure 5.4: Emission-line diagnostics for galaxy 2259−0019 in the KCWI sample. (a) Composite emission-line map combining [O III] (blue), Hα (green), and [N II] (red), with the green circle showing the 3″ SDSS fiber aperture. (b) Map of the [O II]$\lambda\lambda$7320,7330 auroral lines where detected at $> 3\sigma$. Panels (c)–(f) show spatially resolved diagnostic diagrams: (c) the [N II] BPT diagram, (d) the [S II] BPT diagram, (e) the R23 vs. O32 diagram, and (f) the O3N2 vs. N2O2. Each point corresponds to a spaxel, color-coded as in panel (a). The yellow star represents the measurement of the global spectrum obtained from summing all spaxels with S/N$_g$ > 0.5; the green circle shows the measurement within the SDSS-equivalent 3″ aperture. White contours in (c)-(f) show the distribution of SDSS star-forming galaxies from the MPA-JHU catalogs at 1–2σ density. Gray crosses are the H II regions compiled by Pilyugin and Thuan (2005). Demarcation lines in (c) and (d) follow Kauffmann et al. (2003b), Kewley et al. (2001), and Kewley et al. (2006) as described in the main text.

Kewley et al. (2006). The spaxels span a similarly broad range in [S II]/Hα (S2), with a spread of $\sim$ 1 dex. Off-center star-forming knots show notably lower S2 than the central regions with less star formation, resulting in a $\sim$ 0.3 dex difference in S2 between the global and SDSS-equivalent spectra. The discrepancy between SDSS galaxies and individual H II regions is even more pronounced in this diagram: most H II regions lie outside the 2σ SDSS contour, indicating the different ionization conditions. Spaxels from the bluest star-forming regions match the H II region distribution, whereas the rest (with lower $\Sigma_{\rm SFR}$) align with SDSS fiber-based measurements.

Panels (e) and (f) show additional diagnostic diagrams that are sensitive to gas-phase metallicity, nitrogen enrichment, and ionization parameters. The R23–O32 diagram (panel e) shows considerable variation in O32 ($\sim$ 1 dex), while the R23 values display smaller dispersion. This is likely because the R_{23} ratios of most spaxels are near the saturation limit of $\sim$ 1, where R23 becomes relatively insensitive to changes in metallicity. In the O3N2–N2O2 diagram (f), we observe dispersions of $\sim$ 1.5 dex in O3N2 and $\sim$ 0.8 dex in N2O2, again exceeding typical measurement uncertainties and revealing the diversity in ionized gas conditions.

Although strong nebular lines are detected throughout the galaxy, the auroral lines [O II]$\lambda\lambda$7320,7330, which are essential for determining direct T_e-based metallicities from KCWI red-channel data cubes, are only detected in a few spaxels located at the centers of the star-forming knots (panel b). However, we detect [O II]$\lambda\lambda$7320,7330 in the global spectrum at a significance level of 6.7σ. Given that the strong nebular [O II] and [O III] lines are observed across all spaxels, it is likely that the T_e metallicity derived from the global spectrum differs from that of the individual spaxels where the auroral lines are detected. A systematic comparison between T_e metallicities derived from the global spectrum and from individual spaxels will be crucial for understanding how to reconcile empirical strong-line calibrations based on T_e measurements of individual H II regions (Pilyugin, Grebel, and Mattsson, 2012) with those inferred from stacked SDSS spectra (Curti et al., 2020).

Taken together, these results demonstrate that line ratios measured from integrated spectra, whether using small, centered or larger, global apertures, can differ significantly from spatially resolved measurements. This reflects the complexity and heterogeneity of nebular conditions within galaxies and suggests that integrated diagnostics may overlook small-scale structures and gradients. Consequently, a systematic analysis of how line fluxes and derived quantities like metallicity vary with the choice of aperture is crucial. We also need to explore whether these biases depend on global galaxy properties such as stellar mass, size, and SFR to understand whether any corrections would be needed when only an integrated spectrum is available.

5.4 Appendix: KCWI Maps of the Entire Sample

Below, I present the color images and spatially resolved properties for the remaining galaxies in my KCWI sample, following the format of Figure 5.3.

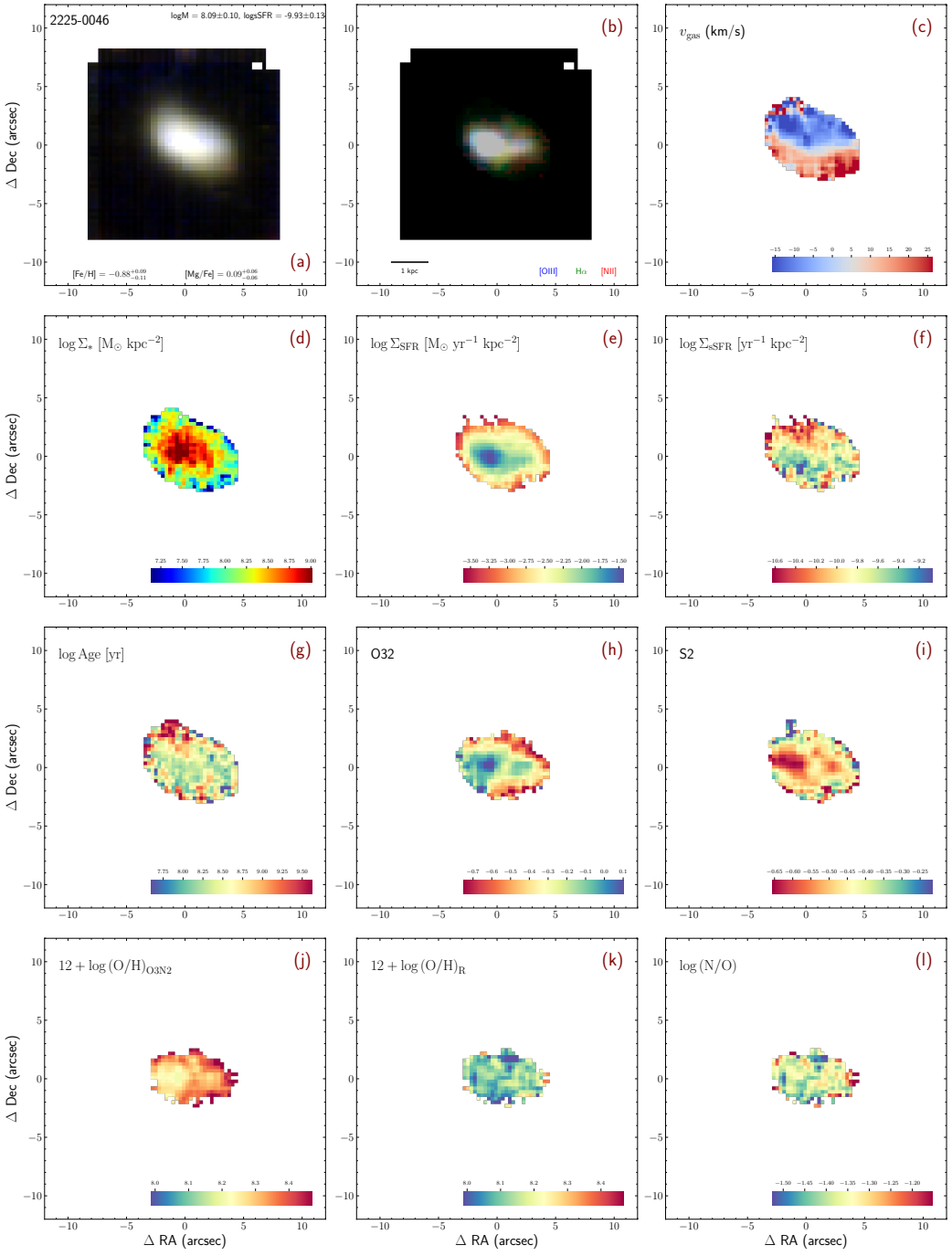

Figure 5.5: Same as Figure 5.3, but for galaxy 2225-0046.

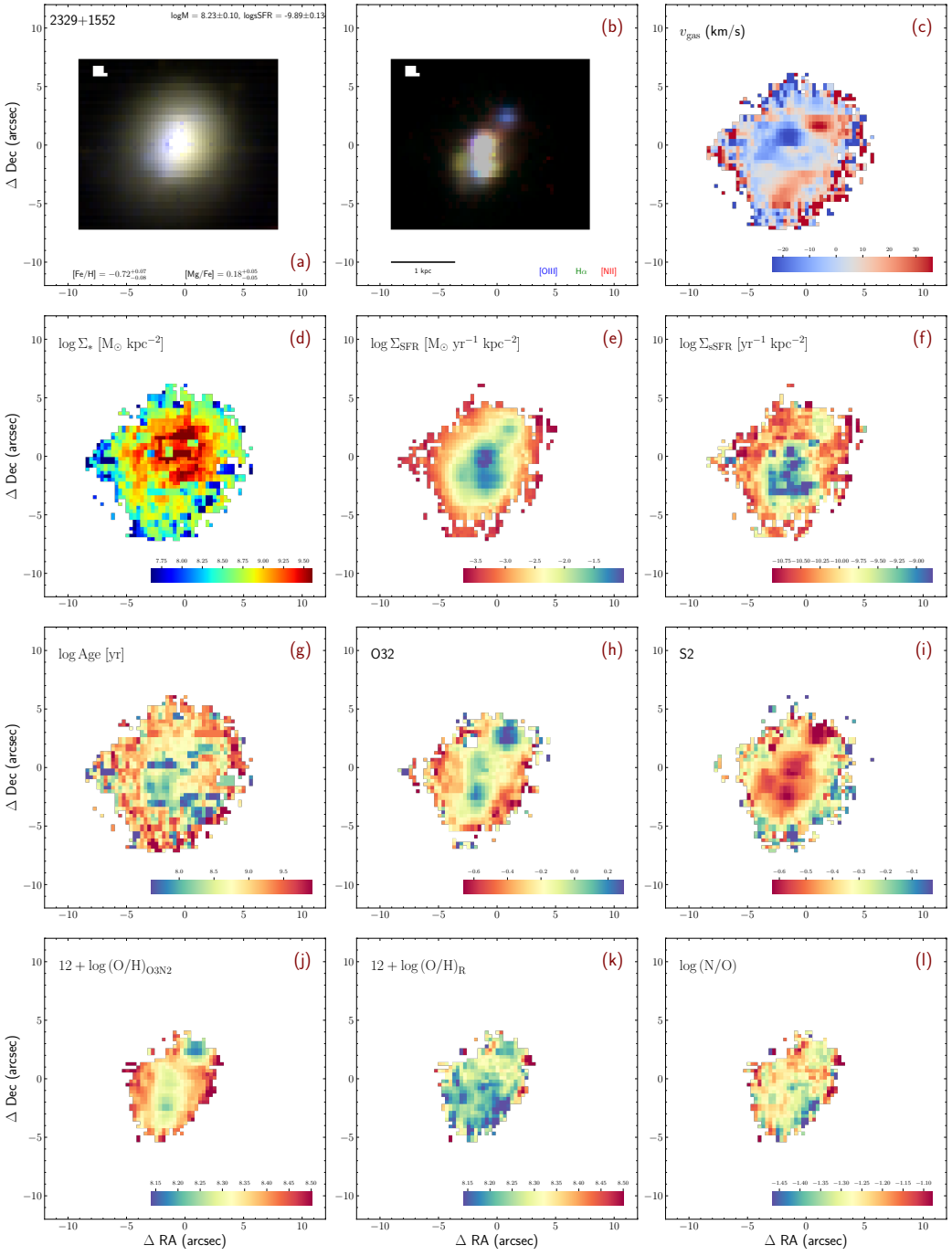

Figure 5.6: Same as Figure 5.3, but for galaxy 2329+1552.

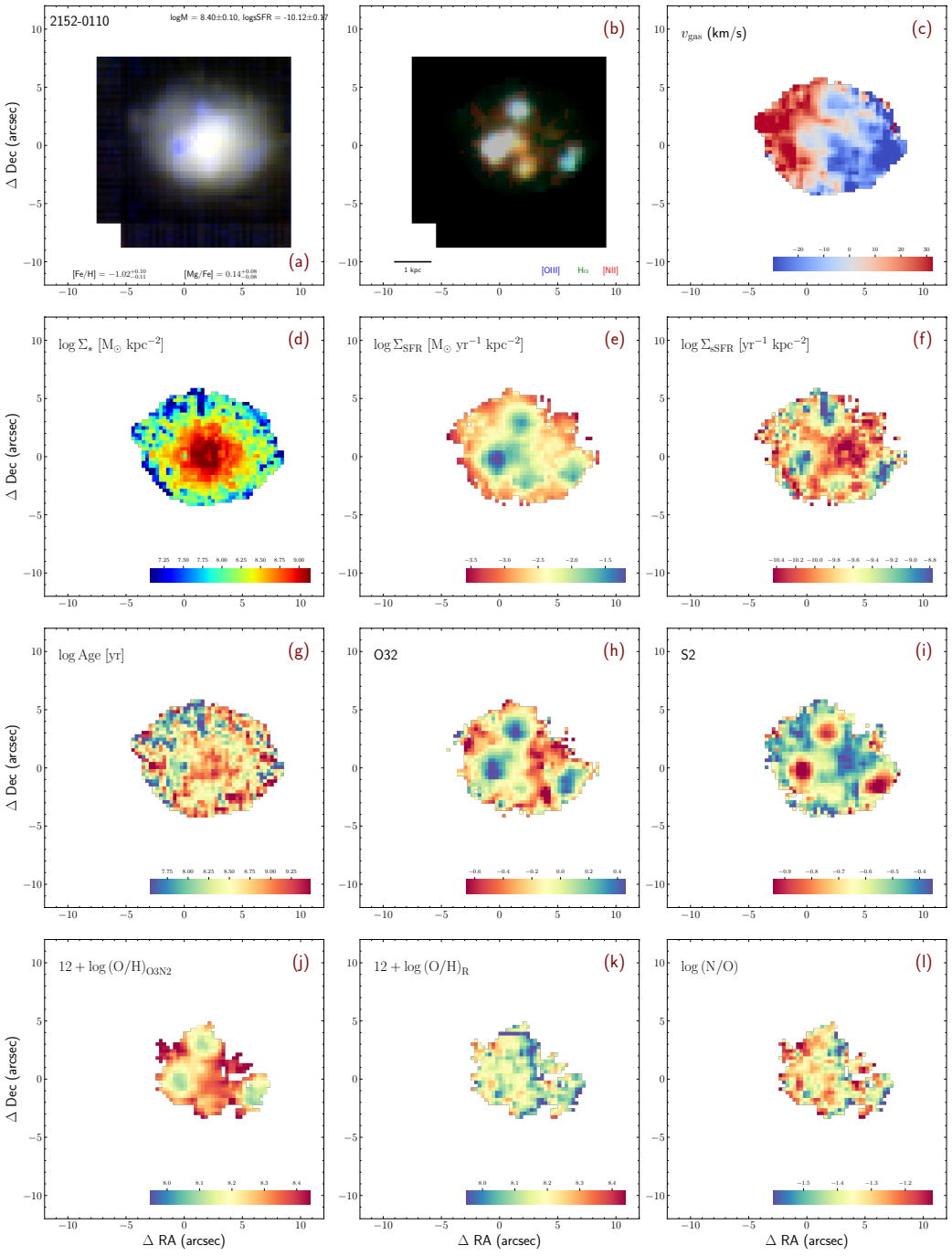

Figure 5.7: Same as Figure 5.3, but for galaxy 2152-0110.

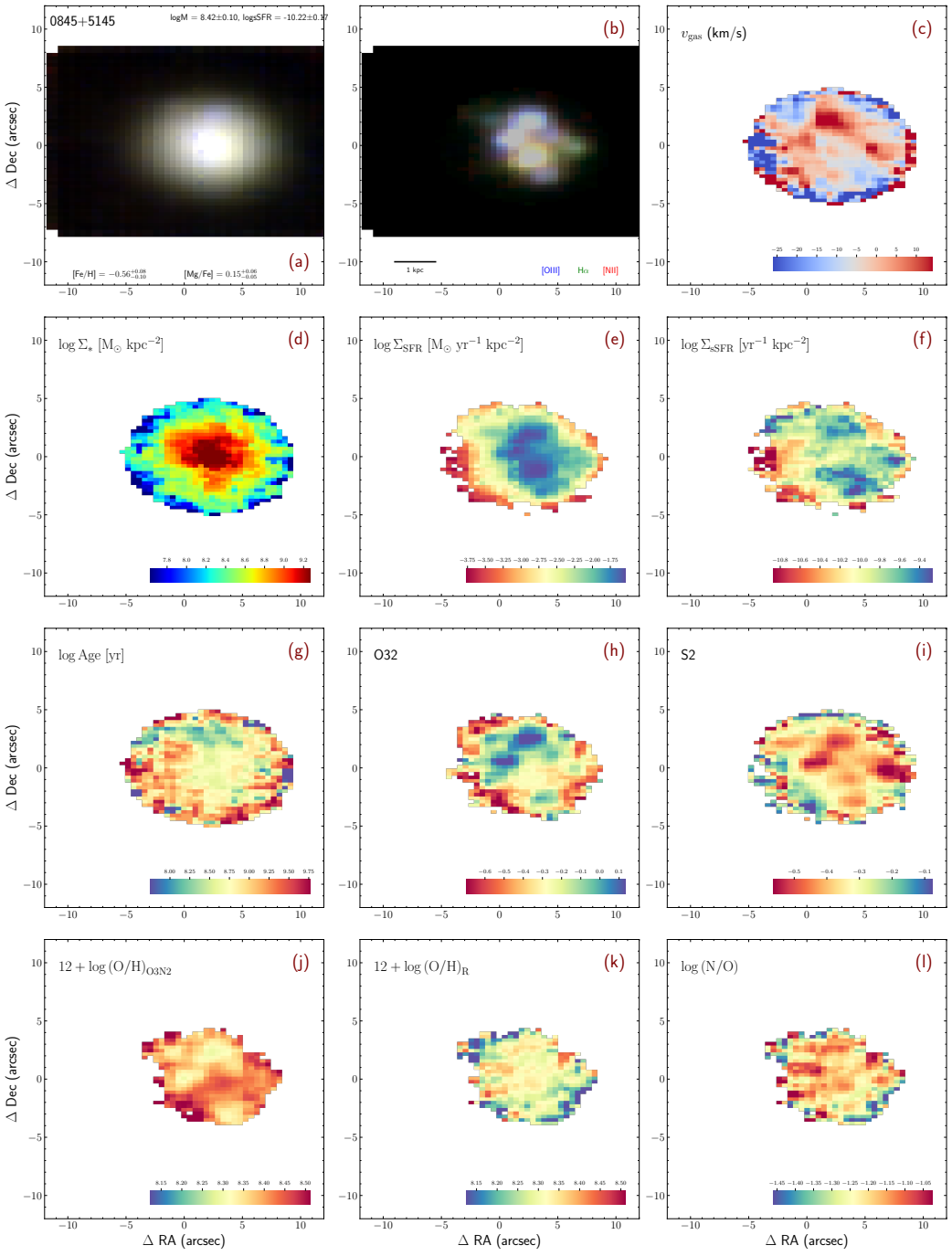

Figure 5.8: Same as Figure 5.3, but for galaxy 0845+5145.

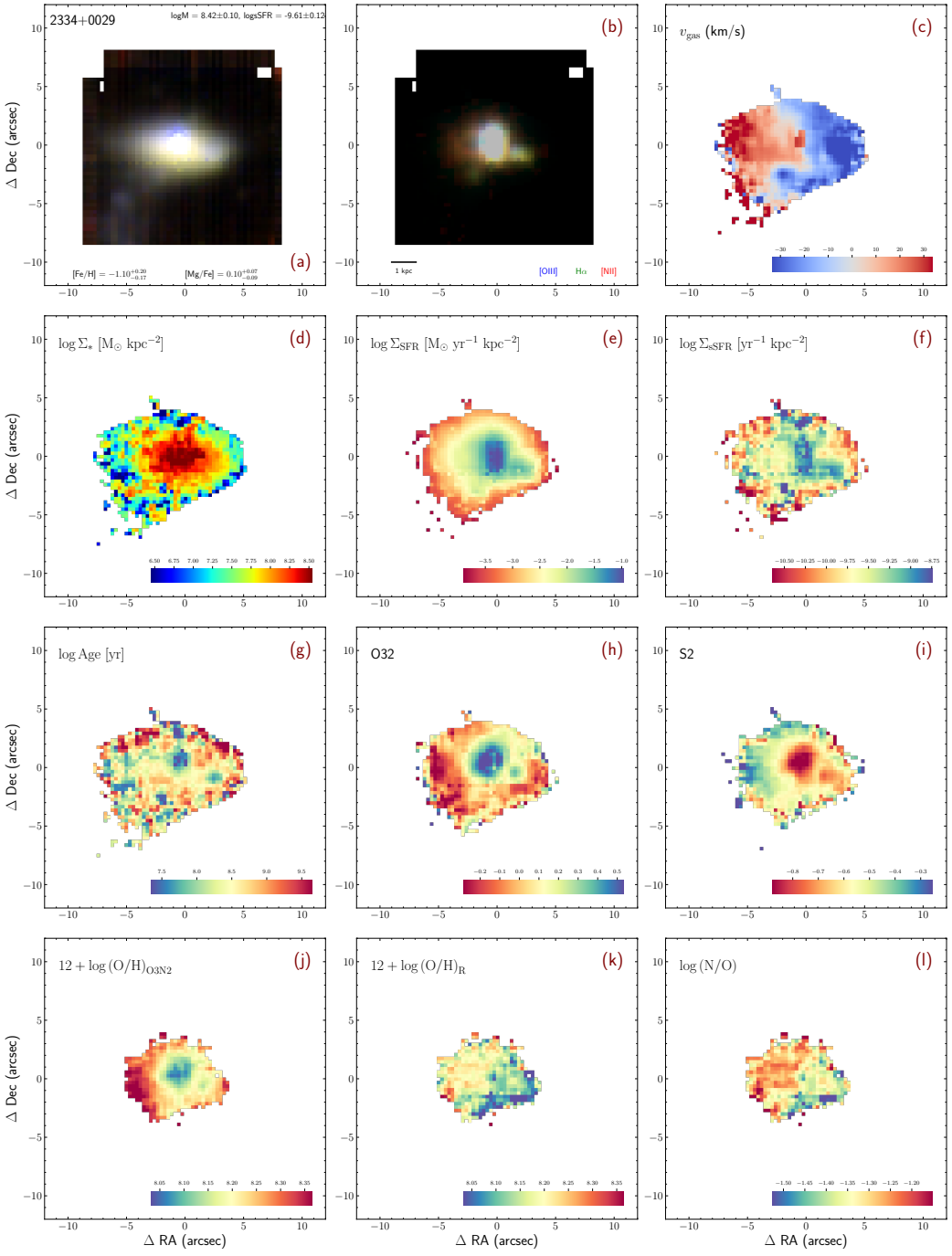

Figure 5.9: Same as Figure 5.3, but for galaxy 2334+0029.

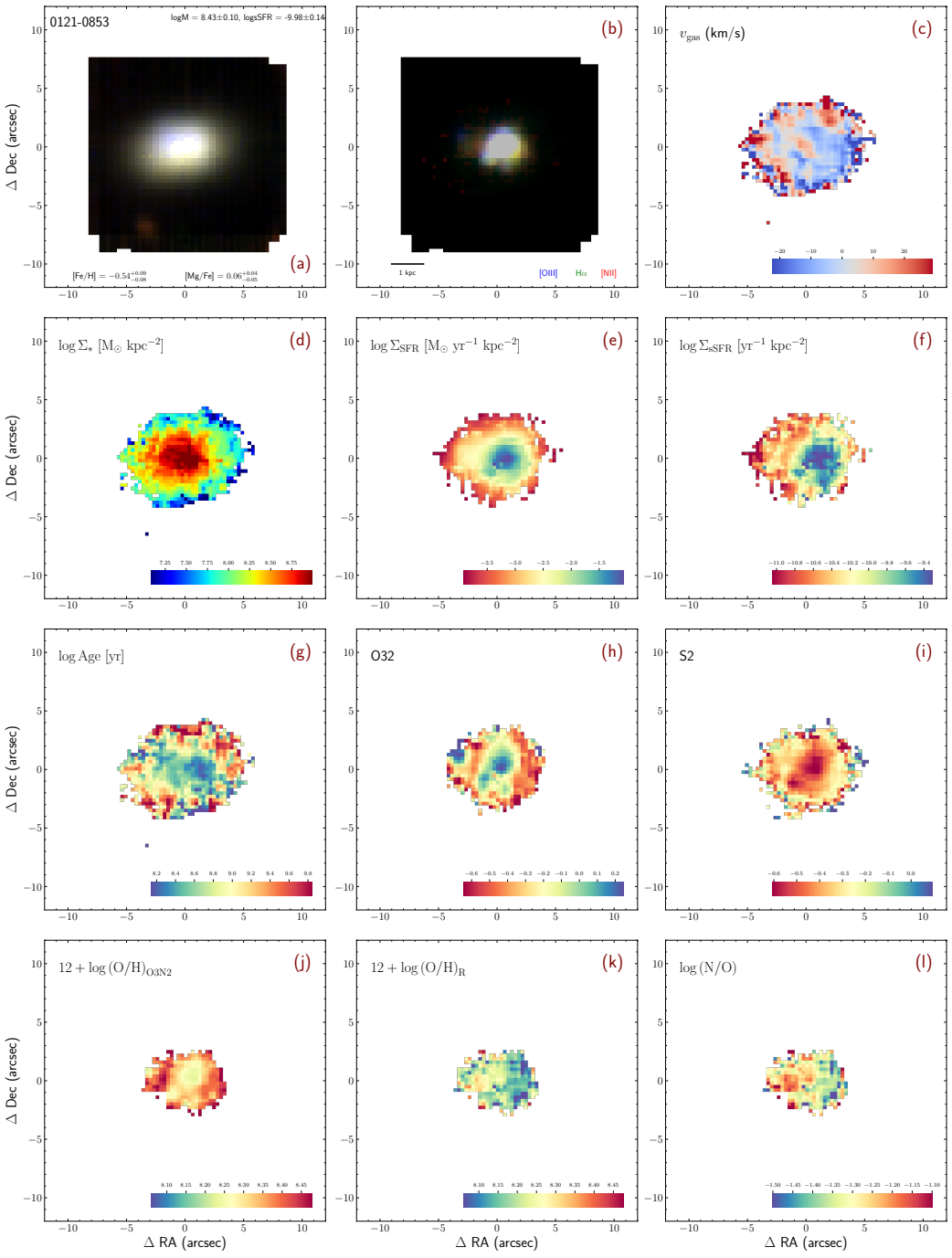

Figure 5.10: Same as Figure 5.3, but for galaxy 0121-0853.

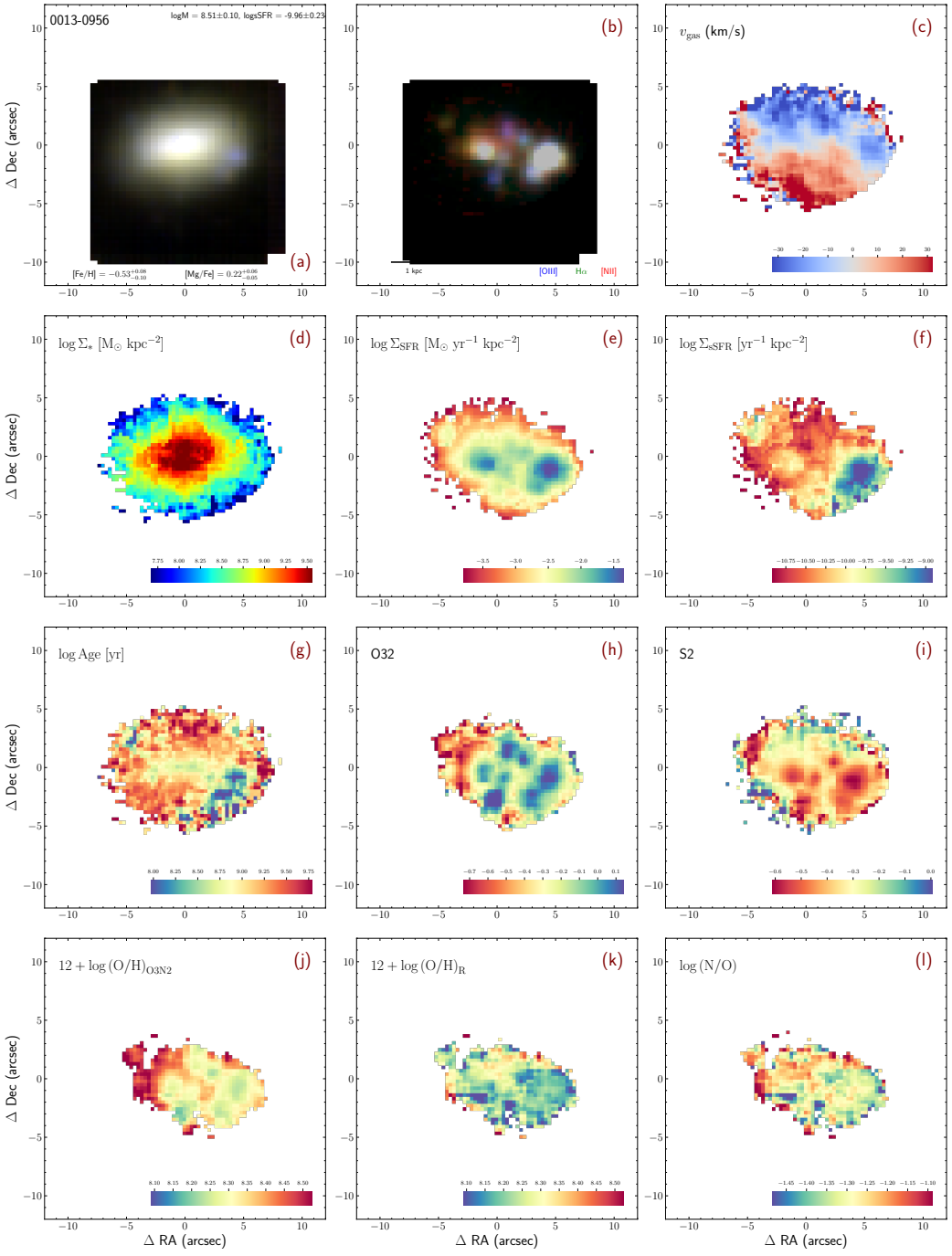

Figure 5.11: Same as Figure 5.3, but for galaxy 0013-0956.

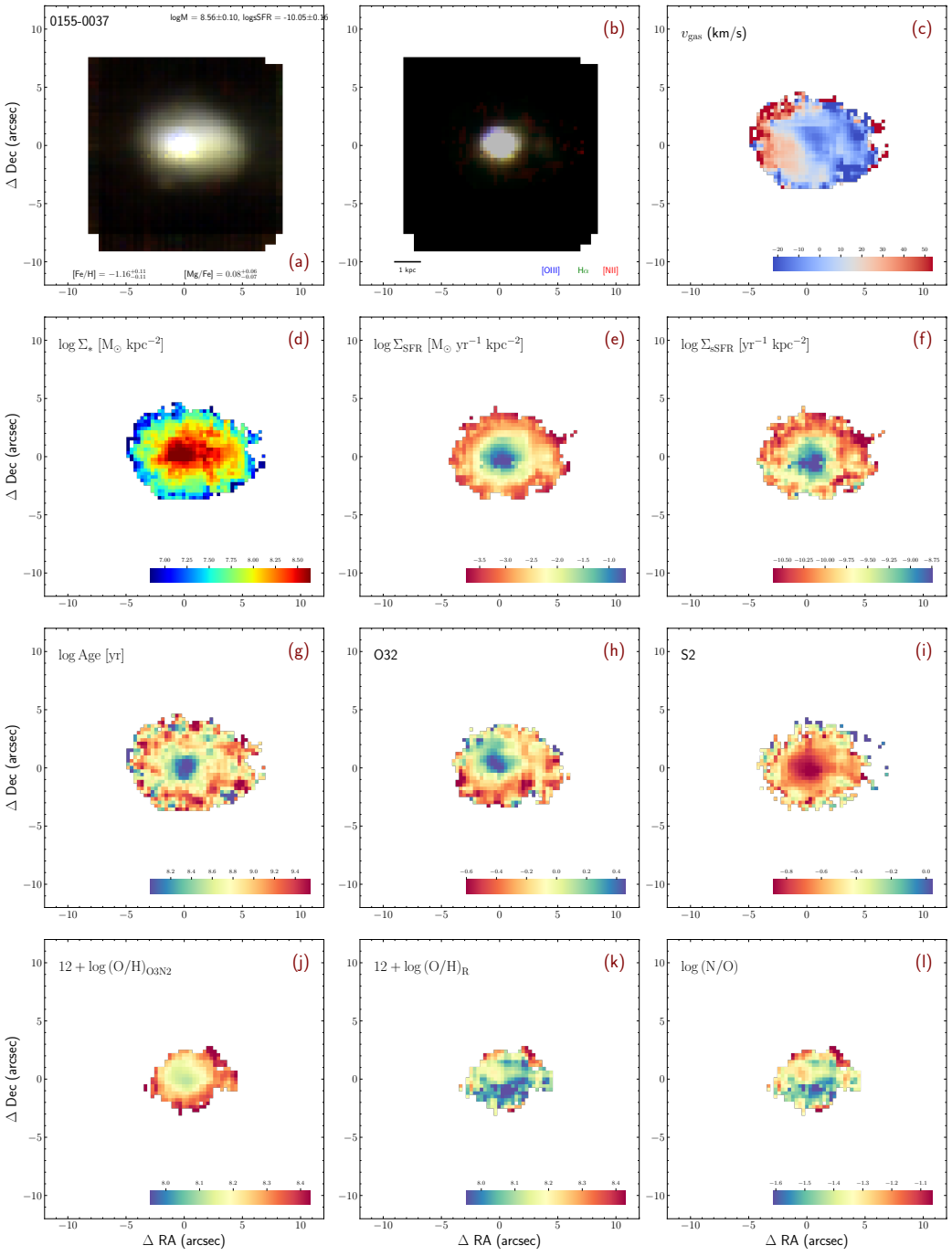

Figure 5.12: Same as Figure 5.3, but for galaxy 0155-0037.

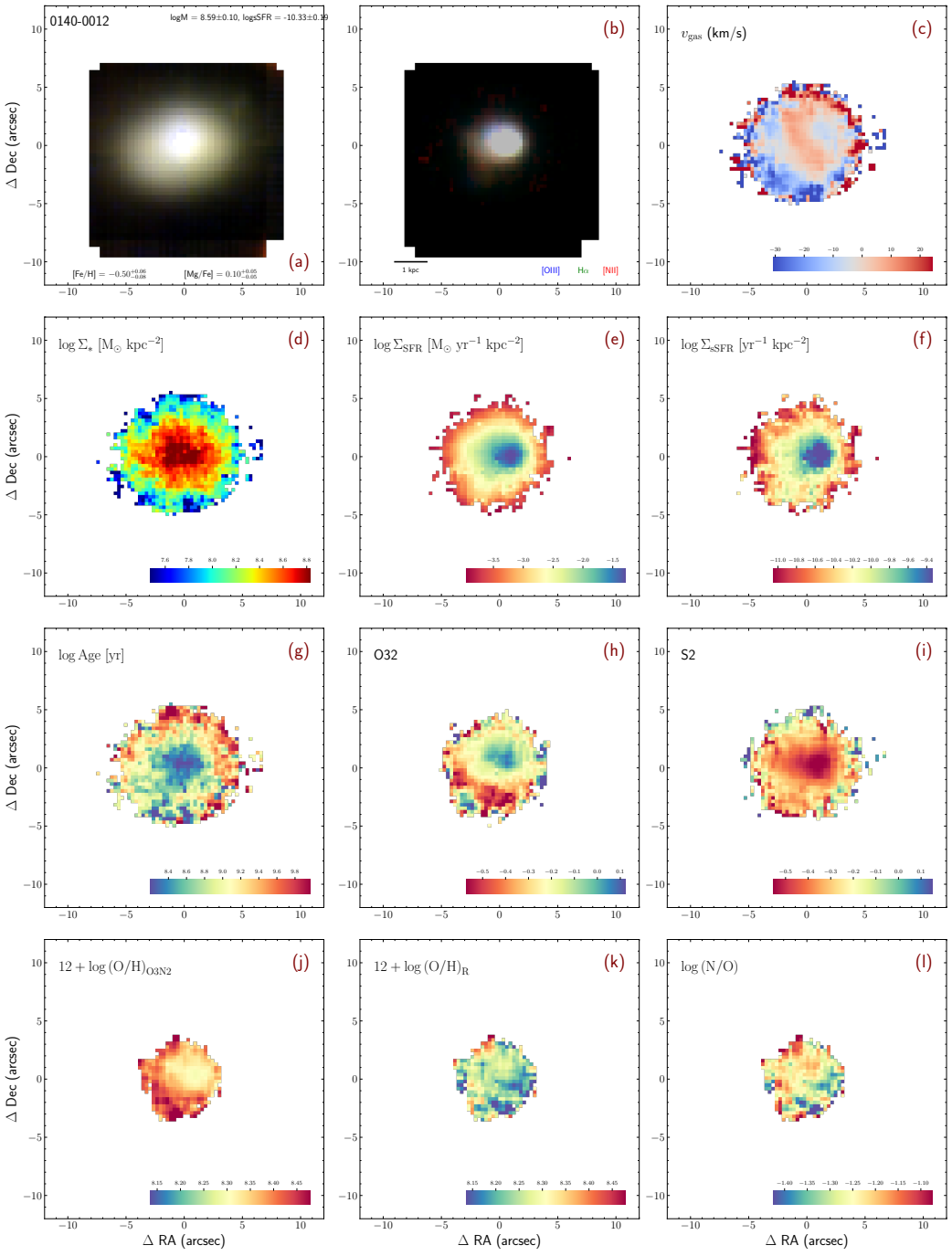

Figure 5.13: Same as Figure 5.3, but for galaxy 0140-0012.

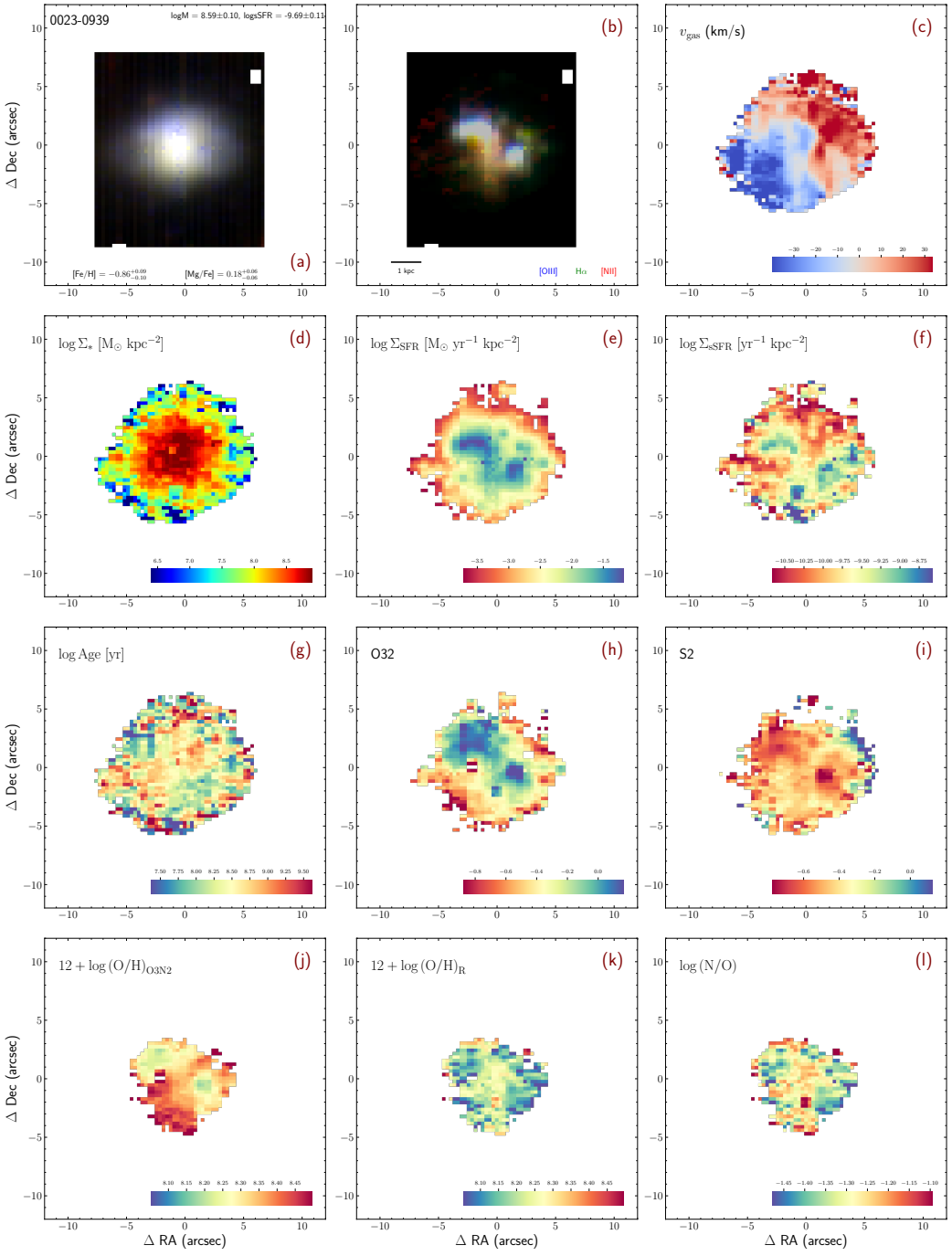

Figure 5.14: Same as Figure 5.3, but for galaxy 0023-0939.

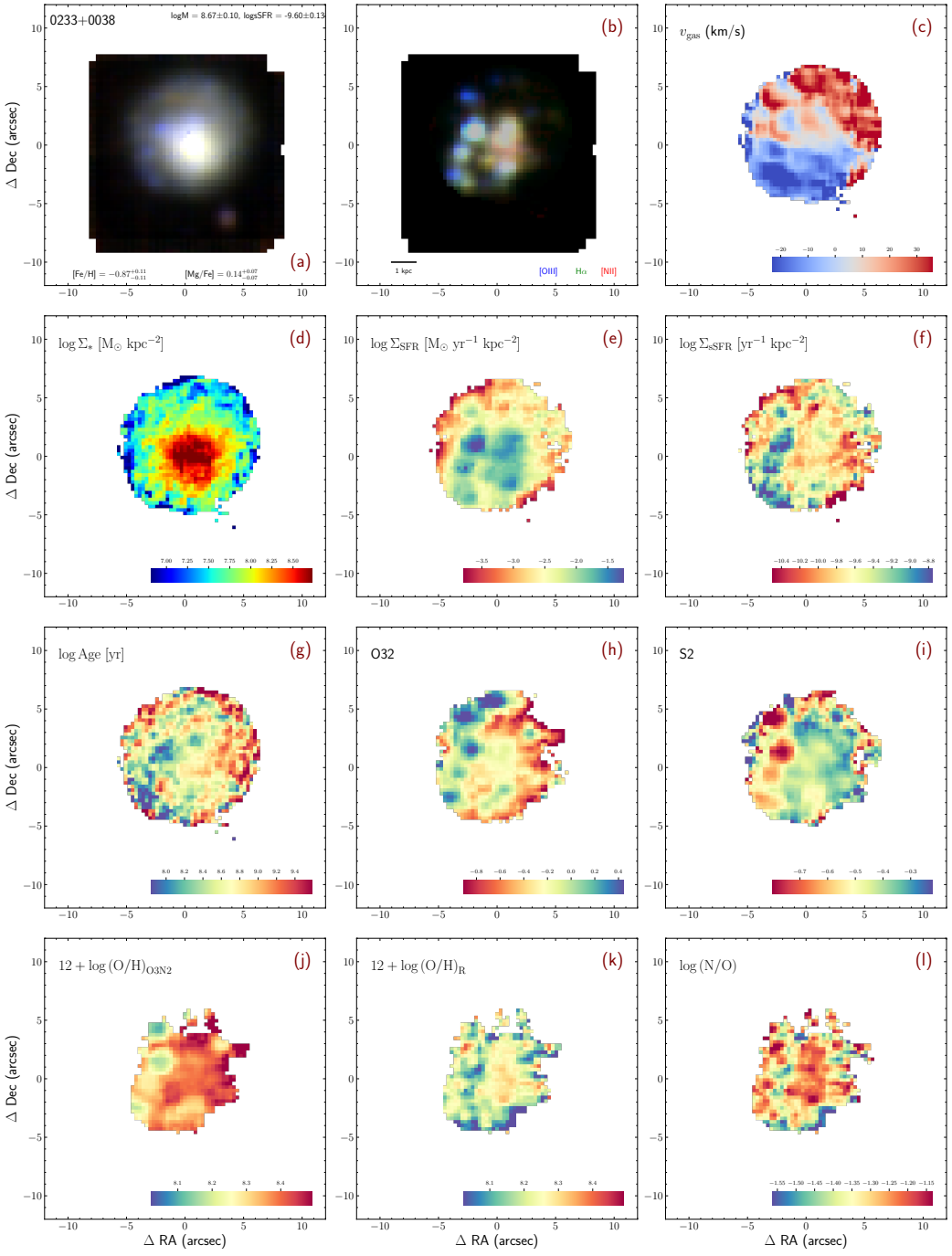

Figure 5.15: Same as Figure 5.3, but for galaxy 0233+0038.

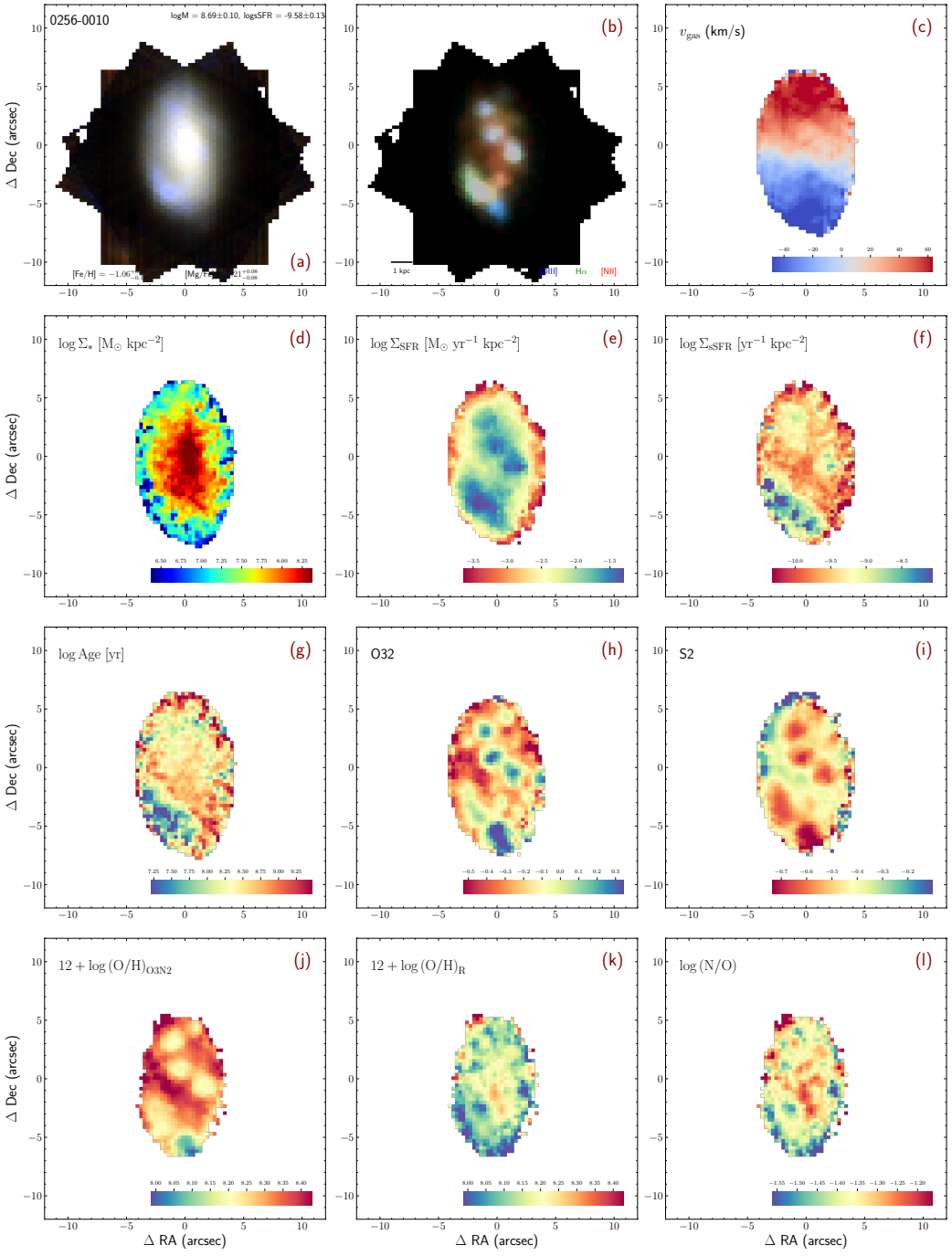

Figure 5.16: Same as Figure 5.3, but for galaxy 0256-0010.

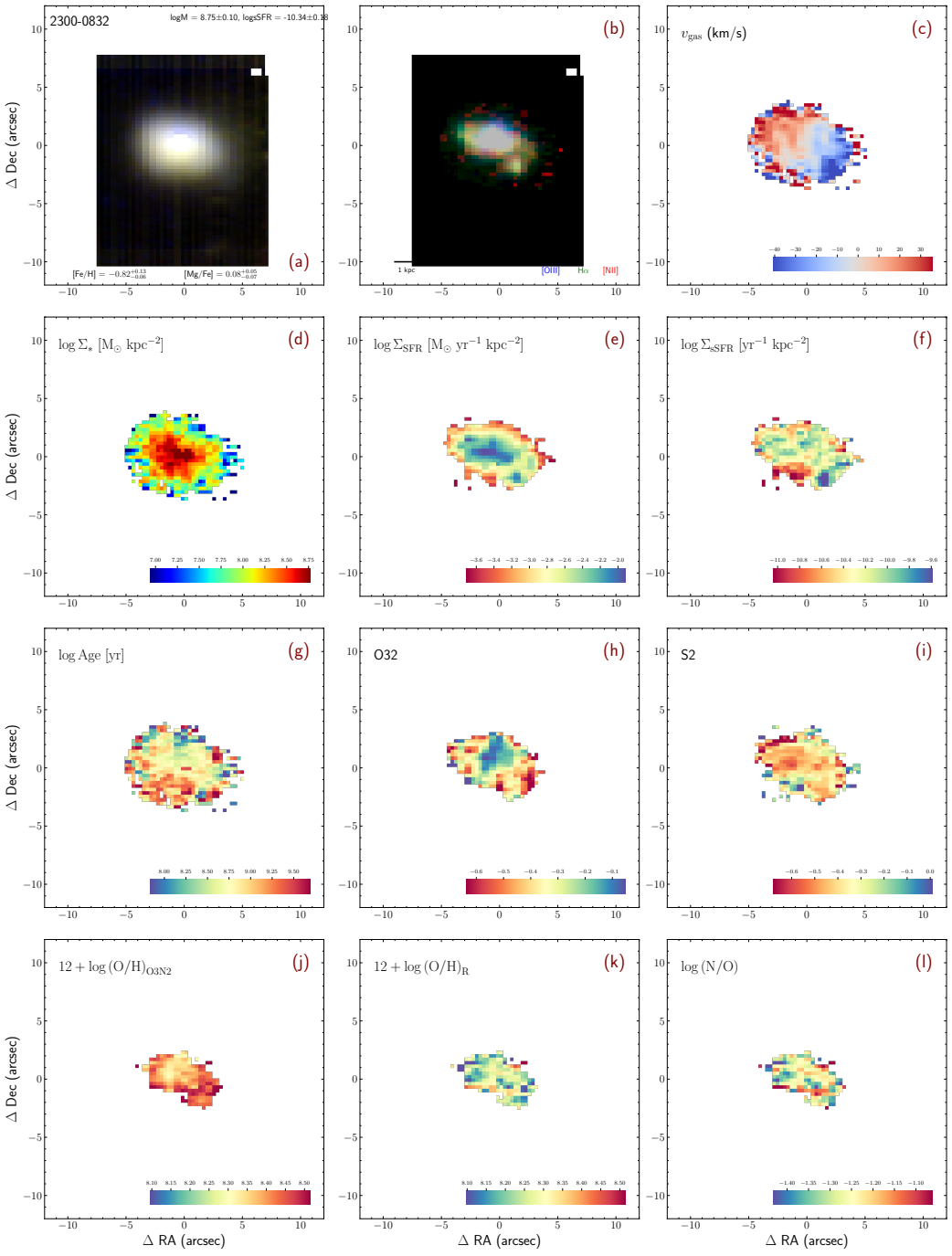

Figure 5.17: Same as Figure 5.3, but for galaxy 2300-0832.

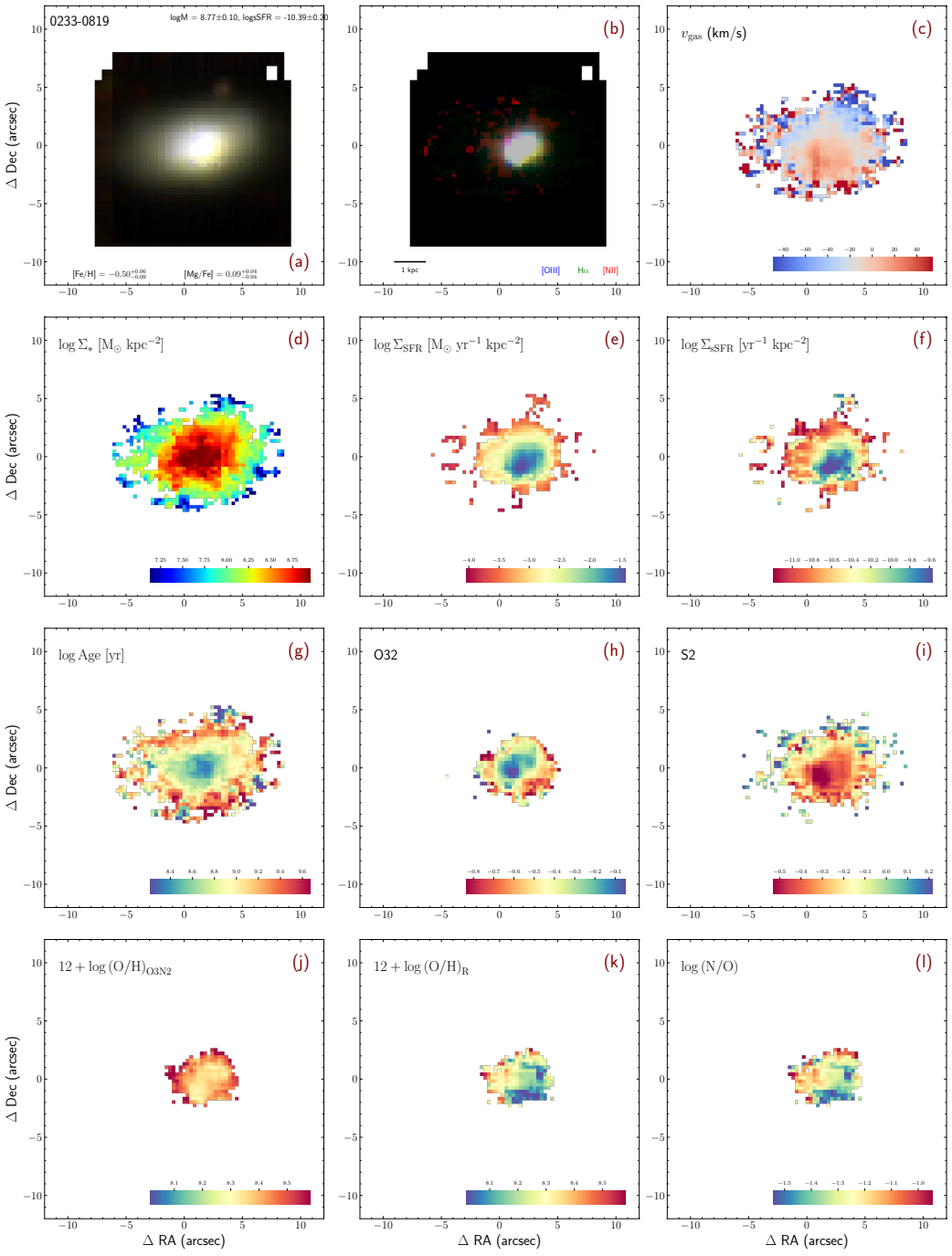

Figure 5.18: Same as Figure 5.3, but for galaxy 0233-0819.

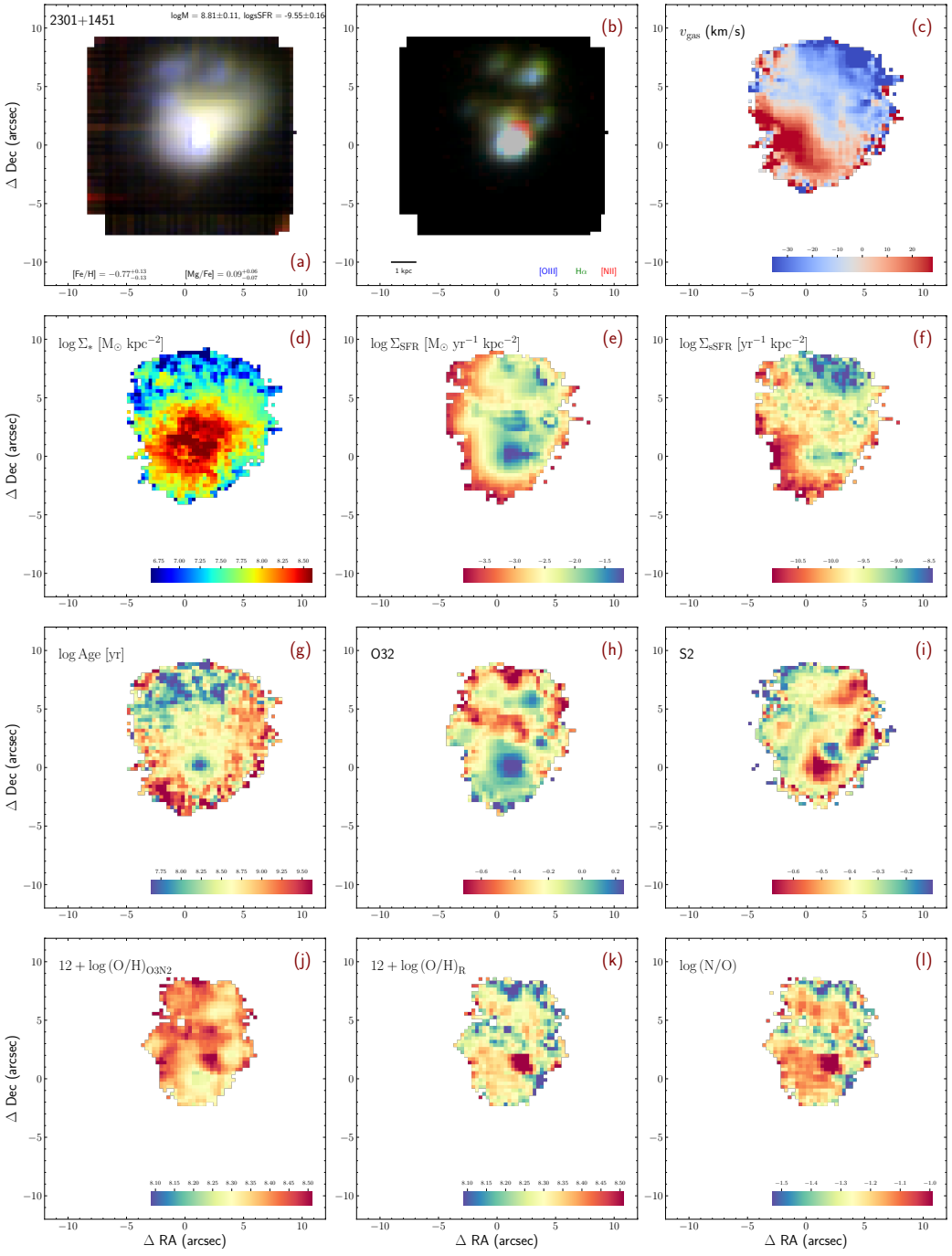

Figure 5.19: Same as Figure 5.3, but for galaxy 2301+1451.

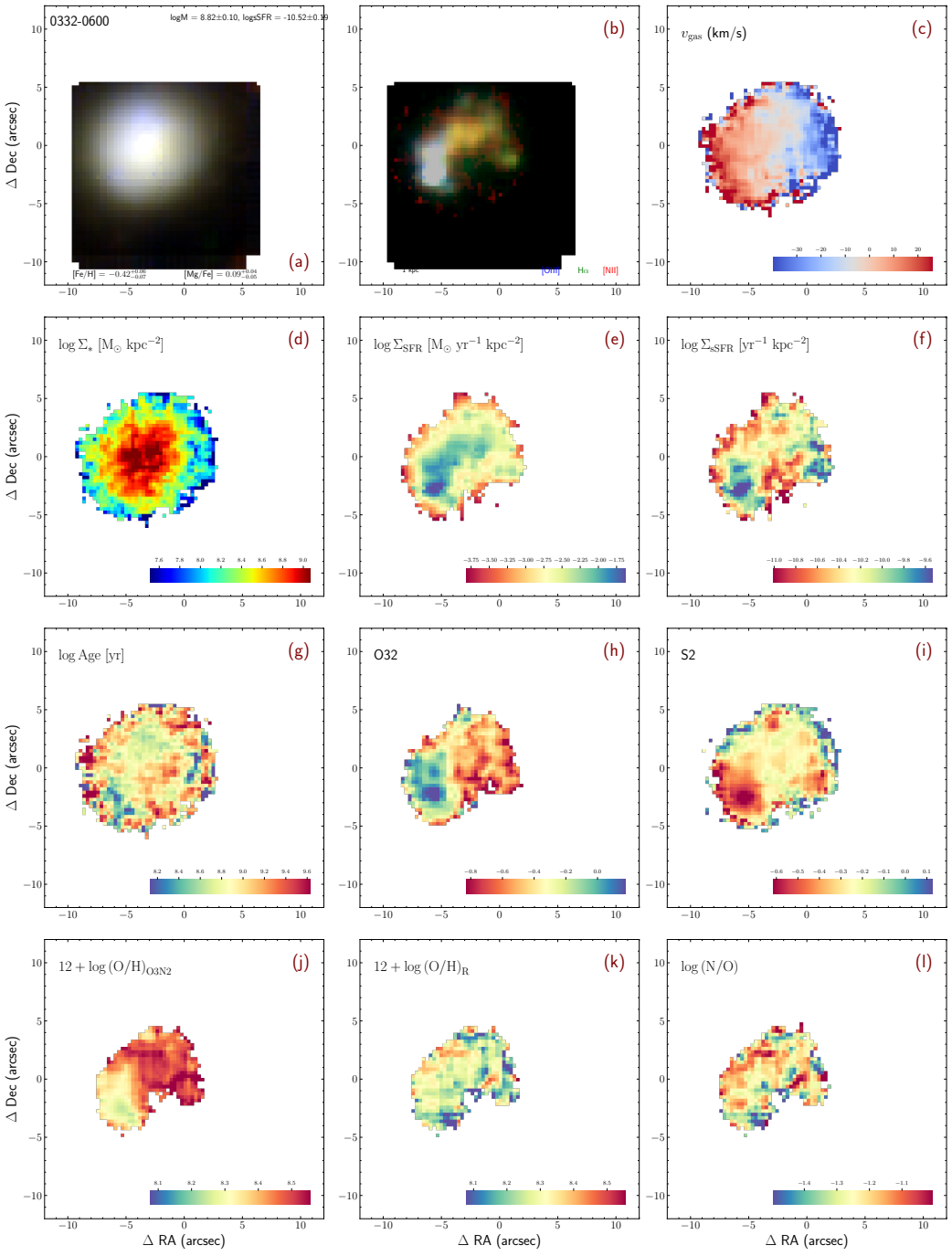

Figure 5.20: Same as Figure 5.3, but for galaxy 0332-0600.

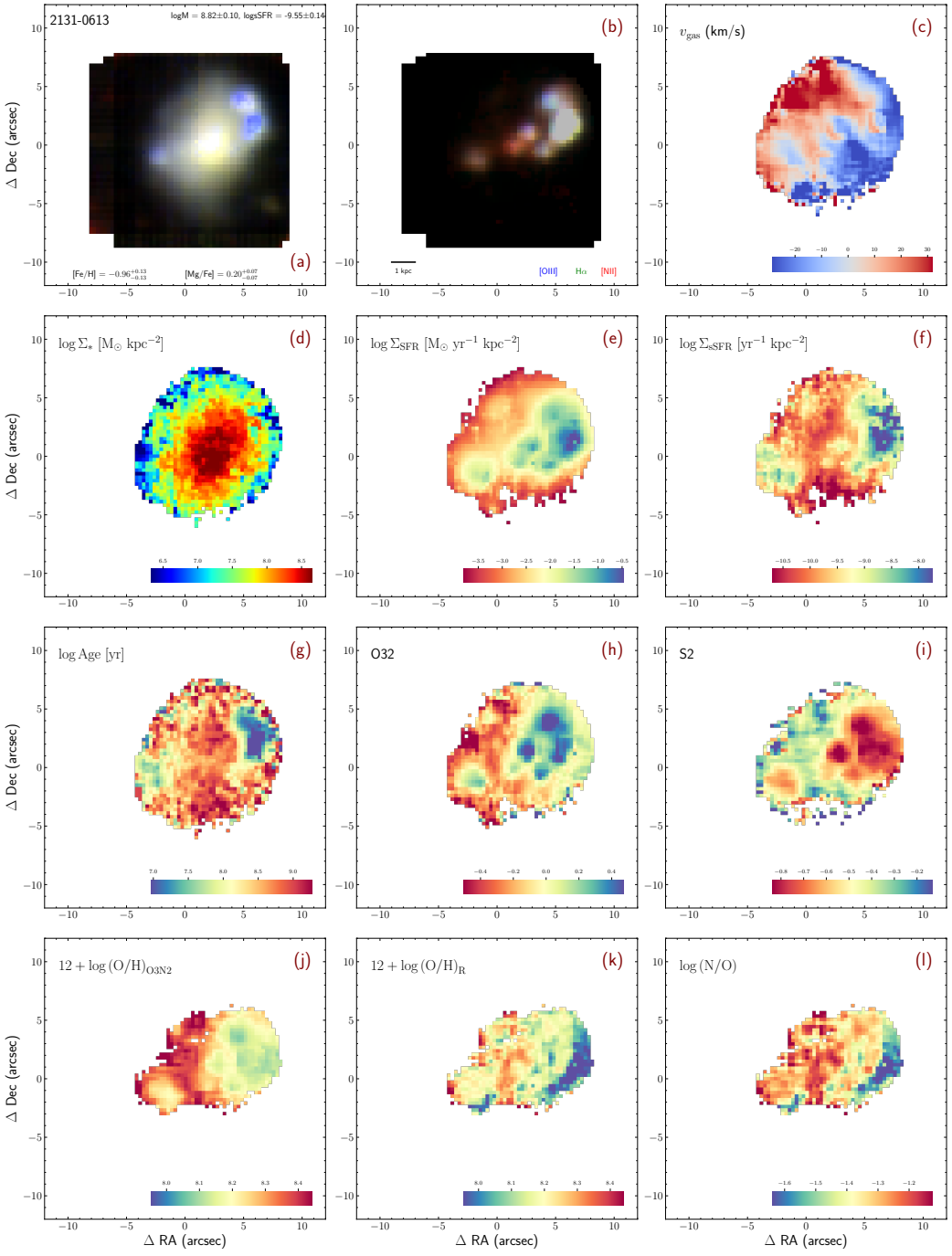

Figure 5.21: Same as Figure 5.3, but for galaxy 2131-0613.

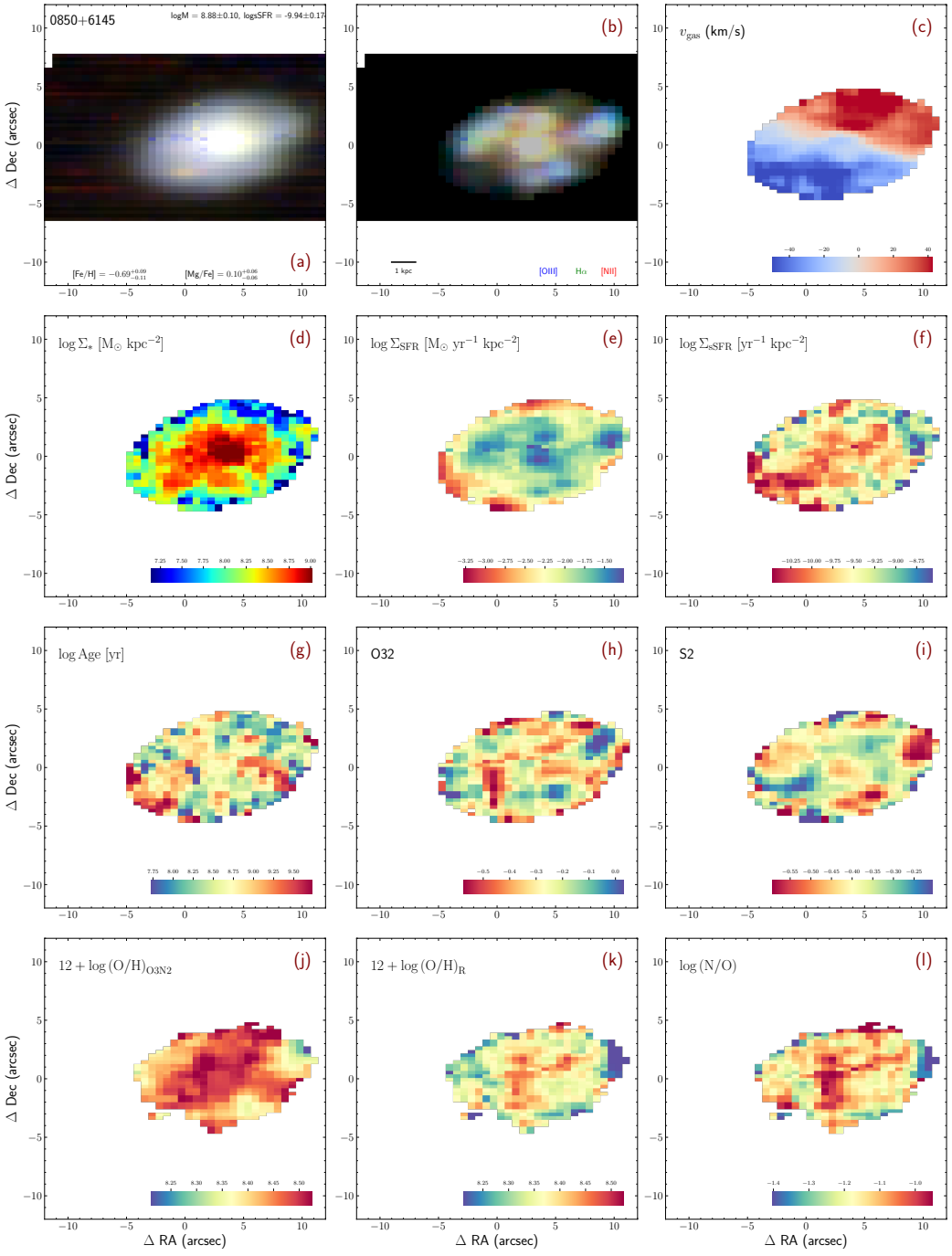

Figure 5.22: Same as Figure 5.3, but for galaxy 0850+6145.

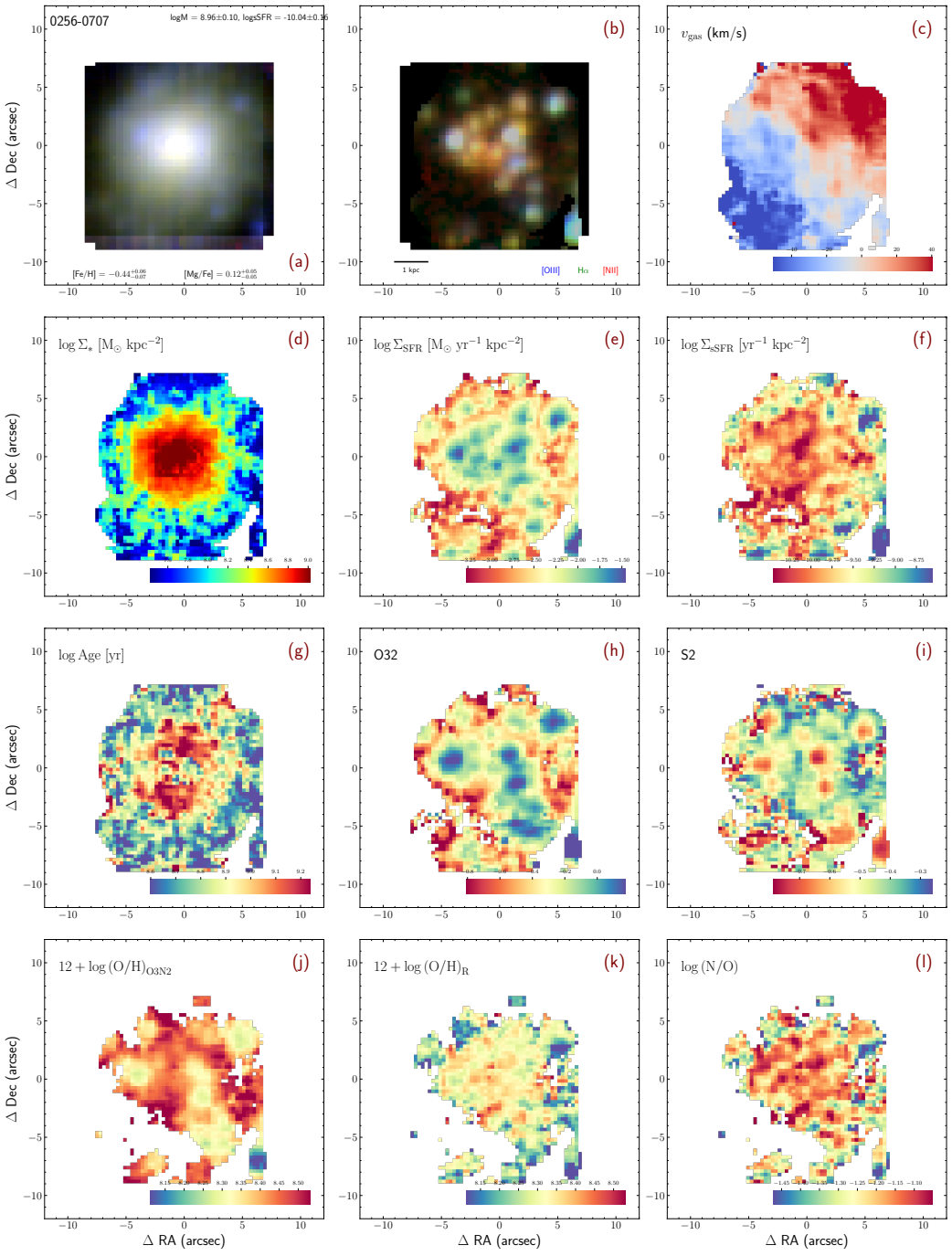

Figure 5.23: Same as Figure 5.3, but for galaxy 0256-0707.

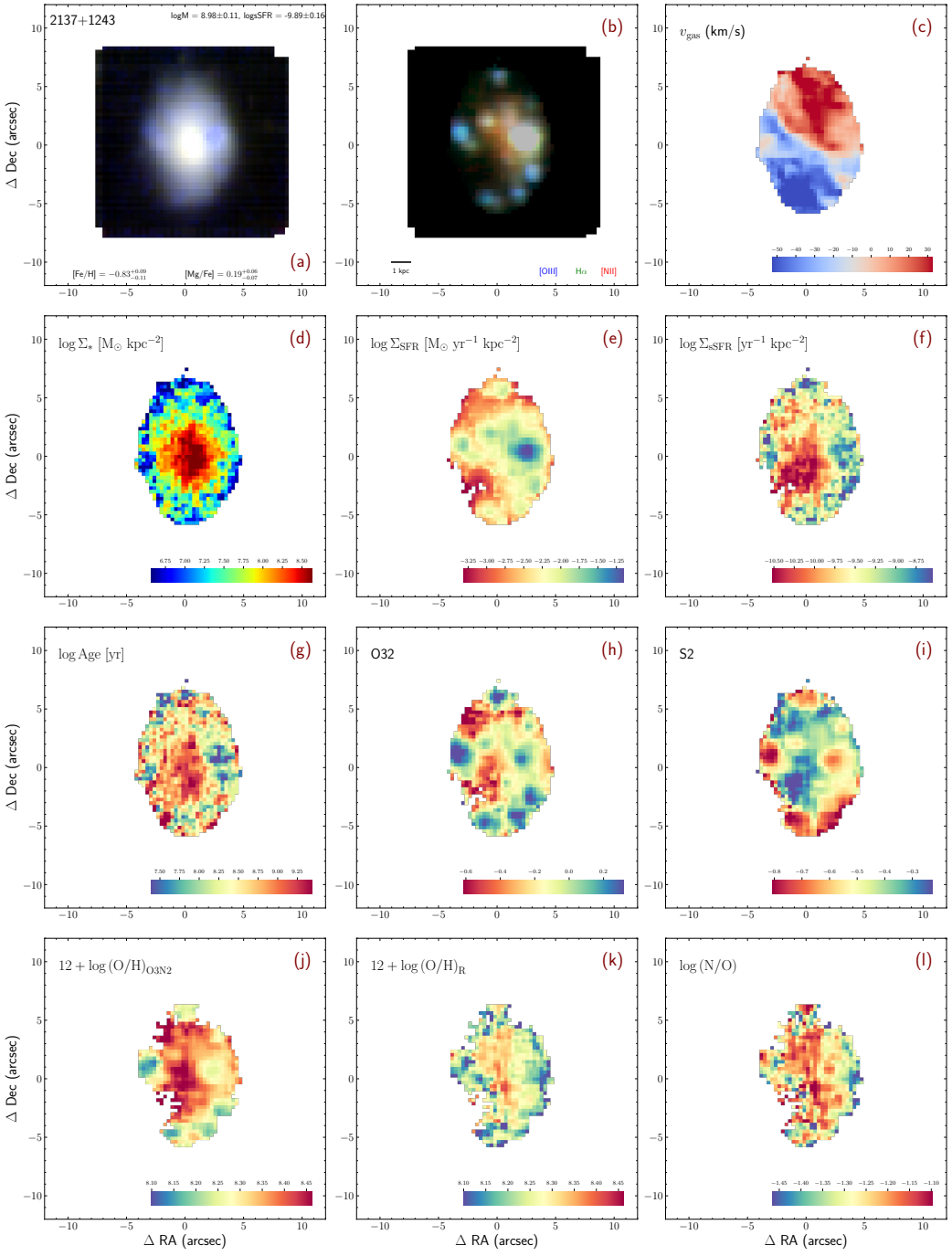

Figure 5.24: Same as Figure 5.3, but for galaxy 2137+1243.

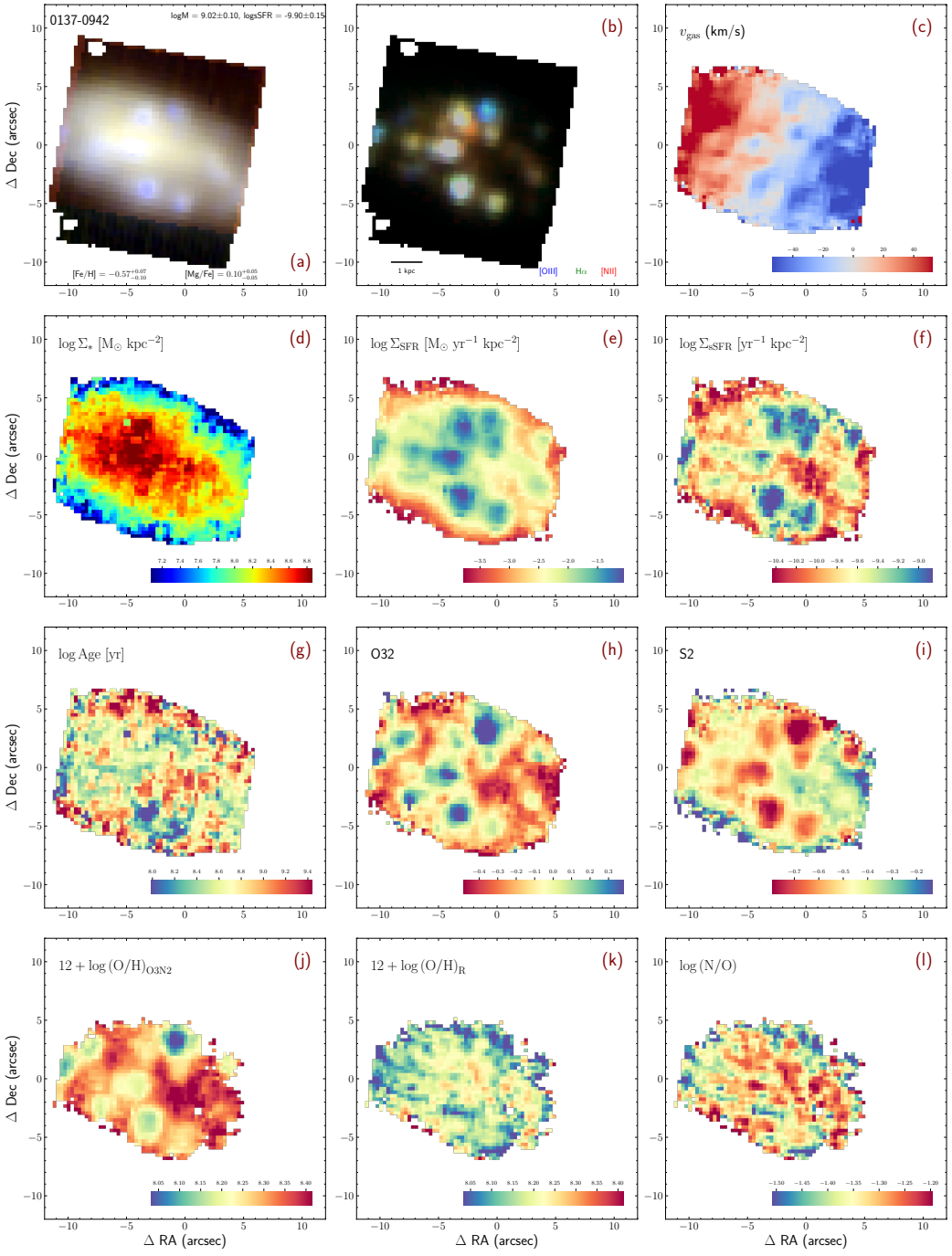

Figure 5.25: Same as Figure 5.3, but for galaxy 0137-0942.

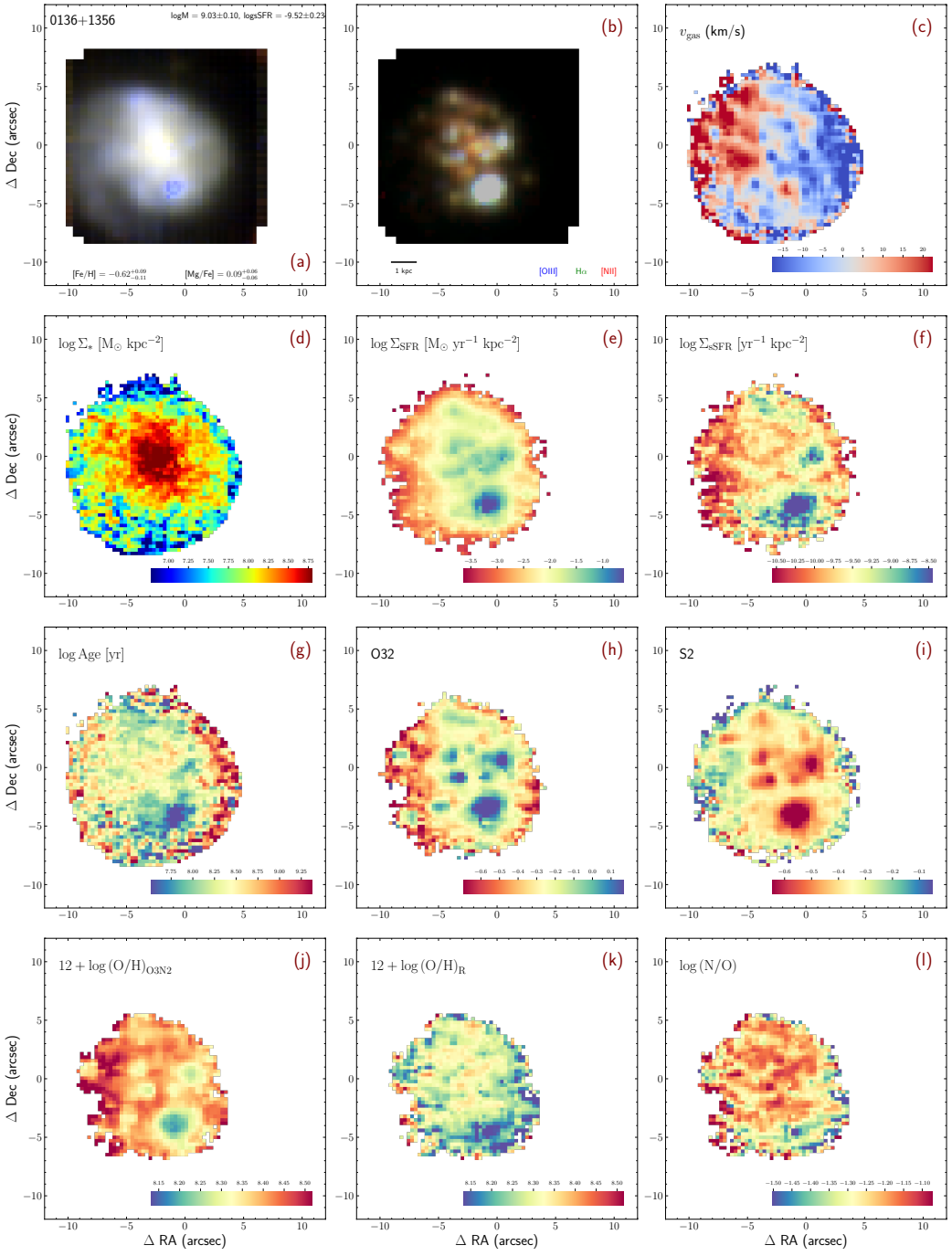

Figure 5.26: Same as Figure 5.3, but for galaxy 0136+1356.

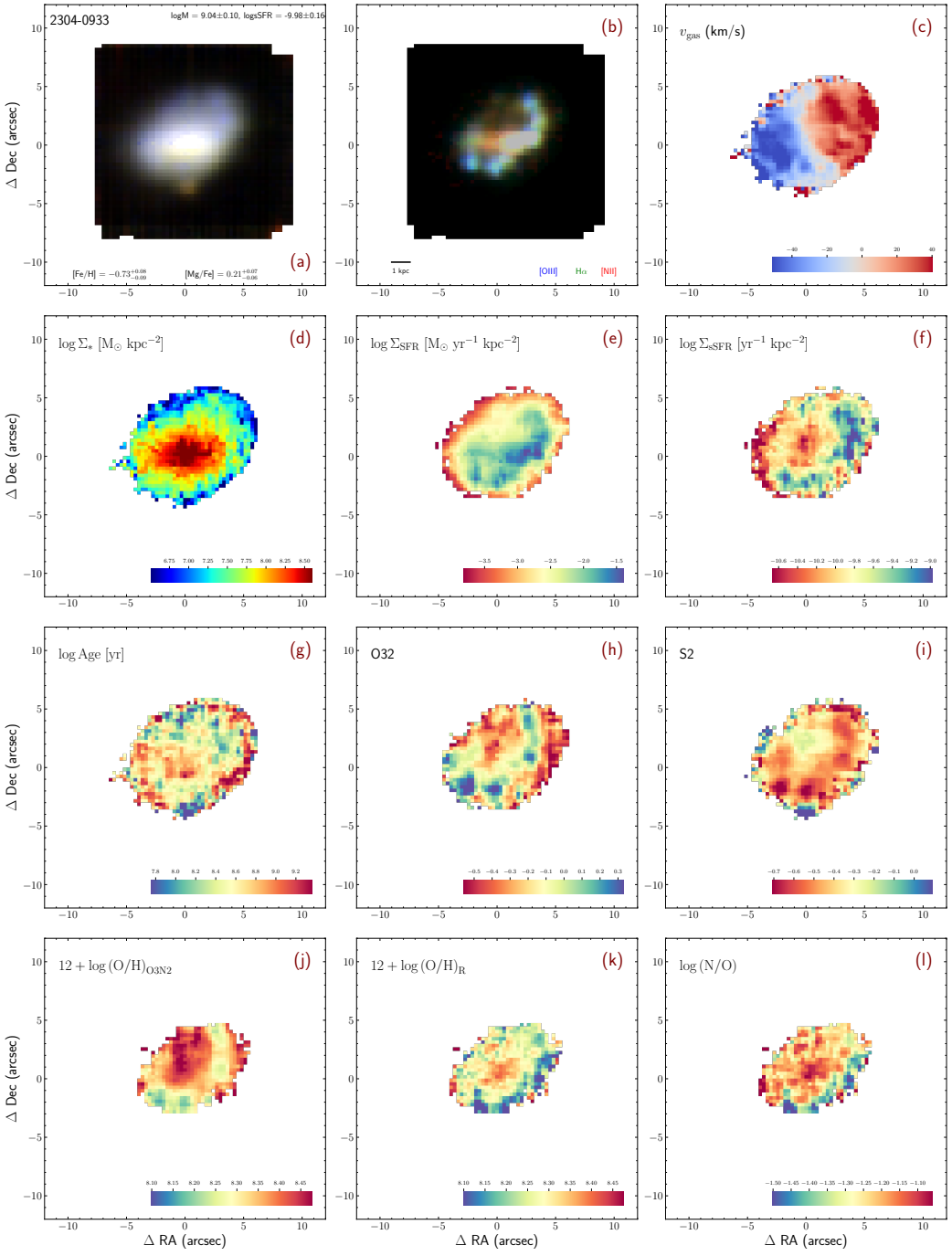

Figure 5.27: Same as Figure 5.3, but for galaxy 2304-0933.

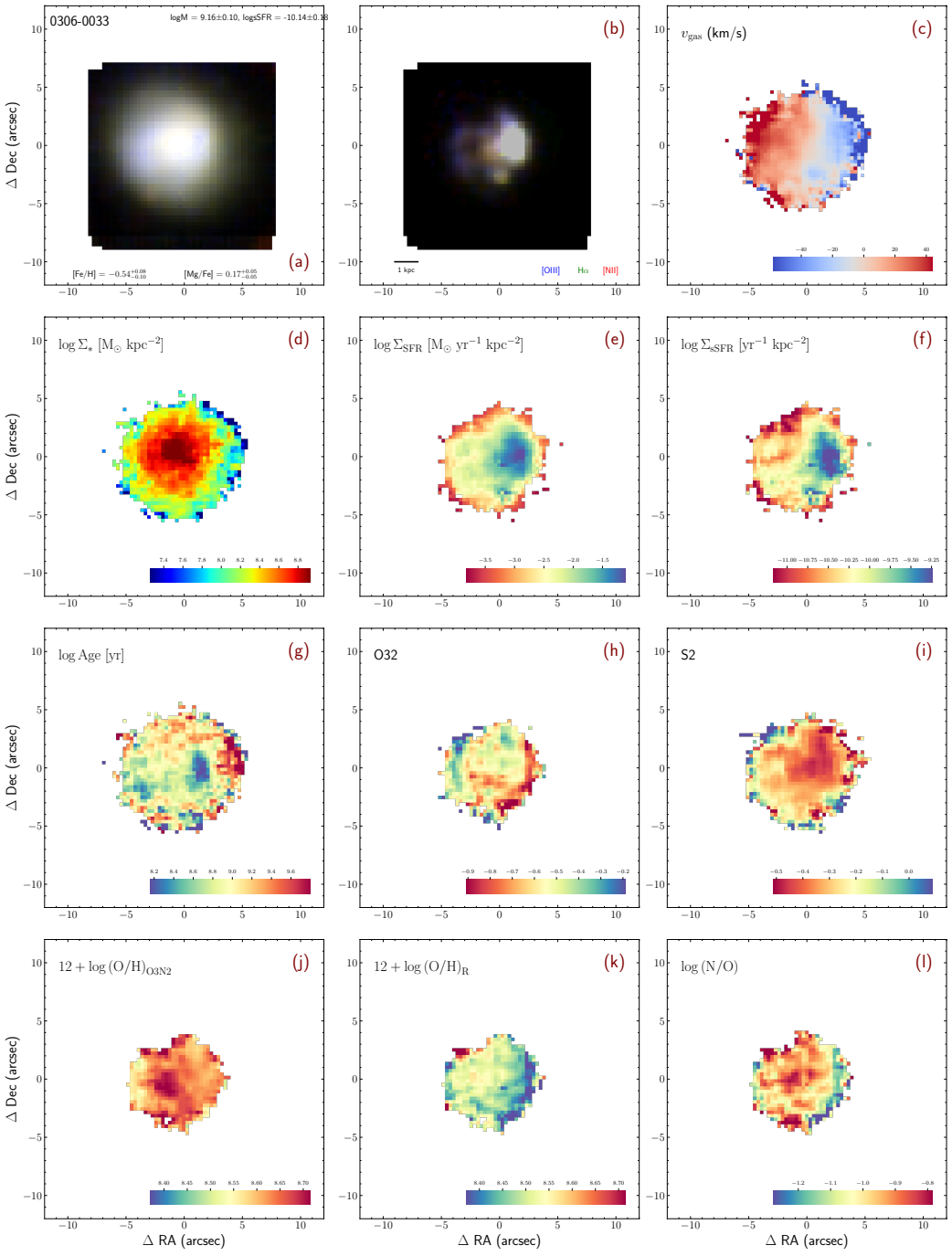

Figure 5.28: Same as Figure 5.3, but for galaxy 0306-0033.

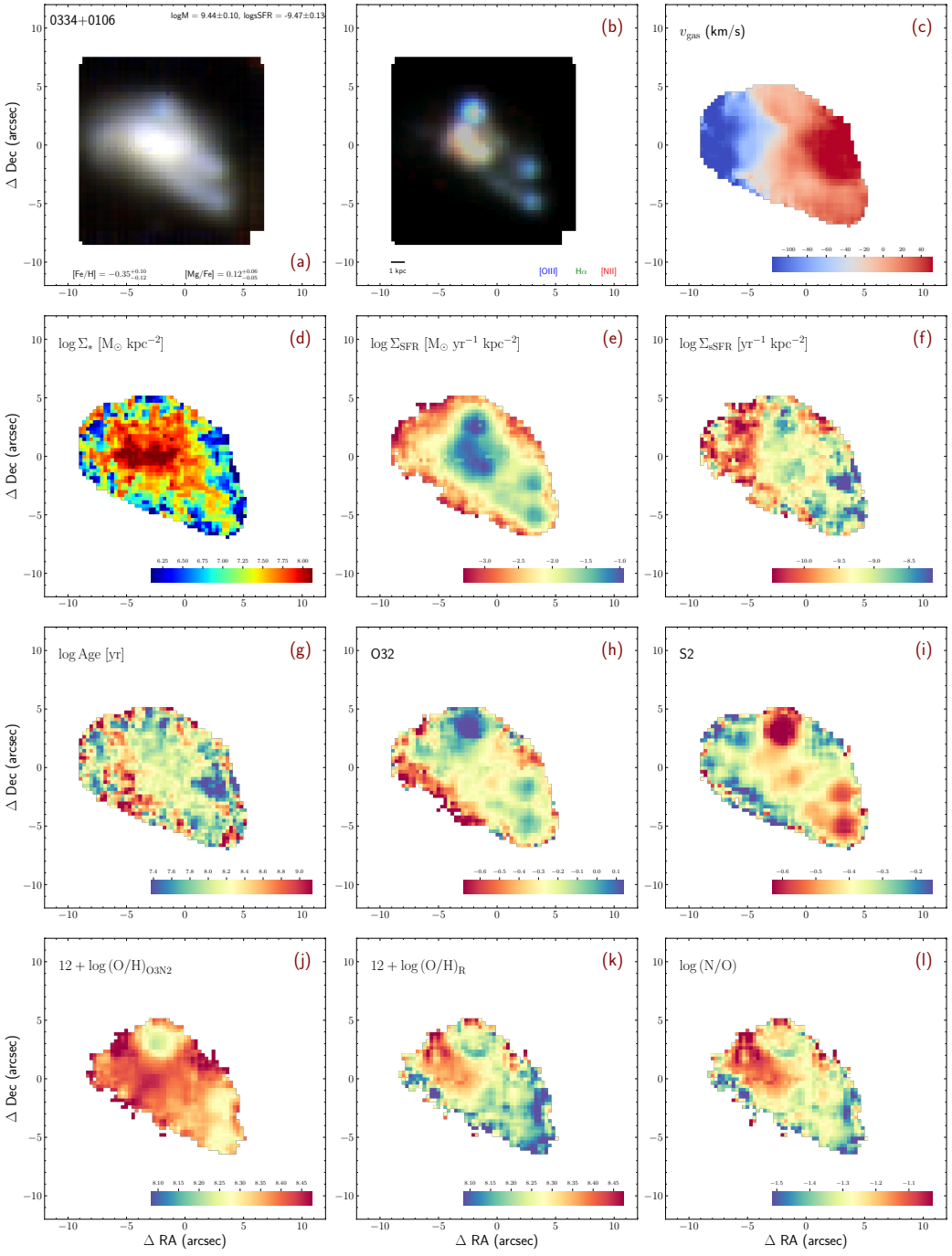

Figure 5.29: Same as Figure 5.3, but for galaxy 0334+0106.

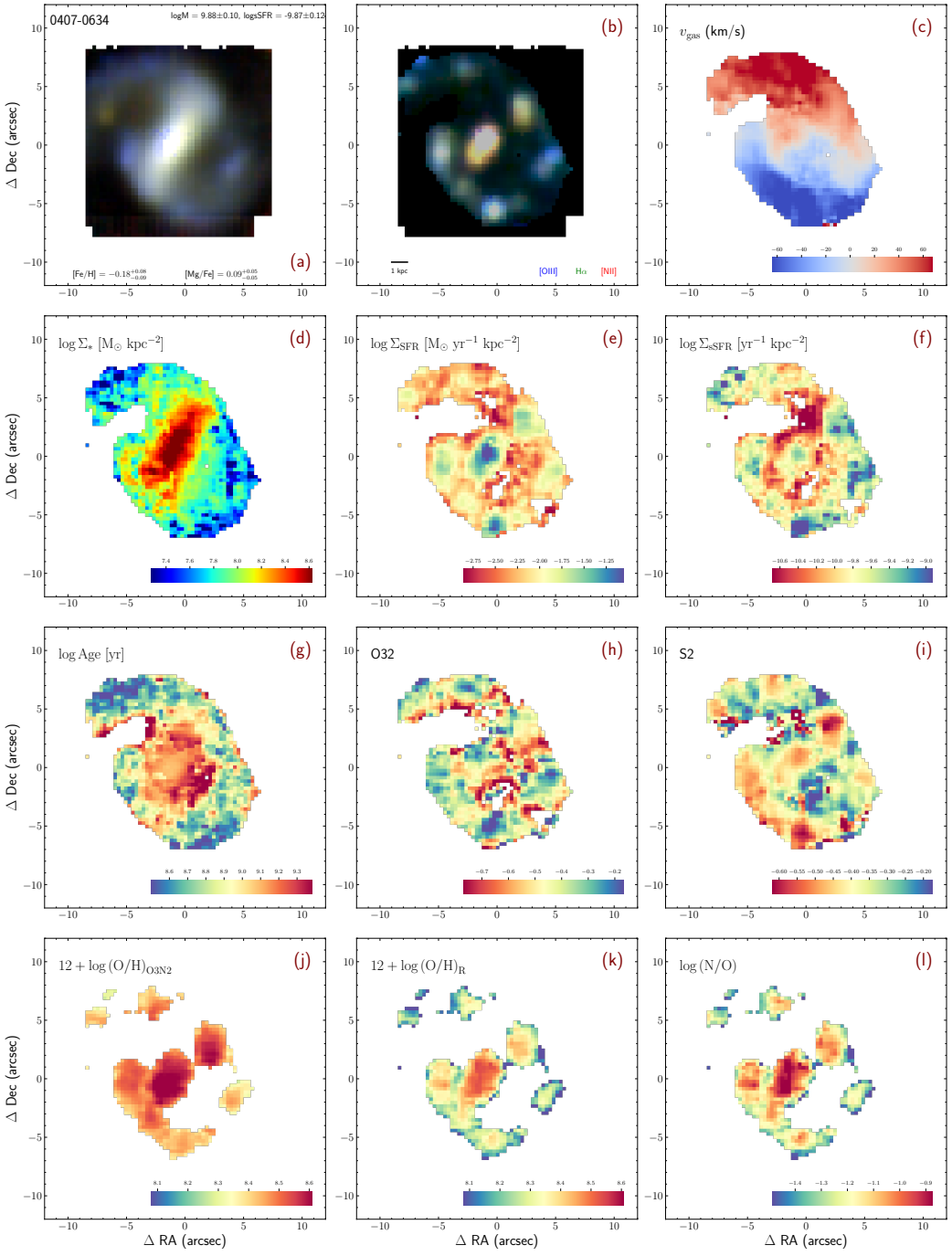

Figure 5.30: Same as Figure 5.3, but for galaxy 0407-0634.

Acknowledgments

I acknowledge the use of ChatGPT (OpenAI, 2024) for assistance with improving English usage and grammar in this chapter. The prompts were phrased along the lines of “Please improve the language and clarity of the following sentences.” All outputs were carefully reviewed and edited by me to ensure that they accurately convey the original meaning.

Chapter 6

CONCLUSION

6.1 Summary

In this thesis, I presented a series of spectroscopic studies examining multi-elemental abundances in galaxies across a range of masses and redshifts, with the goal of better characterizing the shapes of MZRs for different elements and probing the physical processes that govern chemical enrichment during galaxy assembly.

In Chapter 2, I conducted one of the first direct comparisons between stellar metallicities derived from resolved stellar spectroscopy and those from integrated-light spectroscopy in galaxies with complex stellar populations. Focusing on NGC 147, a Local Group satellite suitable for both approaches, I measured $[\mathrm{Fe/H}]_*$ using integrated-light spectra from the PCWI and found consistency with existing resolved stellar measurements (Kirby et al., 2013) to within 0.1 dex. While the recovered metallicity remained robust against the SSP assumptions, the inferred stellar age was more sensitive to those assumptions. This study provides the first evidence that it is reasonable to put the low-mass and high-mass MZRs measured from distinct approaches on the *same* absolute scale to jointly constrain the shape of the stellar MZR.

In Chapter 4, I introduced a new sample of 46 low-redshift star-forming galaxies with $M_* \sim 10^{8-10} M_\odot$, along with two quiescent galaxies at $M_* \sim 10^{8.8} M_\odot$, observed with Keck/KCWI. I developed a novel technique to simultaneously measure $[\mathrm{Fe/H}]_*$ and $[\mathrm{Mg/H}]_*$ in star-forming galaxies. Combining this sample with SDSS spectra, I constructed the first Fe- and Mg-MZRs measured consistently across a stellar mass range spanning 10^8 to $10^{11.5} M_\odot$. I found that galaxies lying closer to the extrapolated high-mass MZRs tend to have lower sSFRs, indicating that variations in sSFR drive the transition in MZR shape at $M_* \sim 10^9 M_\odot$. This suggests that galaxies approaching quiescence enrich efficiently and rapidly arrive on the high-mass MZR, consistent with trends observed in post-starburst galaxies. The distinct stellar abundances of two quiescent galaxies at similar masses suggest that environmental factors also influence the transition: The metal-poor quiescent galaxy, likely a satellite, aligns with the extrapolation of the low-mass MZR of Local Group satellites, while the more metal-rich quiescent galaxy, likely an isolated dwarf, lies

above the extrapolated low-mass MZR.

Chapter 4 also includes the first comparison of α element in ionized gas and stars beyond the Local Group, through direct measurements of gas-phase oxygen and stellar magnesium in the KCWI sample. I found that $[Mg/H]_*$ tracks $[O/H]_g$ more closely than $[Fe/H]_*$, and their ratio is less sensitive to sSFR, corroborating that Mg_* is a better analog to O_g in stellar–gas abundance comparisons. Most galaxies exhibit $[O/H]_g > [Mg/H]_*$, suggesting that current star formation is fueled by chemically enriched gas, rather than recently accreted, metal-poor inflows—indicating relatively well-mixed ISM.

In Chapter 5, I performed a spatially resolved analysis of the nebular and stellar properties of the same KCWI sample. The preliminary results reveal that star-forming dwarf galaxies host irregular, clumpy star formation and exhibit significant spatial variation in ionization conditions, whereas their stellar mass distributions are much smoother. Many systems show established gas-phase metallicity gradients, though these may be biased by contributions from DIG. In addition, I also discussed some possible next steps to further analyze and interpret the existing dataset.

Finally, in Chapter 3, I extended my analysis to the high-redshift universe, studying the stellar abundances and SFHs of quiescent galaxies at $z \gtrsim 1$. Leveraging gravitational lensing, I obtained deep rest-frame optical spectra of two quiescent galaxies at $z \gtrsim 1$ using the Keck I telescope, and successfully measured their $[Fe/H]_*$, $[Mg/H]_*$, and stellar population ages. Like other quiescent galaxies at $z \sim 1$, they exhibit lower $[Fe/H]_*$ and $[Mg/H]_*$ than local ellipticals of similar mass. However, despite forming the majority of their stars within 2 Gyr of the Big Bang and quenching shortly thereafter, both galaxies have [Mg/Fe] ratios comparable to those of their local counterparts. Treating Mg as an instantaneously recycled element, I used a simple chemical evolution model to infer their mass-loading factors over time. The results show that quiescent galaxies at $z \sim 1$ formed much more rapidly and experienced enhanced outflows during star formation compared to most present-day ellipticals at similar masses, which may explain why they quenched early.

In conclusion, this thesis has shown that chemical abundances derived from high-quality spectroscopy are powerful tools for probing the assembly history of galaxies, both in the local universe and at high redshift. Integral field unit (IFU) spectroscopy and traditional slit spectroscopy complement each other in revealing physical processes operating at different spatial and temporal scales across cosmic time. Most importantly, the relationship between the gas and stellar components of galaxies is

far more complex than what can be captured by simple theoretical models. As such, detailed studies that explicitly focus on the connection between gas and stars are essential for uncovering the full picture of galaxy evolution.

6.2 Looking Forward

In this section, I outline potential directions for future research related to the questions explored in this thesis.

6.2.1 Evolution in the Low-Redshift Star-Forming Dwarfs

An Evolutionary Pathway from Chaos to Organization

Preliminary KCWI maps of our sample reveal distinct spatial distributions between ionized gas and stellar populations within individual dwarf galaxies (Figure 5.3). Our findings are consistent with a recent IFU study of more massive galaxies ($M_* > 10^9, M_\odot$) from the CALIFA survey, which shows that ionized gas tends to be more extended and clumpier than the stellar component, especially in systems with high sSFR (Nersesian et al., 2023). A similar trend has been reported for low-mass star-forming galaxies ($\sim 10^{8-10} M_\odot$) based on medium-band imaging from the Merian survey (Mintz et al., 2024).

However, our results also seem to suggest an underlying order within this apparent chaos. On average, the spatial profiles of stellar population properties are smoother than those of nebular properties. Within the stellar component, the mass distribution is more spatially coherent than the distribution of the light-weighted age. Among the nebular properties, oxygen and nitrogen abundance profiles are less irregular than the patchy distributions of recent star formation, while ionization conditions display the most varied and complex morphologies.

These observations indicate that a systematic morphological analysis of the spatially resolved properties within each galaxy will be essential to revealing how galaxies transition from irregular, clumpy structures to more organized systems, and how stochastic processes like local starbursts in a small region or minor mergers can perturb established gradients.

As a next step, I will apply a nonparametric morphological analysis similar to that of Nersesian et al. (2023), using structural parameters such as the Gini–M_{20} statistics (Abraham, van den Bergh, and Nair, 2003; Lotz, Primack, and Madau, 2004) and the concentration–asymmetry–smoothness (CAS) indices (Conselice, 2003). While Nersesian et al. (2023) focused on the morphology of the stellar continuum

and bright emission lines ([O III]λ5007, Hα, and [N II]λ6583), I will extend this framework to include line ratios and derived physical quantities. This will allow us to better characterize the spatial structure of both the ionized gas and the underlying stellar populations in star-forming dwarf galaxies.

Possible Biases in Metallicity Measurement Due to the Presence of DIG

As discussed in Section 5.3.6, star-forming dwarf galaxies exhibit significant spatial variations in observed emission-line ratios. The trends shown in Figure 5.4 likely arise from two main factors. First, galaxies can exhibit *intrinsic* metallicity gradients as a result of inside-out formation (Chiosi, 1980; Matteucci and Francois, 1989; Boissier and Prantzos, 1999; Chiappini, Matteucci, and Romano, 2001). All the line ratios discussed above are at least moderately sensitive to metallicity, so their spatial variations can be interpreted, in part, as reflecting such gradients. Second, DIG, which is thought to occupy the regions outside H II regions, tends to exhibit enhanced strengths in low-ionization lines. This can systematically affect emission-line diagnostics such as R2, N2, and S2 (Zhang et al., 2017). Consequently, applying strong-line calibrations based on T_e metallicities derived from H II regions may lead to biased metallicity measurements in DIG-dominated regions. Indeed, using the criterion from Zhang et al. (2017) that defines DIG-dominated regions as those with $\Sigma_{\mathrm{H}\alpha} < 10^{39}\,\mathrm{erg\ s^{-1}\ kpc^{-2}}$, most spaxels located outside the star-forming knots in our sample appear to be DIG-dominated.

To assess whether the spaxels with lower Σ_{SFR} are truly dominated by DIG, I will measure the shape of the ionizing spectrum using `Cue` (Li et al., 2024), a Bayesian inference-based tool that estimates ionization parameter, ionizing spectrum shape, and elemental abundances by comparing to theoretical photoionization models. As suggested by Zhang et al. (2017), DIG is primarily ionized by hot, evolved stars that have a harder ionizing spectrum than massive OB stars. Therefore, accounting for variations in the ionizing spectrum when inferring nebular abundances will not only improve constraints on abundance measurements and their spatial gradients in star-forming dwarf galaxies, but also allow us to test whether regions identified as DIG-dominated indeed exhibit harder ionizing radiation.

Spatially Resolved Stellar Abundances

In the previous chapter, we compared the global stellar and gas-phase abundances of our KCWI sample and found that the gas-to-stellar abundance ratio correlates

with the global sSFR. In other words, galaxies with higher sSFRs tend to exhibit larger differences between gas-phase and stellar metallicities. A natural next step is to investigate whether this correlation persists on local scales within galaxies.

However, accurately measuring spatially resolved stellar abundances is much more challenging due to the low signal-to-noise ratio (S/N) of the stellar continuum in individual spaxels. To overcome this limitation, spectral binning is necessary. Although Voronoi binning is widely used in IFU studies to increase the S/N of stellar continua (Cappellari and Copin, 2003), it does not account for the morphology of the ionized gas, which can exhibit spatially distinct chemical abundances as suggested by the KCWI maps shown in Figure 5.3. A promising solution to this issue was recently proposed by de Souza et al. (2024), who applied hierarchical clustering to classify spaxels into physically motivated substructures of the MaNGA sample, thereby boosting S/N while preserving meaningful spatial variation.

In future work, I plan to explore a similar approach to simultaneously determine stellar and nebular abundances within each substructure. This will enable us to investigate metal recycling processes on small spatial scales in star-forming dwarf galaxies.

6.2.2 The Interplay Between Stellar Population and Ionized Gas beyond the Local Universe

Distant high-z star-forming galaxies also provide a unique perspective for studying the interaction between massive stars and ionized gas. In contrast with low-redshift, star-forming galaxies, where stellar populations can be constrained using the optical absorption features, astronomers studying high-z galaxies at cosmic noon typically rely on rest-FUV spectroscopy (e.g., Steidel et al., 2016; Topping et al., 2020; Chartab et al., 2024). At this epoch, the light from star-forming galaxies is dominated by massive OB stars, which emit primarily in the UV. The stellar features of older stars residing in the rest-optical are outshined by these massive stars and have remained elusive even in the deepest observations from 10-meter ground-based telescopes Steidel et al., 2016. As a result, prior to JWST, rest-optical spectra of star-forming galaxies were used exclusively for nebular studies of high-z galaxies.

With the incredible capabilities of JWST, it is now possible to probe the stellar populations of quiescent galaxies at $z \gtrsim 2$ by fitting the rest-optical continuum (e.g., Carnall et al., 2023; Beverage et al., 2024). However, stellar properties derived from rest-optical and rest-FUV spectra reflect very different stellar populations:

FUV light traces high-mass stars forming "now," while optical light captures lower-mass stars accumulated over a galaxy's lifetime. Consequently, stellar metallicities and SFHs inferred from these different approaches might not align, complicating comparisons between star-forming and quiescent galaxies at high redshift.

The way forward is to look for faint optical absorption in the deepest JWST spectra of star-forming galaxies at cosmic noon. JWST has already delivered high-quality spectra at high redshifts (e.g., Strom et al., 2023), enabling the detection not only of nebular emission lines—including temperature-sensitive auroral lines—but also possible stellar continua through stacked spectra of galaxies with similar properties. Some JWST programs have obtained ultra-deep rest-frame FUV spectra, making it possible to directly compare the properties of massive stars (traced by FUV light) with those of older, lower-mass stars (traced by optical light). This combined dataset provides a powerful constraint on SFHs by probing stellar populations formed at different epochs. Such comparisons will also test the reliability of SFHs inferred from Bayesian spectral energy distribution (SED) fitting codes like Prospector (Leja et al., 2019) and BAGPIPES (Carnall et al., 2018). For example, it will be valuable to assess whether joint fitting of broadband photometry and rest-frame FUV spectra without access to rest-frame optical spectra can accurately recover SFHs. This is particularly important for interpreting the demographics of star-forming galaxies at $z \sim 3$ that will be observed by the Prime Focus Spectrograph (PFS) Galaxy Evolution Survey, which will lack rest-frame optical coverage.

The PFS Galaxy Evolution Survey, a 130-night program on the Subaru Telescope that began in March 2025, will ultimately obtain high-quality spectra for approximately 14,000 galaxies at $z = 0.7$–2.0 (the low-z deep sample, $J < 22.8$ mag) and another ∼14,000 galaxies at $z = 2.1$–3.5 (the high-z IGM sample, $y < 24.3$ mag), each observed with ∼12 hours of integration time (Greene et al., 2022). Building on the tools and methods developed in this thesis and extending them in future work will place us in a strong position to interpret this unprecedented dataset. In particular, it will significantly improve our understanding of galaxy-wide chemical abundances in a mass-complete sample and the interplay between gas and stars in the early universe.

BIBLIOGRAPHY

Abbott, T. M. C. et al. (Dec. 2018). "The Dark Energy Survey: Data Release 1". In: *ApJS* 239.2, p. 18. DOI: 10.3847/1538-4365/aae9f0.

Abdurro'uf et al. (Apr. 2022). "The Seventeenth Data Release of the Sloan Digital Sky Surveys: Complete Release of MaNGA, MaStar, and APOGEE-2 Data". In: *ApJS* 259.2, p. 35. DOI: 10.3847/1538-4365/ac4414.

Abraham, R. G., S. van den Bergh, and P. Nair (May 2003). "A New Approach to Galaxy Morphology. I. Analysis of the Sloan Digital Sky Survey Early Data Release". In: *ApJ* 588.1, pp. 218–229. DOI: 10.1086/373919.

Adams, D. et al. (May 2022). "Galaxy Zoo: Clump Scout: Surveying the Local Universe for Giant Star-forming Clumps". In: *ApJ* 931.1, p. 16. DOI: 10.3847/1538-4357/ac6512.

Aihara, H. et al. (Apr. 2022). "Third data release of the Hyper Suprime-Cam Subaru Strategic Program". In: *PASJ* 74.2, pp. 247–272. DOI: 10.1093/pasj/psab122.

Akritas, M. G. and M. A. Bershady (Oct. 1996). "Linear Regression for Astronomical Data with Measurement Errors and Intrinsic Scatter". In: *ApJ* 470, p. 706. DOI: 10.1086/177901.

Alfaro-Cuello, M. et al. (Nov. 2019). "A Deep View into the Nucleus of the Sagittarius Dwarf Spheroidal Galaxy with MUSE. I. Data and Stellar Population Characterization". In: *ApJ* 886.1, p. 57. DOI: 10.3847/1538-4357/ab1b2c.

Andrews, B. H. and P. Martini (Mar. 2013). "The Mass-Metallicity Relation with the Direct Method on Stacked Spectra of SDSS Galaxies". In: *ApJ* 765.2, p. 140. DOI: 10.1088/0004-637X/765/2/140.

Asplund, M. et al. (Sept. 2009). "The Chemical Composition of the Sun". In: *ARA&A* 47.1, pp. 481–522. DOI: 10.1146/annurev.astro.46.060407.145222.

Balogh, M. L. et al. (Dec. 1999). "Differential Galaxy Evolution in Cluster and Field Galaxies at z$\backsim$0.3". In: *ApJ* 527.1, pp. 54–79. DOI: 10.1086/308056.

Barber, C. et al. (June 2014). "Validation of optimized population synthesis through mock spectra and Galactic globular clusters". In: *MNRAS* 440.4, pp. 2953–2968. DOI: 10.1093/mnras/stu439.

Belfiore, F. et al. (May 2015). "P-MaNGA Galaxies: emission-lines properties - gas ionization and chemical abundances from prototype observations". In: *MNRAS* 449.1, pp. 867–900. DOI: 10.1093/mnras/stv296.

Belfiore, F. et al. (July 2017). "SDSS IV MaNGA - metallicity and nitrogen abundance gradients in local galaxies". In: *MNRAS* 469.1, pp. 151–170. DOI: 10.1093/mnras/stx789.

Belfiore, F. et al. (Oct. 2019). "The Data Analysis Pipeline for the SDSS-IV MaNGA IFU Galaxy Survey: Emission-line Modeling". In: *AJ* 158.4, p. 160. DOI: 10.3847/1538-3881/ab3e4e.

Belli, S., A. B. Newman, and R. S. Ellis (Mar. 2014). "Velocity Dispersions and Dynamical Masses for a Large Sample of Quiescent Galaxies at z > 1: Improved Measures of the Growth in Mass and Size". In: *ApJ* 783.2, p. 117. DOI: 10.1088/0004-637X/783/2/117.

Benítez-Llambay, A. et al. (Feb. 2016). "Mergers and the outside-in formation of dwarf spheroidals". In: *MNRAS* 456.2, pp. 1185–1194. DOI: 10.1093/mnras/stv2722.

Berg, D. A. et al. (Aug. 2012). "Direct Oxygen Abundances for Low-luminosity LVL Galaxies". In: *ApJ* 754.2, p. 98. DOI: 10.1088/0004-637X/754/2/98.

Berg, D. A. et al. (Apr. 2020). "CHAOS IV: Gas-phase Abundance Trends from the First Four CHAOS Galaxies". In: *ApJ* 893.2, p. 96. DOI: 10.3847/1538-4357/ab7eab.

Bertin, E. and S. Arnouts (June 1996). "SExtractor: Software for source extraction." In: *A&AS* 117, pp. 393–404. DOI: 10.1051/aas:1996164.

Beverage, A. G. et al. (Aug. 2021). "Elemental Abundances and Ages of z 0.7 Quiescent Galaxies on the Mass-Size Plane: Implication for Chemical Enrichment and Star Formation Quenching". In: *ApJL* 917.1, p. L1. DOI: 10.3847/2041-8213/ac12cd.

Beverage, A. G. et al. (May 2023). "From Carbon to Cobalt: Chemical Compositions and Ages of z 0.7 Quiescent Galaxies". In: *ApJ* 948.2, p. 140. DOI: 10.3847/1538-4357/acc176.

Beverage, A. G. et al. (May 2024). "The Heavy Metal Survey: The Evolution of Stellar Metallicities, Abundance Ratios, and Ages of Massive Quiescent Galaxies since z ∼ 2". In: *ApJ* 966.2, p. 234. DOI: 10.3847/1538-4357/ad372d.

Blanc, G. A. et al. (Jan. 2015). "IZI: Inferring the Gas Phase Metallicity (Z) and Ionization Parameter (q) of Ionized Nebulae Using Bayesian Statistics". In: *ApJ* 798.2, p. 99. DOI: 10.1088/0004-637X/798/2/99.

Blanc, G. A. et al. (May 2019). "A Characteristic Mass Scale in the Mass-Metallicity Relation of Galaxies". In: *ApJ* 877.1, p. 6. DOI: 10.3847/1538-4357/ab16ec.

Boecker, A. et al. (June 2020). "Recovering Age-Metallicity Distributions from Integrated Spectra: Validation with MUSE Data of a Nearby Nuclear Star Cluster". In: *ApJ* 896.1, p. 13. DOI: 10.3847/1538-4357/ab919d.

Boissier, S. and N. Prantzos (Aug. 1999). "Chemo-spectrophotometric evolution of spiral galaxies - I. The model and the Milky Way". In: *MNRAS* 307.4, pp. 857–876. DOI: 10.1046/j.1365-8711.1999.02699.x.

Bournaud, F. et al. (Jan. 2014). "The Long Lives of Giant Clumps and the Birth of Outflows in Gas-rich Galaxies at High Redshift". In: *ApJ* 780.1, p. 57. DOI: 10.1088/0004-637X/780/1/57.

Brinchmann, J. et al. (July 2004). "The physical properties of star-forming galaxies in the low-redshift Universe". In: *MNRAS* 351.4, pp. 1151–1179. DOI: 10.1111/j.1365-2966.2004.07881.x.

Bruzual, G. and S. Charlot (Oct. 2003). "Stellar population synthesis at the resolution of 2003". In: *MNRAS* 344.4, pp. 1000–1028. DOI: 10.1046/j.1365-8711.2003.06897.x.

Bundy, K. et al. (Jan. 2015). "Overview of the SDSS-IV MaNGA Survey: Mapping nearby Galaxies at Apache Point Observatory". In: *ApJ* 798.1, p. 7. DOI: 10.1088/0004-637X/798/1/7.

Burbidge, E. M. et al. (Jan. 1957). "Synthesis of the Elements in Stars". In: *Reviews of Modern Physics* 29.4, pp. 547–650. DOI: 10.1103/RevModPhys.29.547.

Byler, N. et al. (May 2017). "Nebular Continuum and Line Emission in Stellar Population Synthesis Models". In: *ApJ* 840.1, p. 44. DOI: 10.3847/1538-4357/aa6c66.

Calura, F. et al. (Sept. 2009). "The evolution of the mass-metallicity relation in galaxies of different morphological types". In: *A&A* 504.2, pp. 373–388. DOI: 10.1051/0004-6361/200911756.

Calzetti, D. et al. (Apr. 2000). "The Dust Content and Opacity of Actively Star-forming Galaxies". In: *ApJ* 533.2, pp. 682–695. DOI: 10.1086/308692.

Cappellari, M. (Apr. 2017). "Improving the full spectrum fitting method: accurate convolution with Gauss-Hermite functions". In: *MNRAS* 466.1, pp. 798–811. DOI: 10.1093/mnras/stw3020.

Cappellari, M. (Dec. 2023). "Full spectrum fitting with photometry in PPXF: stellar population versus dynamical masses, non-parametric star formation history and metallicity for 3200 LEGA-C galaxies at redshift $z \approx 0.8$". In: *MNRAS* 526.3, pp. 3273–3300. DOI: 10.1093/mnras/stad2597.

Cappellari, M. and Y. Copin (June 2003). "Adaptive spatial binning of integral-field spectroscopic data using Voronoi tessellations". In: *MNRAS* 342.2, pp. 345–354. DOI: 10.1046/j.1365-8711.2003.06541.x.

Cappellari, M. and E. Emsellem (Feb. 2004). "Parametric Recovery of Line-of-Sight Velocity Distributions from Absorption-Line Spectra of Galaxies via Penalized Likelihood". In: *PASP* 116.816, pp. 138–147. DOI: 10.1086/381875.

Cappellari, M. et al. (May 2011). "The ATLAS^{3D} project - I. A volume-limited sample of 260 nearby early-type galaxies: science goals and selection criteria". In: *MNRAS* 413.2, pp. 813–836. DOI: 10.1111/j.1365-2966.2010.18174.x.

Cardelli, J. A., G. C. Clayton, and J. S. Mathis (Oct. 1989). "The Relationship between Infrared, Optical, and Ultraviolet Extinction". In: *ApJ* 345, p. 245. DOI: 10.1086/167900.

Carnall, A. C. (May 2017). "SpectRes: A Fast Spectral Resampling Tool in Python". In: *arXiv e-prints*, arXiv:1705.05165.

Carnall, A. C. et al. (Nov. 2018). "Inferring the star formation histories of massive quiescent galaxies with BAGPIPES: evidence for multiple quenching mechanisms". In: *MNRAS* 480.4, pp. 4379–4401. DOI: 10.1093/mnras/sty2169.

Carnall, A. C. et al. (Mar. 2019). "How to Measure Galaxy Star Formation Histories. I. Parametric Models". In: *ApJ* 873.1, p. 44. DOI: 10.3847/1538-4357/ab04a2.

Carnall, A. C. et al. (Apr. 2022). "The Stellar Metallicities of Massive Quiescent Galaxies at 1.0 < z < 1.3 from KMOS + VANDELS". In: *ApJ* 929.2, p. 131. DOI: 10.3847/1538-4357/ac5b62.

Carnall, A. C. et al. (July 2023). "A massive quiescent galaxy at redshift 4.658". In: *Nature* 619.7971, pp. 716–719. DOI: 10.1038/s41586-023-06158-6.

Chabrier, G. (July 2003). "Galactic Stellar and Substellar Initial Mass Function". In: *PASP* 115.809, pp. 763–795. DOI: 10.1086/376392.

Chartab, N. et al. (Jan. 2024). "LATIS: The Stellar Mass-Metallicity Relation of Star-forming Galaxies at z 2.5". In: *ApJ* 960.1, p. 73. DOI: 10.3847/1538-4357/ad0554.

Chen, X., L. Hu, and L. Wang (Nov. 2021). "Constraining Type Ia Supernova Delay Time with Spatially Resolved Star Formation Histories". In: *ApJ* 922.1, p. 15. DOI: 10.3847/1538-4357/ac178d.

Chen, Y. et al. (Nov. 2021). "The KBSS-KCWI survey: the connection between extended Ly α haloes and galaxy azimuthal angle at z 2-3". In: *MNRAS* 508.1, pp. 19–43. DOI: 10.1093/mnras/stab2383.

Chiappini, C., F. Matteucci, and D. Romano (June 2001). "Abundance Gradients and the Formation of the Milky Way". In: *ApJ* 554.2, pp. 1044–1058. DOI: 10.1086/321427.

Chiosi, C. (Mar. 1980). "Chemical evolution of the galactic disk: the inflow problem." In: *A&A* 83, pp. 206–216.

Choi, J. et al. (Sept. 2014). "The Assembly Histories of Quiescent Galaxies since z = 0.7 from Absorption Line Spectroscopy". In: *ApJ* 792.2, p. 95. DOI: 10.1088/0004-637X/792/2/95.

Choi, J. et al. (June 2016). "Mesa Isochrones and Stellar Tracks (MIST). I. Solar-scaled Models". In: *ApJ* 823.2, p. 102. DOI: 10.3847/0004-637X/823/2/102.

Cid Fernandes, R. et al. (Apr. 2005). "Semi-empirical analysis of Sloan Digital Sky Survey galaxies - I. Spectral synthesis method". In: *MNRAS* 358.2, pp. 363–378. DOI: 10.1111/j.1365-2966.2005.08752.x.

Conn, A. R. et al. (Oct. 2012). "A Bayesian Approach to Locating the Red Giant Branch Tip Magnitude. II. Distances to the Satellites of M31". In: *ApJ* 758.1, p. 11. DOI: 10.1088/0004-637X/758/1/11.

Conroy, C. (Aug. 2013). "Modeling the Panchromatic Spectral Energy Distributions of Galaxies". In: *ARA&A* 51.1, pp. 393–455. DOI: 10.1146/annurev-astro-082812-141017.

Conroy, C., G. J. Graves, and P. G. van Dokkum (Jan. 2014). "Early-type Galaxy Archeology: Ages, Abundance Ratios, and Effective Temperatures from Full-spectrum Fitting". In: *ApJ* 780.1, p. 33. DOI: 10.1088/0004-637X/780/1/33.

Conroy, C. and J. E. Gunn (Apr. 2010). "The Propagation of Uncertainties in Stellar Population Synthesis Modeling. III. Model Calibration, Comparison, and Evaluation". In: *ApJ* 712.2, pp. 833–857. DOI: 10.1088/0004-637X/712/2/833.

Conroy, C., J. E. Gunn, and M. White (July 2009). "The Propagation of Uncertainties in Stellar Population Synthesis Modeling. I. The Relevance of Uncertain Aspects of Stellar Evolution and the Initial Mass Function to the Derived Physical Properties of Galaxies". In: *ApJ* 699.1, pp. 486–506. DOI: 10.1088/0004-637X/699/1/486.

Conroy, C. and P. G. van Dokkum (Nov. 2012). "The Stellar Initial Mass Function in Early-type Galaxies From Absorption Line Spectroscopy. II. Results". In: *ApJ* 760.1, p. 71. DOI: 10.1088/0004-637X/760/1/71.

Conroy, C., M. White, and J. E. Gunn (Jan. 2010). "The Propagation of Uncertainties in Stellar Population Synthesis Modeling. II. The Challenge of Comparing Galaxy Evolution Models to Observations". In: *ApJ* 708.1, pp. 58–70. DOI: 10.1088/0004-637X/708/1/58.

Conroy, C. et al. (Feb. 2018). "Metal-rich, Metal-poor: Updated Stellar Population Models for Old Stellar Systems". In: *ApJ* 854.2, p. 139. DOI: 10.3847/1538-4357/aaab49.

Conselice, C. J. (July 2003). "The Relationship between Stellar Light Distributions of Galaxies and Their Formation Histories". In: *ApJS* 147.1, pp. 1–28. DOI: 10.1086/375001.

Cooper, M. C. et al. (Feb. 2012). "The DEEP3 Galaxy Redshift Survey: the impact of environment on the size evolution of massive early-type galaxies at intermediate redshift". In: *MNRAS* 419.4, pp. 3018–3027. DOI: 10.1111/j.1365-2966.2011.19938.x.

Crnojević, D. et al. (Dec. 2014). "A PAndAS view of M31 dwarf elliptical satellites: NGC 147 and NGC 185". In: *MNRAS* 445.4, pp. 3862–3877. DOI: 10.1093/mnras/stu2003.

Croom, S. M. et al. (Mar. 2012). "The Sydney-AAO Multi-object Integral field spectrograph". In: *MNRAS* 421.1, pp. 872–893. DOI: 10.1111/j.1365-2966.2011.20365.x.

Croom, S. M. et al. (July 2021). "The SAMI Galaxy Survey: the third and final data release". In: *MNRAS* 505.1, pp. 991–1016. DOI: 10.1093/mnras/stab229.

Curti, M. et al. (Jan. 2020). "The mass-metallicity and the fundamental metallicity relation revisited on a fully T_e-based abundance scale for galaxies". In: *MNRAS* 491.1, pp. 944–964. DOI: 10.1093/mnras/stz2910.

Curti, M. et al. (Apr. 2023). "JADES: Insights on the low-mass end of the mass–metallicity–star-formation rate relation at $3 < z < 10$ from deep JWST/NIRSpec spectroscopy". In: *arXiv e-prints*, arXiv:2304.08516. DOI: 10.48550/arXiv.2304.08516.

Dale, D. A. et al. (June 2023). "Spectral Energy Distributions for 258 Local Volume Galaxies". In: *AJ* 165.6, p. 260. DOI: 10.3847/1538-3881/accffe.

Davé, R., K. Finlator, and B. D. Oppenheimer (Mar. 2012). "An analytic model for the evolution of the stellar, gas and metal content of galaxies". In: *MNRAS* 421.1, pp. 98–107. DOI: 10.1111/j.1365-2966.2011.20148.x.

Davidge, T. J. (Nov. 2005). "The Evolved Stellar Content of NGC 147, NGC 185, and NGC 205". In: *AJ* 130.5, pp. 2087–2103. DOI: 10.1086/491706.

Davidson, R. and E. Flachaire (2008). "The wild bootstrap, tamed at last". In: *Journal of Econometrics* 146.1, pp. 162–169. ISSN: 0304-4076. DOI: https://doi.org/10.1016/j.jeconom.2008.08.003.

de los Reyes, M. A. C. et al. (Mar. 2020). "Manganese Indicates a Transition from Sub- to Near-Chandrasekhar Type Ia Supernovae in Dwarf Galaxies". In: *ApJ* 891.1, p. 85. DOI: 10.3847/1538-4357/ab736f.

de los Reyes, M. A. C. et al. (Jan. 2022). "Simultaneous Constraints on the Star Formation History and Nucleosynthesis of Sculptor dSph". In: *ApJ* 925.1, p. 66. DOI: 10.3847/1538-4357/ac332b.

de los Reyes, M. A. C. et al. (July 2023). "Dwarfs in Void Environments (DIVE): The Stellar Kinematics of Void Dwarf Galaxies Using the Keck Cosmic Web Imager". In: *ApJ* 951.1, p. 52. DOI: 10.3847/1538-4357/acd189.

De Rossi, M. E. et al. (Dec. 2017). "Galaxy metallicity scaling relations in the EAGLE simulations". In: *MNRAS* 472.3, pp. 3354–3377. DOI: 10.1093/mnras/stx2158.

de Souza, R. S. et al. (Oct. 2024). "Capivara: A Spectral-based Segmentation Method for IFU Data Cubes". In: *arXiv e-prints*, arXiv:2410.21962. DOI: 10.48550/arXiv.2410.21962.

Dekel, A. and J. Silk (Apr. 1986). "The Origin of Dwarf Galaxies, Cold Dark Matter, and Biased Galaxy Formation". In: *ApJ* 303, p. 39. DOI: 10.1086/164050.

Dey, A. et al. (May 2019). "Overview of the DESI Legacy Imaging Surveys". In: *AJ* 157.5, p. 168. DOI: 10.3847/1538-3881/ab089d.

Dotter, A. (Jan. 2016). "MESA Isochrones and Stellar Tracks (MIST) 0: Methods for the Construction of Stellar Isochrones". In: *ApJS* 222.1, p. 8. DOI: 10.3847/0067-0049/222/1/8.

Emami, N. et al. (Aug. 2019). "A Closer Look at Bursty Star Formation with L $_{H\alpha}$ and L $_{UV}$ Distributions". In: *ApJ* 881.1, p. 71. DOI: 10.3847/1538-4357/ab211a.

Erb, D. K. et al. (June 2006). "The Mass-Metallicity Relation at z>$\sim$2". In: *ApJ* 644.2, pp. 813–828. DOI: 10.1086/503623.

Esteban, C. et al. (Sept. 2014). "Carbon and oxygen abundances from recombination lines in low-metallicity star-forming galaxies. Implications for chemical evolution". In: *MNRAS* 443.1, pp. 624–647. DOI: 10.1093/mnras/stu1177.

Estrada-Carpenter, V. et al. (Jan. 2019). "CLEAR. I. Ages and Metallicities of Quiescent Galaxies at 1.0 < z < 1.8 Derived from Deep Hubble Space Telescope Grism Data". In: *ApJ* 870.2, p. 133. DOI: 10.3847/1538-4357/aaf22e.

Faber, S. M. et al. (Mar. 2003). "The DEIMOS spectrograph for the Keck II Telescope: integration and testing". In: *Instrument Design and Performance for Optical/Infrared Ground-based Telescopes*. Ed. by M. Iye and A. F. M. Moorwood. Vol. 4841. Society of Photo-Optical Instrumentation Engineers (SPIE) Conference Series, pp. 1657–1669. DOI: 10.1117/12.460346.

Faucher-Giguère, C.-A., E. Quataert, and P. F. Hopkins (Aug. 2013). "Feedback-regulated star formation in molecular clouds and galactic discs". In: *MNRAS* 433.3, pp. 1970–1990. DOI: 10.1093/mnras/stt866.

Ferland, G. J. et al. (Oct. 2017). "The 2017 Release Cloudy". In: *RMxAA* 53, pp. 385–438. DOI: 10.48550/arXiv.1705.10877.

Finlator, K. and R. Davé (Apr. 2008). "The origin of the galaxy mass-metallicity relation and implications for galactic outflows". In: *MNRAS* 385.4, pp. 2181–2204. DOI: 10.1111/j.1365-2966.2008.12991.x.

Flewelling, H. A. et al. (Nov. 2020). "The Pan-STARRS1 Database and Data Products". In: *ApJS* 251.1, p. 7. DOI: 10.3847/1538-4365/abb82d.

Forbes, D. A. et al. (Nov. 2019). "Dark matter and no dark matter: on the halo mass of NGC 1052". In: *MNRAS* 489.3, pp. 3665–3669. DOI: 10.1093/mnras/stz2420.

Forbes, J. C. et al. (Feb. 2014). "Balance among gravitational instability, star formation and accretion determines the structure and evolution of disc galaxies". In: *MNRAS* 438.2, pp. 1552–1576. DOI: 10.1093/mnras/stt2294.

Foreman-Mackey, D., J. Sick, and B. Johnson (Oct. 2014). *python-fsps: Python bindings to FSPS (v0.1.1)*. Zenodo. Version v0.1.1. DOI: 10.5281/zenodo.12157.

Foreman-Mackey, D. et al. (Mar. 2013). "emcee: The MCMC Hammer". In: *PASP* 125.925, p. 306. DOI: 10.1086/670067.

Fraser-McKelvie, A. et al. (Feb. 2022). "The SAMI Galaxy Survey: the drivers of gas and stellar metallicity differences in galaxies". In: *MNRAS* 510.1, pp. 320–333. DOI: 10.1093/mnras/stab3430.

Gallazzi, A. et al. (Sept. 2005). "The ages and metallicities of galaxies in the local universe". In: *MNRAS* 362.1, pp. 41–58. DOI: 10.1111/j.1365-2966.2005.09321.x.

Gallazzi, A. et al. (June 2014). "Charting the Evolution of the Ages and Metallicities of Massive Galaxies since z = 0.7". In: *ApJ* 788.1, p. 72. DOI: 10.1088/0004-637X/788/1/72.

Gallazzi, A. R. et al. (Apr. 2021). "Galaxy evolution across environments as probed by the ages, stellar metallicities, and [α /Fe] of central and satellite galaxies". In: *MNRAS* 502.3, pp. 4457–4478. DOI: 10.1093/mnras/stab265.

Garcia, A. M. et al. (Jan. 2024). "Interplay of Stellar and Gas-Phase Metallicities: Unveiling Insights for Stellar Feedback Modeling with Illustris, IllustrisTNG, and EAGLE". In: *arXiv e-prints*, arXiv:2401.12310. DOI: 10.48550/arXiv.2401.12310.

García-Rojas, J. and C. Esteban (Nov. 2007). "On the Abundance Discrepancy Problem in H II Regions". In: *ApJ* 670.1, pp. 457–470. DOI: 10.1086/521871.

Geda, R. et al. (May 2022). "PetroFit: A Python Package for Computing Petrosian Radii and Fitting Galaxy Light Profiles". In: *AJ* 163.5, p. 202. DOI: 10.3847/1538-3881/ac5908.

Geha, M. et al. (Jan. 2006). "Local Group Dwarf Elliptical Galaxies. I. Mapping the Dynamics of NGC 205 Beyond the Tidal Radius". In: *AJ* 131.1, pp. 332–342. DOI: 10.1086/498686.

Geha, M. et al. (Mar. 2010). "Local Group Dwarf Elliptical Galaxies. II. Stellar Kinematics to Large Radii in NGC 147 and NGC 185". In: *ApJ* 711.1, pp. 361–373. DOI: 10.1088/0004-637X/711/1/361.

Geha, M. et al. (Oct. 2015). "HST/ACS Direct Ages of the Dwarf Elliptical Galaxies NGC 147 and NGC 185". In: *ApJ* 811.2, p. 114. DOI: 10.1088/0004-637X/811/2/114.

Genina, A. et al. (Sept. 2019). "The distinct stellar metallicity populations of simulated Local Group dwarfs". In: *MNRAS* 488.2, pp. 2312–2331. DOI: 10.1093/mnras/stz1852.

Goddard, D. et al. (Apr. 2017). "SDSS-IV MaNGA: Spatially resolved star formation histories in galaxies as a function of galaxy mass and type". In: *MNRAS* 466.4, pp. 4731–4758. DOI: 10.1093/mnras/stw3371.

Gonçalves, D. R. et al. (Feb. 2007). "The chemical content of nearby galaxies from planetary nebulae: NGC 147". In: *MNRAS* 375.2, pp. 715–724. DOI: 10.1111/j.1365-2966.2006.11339.x.

González Delgado, R. M. et al. (May 2016). "Star formation along the Hubble sequence. Radial structure of the star formation of CALIFA galaxies". In: *A&A* 590, A44. DOI: 10.1051/0004-6361/201628174.

González Delgado, R. M. and R. Cid Fernandes (Apr. 2010). "Testing spectral models for stellar populations with star clusters - II. Results". In: *MNRAS* 403.2, pp. 797–816. DOI: 10.1111/j.1365-2966.2009.16152.x.

Greene, J. et al. (June 2022). "The Prime Focus Spectrograph Galaxy Evolution Survey". In: *arXiv e-prints*, arXiv:2206.14908. DOI: 10.48550/arXiv.2206.14908.

Greene, J. E. et al. (Oct. 2013). "The Stellar Halos of Massive Elliptical Galaxies. II. Detailed Abundance Ratios at Large Radius". In: *ApJ* 776.2, p. 64. DOI: 10.1088/0004-637X/776/2/64.

Gu, M. et al. (June 2022). "The MASSIVE Survey. XVI. The Stellar Initial Mass Function in the Center of MASSIVE Early-type Galaxies". In: *ApJ* 932.2, p. 103. DOI: 10.3847/1538-4357/ac69ea.

Gunn, J. E. and I. Gott J. Richard (Aug. 1972). "On the Infall of Matter Into Clusters of Galaxies and Some Effects on Their Evolution". In: *ApJ* 176, p. 1. DOI: 10.1086/151605.

Guo, Y. et al. (Feb. 2015). "Clumpy Galaxies in CANDELS. I. The Definition of UV Clumps and the Fraction of Clumpy Galaxies at 0.5 < z < 3". In: *ApJ* 800.1, p. 39. DOI: 10.1088/0004-637X/800/1/39.

Han, M. et al. (Mar. 1997). "Stellar Populations in the Dwarf Elliptical Galaxy NGC 147". In: *AJ* 113, p. 1001. DOI: 10.1086/118316.

Hayden, M. R. et al. (Aug. 2015). "Chemical Cartography with APOGEE: Metallicity Distribution Functions and the Chemical Structure of the Milky Way Disk". In: *ApJ* 808.2, p. 132. DOI: 10.1088/0004-637X/808/2/132.

Hayward, C. C. and P. F. Hopkins (Feb. 2017). "How stellar feedback simultaneously regulates star formation and drives outflows". In: *MNRAS* 465.2, pp. 1682–1698. DOI: 10.1093/mnras/stw2888.

Hopkins, P. F., E. Quataert, and N. Murray (Apr. 2012). "Stellar feedback in galaxies and the origin of galaxy-scale winds". In: *MNRAS* 421.4, pp. 3522–3537. DOI: 10.1111/j.1365-2966.2012.20593.x.

Hopkins, P. F. et al. (Nov. 2014). "Galaxies on FIRE (Feedback In Realistic Environments): stellar feedback explains cosmologically inefficient star formation". In: *MNRAS* 445.1, pp. 581–603. DOI: 10.1093/mnras/stu1738.

Hopkins, P. F. et al. (Oct. 2023). "What causes the formation of discs and end of bursty star formation?" In: *MNRAS* 525.2, pp. 2241–2286. DOI: 10.1093/mnras/stad1902.

Horne, K. (June 1986). “An optimal extraction algorithm for CCD spectroscopy.” In: *PASP* 98, pp. 609–617. DOI: 10.1086/131801.

Jacobs, C. et al. (July 2019). “An Extended Catalog of Galaxy-Galaxy Strong Gravitational Lenses Discovered in DES Using Convolutional Neural Networks”. In: *ApJS* 243.1, p. 17. DOI: 10.3847/1538-4365/ab26b6.

Jacobs, C. et al. (Apr. 2019). “Finding high-redshift strong lenses in DES using convolutional neural networks”. In: *MNRAS* 484.4, pp. 5330–5349. DOI: 10.1093/mnras/stz272.

Jafariyazani, M. et al. (July 2020). “Resolved Multi-element Stellar Chemical Abundances in the Brightest Quiescent Galaxy at z ∼ 2”. In: *ApJL* 897.2, p. L42. DOI: 10.3847/2041-8213/aba11c.

Johnson, B. D. et al. (June 2021). “Stellar Population Inference with Prospector”. In: *ApJS* 254.2, p. 22. DOI: 10.3847/1538-4365/abef67.

Jullo, E. et al. (Dec. 2007). “A Bayesian approach to strong lensing modelling of galaxy clusters”. In: *New Journal of Physics* 9.12, p. 447. DOI: 10.1088/1367-2630/9/12/447.

Kacprzak, G. G. et al. (July 2016). “Cold-mode Accretion: Driving the Fundamental Mass-Metallicity Relation at z ∼2”. In: *ApJL* 826.1, p. L11. DOI: 10.3847/2041-8205/826/1/L11.

Kado-Fong, E. et al. (Mar. 2020). “Star Formation in Isolated Dwarf Galaxies Hosting Tidal Debris: Extending the Dwarf-Dwarf Merger Sequence”. In: *AJ* 159.3, p. 103. DOI: 10.3847/1538-3881/ab6ef3.

Kauffmann, G. et al. (May 2003). “Stellar masses and star formation histories for 10^5 galaxies from the Sloan Digital Sky Survey”. In: *MNRAS* 341.1, pp. 33–53. DOI: 10.1046/j.1365-8711.2003.06291.x.

Kauffmann, G. et al. (Dec. 2003). “The host galaxies of active galactic nuclei”. In: *MNRAS* 346.4, pp. 1055–1077. DOI: 10.1111/j.1365-2966.2003.07154.x.

Kennicutt Jr., R. C. (Jan. 1998). “Star Formation in Galaxies Along the Hubble Sequence”. In: *ARA&A* 36, pp. 189–232. DOI: 10.1146/annurev.astro.36.1.189.

Kereš, D. et al. (Oct. 2005). “How do galaxies get their gas?” In: *MNRAS* 363.1, pp. 2–28. DOI: 10.1111/j.1365-2966.2005.09451.x.

Kewley, L. J. et al. (July 2001). “Theoretical Modeling of Starburst Galaxies”. In: *ApJ* 556.1, pp. 121–140. DOI: 10.1086/321545.

Kewley, L. J. and S. L. Ellison (July 2008). “Metallicity Calibrations and the Mass-Metallicity Relation for Star-forming Galaxies”. In: *ApJ* 681.2, pp. 1183–1204. DOI: 10.1086/587500.

Kewley, L. J. et al. (Nov. 2006). "The host galaxies and classification of active galactic nuclei". In: *MNRAS* 372.3, pp. 961–976. DOI: 10.1111/j.1365-2966.2006.10859.x.

Kirby, E. N., P. Guhathakurta, and C. Sneden (Aug. 2008). "Metallicity and Alpha-Element Abundance Measurement in Red Giant Stars from Medium-Resolution Spectra". In: *ApJ* 682.2, pp. 1217–1233. DOI: 10.1086/589627.

Kirby, E. N. et al. (Nov. 2009). "Multi-element Abundance Measurements from Medium-resolution Spectra. I. The Sculptor Dwarf Spheroidal Galaxy". In: *ApJ* 705.1, pp. 328–346. DOI: 10.1088/0004-637X/705/1/328.

Kirby, E. N. et al. (Dec. 2010). "Multi-element Abundance Measurements from Medium-resolution Spectra. II. Catalog of Stars in Milky Way Dwarf Satellite Galaxies". In: *ApJS* 191.2, pp. 352–375. DOI: 10.1088/0067-0049/191/2/352.

Kirby, E. N. et al. (Feb. 2011). "Multi-element Abundance Measurements from Medium-resolution Spectra. III. Metallicity Distributions of Milky Way Dwarf Satellite Galaxies". In: *ApJ* 727.2, p. 78. DOI: 10.1088/0004-637X/727/2/78.

Kirby, E. N. et al. (Feb. 2011). "Multi-element Abundance Measurements from Medium-resolution Spectra. IV. Alpha Element Distributions in Milky Way Satellite Galaxies". In: *ApJ* 727.2, p. 79. DOI: 10.1088/0004-637X/727/2/79.

Kirby, E. N. et al. (Dec. 2013). "The Universal Stellar Mass-Stellar Metallicity Relation for Dwarf Galaxies". In: *ApJ* 779.2, p. 102. DOI: 10.1088/0004-637X/779/2/102.

Kirby, E. N. et al. (Jan. 2017). "Chemistry and Kinematics of the Late-forming Dwarf Irregular Galaxies Leo A, Aquarius, and Sagittarius DIG". In: *ApJ* 834.1, p. 9. DOI: 10.3847/1538-4357/834/1/9.

Kirby, E. N. et al. (Feb. 2020). "Elemental Abundances in M31: The Kinematics and Chemical Evolution of Dwarf Spheroidal Satellite Galaxies". In: *AJ* 159.2, p. 46. DOI: 10.3847/1538-3881/ab5f0f.

Knowles, A. T. et al. (Aug. 2023). "sMILES SSPs: a library of semi-empirical MILES stellar population models with variable [α/Fe] abundances". In: *MNRAS* 523.3, pp. 3450–3470. DOI: 10.1093/mnras/stad1647.

Kobayashi, C., A. I. Karakas, and M. Lugaro (Sept. 2020). "The Origin of Elements from Carbon to Uranium". In: *ApJ* 900.2, p. 179. DOI: 10.3847/1538-4357/abae65.

Koleva, M. et al. (Nov. 2011). "Age and metallicity gradients in early-type galaxies: a dwarf-to-giant sequence". In: *MNRAS* 417.3, pp. 1643–1671. DOI: 10.1111/j.1365-2966.2011.19057.x.

Kormendy, J. (Aug. 1985). "Families of ellipsoidal stellar systems and the formation of dwarf elliptical galaxies." In: *ApJ* 295, pp. 73–79. DOI: 10.1086/163350.

Kormendy, J. and R. Bender (Jan. 2012). "A Revised Parallel-sequence Morphological Classification of Galaxies: Structure and Formation of S0 and Spheroidal Galaxies". In: *ApJS* 198.1, p. 2. DOI: 10.1088/0067-0049/198/1/2.

Kormendy, J. et al. (May 2009). "Structure and Formation of Elliptical and Spheroidal Galaxies". In: *ApJS* 182.1, pp. 216–309. DOI: 10.1088/0067-0049/182/1/216.

Kriek, M. et al. (Dec. 2016). "A massive, quiescent, population II galaxy at a redshift of 2.1". In: *Nature* 540.7632, pp. 248–251. DOI: 10.1038/nature20570.

Kriek, M. et al. (Aug. 2019). "Stellar Metallicities and Elemental Abundance Ratios of z ∼ 1.4 Massive Quiescent Galaxies". In: *ApJL* 880.2, p. L31. DOI: 10.3847/2041-8213/ab2e75.

Kron, R. G. (June 1980). "Photometry of a complete sample of faint galaxies." In: *ApJS* 43, pp. 305–325. DOI: 10.1086/190669.

Kroupa, P. (Apr. 2001). "On the variation of the initial mass function". In: *MNRAS* 322.2, pp. 231–246. DOI: 10.1046/j.1365-8711.2001.04022.x.

Lang, D. (May 2014). "unWISE: Unblurred Coadds of the WISE Imaging". In: *AJ* 147.5, p. 108. DOI: 10.1088/0004-6256/147/5/108.

Lee, H. et al. (Aug. 2006). "On Extending the Mass-Metallicity Relation of Galaxies by 2.5 Decades in Stellar Mass". In: *ApJ* 647.2, pp. 970–983. DOI: 10.1086/505573.

Leethochawalit, N. et al. (Apr. 2016). "A Keck Adaptive Optics Survey of a Representative Sample of Gravitationally Lensed Star-forming Galaxies: High Spatial Resolution Studies of Kinematics and Metallicity Gradients". In: *ApJ* 820.2, p. 84. DOI: 10.3847/0004-637X/820/2/84.

Leethochawalit, N. et al. (Mar. 2018). "Evolution of the Stellar Mass-Metallicity Relation. I. Galaxies in the z ∼ 0.4 Cluster Cl0024". In: *ApJ* 856.1, p. 15. DOI: 10.3847/1538-4357/aab26a.

Leethochawalit, N. et al. (Mar. 2018). "Evolution of the Stellar Mass-Metallicity Relation. I. Galaxies in the z ∼ 0.4 Cluster Cl0024". In: *ApJ* 856.1, p. 15. DOI: 10.3847/1538-4357/aab26a.

Leethochawalit, N. et al. (Nov. 2019). "Evolution of the Stellar Mass-Metallicity Relation. II. Constraints on Galactic Outflows from the Mg Abundances of Quiescent Galaxies". In: *ApJ* 885.2, p. 100. DOI: 10.3847/1538-4357/ab4809.

Leja, J. et al. (May 2019). "How to Measure Galaxy Star Formation Histories. II. Nonparametric Models". In: *ApJ* 876.1, p. 3. DOI: 10.3847/1538-4357/ab133c.

Lequeux, J. et al. (Dec. 1979). "Chemical Composition and Evolution of Irregular and Blue Compact Galaxies". In: *A&A* 80, p. 155.

Lequeux, J. et al. (Dec. 1979). “Reprint of 1979A&A....80..155L. Chemical composition and evolution of irregular and blue compact galaxies.” In: *A&A* 500, pp. 145–156.

Leung, H.-H. et al. (Mar. 2024). “Chemical evolution of local post-starburst galaxies: implications for the mass-metallicity relation”. In: *MNRAS* 528.3, pp. 4029–4052. DOI: 10.1093/mnras/stae225.

Li, Y. et al. (May 2024). “Cue: A Fast and Flexible Photoionization Emulator for Modeling Nebular Emission Powered By Almost Any Ionizing Source”. In: *arXiv e-prints*, arXiv:2405.04598. DOI: 10.48550/arXiv.2405.04598.

Lian, J. et al. (May 2018). “SDSS-IV MaNGA: modelling the metallicity gradients of gas and stars - radially dependent metal outflow versus IMF”. In: *MNRAS* 476.3, pp. 3883–3901. DOI: 10.1093/mnras/sty425.

Lian, J. et al. (Feb. 2018). “The mass-metallicity relations for gas and stars in star-forming galaxies: strong outflow versus variable IMF”. In: *MNRAS* 474.1, pp. 1143–1164. DOI: 10.1093/mnras/stx2829.

Lonoce, I. et al. (Dec. 2015). “Old age and supersolar metallicity in a massive z $\sim$ 1.4 early-type galaxy from VLT/X-Shooter spectroscopy”. In: *MNRAS* 454.4, pp. 3912–3919. DOI: 10.1093/mnras/stv2150.

Looser, T. J. et al. (Jan. 2024). “The stellar Fundamental Metallicity Relation: the correlation between stellar mass, star-formation rate and stellar metallicity”. In: *arXiv e-prints*, arXiv:2401.08769. DOI: 10.48550/arXiv.2401.08769.

Lotz, J. M., J. Primack, and P. Madau (July 2004). “A New Nonparametric Approach to Galaxy Morphological Classification”. In: *AJ* 128.1, pp. 163–182. DOI: 10.1086/421849.

Lu, Y., G. A. Blanc, and A. Benson (Aug. 2015). “An Analytical Model for Galaxy Metallicity: What do Metallicity Relations Tell Us about Star Formation and Outflow?” In: *ApJ* 808.2, p. 129. DOI: 10.1088/0004-637X/808/2/129.

Ludlow, A. D. et al. (Aug. 2016). “The mass-concentration-redshift relation of cold and warm dark matter haloes”. In: *MNRAS* 460.2, pp. 1214–1232. DOI: 10.1093/mnras/stw1046.

Lupton, R. et al. (Feb. 2004). “Preparing Red-Green-Blue Images from CCD Data”. In: *PASP* 116.816, pp. 133–137. DOI: 10.1086/382245.

Ma, X. et al. (Feb. 2016). “The origin and evolution of the galaxy mass-metallicity relation”. In: *MNRAS* 456.2, pp. 2140–2156. DOI: 10.1093/mnras/stv2659.

Magrini, L. et al. (Dec. 2012). “Scaling relations of metallicity, stellar mass and star formation rate in metal-poor starbursts - II. Theoretical models”. In: *MNRAS* 427.2, pp. 1075–1088. DOI: 10.1111/j.1365-2966.2012.22055.x.

Maiolino, R. and F. Mannucci (Feb. 2019). "De re metallica: the cosmic chemical evolution of galaxies". In: *A&A Rv* 27.1, p. 3. DOI: 10.1007/s00159-018-0112-2.

Majewski, S. R. et al. (Sept. 2017). "The Apache Point Observatory Galactic Evolution Experiment (APOGEE)". In: *AJ* 154.3, p. 94. DOI: 10.3847/1538-3881/aa784d.

Man, A. W. S. et al. (Sept. 2021). "An Exquisitely Deep View of Quenching Galaxies through the Gravitational Lens: Stellar Population, Morphology, and Ionized Gas". In: *ApJ* 919.1, p. 20. DOI: 10.3847/1538-4357/ac0ae3.

Mandelker, N. et al. (Oct. 2014). "The population of giant clumps in simulated high-z galaxies: in situ and ex situ migration and survival". In: *MNRAS* 443.4, pp. 3675–3702. DOI: 10.1093/mnras/stu1340.

Mannucci, F. et al. (Nov. 2010). "A fundamental relation between mass, star formation rate and metallicity in local and high-redshift galaxies". In: *MNRAS* 408.4, pp. 2115–2127. DOI: 10.1111/j.1365-2966.2010.17291.x.

Maoz, D., F. Mannucci, and T. D. Brandt (Nov. 2012). "The delay-time distribution of Type Ia supernovae from Sloan II". In: *MNRAS* 426.4, pp. 3282–3294. DOI: 10.1111/j.1365-2966.2012.21871.x.

Marigo, P. and L. Girardi (July 2007). "Evolution of asymptotic giant branch stars. I. Updated synthetic TP-AGB models and their basic calibration". In: *A&A* 469.1, pp. 239–263. DOI: 10.1051/0004-6361:20066772.

Martin, D. C. et al. (Jan. 2005). "The Galaxy Evolution Explorer: A Space Ultraviolet Survey Mission". In: *ApJL* 619.1, pp. L1–L6. DOI: 10.1086/426387.

Martin, N. F. et al. (Oct. 2013). "The PAndAS View of the Andromeda Satellite System. I. A Bayesian Search for Dwarf Galaxies Using Spatial and Color-Magnitude Information". In: *ApJ* 776.2, p. 80. DOI: 10.1088/0004-637X/776/2/80.

Matteucci, F. and P. Francois (Aug. 1989). "Galactic chemical evolution : abundance gradients of individual elements." In: *MNRAS* 239, pp. 885–904. DOI: 10.1093/mnras/239.3.885.

Mayer, L. et al. (July 2006). "Simultaneous ram pressure and tidal stripping; how dwarf spheroidals lost their gas". In: *MNRAS* 369.3, pp. 1021–1038. DOI: 10.1111/j.1365-2966.2006.10403.x.

McClure, R. D. and S. van den Bergh (June 1968). "Five-color intermediate-band photometry of stars, clusters, and galaxies." In: *AJ* 73, pp. 313–337. DOI: 10.1086/110634.

McCully, C. et al. (Nov. 2018). *astropy/astroscrappy: v1.0.5 Zenodo Release*. Version v1.0.5. DOI: 10.5281/zenodo.1482019.

McGaugh, S. S. (Oct. 1991). "H II Region Abundances: Model Oxygen Line Ratios". In: *ApJ* 380, p. 140. DOI: 10.1086/170569.

Mehta, V. et al. (May 2021). “Investigating Clumpy Galaxies in the Sloan Digital Sky Survey Stripe 82 Using the Galaxy Zoo”. In: *ApJ* 912.1, p. 49. DOI: 10.3847/1538-4357/abed5b.

Mendel, J. T. et al. (Aug. 2020). “The Kinematics of Massive Quiescent Galaxies at 1.4 < z < 2.1: Dark Matter Fractions, IMF Variation, and the Relation to Local Early-type Galaxies”. In: *ApJ* 899.1, p. 87. DOI: 10.3847/1538-4357/ab9ffc.

Mentz, J. J. et al. (Dec. 2016). “Abundance ratios and IMF slopes in the dwarf elliptical galaxy NGC 1396 with MUSE”. In: *MNRAS* 463.3, pp. 2819–2838. DOI: 10.1093/mnras/stw2129.

Milone, A. D. C., A. E. Sansom, and P. Sánchez-Blázquez (June 2011). “Element abundances in the stars of the MILES spectral library: the Mg/Fe ratio”. In: *MNRAS* 414.2, pp. 1227–1252. DOI: 10.1111/j.1365-2966.2011.18457.x.

Mintz, A. et al. (Oct. 2024). “A Nonparametric Morphological Analysis of Hα Emission in Bright Dwarfs Using the Merian Survey”. In: *ApJ* 974.2, p. 273. DOI: 10.3847/1538-4357/ad6861.

Miranda, H. et al. (Feb. 2025). “Importance of modelling the nebular continuum in galaxy spectra”. In: *A&A* 694, A102. DOI: 10.1051/0004-6361/202451648.

Morishita, T. et al. (Mar. 2018). “Metal Deficiency in Two Massive Dead Galaxies at z $\sim$ 2”. In: *ApJL* 856.1, p. L4. DOI: 10.3847/2041-8213/aab493.

Morrissey, P. et al. (Sept. 2018). “The Keck Cosmic Web Imager Integral Field Spectrograph”. In: *ApJ* 864.1, p. 93. DOI: 10.3847/1538-4357/aad597.

Murray, N., E. Quataert, and T. A. Thompson (Jan. 2005). “On the Maximum Luminosity of Galaxies and Their Central Black Holes: Feedback from Momentum-driven Winds”. In: *ApJ* 618.2, pp. 569–585. DOI: 10.1086/426067.

Nagao, T., R. Maiolino, and A. Marconi (Nov. 2006). “Gas metallicity diagnostics in star-forming galaxies”. In: *A&A* 459.1, pp. 85–101. DOI: 10.1051/0004-6361:20065216.

Nanayakkara, T. et al. (Jan. 2022). “Massive high-redshift quiescent galaxies with JWST”. In: *PASA* 39, e002. DOI: 10.1017/pasa.2021.61.

Navarro, J. F., C. S. Frenk, and S. D. M. White (Dec. 1997). “A Universal Density Profile from Hierarchical Clustering”. In: *ApJ* 490.2, pp. 493–508. DOI: 10.1086/304888.

Nersesian, A. et al. (May 2023). “Non-parametric galaxy morphology from stellar and nebular emission with the CALIFA sample”. In: *A&A* 673, A63. DOI: 10.1051/0004-6361/202345962.

Neumann, J. et al. (Dec. 2021). “SDSS-IV MaNGA: drivers of stellar metallicity in nearby galaxies”. In: *MNRAS* 508.4, pp. 4844–4857. DOI: 10.1093/mnras/stab2868.

Newman, A. B. et al. (Aug. 2018). "Resolving Quiescent Galaxies at z $\gtrsim$ 2. II. Direct Measures of Rotational Support". In: *ApJ* 862.2, p. 126. DOI: 10.3847/1538-4357/aacd4f.

Newman, J. A. et al. (Sept. 2013). "The DEEP2 Galaxy Redshift Survey: Design, Observations, Data Reduction, and Redshifts". In: *ApJS* 208.1, p. 5. DOI: 10.1088/0067-0049/208/1/5.

Nicholls, D. C. et al. (Apr. 2017). "Abundance scaling in stars, nebulae and galaxies". In: *MNRAS* 466.4, pp. 4403–4422. DOI: 10.1093/mnras/stw3235.

Nidever, D. L. et al. (Nov. 2014). "Tracing Chemical Evolution over the Extent of the Milky Way's Disk with APOGEE Red Clump Stars". In: *ApJ* 796.1, p. 38. DOI: 10.1088/0004-637X/796/1/38.

Nightingale, J. W. and S. Dye (Sept. 2015). "Adaptive semi-linear inversion of strong gravitational lens imaging". In: *MNRAS* 452.3, pp. 2940–2959. DOI: 10.1093/mnras/stv1455.

Nightingale, J. W., S. Dye, and R. J. Massey (2018). "AutoLens: Automated modeling of a strong lens's light, mass, and source". In: *MNRAS* 478.4, pp. 4738–4784. ISSN: 13652966. DOI: 10.1093/mnras/sty1264.

Nightingale, J. W., R. G. Hayes, and M. Griffiths (2021). "'PyAutoFit': A Classy Probabilistic Programming Language for Model Composition and Fitting". In: *Journal of Open Source Software* 6.58, p. 2550. DOI: 10.21105/joss.02550.

Nightingale, J. W. et al. (2021). "'PyAutoLens': Open-Source Strong Gravitational Lensing". In: *Journal of Open Source Software* 6.58, p. 2825. DOI: 10.21105/joss.02825.

Nomoto, K., C. Kobayashi, and N. Tominaga (Aug. 2013). "Nucleosynthesis in Stars and the Chemical Enrichment of Galaxies". In: *ARA&A* 51.1, pp. 457–509. DOI: 10.1146/annurev-astro-082812-140956.

Nomoto, K. et al. (Oct. 2006). "Nucleosynthesis yields of core-collapse supernovae and hypernovae, and galactic chemical evolution". In: *NuPhA* 777, pp. 424–458. DOI: 10.1016/j.nuclphysa.2006.05.008.

O'Donnell, J. E. (Feb. 1994). "R v-dependent Optical and Near-Ultraviolet Extinction". In: *ApJ* 422, p. 158. DOI: 10.1086/173713.

O'Sullivan, D. and Y. Chen (Nov. 2020). "CWITools: A Python3 Data Analysis Pipeline for the Cosmic Web Imager Instruments". In: *arXiv e-prints*, arXiv:2011.05444.

O'Sullivan, D. B. et al. (May 2020). "The FLASHES Survey. I. Integral Field Spectroscopy of the CGM around 48 z $\simeq$ 2.3-3.1 QSOs". In: *ApJ* 894.1, p. 3. DOI: 10.3847/1538-4357/ab838c.

Oh, K. et al. (Aug. 2011). “Improved and Quality-assessed Emission and Absorption Line Measurements in Sloan Digital Sky Survey Galaxies”. In: *ApJS* 195.2, p. 13. DOI: 10.1088/0067-0049/195/2/13.

Onodera, M. et al. (Aug. 2015). “The Ages, Metallicities, and Element Abundance Ratios of Massive Quenched Galaxies at z ≈ 1.6”. In: *ApJ* 808.2, p. 161. DOI: 10.1088/0004-637X/808/2/161.

OpenAI (2024). “” In: *ChatGPT-4o (May 13 version) [Large Language Model], https://chat.openai.com/chat*.

Oser, L. et al. (Dec. 2010). “The Two Phases of Galaxy Formation”. In: *ApJ* 725.2, pp. 2312–2323. DOI: 10.1088/0004-637X/725/2/2312.

Osterbrock, D. E. and G. J. Ferland (2006). *Astrophysics of gaseous nebulae and active galactic nuclei*.

Oyarzún, G. A. et al. (Aug. 2019). “Signatures of Stellar Accretion in MaNGA Early-type Galaxies”. In: *ApJ* 880.2, p. 111. DOI: 10.3847/1538-4357/ab297c.

Panter, B. et al. (Dec. 2008). “The cosmic evolution of metallicity from the SDSS fossil record”. In: *MNRAS* 391.3, pp. 1117–1126. DOI: 10.1111/j.1365-2966.2008.13981.x.

Peng, Y., R. Maiolino, and R. Cochrane (May 2015). “Strangulation as the primary mechanism for shutting down star formation in galaxies”. In: *Nature* 521.7551, pp. 192–195. DOI: 10.1038/nature14439.

Petrosian, V. (Dec. 1976). “Surface Brightness and Evolution of Galaxies”. In: *ApJL* 210, p. L53. DOI: 10.1086/18230110.1086/182253.

Pettini, M. and B. E. J. Pagel (Mar. 2004). “[OIII]/[NII] as an abundance indicator at high redshift”. In: *MNRAS* 348.3, pp. L59–L63. DOI: 10.1111/j.1365-2966.2004.07591.x.

Pietrinferni, A. et al. (Sept. 2004). “A Large Stellar Evolution Database for Population Synthesis Studies. I. Scaled Solar Models and Isochrones”. In: *ApJ* 612.1, pp. 168–190. DOI: 10.1086/422498.

Pilyugin, L. S. and E. K. Grebel (Apr. 2016). “New calibrations for abundance determinations in H II regions”. In: *MNRAS* 457.4, pp. 3678–3692. DOI: 10.1093/mnras/stw238.

Pilyugin, L. S., E. K. Grebel, and L. Mattsson (Aug. 2012). “’Counterpart’ method for abundance determinations in H II regions”. In: *MNRAS* 424.3, pp. 2316–2329. DOI: 10.1111/j.1365-2966.2012.21398.x.

Pilyugin, L. S. et al. (May 2018). “Validity of abundances derived from spaxel spectra of the MaNGA survey”. In: *A&A* 613, A1. DOI: 10.1051/0004-6361/201732185.

Pilyugin, L. S. and T. X. Thuan (Sept. 2005). "Oxygen Abundance Determination in H II Regions: The Strong Line Intensities-Abundance Calibration Revisited". In: *ApJ* 631.1, pp. 231–243. DOI: 10.1086/432408.

Prochaska, J. X. et al. (2020). "PypeIt: The Python Spectroscopic Data Reduction Pipeline". In: *Journal of Open Source Software* 5.56, p. 2308. DOI: 10.21105/joss.02308.

Prochaska, J. X. et al. (Apr. 2020). *pypeit/PypeIt: Release 1.0.0*. Version v1.0.0. DOI: 10.5281/zenodo.3743493.

Prusinski, N. Z. and Y. Chen (Apr. 2024). *KCWIKit: KCWI Post-Processing and Improvements*. Astrophysics Source Code Library, record ascl:2404.003.

Revaz, Y. and P. Jablonka (Aug. 2018). "Pushing back the limits: detailed properties of dwarf galaxies in a ΛCDM universe". In: *A&A* 616, A96. DOI: 10.1051/0004-6361/201832669.

Román, J., A. Castilla, and J. Pascual-Granado (Dec. 2021). "Discovery and analysis of low-surface-brightness galaxies in the environment of NGC 1052". In: *A&A* 656, A44. DOI: 10.1051/0004-6361/202142161.

Ruiz-Lara, T. et al. (Sept. 2018). "Integrated-light analyses vs. colour-magnitude diagrams. II. Leo A: an extremely young dwarf in the Local Group". In: *A&A* 617, A18. DOI: 10.1051/0004-6361/201732398.

Salim, S., M. Boquien, and J. C. Lee (May 2018). "Dust Attenuation Curves in the Local Universe: Demographics and New Laws for Star-forming Galaxies and High-redshift Analogs". In: *ApJ* 859.1, p. 11. DOI: 10.3847/1538-4357/aabf3c.

Salim, S. et al. (Dec. 2007). "UV Star Formation Rates in the Local Universe". In: *ApJS* 173.2, pp. 267–292. DOI: 10.1086/519218.

Salim, S. et al. (Nov. 2016). "GALEX-SDSS-WISE Legacy Catalog (GSWLC): Star Formation Rates, Stellar Masses, and Dust Attenuations of 700,000 Low-redshift Galaxies". In: *ApJS* 227.1, p. 2. DOI: 10.3847/0067-0049/227/1/2.

Sánchez, S. F. et al. (Feb. 2012). "CALIFA, the Calar Alto Legacy Integral Field Area survey. I. Survey presentation". In: *A&A* 538, A8. DOI: 10.1051/0004-6361/201117353.

Sánchez, S. F. et al. (June 2013). "Mass-metallicity relation explored with CALIFA. I. Is there a dependence on the star-formation rate?" In: *A&A* 554, A58. DOI: 10.1051/0004-6361/201220669.

Sánchez-Blázquez, P. et al. (Sept. 2006). "Medium-resolution Isaac Newton Telescope library of empirical spectra". In: *MNRAS* 371.2, pp. 703–718. DOI: 10.1111/j.1365-2966.2006.10699.x.

Sanders, R. L. et al. (Dec. 2017). "Biases in Metallicity Measurements from Global Galaxy Spectra: The Effects of Flux Weighting and Diffuse Ionized Gas Contamination". In: *ApJ* 850.2, p. 136. DOI: 10.3847/1538-4357/aa93e4.

Sanders, R. L. et al. (Jan. 2020). "The MOSDEF survey: direct-method metallicities and ISM conditions at z ∼ 1.5-3.5". In: *MNRAS* 491.1, pp. 1427–1455. DOI: 10.1093/mnras/stz3032.

Sanders, R. L. et al. (June 2021). "The MOSDEF Survey: The Evolution of the Mass-Metallicity Relation from z = 0 to z 3.3". In: *ApJ* 914.1, p. 19. DOI: 10.3847/1538-4357/abf4c1.

Sarzi, M. et al. (Mar. 2006). "The SAURON project - V. Integral-field emission-line kinematics of 48 elliptical and lenticular galaxies". In: *MNRAS* 366.4, pp. 1151–1200. DOI: 10.1111/j.1365-2966.2005.09839.x.

Schlafly, E. F. and D. P. Finkbeiner (Aug. 2011). "Measuring Reddening with Sloan Digital Sky Survey Stellar Spectra and Recalibrating SFD". In: *ApJ* 737.2, p. 103. DOI: 10.1088/0004-637X/737/2/103.

Shajib, A. J. et al. (Oct. 2022). "LensingETC: A Tool to Optimize Multifilter Imaging Campaigns of Galaxy-scale Strong Lensing Systems". In: *ApJ* 938.2, p. 141. DOI: 10.3847/1538-4357/ac927b.

Shajib, A. J. et al. (Oct. 2022). *LensingETC: Lensing Exposure Time Calculator*. Astrophysics Source Code Library, record ascl:2210.027.

Shibuya, T. et al. (Apr. 2016). "Morphologies of ∼190,000 Galaxies at z = 0-10 Revealed with HST Legacy Data. II. Evolution of Clumpy Galaxies". In: *ApJ* 821.2, p. 72. DOI: 10.3847/0004-637X/821/2/72.

Siegel, M. H. et al. (Sept. 2007). "The ACS Survey of Galactic Globular Clusters: M54 and Young Populations in the Sagittarius Dwarf Spheroidal Galaxy". In: *ApJL* 667.1, pp. L57–L60. DOI: 10.1086/522003.

Skrutskie, M. F. et al. (Feb. 2006). "The Two Micron All Sky Survey (2MASS)". In: *AJ* 131.2, pp. 1163–1183. DOI: 10.1086/498708.

Soderblom, D. R. (Sept. 2010). "The Ages of Stars". In: *ARA&A* 48, pp. 581–629. DOI: 10.1146/annurev-astro-081309-130806.

Soto, K. T. et al. (May 2016). "ZAP - enhanced PCA sky subtraction for integral field spectroscopy". In: *MNRAS* 458.3, pp. 3210–3220. DOI: 10.1093/mnras/stw474.

Speagle, J. S. (Apr. 2020). "DYNESTY: a dynamic nested sampling package for estimating Bayesian posteriors and evidences". In: *MNRAS* 493.3, pp. 3132–3158. DOI: 10.1093/mnras/staa278.

Steidel, C. C. et al. (Nov. 2014). "Strong Nebular Line Ratios in the Spectra of z ∼2-3 Star Forming Galaxies: First Results from KBSS-MOSFIRE". In: *ApJ* 795.2, p. 165. DOI: 10.1088/0004-637X/795/2/165.

Steidel, C. C. et al. (Aug. 2016). "Reconciling the Stellar and Nebular Spectra of High-redshift Galaxies". In: *ApJ* 826.2, p. 159. DOI: 10.3847/0004-637X/826/2/159.

Strom, A. L. et al. (Feb. 2017). "Nebular Emission Line Ratios in z ≃ 2-3 Star-forming Galaxies with KBSS-MOSFIRE: Exploring the Impact of Ionization, Excitation, and Nitrogen-to-Oxygen Ratio". In: *ApJ* 836.2, p. 164. DOI: 10.3847/1538-4357/836/2/164.

Strom, A. L. et al. (Dec. 2018). "Measuring the Physical Conditions in High-redshift Star-forming Galaxies: Insights from KBSS-MOSFIRE". In: *ApJ* 868.2, p. 117. DOI: 10.3847/1538-4357/aae1a5.

Strom, A. L. et al. (Feb. 2022). "Chemical Abundance Scaling Relations for Multiple Elements in z ≃ 2-3 Star-forming Galaxies". In: *ApJ* 925.2, p. 116. DOI: 10.3847/1538-4357/ac38a3.

Strom, A. L. et al. (Nov. 2023). "CECILIA: The Faint Emission Line Spectrum of z 2-3 Star-forming Galaxies". In: *ApJL* 958.1, p. L11. DOI: 10.3847/2041-8213/ad07dc.

Sukay, E. et al. (Mar. 2022). "COOL-LAMPS II. Characterizing the Size and Star Formation History of a Bright Strongly Lensed Early-Type Galaxy at Redshift 1.02". In: *arXiv e-prints*, arXiv:2203.11957.

Sybilska, A. et al. (Sept. 2017). "The hELENa project - I. Stellar populations of early-type galaxies linked with local environment and galaxy mass". In: *MNRAS* 470.1, pp. 815–838. DOI: 10.1093/mnras/stx1138.

Thomas, D., C. Maraston, and R. Bender (July 2003). "New clues on the calcium underabundance in early-type galaxies". In: *MNRAS* 343.1, pp. 279–283. DOI: 10.1046/j.1365-8711.2003.06659.x.

Thomas, D. et al. (Mar. 2005). "The Epochs of Early-Type Galaxy Formation as a Function of Environment". In: *ApJ* 621.2, pp. 673–694. DOI: 10.1086/426932.

Thomas, D. et al. (June 2010). "Environment and self-regulation in galaxy formation". In: *MNRAS* 404.4, pp. 1775–1789. DOI: 10.1111/j.1365-2966.2010.16427.x.

Tinsley, B. M. (Jan. 1980). "Evolution of the Stars and Gas in Galaxies". In: *FCPh* 5, pp. 287–388. DOI: 10.48550/arXiv.2203.02041.

Toft, S. et al. (July 2012). "Deep Absorption Line Studies of Quiescent Galaxies at z ∼2: The Dynamical-mass-Size Relation and First Constraints on the Fundamental Plane". In: *ApJ* 754.1, p. 3. DOI: 10.1088/0004-637X/754/1/3.

Tomczak, A. R. et al. (Mar. 2014). "Galaxy Stellar Mass Functions from ZFOURGE/CANDELS: An Excess of Low-mass Galaxies since z = 2 and the Rapid Buildup of Quiescent Galaxies". In: *ApJ* 783.2, p. 85. DOI: 10.1088/0004-637X/783/2/85.

Topping, M. W. et al. (July 2020). "The MOSDEF-LRIS Survey: the interplay between massive stars and ionized gas in high-redshift star-forming galaxies". In: *MNRAS* 495.4, pp. 4430–4444. DOI: 10.1093/mnras/staa1410.

Torrey, P. et al. (Apr. 2019). "The evolution of the mass-metallicity relation and its scatter in IllustrisTNG". In: *MNRAS* 484.4, pp. 5587–5607. DOI: 10.1093/mnras/stz243.

Tran, K.-V. H. et al. (Oct. 2022). "The AGEL Survey: Spectroscopic Confirmation of Strong Gravitational Lenses in the DES and DECaLS Fields Selected Using Convolutional Neural Networks". In: *AJ* 164.4, p. 148. DOI: 10.3847/1538-3881/ac7da2.

Tremonti, C. A. et al. (Oct. 2004). "The Origin of the Mass-Metallicity Relation: Insights from 53,000 Star-forming Galaxies in the Sloan Digital Sky Survey". In: *ApJ* 613.2, pp. 898–913. DOI: 10.1086/423264.

Trussler, J. et al. (Feb. 2020). "Both starvation and outflows drive galaxy quenching". In: *MNRAS* 491.4, pp. 5406–5434. DOI: 10.1093/mnras/stz3286.

Vale Asari, N. et al. (Nov. 2019). "Diffuse ionized gas and its effects on nebular metallicity estimates of star-forming galaxies". In: *MNRAS* 489.4, pp. 4721–4733. DOI: 10.1093/mnras/stz2470.

Vargas, L. C., M. C. Geha, and E. J. Tollerud (July 2014). "The Distribution of Alpha Elements in Andromeda Dwarf Galaxies". In: *ApJ* 790.1, p. 73. DOI: 10.1088/0004-637X/790/1/73.

Vaughan, S. P. et al. (Oct. 2022). "The SAMI galaxy survey: Galaxy size can explain the offset between star-forming and passive galaxies in the mass-metallicity relationship". In: *MNRAS* 516.2, pp. 2971–2987. DOI: 10.1093/mnras/stac2304.

Vazdekis, A. et al. (May 2015). "Evolutionary stellar population synthesis with MILES - II. Scaled-solar and α-enhanced models". In: *MNRAS* 449.2, pp. 1177–1214. DOI: 10.1093/mnras/stv151.

Vazdekis, A. et al. (Dec. 2016). "UV-extended E-MILES stellar population models: young components in massive early-type galaxies". In: *MNRAS* 463.4, pp. 3409–3436. DOI: 10.1093/mnras/stw2231.

Veilleux, S., G. Cecil, and J. Bland-Hawthorn (Sept. 2005). "Galactic Winds". In: *ARA&A* 43.1, pp. 769–826. DOI: 10.1146/annurev.astro.43.072103.150610.

Villaume, A. et al. (June 2017). "The Extended IRTF Spectral Library: Expanded Coverage in Metallicity, Temperature, and Surface Gravity". In: *ApJS* 230.2, p. 23. DOI: 10.3847/1538-4365/aa72ed.

Walcher, C. J. et al. (Oct. 2015). "Abundance patterns in early-type galaxies: is there a "knee" in the [Fe/H] vs. [α/Fe] relation?" In: *A&A* 582, A46. DOI: 10.1051/0004-6361/201525924.

Weinberger, R. et al. (Sept. 2018). "Supermassive black holes and their feedback effects in the IllustrisTNG simulation". In: *MNRAS* 479.3, pp. 4056–4072. DOI: 10.1093/mnras/sty1733.

Weisz, D. R. et al. (July 2014). "The Star Formation Histories of Local Group Dwarf Galaxies. I. Hubble Space Telescope/Wide Field Planetary Camera 2 Observations". In: *ApJ* 789.2, p. 147. DOI: 10.1088/0004-637X/789/2/147.

Westfall, K. B. et al. (Dec. 2019). "The Data Analysis Pipeline for the SDSS-IV MaNGA IFU Galaxy Survey: Overview". In: *AJ* 158.6, p. 231. DOI: 10.3847/1538-3881/ab44a2.

Wright, E. L. et al. (Dec. 2010). "The Wide-field Infrared Survey Explorer (WISE): Mission Description and Initial On-orbit Performance". In: *AJ* 140.6, pp. 1868–1881. DOI: 10.1088/0004-6256/140/6/1868.

Yates, R. M. et al. (Feb. 2020). "Present-day mass-metallicity relation for galaxies using a new electron temperature method". In: *A&A* 634, A107. DOI: 10.1051/0004-6361/201936506.

York, D. G. et al. (Sept. 2000). "The Sloan Digital Sky Survey: Technical Summary". In: *AJ* 120.3, pp. 1579–1587. DOI: 10.1086/301513.

Young, L. M. and K. Y. Lo (Feb. 1997). "The Neutral Interstellar Medium in Nearby Dwarf Galaxies. II. NGC 185, NGC 205, and NGC 147". In: *ApJ* 476.1, pp. 127–143. DOI: 10.1086/303618.

Zahid, H. J. et al. (July 2013). "The Chemical Evolution of Star-forming Galaxies over the Last 11 Billion Years". In: *ApJL* 771.2, p. L19. DOI: 10.1088/2041-8205/771/2/L19.

Zahid, H. J. et al. (Sept. 2017). "Stellar Absorption Line Analysis of Local Star-forming Galaxies: The Relation between Stellar Mass, Metallicity, Dust Attenuation, and Star Formation Rate". In: *ApJ* 847.1, p. 18. DOI: 10.3847/1538-4357/aa88ae.

Zhang, K. et al. (Apr. 2017). "SDSS-IV MaNGA: the impact of diffuse ionized gas on emission-line ratios, interpretation of diagnostic diagrams and gas metallicity measurements". In: *MNRAS* 466.3, pp. 3217–3243. DOI: 10.1093/mnras/stw3308.

Zhuang, Z. et al. (Oct. 2021). "NGC 147 Corroborates the Break in the Stellar Mass-Stellar Metallicity Relation for Galaxies". In: *ApJ* 920.1, p. 63. DOI: 10.3847/1538-4357/ac1340.

Zhuang, Z. et al. (May 2023). "A Glimpse of the Stellar Populations and Elemental Abundances of Gravitationally Lensed, Quiescent Galaxies at z $\gtrsim$ 1 with Keck Deep Spectroscopy". In: *ApJ* 948.2, p. 132. DOI: 10.3847/1538-4357/acc79b.

Zhuang, Z. et al. (Sept. 2024). "Metals in Star-forming Galaxies with KCWI. I. Methodology and First Results on the Abundances of Iron, Magnesium, and Oxygen". In: *ApJ* 972.2, p. 182. DOI: 10.3847/1538-4357/ad5ff8.

Zibetti, S. et al. (Jan. 2020). “Insights into formation scenarios of massive early-type galaxies from spatially resolved stellar population analysis in CALIFA”. In: *MNRAS* 491.3, pp. 3562–3585. DOI: 10.1093/mnras/stz3205.